UNIVERSITÀ DI PARMA

UNIVERSITA' DEGLI STUDI DI PARMA

DOTTORATO DI RICERCA IN INGEGNERIA INDUSTRIALE

CICLO XXXII

UNCERTAINTY QUANTIFICATION METHODOLOGIES FOR COOLING SYSTEMS IN GAS TURBINE APPLICATIONS

Coordinatore:
Chiar.mo Prof. Gianni Royer Carfagni

Tutore:
Chiar.mo Prof. Marco Silvestri

Co-Tutore:
Chiar.mo Prof. Bruno Facchini

Dottorando: Andrea Gamannossi

Anni 2016/2019

Vorrei ringraziare il mio relatore, il Prof. Marco Silvestri e l'Università degli Studi di Parma per avermi permesso di intraprendere questa bellissima opportunità e per aver creduto in me fin dall'inizio. Vorrei ringraziare inoltre il mio co-relatore Prof. Bruno Facchini e il Prof. Antonio Andreini per la pazienza e la disponibilità mostrata nei miei confronti, nonché per il supporto tecnico fornitomi durante tutti questi tre anni di percorso e per avermi permesso di intraprendere svariate collaborazioni aziendali. Un ringraziamento speciale lo devo all'Università degli Studi di Firenze, e in particolar modo l'HTC Group del Prof. Facchini, per avermi messo a disposizione mezzi e persone straordinarie che mi hanno aiutato durante tutto il percorso di tesi. È stato veramente un piacere collaborare con loro per raggiungere gli obiettivi prefissati. Vorrei citare in particolar modo l'Ing. Lorenzo Mazzei per tutto il supporto e l'aiuto fornitomi nel portare a termine questo percorso e per non aver mai smesso di credere in me. Mi piacerebbe inoltre ringraziare Alberto Amerini per la stretta collaborazione che ci ha visto uniti nella fase finale di tesi e per il suo prezioso aiuto.

Mi piacerebbe dedicare questo traguardo alla mia famiglia che mi ha sempre incoraggiato e supportato in questo percorso senza mai ostacolarmi in alcun modo e lasciandomi libero di prendere le decisioni che meglio credevo.

Vorrei infine ringraziare Martina, che malgrado la distanza mi è stata vicina fin dall'inizio e mi ha sempre incoraggiato in questo percorso nonostante le varie difficoltà affrontate.

Abstract

Historically, the design of turbomachinery components was mainly done through experimental tests; over the years, with the increase of computing resources, there has been increasing use of computational analysis. Numerical simulations are important tools for designers because they allow having a complete understanding of the problem, in relatively short times and with low general costs. Although these analyses have a good predictive level, they are often used when input quantities that characterize the problem are roughly known. These gaps lead to the inclusion of uncertainties within the code, which propagate and eventually influence the solution. In the last fifteen years, statistical aspects have been combined into numerical simulations in order to assess the influence of the unknown parameters in the initial stages of the project. The final common objective is to optimize the various components in order to find out the configuration in which the machine is independent of the uncertainties that may afflict it, thus arriving at a robust design.

The aim of this thesis was to explore and apply several methodologies of "uncertainty quantification" (UQ) to numerical codes used in turbomachinery applications, which allow estimating the uncertainties that affect the results of numerical simulations. Both sampling-based methods and stochastic expansion methods were investigated. After an initial benchmarking phase, the software DAKOTA was selected to carry out the UQ analyses.

The first part of the work involved a 1-D thermal analysis on a full annular lean-burn aeronautical combustor tested at CIAM during the LEMCOTEC (Low Emissions COre-engine TEChnologies) European project. The analysis was carried out using the one-dimensional code "Therm-1D", developed by DIEF of the University of Florence. Three main uncertainty analyses were investigated depending on the input parameters considered: geometrical, heat transfer coefficient tuning factors, and thermal loads. In particular, the classical Monte Carlo analysis is compared with four stochastic expansion processes: Gauss quadrature, total order with LHS sampling, stochastic collocation, and Smolyak. The analyses proved how these methods give optimum results with a sensible lower amount of simulations. Lastly, an analysis including all the input variables considered was performed and results were compared with experimental data. Working on a 1-D solver has allowed obtaining a large amount of data with modest computational costs: this part was crucial in order to better understand the different methodologies and to have a clearer picture of the potentialities of the software.

The second part of the work focused on applying the acquired concepts to a high-fidelity code. Based on an experimental study, a full 3-D computational fluid dynamic (CFD) study using the software ANSYS was carried out in order to assess the film cooling performance of a prismatic gas turbine vane made by additive manufacturing. Both steady and unsteady simulations were performed: the first ones using a RANS approach and the latter using a hybrid LES-RANS approach. For the UQ analysis, only RANS simulations in conjunction with a specific stochastic expansion method were adopted to save computational resources. The influences of the geometric uncertainties of the holes were evaluated: the hole dimension, the streamwise inclination

angle and the inlet fillet radius of the hole. Output parameters considered were the film cooling effectiveness, the blowing ratio and the discharge coefficients of the holes. Results will show how a polynomial chaos approach that required 8 evaluations is able to reproduce what the standard Monte Carlo analysis does (with more than 1000 evaluations) with an optimum grade of accuracy. Moreover, results prove how the position tolerance of the holes on the blade, as well as the hole dimension, is extremely important for the film cooling effectiveness, in particular when dealing with additive manufacturing processes.

Table of Contents

1 - Introduction 1
1.1 - Details of Uncertainty Quantification 3
1.2 - Uncertainties related to turbomachinery 4
1.2.1 - Manufacturing processes and roughness 8
1.3 - Uncertainty Quantification procedures 9
1.4 - Heat transfer and cooling in gas turbine 12
1.4.1 - Basics of heat transfer 12
1.4.2 - Cooling techniques 14
1.5 - Additive manufacturing 17
1.6 - Thesis structure 19
2 - Uncertainty Quantification 21
2.1 - Probability theory 21
2.1.1 - Probability and distribution 22
2.1.2 - Continuous random variable 23
2.1.3 - Statistical moments 26
2.2 - Stochastic processes 28
2.2.1 - Convergence in distribution 29
2.3 - Theory of approximation 29
2.3.1 - Orthogonal polynomials 29
2.3.2 - Polynomial interpolation 32
2.3.3 - Stochastic systems 32
2.4 - Uncertainty quantification methodologies 33
2.4.1 - Sampling based methods 33
2.4.2 - Stochastic expansion methods 34
2.4.3 - Spectral projection 38
2.4.4 - Linear regression 40
2.4.5 - Analytics moments 41
2.5 - UQ software 41
2.5.1 - DAKOTA 42
2.5.2 - Python libraries 43
2.5.3 - MATLAB environment 44
2.6 - Sensitivity analysis 44
2.7 - Bibliography 45
3 - UQ analysis on low-order-code 53

3.1 - Aeronautical combustors 53
3.1.1 - RQL combustors 55
3.1.2 - Lean combustors 56
3.1.3 - Combustor cooling 57
3.2 - LEMCOTEC project 59
3.2.1 - One-dimensional approach 60
3.2.2 - Therm-1D 61
3.3 - Uncertainty quantification analysis 62
3.3.1 - Test case 63
3.3.2 - Uncertain variables and simulations 64
3.3.3 - DAKOTA / Therm-1D interface 67
3.4 - Results 68
3.4.1 - Geometric analysis results 70
3.4.2 - Heat transfer factor analysis results 76
3.4.3 - Boundary conditions analysis results 78
3.4.4 - Comparison among analyses 81
3.4.5 - Overall analysis and Smolyak grid validation 82
4 - UQ analysis applied to CFD 87
4.1 - Film cooling 87
4.1.1 - Literature review 89
4.2 - Test case 94
4.2.1 - Mass transfer analogy 95
4.2.2 - Results 96
4.3 - Numerical methodology 98
4.3.1 - Numerical setup 101
4.3.2 - Results validation 104
4.3.3 - Unsteady approach 109
4.4 - UQ analysis 112
4.4.1 - Uncertain variables 113
4.4.2 - Results 118
Conclusion 127
Bibliography 131

List of Figures

FIGURE 1.1 – TIT INCREASING OVER THE YEARS [1] 1
FIGURE 1.2 – GAS TURBINE MAIN UNCERTAINTIES [2] 2
FIGURE 1.3 – SCHEME OF A DETERMINISTIC SIMULATION [4] 2
FIGURE 1.4 – ERRORS [9] 3
FIGURE 1.5 – UNCERTAINTIES [9] 4
FIGURE 1.6 – BLADE COOLING SYSTEM [27] 6
FIGURE 1.7 – MANUFACTURING TOLERANCES AND EFFECTS ON BLADE COOLING [2] 7
FIGURE 1.8 – RESULTS OBTAINED IN [17] 8
FIGURE 1.9 – (A) AM COOLING HOLE, VERTICAL (B) AM COOLING HOLE, HORIZONTAL (C) EDM COOLING HOLE [29] 9
FIGURE 1.10 – UNCERTAINTIES IN AERONAUTICAL GAS TURBINES [17] 9
FIGURE 1.11 – SCHEMATIC PROCEDURE OF A UQ ANALYSIS [4] 11
FIGURE 1.12 – UNCERTAINTY QUANTIFICATION PROCEDURE [7] 11
FIGURE 1.13 – DEVELOPMENT OF THE VELOCITY BOUNDARY LAYER (*COURTESY OF UNIVERSITY OF FLORENCE*) 13
FIGURE 1.14 – THERMAL BOUNDARY LAYER OVER A FLAT PLATE (*COURTESY OF UNIVERSITY OF FLORENCE*) 13
FIGURE 1.15 – THERMAL BOUNDARY LAYER (*COURTESY OF UNIVERSITY OF FLORENCE*) 14
FIGURE 1.16 – TYPICAL AIRFOIL COOLING DESIGN FOR A MODERN HIGH-PRESSURE GAS TURBINE BLADE [38] 15
FIGURE 1.17 – TURBINE VANE CROSS-SECTION WITH IMPINGEMENT AND TE PIN-FINS [39] 16
FIGURE 1.18 – ORTHOGONAL, ANGLED AND V-SHAPED RIB-INDUCED SECONDARY FLOW [40] 16
FIGURE 1.19 – POWDER BED AM TECHNIQUE [48] 18
FIGURE 1.20 – POWDER FEED AM TECHNIQUE [48] 18
FIGURE 1.21 – WIRE FEED AM TECHNIQUE [48] 18
FIGURE 2.1 – FUNCTION X(Ω) [51] 22
FIGURE 2.2 – PROBABILITY AND CUMULATIVE FUNCTIONS FOR GAUSSIAN DISTRIBUTION 23
FIGURE 2.3 – NORMAL DISTRIBUTION 24
FIGURE 2.4 – NORMAL DISTRIBUTIONS WITH DIFFERENT MEAN VALUE AND STANDARD DEVIATION 25
FIGURE 2.5 – STANDARDISED NORMAL DISTRIBUTION INTERVALS 26
FIGURE 2.6 – NON-SYMMETRIC DISTRIBUTION 27
FIGURE 2.7 – DIFFERENT KURTOSIS PDF 27
FIGURE 2.8 – ASKEY'S SCHEME FOR DIFFERENT POLYNOMIALS [57] 30
FIGURE 2.9 – GRAPHIC REPRESENTATION OF THE FIRST 6 LEGENDRE'S POLYNOMIALS 31

FIGURE 2.10 – GRAPHIC REPRESENTATION OF THE FIRST 6 HERMITE'S POLYNOMIALS 31

FIGURE 2.11 – LHS SAMPLING FOR TWO VARIABLES 34

FIGURE 2.12 – TOTAL-ORDER EXPANSION (LEFT); TENSOR-PRODUCT EXPANSION (RIGHT) [57] 36

FIGURE 2.13 – NUMBER OF EVALUATIONS REQUIRED FOR DIFFERENT ORDER (A) AND VARIABLES (B) [57] 37

FIGURE 2.14 – POINTS REQUIRED WITH THE GAUSS GRID (5TH ORDER) AND SMOLYAK (1ST LEVEL) [51] 40

FIGURE 2.15 – VISUAL COMPARISON FOR DIFFERENT LEVELS OF SMOLYAK AND GAUSS FOR A TWO VARIABLES PROBLEM [51] 40

FIGURE 2.16 – GENERAL UQ ANALYSIS PROCEDURE USING DAKOTA [57] 42

FIGURE 2.17 – MAIN CHARACTERISTICS OF DIFFERENT SOFTWARE [63] 43

FIGURE 2.18 – ANALYSES AND RESULTS CARRIED OUT BY DUROCHER ET AL. [67] 46

FIGURE 2.19 – (A) CONFIDENCE INTERVAL OF 99% FOR TEMPERATURE AS A FUNCTION OF MIXTURE FRACTION; (B) CONFIDENCE INTERVAL OF 99% FOR THE MASS FRACTION OF CO; (C) COMPARISON OF AVERAGE OVER-TIME RADIAL TEMPERATURE PROFILE; (D) COMPARISON OF AVERAGE RADIAL FRACTION PROFILE BY MASS OF CO [69] 47

FIGURE 2.20 – TEST CASE ANALYSED BY D'AMMARO ET AL. [70] 48

FIGURE 2.21 – FILM COOLING EFFECTIVENESS FOR MC APPROACH AND PCE 2ND AND 4TH ORDER [70] 48

FIGURE 2.22 – EVOLUTION $\sigma T/\mathbb{E}(T)$ FOR DIFFERENT BR (A); EFFECTIVENESS AND RELATIVE UNCERTAINTY (B) [71] 49

FIGURE 2.23 – (A) EFFECTIVENESS ON THE CENTRELINE AND SPANWISE AVERAGE IN 95% CONFIDENCE INTERVAL; (B) COMPARISON OF PROBABILITY DISTRIBUTION OF Cd. SHI ET AL. [73] 50

FIGURE 2.24 – (A) 1ST STAGE NOZZLE ANALYSED; (B) PROBABILITY DISTRIBUTION [26] 50

FIGURE 2.25 – (A) BLADE TEMPERATURE DISTRIBUTION; (B) SENSITIVITY ANALYSIS [26] 51

FIGURE 3.1 – GENERAL LAYOUT OF AN AERONAUTICAL COMBUSTOR [74] 53

FIGURE 3.2 – NOx EMISSION LIMITS FOR ENGINES WITH THRUST GREATER THAN $89kN$ [75] 54

FIGURE 3.3 – EUROPEAN PROJECT CLEAN SKY OBJECTIVES [76] 54

FIGURE 3.4 – (A) EMISSIONS AS A FUNCTION OF Φ. (B) RQL COMBUSTOR CONDITIONS [74] 55

FIGURE 3.5 – LEAN COMBUSTOR PERFORMANCE 56

FIGURE 3.6 – AIR SPLITTING FOR RQL (A) AND LEAN (B) [78] 56

FIGURE 3.7 – MAIN COOLING TECHNIQUES: CONVECTIVE AND TRANSPIRATION [79] 57

FIGURE 3.8 – (A) EFFUSION COOLING (B) HEAT REMOVAL AND PROTECTION 57

FIGURE 3.9 – KREWINKEL RESULTS [82] 58

FIGURE 3.10 – ADIABATIC EFFECTIVENESS WITH VARYING BR AND Tu [86] 58

FIGURE 3.11 – (A) NEWAC COMBUSTOR (GE AVIO) (B) TEMPERATURE DISTRIBUTION FOR THE APPROACH CONDITION ESTIMATED BY BERTINI ET AL. [90]. 59

FIGURE 3.12 – CONDITIONS TESTED AT CIAM AND SIMULATED (TAKE-OFF) OF THE LEMCOTEC COMBUSTOR [77] 59

FIGURE 3.13 – (A) HEAT TRANSFER IN THE COMBUSTOR [74] (B) 1D THERMAL FLUX SCHEME [92] 60

FIGURE 3.14 – THERM-1D PROCEDURE 61

FIGURE 3.15 – FLOW NETWORK DISCRETIZATION 63
FIGURE 3.16 – INCLINATION ANGLE 65
FIGURE 3.17 – UQ ANALYSIS DIAGRAM WITH THERM-1D 68
FIGURE 3.18 – COMPARISON AMONG RESULTS: THERM-1D, EXPERIMENTAL TEST AT CIAM, AND CFD [77] 69
FIGURE 3.19 – MEAN VALUES OF Tw 70
FIGURE 3.20 – (A) MAXIMUM AND MINIMUM VALUES OF Tw (B) STANDARD DEVIATION 71
FIGURE 3.21 – COMPARISON PCE (QUADRATURE ORDER) AND SC 72
FIGURE 3.22 – ORDER SENSITIVITY FOR PCE QUADRATURE ORDER (A) AND SC (B) 72
FIGURE 3.23 – PCE TOTAL ORDER 2 WITHOUT OVER-SAMPLING (A) AND WITH DOUBLE OVER-SAMPLING (B) 73
FIGURE 3.24 – MEAN VALUES FOR DIFFERENT ORDERS OF PCE WITH TOTAL ORDER 73
FIGURE 3.25 – (A) MAXIMUM AND MINIMUM VALUES FOR PCE TOTAL ORDER (B) STANDARD DEVIATION 74
FIGURE 3.26 – COMPARISON BETWEEN MC AND PCE FOR MEAN VALUES (A) AND STANDARD DEVIATION (B) 74
FIGURE 3.27 – GEOMETRIC ANALYSIS OUTPUT PROBABILITY: (A) MC (B) PCE TENSOR-PRODUCT (C) PCE TOTAL ORDER (D) SC 75
FIGURE 3.28 – SENSITIVITY ANALYSIS FOR GEOMETRIC PARAMETERS 76
FIGURE 3.29 – COMPARISON HTC ANALYSIS (A) TEMPERATURE (B) STANDARD DEVIATION 77
FIGURE 3.30 – SENSITIVITY ANALYSIS FOR HEAT TRANSFER TUNING FACTORS ANALYSIS 77
FIGURE 3.31 – OUTPUT PROBABILITY FOR HTC ANALYSIS (A) MC (B) PCE TENSOR PRODUCT (C) PCE TOTAL ORDER (D) SC 78
FIGURE 3.32 – BOUNDARY CONDITION ANALYSIS COMPARISON (A) Tw (B) STANDARD DEVIATION 79
FIGURE 3.33 – BOUNDARY CONDITIONS SENSITIVITY ANALYSIS 79
FIGURE 3.34 – BOUNDARY CONDITIONS ANALYSIS OUTPUT PROBABILITY (A) MC (B) PCE TENSOR PRODUCT (C) PCE TOTAL ORDER (D) SC 80
FIGURE 3.35 – PROBABILISTIC MAP INCLUDING EXPERIMENTAL DATA 81
FIGURE 3.36 – COMPARISON FOR (A) Tw (B) STANDARD DEVIATION 82
FIGURE 3.37 – NUMBER OF EVALUATIONS REQUIRED BY EACH METHOD 83
FIGURE 3.38 – MONTE CARLO SENSITIVITY ANALYSIS (A) Tw (B) STANDARD DEVIATION 83
FIGURE 3.39 – SMOLYAK GRID ORDER SENSITIVITY (A) Tw (B) STANDARD DEVIATION 84
FIGURE 3.40 – COMPARISONS (A) Tw (B) STANDARD DEVIATION 84
FIGURE 3.41 – PROBABILISTIC MAPS (A) MC (B) PCE SMOLYAK (C) PCE GAUSS (D) PCE TOTAL ORDER 85
FIGURE 3.42 – SENSITIVITY ANALYSIS FOR THE OVERALL ANALYSIS 86
FIGURE 4.1 – FILM COOLING CONFIGURATION [94] 87
FIGURE 4.2 – FILM COOLING CHARACTERISTICS 88
FIGURE 4.3 – FILM COOLING EFFECTIVENESS FOR A SINGLE HOLE FOR DIFFERENT DISTANCES AND M [95] 89
FIGURE 4.4 – MEAN FILM COOLING EFFECTIVENESS ALONG STREAMWISE DIRECTION FOR DIFFERENT M [96] 89

FIGURE 4.5 – COMPARISON BETWEEN STANDARD AND SHAPED COOLING HOLES [98] 90
FIGURE 4.6 – COMPARISON OF GEOMETRIES FOR DIFFERENT OPERATING CONDITIONS [100] 91
FIGURE 4.7 – FILM COOLING EFFECTIVENESS PERFORMANCE VARYING DENSITY RATIO [102] 91
FIGURE 4.8 – COMPARISON BETWEEN STRAIGHT COOLING HOLES (TOP) AND ANGLED (BOTTOM) [103] 92
FIGURE 4.9 – COMPARISON OF FILM COOLING PERFORMANCE BETWEEN IDEAL AND REAL GEOMETRY AT DIFFERENT BR [110] 93
FIGURE 4.10 – FILM COOLING EFFECTIVENESS FOR DIFFERENT ADDITIVE MANUFACTURING PROCESSES [112] 93
FIGURE 4.11 – INTERNAL CONVECTIVE COOLING CHANNEL [113] 94
FIGURE 4.12 – (A) TEST RIG (B) BLADE OPTICAL ACCESSES DETAILS [114] 94
FIGURE 4.13 – ANALOGY BETWEEN HEAT (A) AND MASS TRANSFER (B) [94] 95
FIGURE 4.14 – PSP MEASURING TECHNIQUE, PRINCIPLE OF OPERATION AND COMPONENTS [94] 96
FIGURE 4.15 – GEOMETRICAL DETAIL OF THE VANE CONSIDERED [114] 97
FIGURE 4.16 – OPERATING CONDITIONS [114] 97
FIGURE 4.17 – AVERAGE FILM COOLING EFFECTIVENESS 1D PROFILE [114] 98
FIGURE 4.18 – GEOMETRIC DETAILS OF THE SHAPED HOLES 99
FIGURE 4.19 – (A) FLUID DOMAIN (B) INTERNAL COOLANT CHANNEL 99
FIGURE 4.20 – RESULTING PORTION OF THE FLUID DOMAIN CONSIDERED $hH = 7.3\%$ 100
FIGURE 4.21 – REDUCED FLUID DOMAIN ADOPTED FOR THE UQ ANALYSIS 101
FIGURE 4.22 – INLET PLENUM FOR $CO2$ AND THE PORTION OF THE AERODYNAMIC PROFILE CONSIDERED IN THE ANALYSIS 102
FIGURE 4.23 – BOUNDARY CONDITIONS IMPOSED FORM THE SIMULATION 103
FIGURE 4.24 – MESH SENSITIVITY RESULTS 104
FIGURE 4.25 – MESH DETAILS 104
FIGURE 4.26 – COMPARISON BETWEEN NUMERICAL AND EXPERIMENTAL RESULTS OF BACCI ET AL. [114] 105
FIGURE 4.27 – REDUCED DOMAIN RESULTS VALIDATION 106
FIGURE 4.28 – DETAILS OF FILM COOLING EFFECTIVENESS MAPS 107
FIGURE 4.29 – COMPARISON BETWEEN EXPERIMENTAL (A) AND NUMERICAL RESULTS (B) 108
FIGURE 4.30 – MACH NUMBER INSIDE THE HOLES 108
FIGURE 4.31 – 32 MILLION ELEMENTS MESH FOR UNSTEADY CALCULATION 110
FIGURE 4.32 – SHIELDING FUNCTION FOR SBES SIMULATION 110
FIGURE 4.33 – INSTANTANEOUS CO_2 MASS FRACTION A) CROSS-SECTIONAL VIEW 1ST AND 3RD HOLE B) SUCTION SIDE 111
FIGURE 4.34 – AVERAGE CO_2 MASS FRACTION FOR THE SUCTION SIDE 111
FIGURE 4.35 – AVERAGE FILM COOLING EFFECTIVENESS PROFILES ON THE SUCTION SIDE 112
FIGURE 4.36 – HOLES GEOMETRIES 114

FIGURE 4.37 – FIRST ROW OF HOLES DRILLING PROBLEM 115

FIGURE 4.38 – INCLINATION ANGLE FOR THE THIRD ROW OF HOLES 115

FIGURE 4.39 – FILLET RADIUS EVALUATED POINTS 116

FIGURE 4.40 – SCALE FACTORS USED FOR THE EVALUATIONS 117

FIGURE 4.41 – SURROGATE MODEL RESULTS 119

FIGURE 4.42 – FILM COOLING EFFECTIVENESS PROBABILITY MAP 120

FIGURE 4.43 – FILM COOLING SENSITIVITY ANALYSIS USING SOBOL'S INDICES 121

FIGURE 4.44 – HOLES LOCATION 122

FIGURE 4.45 – BR PROBABILITY DISTRIBUTION FOR THE THREE ROWS OF HOLES 123

FIGURE 4.46 – BR PROBABILITY DISTRIBUTION 124

FIGURE 4.47 – Cd PROBABILITY DISTRIBUTION FOR THE THREE ROWS OF HOLES 124

FIGURE 4.48 – Cd PROBABILITY DISTRIBUTION 124

FIGURE 4.49 – SENSITIVITY ANALYSIS OF BR AND Cd TO THE THREE VARIABLES FOR THE THREE HOLES 125

List of Tables

TABLE 3.1 – DIFFERENT ANALYSES CARRIED OUT 64

TABLE 3.2 – GEOMETRIC VARIABLES PROBABILITY DISTRIBUTION 66

TABLE 3.3 – PROBABILITY DISTRIBUTION FOR HEAT TRANSFER TUNING FACTORS 66

TABLE 3.4 – PROBABILITY DISTRIBUTION FOR BOUNDARY CONDITIONS VARIABLES 67

TABLE 4.1 – BOUNDARY CONDITIONS 102

TABLE 4.2 – MESH SENSITIVITY DETAILS 103

TABLE 4.3 – EVALUATIONS REQUIRED 118

Nomenclature

Acronyms

AIAA	American Institute of Aeronautics and Astronautics
AR	Area Ratio
AM	Additive Manufacturing
BR	Blowing Ratio
CAD	Computer-Aided Design
CAEP	Committee on Aviation Environmental Protection
CDF	Cumulative Distribution Function
CFD	Computational Fluid Dynamics
CIAM	Central Institute of Aviation Motors
CR	Collocation Ratio
DIEF	Department of Industrial Engineering of Florence
DR	Density Ratio
EDM	Electrical Discharge Machining
FAR	Fuel Air Ratio
FEM	Finite Element Method
GE	General Electric
HTC	Heat Transfer Coefficient
ICAO	International Civil Aviation Organization
LE	Leading Edge
LHS	Latin Hypercube Sampling
MC	Monte Carlo
NHFR	Net Heat Flux Reduction
PCE	Polynomial Chaos Expansion
PDF	Probability Density Distribution
PS	Pressure Side
PSP	Pressure Sensitive Paint
RANS	Reynolds Averaged Navier-Stokes
RQL	Rich-Quench-Lean
SC	Stochastic Collocation
SS	Suction Side
SST	Shear Stress Transport
TE	Trailing Edge
TIT	Turbine Inlet Temperature
UQ	Uncertainty Quantification
VR	Velocity Ratio

Symbols

$\mathcal{B}$	events	
C	Mass fraction	$[-]$
Cov	Covariance	
D	Diameter	$[mm]$
d	Dimension, number of aleatory variables	$[-]$
$\mathbb{E}$	Expected value	
F	Probability distribution	$[-]$
f	Probability density	$[-]$
h	Height	$[mm]$
H	Total height	$[mm]$
He	Hermite's polynomials	
Ku	Kurtosis [-]	$[-]$
l	Smolyak grid level	
L	Length	$[mm]$
Le	Lewis' polynomials	
L_e	Lewis' number	$[-]$
M	Blowing Ratio	$[-]$
N	Sampling dimension	
n	Molar mass	$[kg\ mol^{-1}]$
$\mathcal{N}$	Normal distribution	
P	Probability	$[-]$
P	Pressure	$[Pa]$
p	Geometric pitch	$[mm]$
Q	Interpolating polynomial	
q	Thermal flux	$[W\ m^2\ K^{-1}]$
$\mathbb{R}$	Real numbers	
R	Generic response function	
R	Gas constant	$[J\ kg^{-1}K^{-1}]$
r	Fillet radius	$[mm]$
Re	Reynolds' number	$[-]$
S	Sobol's indices	$[-]$
s	Non-dimensional abscissa	$[-]$
sk	Skewness	$[-]$
T	Temperature	$[K]$
T_u	Turbulence intensity	$[-]$
v	Velocity	$[m/s]$
Var	Variance	
X	Continuous random variable	

Z	Standardised random variable	
Z	Mixture fraction	$[-]$

Greek letters

α	Inclination angle	$[°]$
γ	Adiabatic index	$[-]$
η	Adiabatic effectiveness	$[-]$
ρ	Density	$[kg\ m^{-3}]$
σ	Standard deviation	
μ	Mean value	
Ω	Probability space	
φ	Overall effectiveness	$[-]$
ϕ	Equivalence ratio	$[-]$
ω	Measures space	

Subscripts

aw	Adiabatic wall
w	Wall
c, f	Cooling flow
∞	Main flow
0	Total conditions
is	Isentropic conditions

1 - Introduction

Technological development related to materials and manufacturing processes has led to a significant improvement in the reliability of gas turbines.

Despite the technical progress, the operating conditions of the machines remain critical, this is due to the fact that the greatest contribution to the increase in engine efficiency is given by the increase in the Turbine Inlet Temperature (TIT) (Figure 1.1).

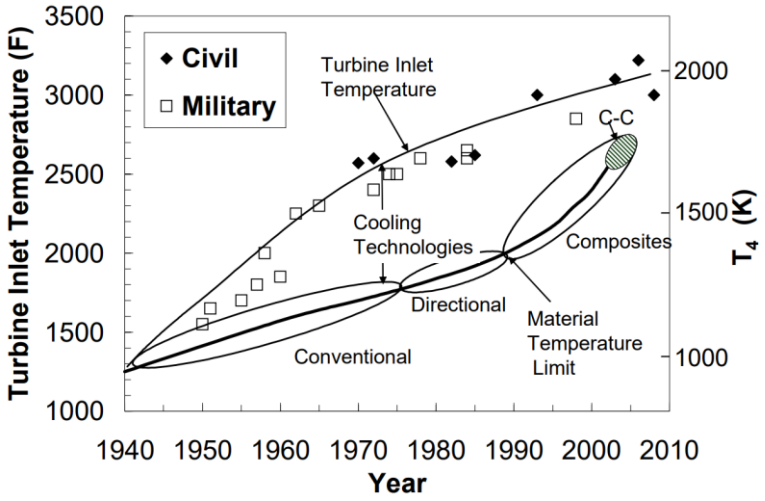

Figure 1.1 – TIT increasing over the years [1]

A careful design of both machines and cooling systems is mandatory, which requires extremely precise manufacturing processes: small geometric variations can have a strong impact on the performance and life of the machines.

Often design is based on simplified approaches; in the initial phase of the design process it is not necessary to have a complete knowledge of all the phenomena involved, but it is essential to know the most promising configurations, which will then be refined with computational fluid dynamics and finally validated with experimental tests.

It is known that each manufacturing process is associated with a certain tolerance that depends on the processing itself, but these aspects are usually not included in the computational analysis.

The uncertainties in numerical simulations are not only of a geometric nature (Figure 1.2), for example all parameters assumed as inputs or boundary conditions that were measured directly or indirectly during experimental campaigns; even in this case, although the instrument can be well calibrated, it is known that the measurement will always be affected by an uncertainty.

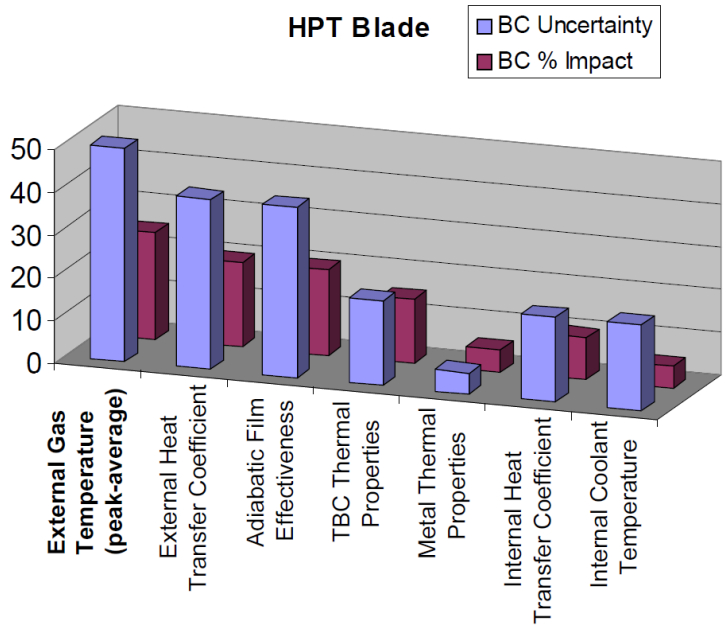

Figure 1.2 – Gas turbine main uncertainties [2]

Another important aspect of the computational approaches is related to the fact that the real initial problem is modelled in order to be solved (Figure 1.3): the studied case can present a reduced domain in comparison to the initial geometry, it is discretized both at spatial level, through a grid of calculation, and mathematical level and finally, as it happens for the great majority of the industrial applications, its turbulence is modelled [3].

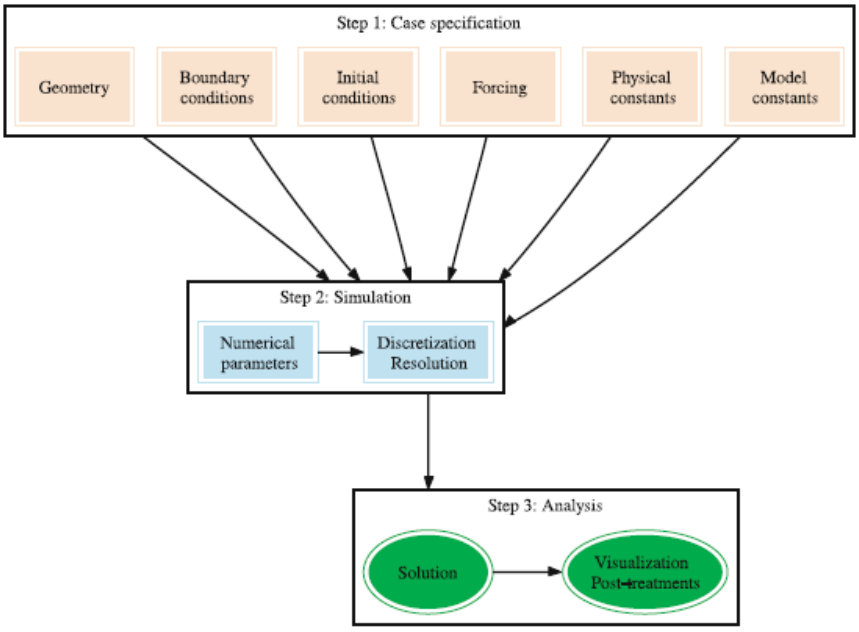

Figure 1.3 – Scheme of a deterministic simulation [4]

In this context, uncertainty quantification plays an important role. With the introduction of this methodology within the design procedure it is possible to define components that are not intrinsically influenced by possible geometric variations and boundary conditions: this procedure is called robust design.
The main difference between an experimental study and the corresponding numerical simulation is that the latter is usually considered a deterministic exercise, while the experiments are intrinsically influenced by uncertainty.
The assessment of uncertainty affecting a measurement is a problem that arose in the 1950s and was addressed by Kline-McClintock [5] and later by Moffat [6]. In the experimental field, it is usual to report also the band of uncertainty connected with the measurement, which provides an index of the accuracy of the measurement itself. In the numerical field, the propagation of uncertainty within the codes is evaluated. This type of study has been developed mainly in recent years due to the fact that only in this period the availability of computational resources has promoted the development and application of this procedure.
As reported by Iaccarino [7], in order to obtain the real predictive capacity of the simulation and, in turn, the correct validation, it is necessary the rigorous evaluation of the uncertainties that are introduced into the numerical code; in the same way as it happens for the tests carried out in the laboratory.

1.1 - Details of Uncertainty Quantification

Uncertainty quantification (UQ) is the science that quantitatively characterizes the uncertainty of a specific system, both in experimental and computational applications, and tries to determine and asses the probability of certain results.
The first applications of these studies were carried out in the field of risk analysis [8].
Before entering in theoretical fields, the definitions of "error" and "uncertainty" given in [9] by the American Institute of Aeronautics and Astronautics (AIAA), to define the concept of uncertainty in the numerical field is:

- Error: Deficiency recognizable at any stage or activity of modelling and simulation not due to lack of knowledge (Figure 1.4).

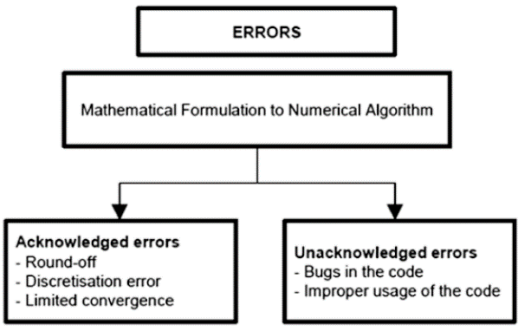

Figure 1.4 – Errors [9]

- Uncertainty: potential shortage at any stage or activity of the modelling process due to lack of knowledge (Figure 1.5).

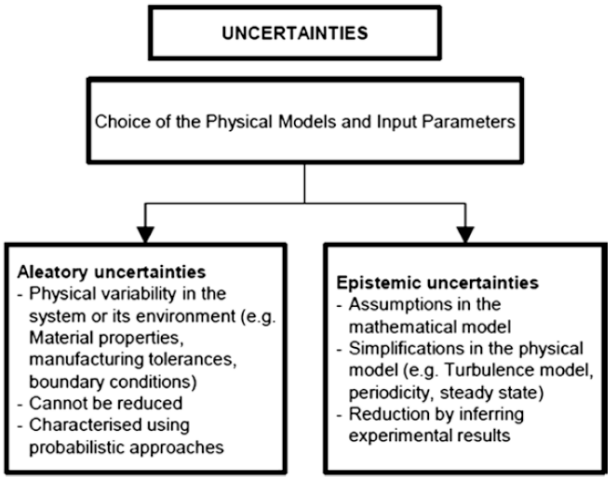

Figure 1.5 – Uncertainties [9]

The uncertainty, according to Casti [10], can be divided into two branches: epistemic and aleatory. Epistemic uncertainty, also called subjective or reducible, arises from incomplete knowledge of the phenomenon and can be reduced by further observations and measures; it can be reduced by increasing knowledge of the physical phenomenon considered.
The aleatory uncertainty is due to the variability and stochastic nature of the studied phenomenon, which is why it cannot be reduced through further observations but can be characterized more accurately through additional studies to reduce its amplitude. Randomness can be interpreted as a probability and, therefore, must be studied using appropriate probabilistic models.
The epistemic uncertainties can be reproduced as a bias in the prediction while aleatory uncertainties is normally characterised using probabilistic approaches [11]. Examples of aleatory uncertainties can be the determination of material properties or the operating conditions.
As suggested by Fersun and Gingbur [12], given the different nature of the two types of uncertainty, they need to be treated differently.

1.2 - Uncertainties related to turbomachinery

The purpose of this chapter is to explore more in detail uncertainties related to turbomachinery and heat transfer.

For "Oil&Gas" applications the first question mark is related to the real working conditions; in fact, with the increasing production of energy from renewable sources, these machines tend to work more and more often in off-design conditions compared to the nominal design conditions.
Transient operation is of critical importance for machines and in this phase the greatest uncertainties related to operation and internal temperatures are found [13].
The other critical point is the composition of the fuel mixture that processes the combustor; this is different depending on the country in which the machine is installed and may undergo annual changes due to the import of gas depending on the country of production.

In recent years, in order to reduce polluting emissions, energy production machines have been working with lean premixed flames that cause combustion at the limit of the stability zone [14]; this can lead to instability and subsequent shutdown even for small variations in the fuel mixture. As reported in [15], variations in fuel composition do not significantly affect the machine and that the main differences occur in terms of pollutant emissions.
In [16] it is pointed out that the responses of the machines are not linear with the variations of the fuel mixture; this aspect is mainly due to the physical phenomena that affect the combustion.

As far as aero engines are concerned, in the work of Montomoli [17] a list of the most important uncertainties is given, followed by a summary.

- Fan: This is the component that suffers the most wear due to external agents carried in suspension in the air (mainly sand and salt) [18]. Over the time, these external agents modify the shape of the blades: the erosion can lead to an increase of the clearance to the tip up to 65% and at the same time a reduction of the rope of 10% [19]; these variations lead to a consequent loss of pressure increase of 9%. Performance fluctuations due to geometric variations are greater for transonic fans, as reported by Klinner [20], which can have an efficiency reduction of up to 3.5%.
  Changes to the geometry due to erosion also have a strong impact on the aeroelastic aspects, which must be properly assessed at the design stage.

- Axial compressor: The performance of this component strongly depends on the fluid-blade interaction; in particular it is essential to ensure the correct angle of incidence: this is the factor that most affects the recovery of pressure. The angle of incidence depends in turn on the shape of the LE. From [21] it can be seen that a variation in the shape of the leading edge (~0,02mm) compared to the nominal one leads to an increase in pressure loss by 30%.
  The blade coating also plays an important role from a performance point of view, as this factor can also lead to changes of 20% in the shape of the LE defined in the design phase [22].
  Another aspect to emphasize is that modern compressors have a radius of curvature at the leading edge of 0.1mm [22]; laser measurement techniques have an accuracy of 15μm [23], which means that this type of measure will have an uncertainty of 10%.

- Combustion chamber: The great uncertainty within the combustors is related to the temperature profile at the outlet that goes to invest the first stage of the turbine.
  Although the TIT is a key parameter for the performance of the entire machine, it is difficult to measure it directly due to the problems related to high temperature and pressure values; the typical conditions of exit from the combustor are around 1800-2300K with pressures up to 40 bar [24].
  Temperature measurements are normally performed with thermocouples "K" and "N" type, whose maximum operating ranges are limited to about 1500K; this is the main reason why the temperature in real machines is typically measured at the second stage of the turbine. In addition, "K" type thermocouples, as reported in [18], provide an uncertainty close to $0{,}4\%$ for $T > 650K$.

For the cooling of the combustor walls, the level of internal turbulence is a key parameter, which, however, is usually estimated only by numerical simulations.
Another important aspect, which presents a high degree of uncertainty, is related to the type of temperature distribution at the outlet of the combustor; Salvadori [25] studies the effect of the different radial distribution, with the same average value, in terms of the useful life of the first nozzle.
On this subject, an uncertainty quantification analysis has been carried out by Montomoli [26] that evaluates, among other parameters, the influence of the position of the hot core coming from the combustion chamber with respect to the blade.
The combustor is very sensitive to changes in the efficiency of the cooling system; this, in turn, is closely dependent on geometric tolerances; so the various uncertainties inherent in the manufacturing processes used are very impacting on the performance of the system.

- Turbine: As already described, the parameter that has the greatest impact on the performance and useful life of the component is the TIT: for the first stage the correct design of the cooling systems is essential. Given the difficult machining operations that must be carried out on the complex blade geometry, the uncertainties involved are not negligible.
  Bunker's study [2] was the first to report geometric tolerances related to blade cooling systems (Figure 1.6).

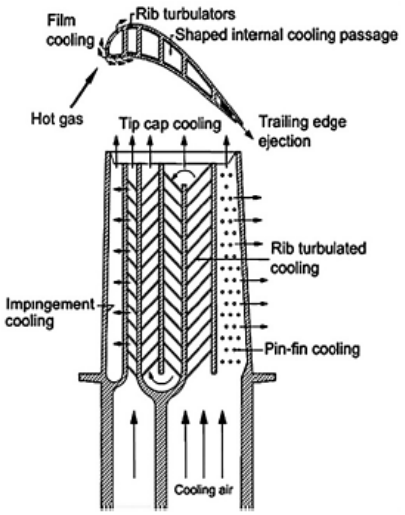

Figure 1.6 – Blade cooling system [27]

Bunker also assesses the impact of tolerances on some thermal-fluid dynamic factors including: the heat transfer inside and outside the blade, the film cooling effectiveness, the blade load and the external heat flow (Figure 1.7).
The author assigns an index, which can take three values (L = Low, M = Medium, H = High), to indicate the impact that this uncertainty has on the parameter being studied. All the results are summarized in Figure 1.7. The greatest geometric tolerances are on the radii of the turbulators, for which there is a variation of up to 50% from the nominal value. The other most influential factors concern the TE of the blade: here, variations of 25% with respect to the design thickness are achieved; this parameter has a strong impact both on the heat transfer and on the effectiveness of

the film. As far as the film cooling is concerned, in addition to the trailing edge, the inclination of the holes (±5°), the diameter of the holes (±10%), the pitch (±10%) and the inclination of the shaped section (±30%) are of considerable influence.

The parameter that most influences the external heat transfer is the surface roughness, the measurement shows a value of 1μm higher than the nominal 2.5μm.

			Effect of factors on cooling design parameter						
Code	Factor	Tolerance	Discharge coefficient	Internal HTC	Friction factor	External HTC	Film effectiveness	Aero load or loss	External heat flux
A1	Aerodynamic profile/shape	±0.05 mm	L	L	L	M	M	M	M
A2	Airfoil incidence angle	±2 deg	L	L	L	M	M	M	M
A3	Surface roughness (initial)	+1 μm	L	L	L	H	M	M	H
B1	Bondcoat thickness	±0.025 mm	L	L	L	L	L	L	L
B2	TBC thickness	±0.05 mm	L	L	L	L	L	M	H
B3	Local wall thickness	±0.125 mm	L	L	L	L	L	L	L
C1	Film hole diameter (effective)	±10%	M	L	L	M	H	M	M
C2	Film hole L/D	±6%	M	L	L	L	M	L	M
C3	Film hole angle to surface tangent	±5 deg	M	L	L	M	H	M	M
C4	Film hole orientation to external flow	±5 deg	M	L	L	M	H	M	M
C5	Film hole orientation to internal flow	±5 deg	H	L	L	L	M	M	M
C6	Film hole P/D	±10%	L	M	L	M	H	M	H
C7	Film hole shaped exit spec	±30%	H	L	L	H	H	H	H
D1	Impingement hole diameter	±10%	L	L	L	L	L	L	L
D2	Impingement array X/D or Y/D	±10%	L	H	M	L	L	L	L
D3	Impingement Z/D	±20%	L	H	M	L	L	L	L
D4	Crossover hole diameter	±10%	H	H	L	L	L	L	L
E1	Cooling passage turn aspect ratios	±10%	L	H	H	L	L	L	L
E2	Passage H/W (or aspect ratio)	±10%	L	M	H	L	L	L	L
F1	Turbulator e/D (blockage)	±20%	M	H	H	L	L	L	L
F2	Turbulator radius r/e	±50%	L	M	H	L	L	L	L
F3	Turbulator P/e	±20%	L	M	H	L	L	L	L
F4	Turbulator angle	±5 deg	M	H	H	L	L	L	L
F5	Turbulator end wrap-around	±50%	L	M	M	L	L	L	L
F6	Turbulator lean	±5 deg	L	M	M	L	L	L	L
G1	Pin diameter	±20%	L	L	M	L	L	L	L
G2	Pin fillet r/H	±20%	L	M	H	L	L	L	L
G3	Pin array S/D	±10%	L	H	H	L	L	L	L
G4	Pin H/D	±20%	L	M	H	L	L	L	L
H1	TE channel blockage e/H	±20%	L	M	M	L	H	M	M
H2	TE exit slot or hole H/W (aspect ratio)	±10%	M	M	H	M	M	M	M
H3	TE lip thickness to slot height ratio t/H	±25%	H	L	L	H	H	M	H

Figure 1.7 – Manufacturing tolerances and effects on blade cooling [2]

These aspects have been further developed by Montomoli et al. [17]: the study focuses on the increase in creep and the reduction in useful life that would occur if the temperature of the metal were to rise due to the levels of uncertainty provided by Bunker's work [2]; results are provided in Figure 1.8.

The creep increment has been calculated using the following exponential formula (Eq. 1-1), similar to that of Arrhenius, in which appears the activation energy ΔH necessary to trigger the creep, the temperature T and the constant of the gases R.

$$r = A \cdot e^{\frac{-\Delta H}{RT}} \qquad \text{Eq. 1-1}$$

The useful life decay has been calculated by the authors with the formulation of Larson-Miller [28].

$$\frac{\Delta T}{T_m} \cdot \left(C + log\, t_{r,2}\right) + log \frac{t_{r,2}}{t_{r,m}} = 0 \qquad \text{Eq. 1-2}$$

This last equation links the temperature variation of the metal ΔT and the expected temperature T_m and its expected life $t_{r,m}$, with the new life $t_{r,2}$.

According to the Larson's study, 90% of the turbine blades have a useful life of 11077 hours at an average temperature of 900K, this value has been assumed in [12] as a reference value for $t_{r,m}$.

	Uncertainty [%]	Metal T increase [K]	Variation [%]	Creep increase [-]	Res life decrease [%]
TET	±0.6%	10.0	0.85	1.48	−37
Vane inc. angle	±2°	1.9	0.16	1.08	−9
Film cooling D	±10.0%	39.4	3.36	4.70	−83
F.C. L/D	±6.0%	39.4	3.36	4.70	−83
F.C angle (internal)	±5°	10.0	0.85	1.48	−37
F.C. angle (external)	±5°	10.0	0.85	1.48	−37
F.C. P/D	±10.0%	19.4	1.65	2.14	−59
Impingement D	±10.0%	22.2	1.89	2.39	−64
Imp. H/D	±10.0%	22.2	1.89	2.39	−64
Imp. P/D	±10.0%	36.1	3.08	4.13	−81
Rib P/L	±20.0%	6.7	0.57	1.30	−27
Rib L/H	±20.0%	10.0	0.85	1.48	−37
Rib angle	±5.0%	3.9	0.33	1.17	−17
Pin fin D	±20.0%	11.1	0.95	1.55	−40
Pin fin P/D	±10.0%	6.1	0.52	1.27	−25
Pin fin H/D	±20.0%	13.9	1.18	1.73	−48
TE exit slot AR	±10.0%	20.0	1.70	2.19	−60
TE th/AR	±25.0%	12.8	1.09	1.65	−45
TBC th	±0.05 mm	12.8	1.09	1.65	−45

Figure 1.8 – Results obtained in [17]

1.2.1 - Manufacturing processes and roughness

The growing use of additive manufacturing (AM) manufacturing processes in the machinery sector will cause a further increase in the geometrical uncertainties listed above; in fact, these methods still present significant critical issues for this type of application.

In the works of Stimpson et al. [29] and [30] a comparison between a film cooling hole obtained by AM and one by electric discharge machining (EDM) is made.

The authors underline how the current AM metal technologies produce parts with a high surface roughness; since this has a strong impact on the external heat transfer [31], further sanding operations are required.

In Figure 1.9 a visual comparison of the results obtained is reported; the holes obtained by AM have a roughness double that the ones obtained by EDM. Smoothing the internal surfaces of the holes, given their small size, is complicated; for this reason, the effects of greater surface roughness, i.e. increased pressure loss and greater heat transfer due to the higher turbulence level, must be taken into account already at the design stage [30].

Stimpson [29] concludes that, nowadays, there are no additive manufacturing processes on the market that could produce holes of a size comparable to those used for this type of application with reliable and predictable behaviour.

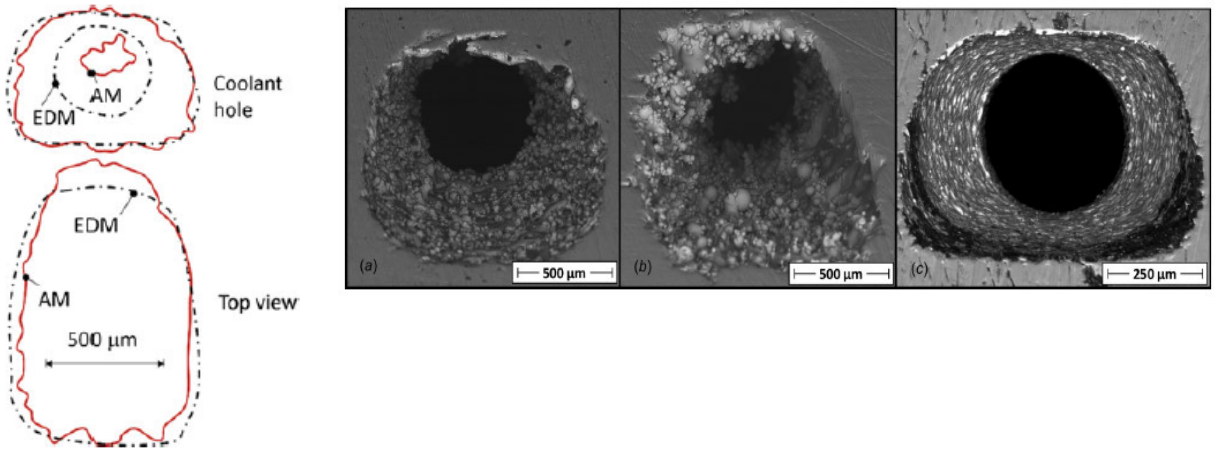

Figure 1.9 – (a) AM cooling hole, vertical (b) AM cooling hole, horizontal (c) EDM cooling hole [29]

In [30] the authors state that the film cooling effectiveness decreases with the surface roughness, therefore the holes made of AM guarantee lower performance. For this reason they provide a correlation for the increase in heat transfer due to the greater roughness.

1.3 - Uncertainty Quantification procedures

The uncertainties listed in the previous chapter are summarised in Figure 1.10 by [12].
The types of uncertainties that afflict the component are reported above the diagram of the aero-engine. As already described, the front parts of the engine are those that are most affected by wear. The compressor features mostly the manufacturing uncertainties, where the aerodynamic effects related to the shape of the leading edge of the blades account for the most and affect the stability of the operation of the entire engine. The early stages of the turbine are in an area where there is greater sensitivity to geometry, where cooling systems play an important role in the life of the machine. In the combustion chamber the uncertainties are related to the lack of directly measured data. The image also shows the potential efficiency losses due to the various uncertainties and their impact on the life of the components.

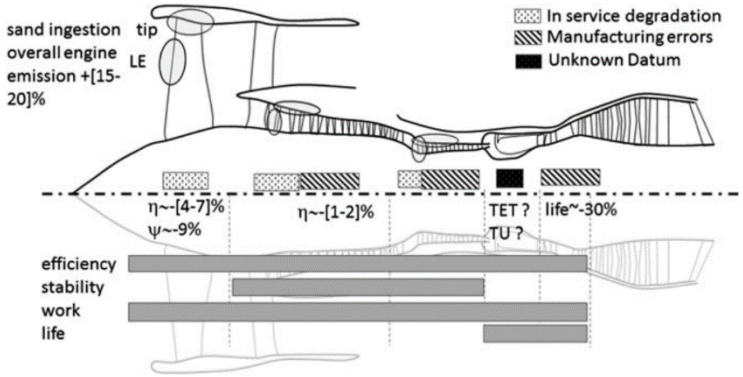

Figure 1.10 – Uncertainties in aeronautical gas turbines [17]

Given the high sources of uncertainty, both aleatory and epistemic, that could be found in the machines, it is appropriate to evaluate the effects within numerical simulations.
The general objective of UQ analyses is to investigate the impact of uncertainties on a quantity of interest obtained as a response from the system, to define a confidence interval for the results obtained, and to assess the probability that a certain result will occur; the whole process leads to a better risk assessment analysis and therefore helps the designer in the decision-making process.
In order to implement this procedure, it is necessary to adopt an approach that is no longer deterministic but probabilistic; this does not affect the standard procedure necessary to set up a simulation, but introduces considerable difficulties in the various phases (Figure 1.11).
The parameters that one wishes to assume as uncertain must be defined as an average value plus an uncertainty range; therefore, the need to characterise the uncertainties described above in quantitative terms arises.

For probabilistic approaches, data with uncertainty are usually random variables that assume certain values within specified intervals. In mathematical terms, this is equivalent to defining random variables with a certain probability distribution function (PDF). The definition of the type of distributions to be used is not easy. For the geometric uncertainties related to the manufacturing processes of components already in the production line, it is possible, through a series of measures, to trace the probability distribution that describes them. This process is expensive and cannot be carried out at the design stage and more in particular at the preliminary design stage.
The same problem is found for all those uncertain parameters related to boundary conditions, often coming from experimental tests. Also in this case, it is necessary to repeat the same measure a certain number of times, in order for it to have statistical value. Unfortunately, this is not always possible because of the unrepeatability of the tests, the short time frames, or the costs associated with the measures. It is also complicated to proceed with methods of statistical inference [32].
In the uncertainty quantification studies reported in the literature all the distributions of uncertain variables are imposed and a priori established by the authors; this choice, given the lack of studies and documentations, does not always have a rigorous scientific basis but is often based on the common sense of the authors.

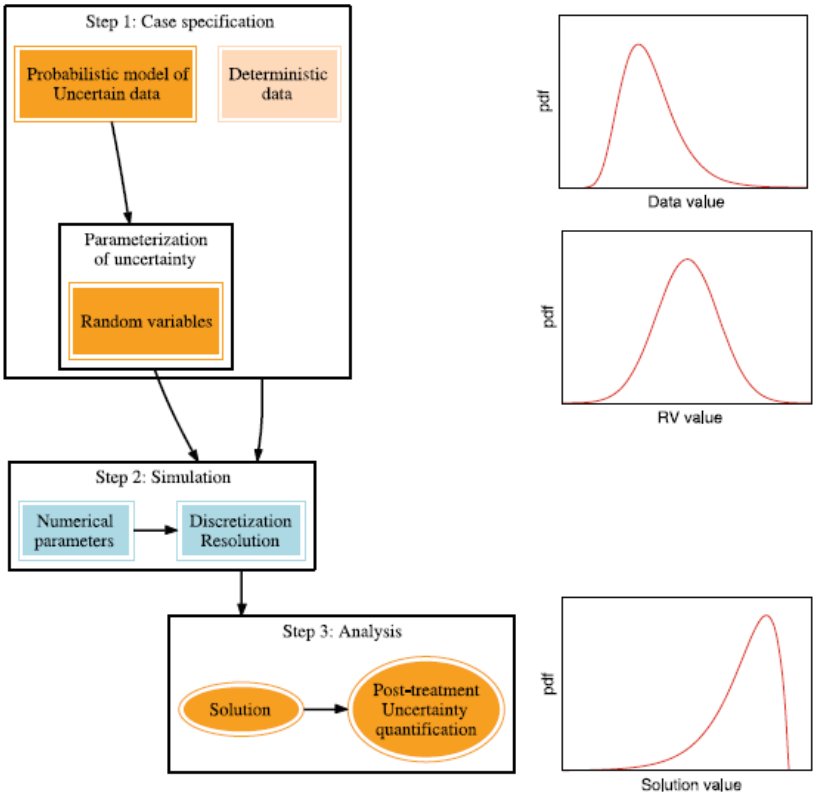

Figure 1.11 – Schematic procedure of a UQ analysis [4]

Once the probability distributions for all the input quantities have been defined, the numerical simulation can be carried out. This passage requires a specific number of evaluations in order to be able to define the statistic of the outputs; this involves an increase of the computational cost tied to the standard deterministic approach. The number of simulations to be carried out depends on the method adopted: different techniques are available, from approaches based on random sampling (for example Monte Carlo), which is simple but requires a high number of evaluations, to more sophisticated stochastic spectral approaches that require a reduced number of simulations. The different methodologies will be described in the next chapter. Once the required simulations have been carried out, it is possible to calculate the probability distribution of the quantities of interest for the output; this result can be compared with the experimental one (if available) in order to estimate the confidence interval of the numerical solution and to validate it (Figure 1.12) [33].

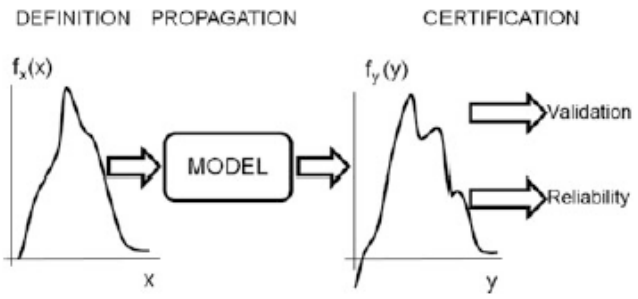

Figure 1.12 – Uncertainty Quantification procedure [7]

This type of result, on the contrary to the one obtained by deterministic approaches, can be subsequently used for reliability studies; this aspect is particularly important for both heavy duty machines [34] and aero-engines [35].
The range of uncertainty of the result will be a function of those uncertainties imposed as an input; this can be further investigated through a sensitivity analyses [36]. This analysis investigates the connection between input and output of the computational model; in particular it allows to identify how the variability of an output quantity of interest is linked to an input variable and which sources of uncertainty will dominate the response of the system.
Indices called "Sobol's indices" are defined, which indicate the weight of each uncertain contribution on the quantity obtained in output [37].
This information is extremely important for robust design and optimization because it allows you to focus the design only on the components that most affect the response function.

1.4 - Heat transfer and cooling in gas turbine

1.4.1 - Basics of heat transfer

The heat transfer is defined as the energy transfer that occurs when two regions are characterized by a temperature difference and can be classified into three different modes: conduction, convection, and radiation. Even though all of them depend on the temperature gradient, the second one is distinguished from the others by its reliance on mass transport. It is beyond the scope of this activity to explore in detail all the principles of these methods and only a brief description of the first two is provided since the radiative heat transfer is not relevant for the following analyses.

The heat conduction is defined by the Fourier's Law which says that the heat flux is directly proportional to the temperature gradient by means of a constant:

$$q = -\lambda \, grad \, T \qquad \text{Eq. 1-3}$$

Where q is the heat flux, λ is the thermal conductivity, which for a material following the Fourier's law is dependent only by the temperature and T is the temperature.

The heat convection occurs between solid and adjacent fluid/gas and involves the combined effects of both heat conduction and mass transfer. Even though the phenomenon is highly complex, it is possible to define the following equation (Newton's law) for the heat convection:

$$q = HTC \cdot (T_w - T_\infty) \qquad \text{Eq. 1-4}$$

The HTC represents the heat transfer coefficient and is a number function of the geometry, the fluid dynamic conditions, and the fluid properties. T_w is the temperature at the interface and $T_\infty$is the temperature of the fluid.

1.4.1.1 – Boundary layer

The layer of fluid in the immediate vicinity of a bounding surface where there is a velocity profile due to the shear stress at the wall is called velocity boundary layer and is depicted in Figure 1.13. The thickness of the boundary layer δ is defined as the distance from the wall to the point where the velocity is 99% of the freestream velocity. The first part of the boundary layer is laminar and is characterized by regular streamlines: here the heat conduction dominates. There is an intermediate zone, or transition region, where the flow starts to become turbulent. The last zone, the turbulent one, features vortices and disordered behaviour which enhances the mass transfer and hence the convection heat transfer. In the region adjacent to the wall there are two particular zones: the viscous sublayer and the buffer sublayer. The first one is a region where the shear stresses are strong enough to keep the fluid in laminar motion whereas the latter features an intermediate behaviour between the viscous sublayer and the turbulent region.

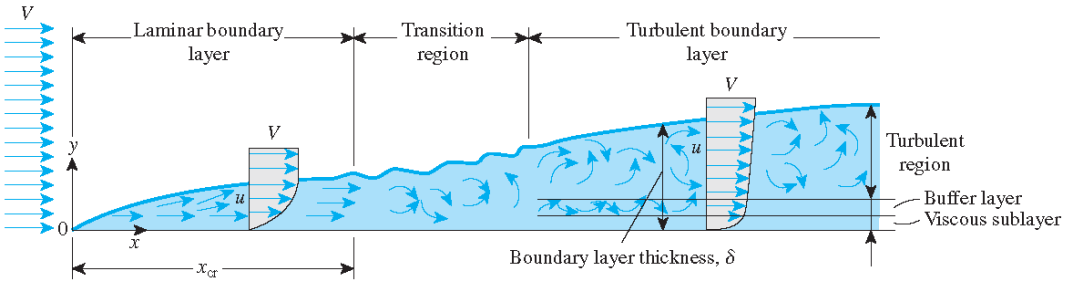

Figure 1.13 – Development of the velocity boundary layer (*Courtesy of University of Florence*)

In analogy with the velocity boundary layer, there is also a thermal boundary layer, which develops as a result of the heat flux between the surface and the fluid and because of viscous dissipation (Figure 1.14).

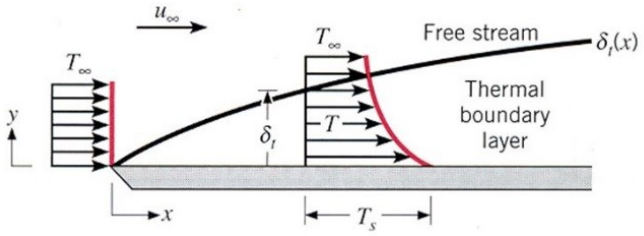

Figure 1.14 – Thermal boundary layer over a flat plate (*Courtesy of University of Florence*)

While far away from the plate the fluid temperature is uniform, the temperature gradient gradually develops when in contact with the hot plate. Similarly to what previously defined for the velocity boundary layer, the thermal boundary layer is defined as the region in which the fluid temperature is less than 99% of freestream temperature.

1.4.1.2 – Reynolds number

The Reynolds number (Re) is a non-dimensional number used in fluid dynamics which is proportional to the ratio of inertia forces to viscous forces. It was firstly introduced by Osbourne Reynolds in 1883 an nowadays

it is one of the most important parameters when dealing with fluid dynamics. Its formulation is explained as follow:

$$Re = \frac{U \cdot \delta}{\nu} = \frac{\rho \cdot U \cdot \delta}{\mu} \qquad \text{Eq. 1-5}$$

Where δ is the characteristic length and μ is the dynamic viscosity of the fluid. The Reynolds number allows to assess whether the flow rate has a laminar regime (low Reynolds number, where the viscous forces dominate) or a turbulent regime (High Reynolds number, where the inertial forces dominate).

1.4.1.3 – Heat transfer coefficient

When dealing with convective heat transfer, for compressible fluid, the concept of adiabatic wall temperature must be specified. The adiabatic wall temperature is the temperature that the wall would attain in adiabatic conditions. Wall temperatures lower or higher than the adiabatic wall temperature causes a heat transfer to or from the surface (Figure 1.15).

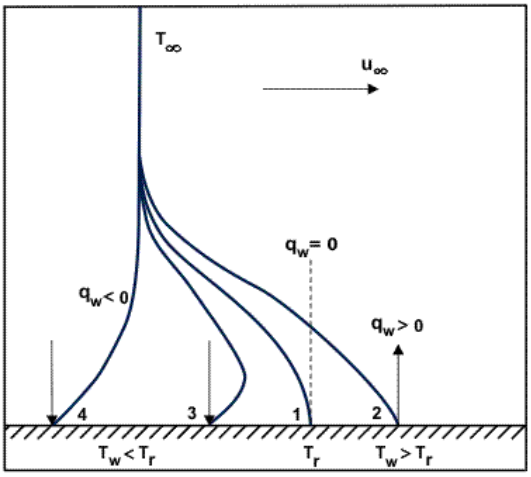

Figure 1.15 – Thermal boundary layer (*Courtesy of University of Florence*)

As a consequence it is possible to define the heat transfer coefficient as follows:

$$HTC = \frac{q}{T_w - T_{aw}} \qquad \text{Eq. 1-6}$$

It is worth underlying that considering the no-slip condition on the bounding surface, because of irreversible dissipation, the adiabatic wall temperature has a different concept with respect to the stagnation temperature, which does not occur precisely at the bounding surface.

1.4.2 - Cooling techniques

Blade cooling has been the main subject of study in the past years and this chapter aim is to underline the major cooling techniques adopted nowadays. It is worth noting that a detailed and extensive literature will

be provided at the beginning of each chapter, respectively Chapter 3 -4 -regarding combustors and Chapter 4 -regarding film cooling, including the state-of-the-art developments. For the sake of clarity, this chapter aims to introduce the major cooling techniques for gas turbine applications.

As already mentioned in Chapter 1 -(see Figure 1.1), the TET has progressively grown over the past years reaching up to 1700K causing continuous research in the field of gas turbine components. Basically, when dealing with blades and stators, blade cooling can be divided into two different groups, depending on whether the coolant inside the blade escapes through the blade or not. For internal cooling techniques, the objective is to design the geometry of the blade in the way the heat transfer between the metal and the coolant is maximized. On the other hand, for external cooling techniques, the objective is to reduce the external heat transfer between the mainflow and the metal. Examples of state-of-the-art internal cooling techniques are the impingement cooling, ribs and pin fins turbulence promoters as well as multi-pass serpentine (Figure 1.16).

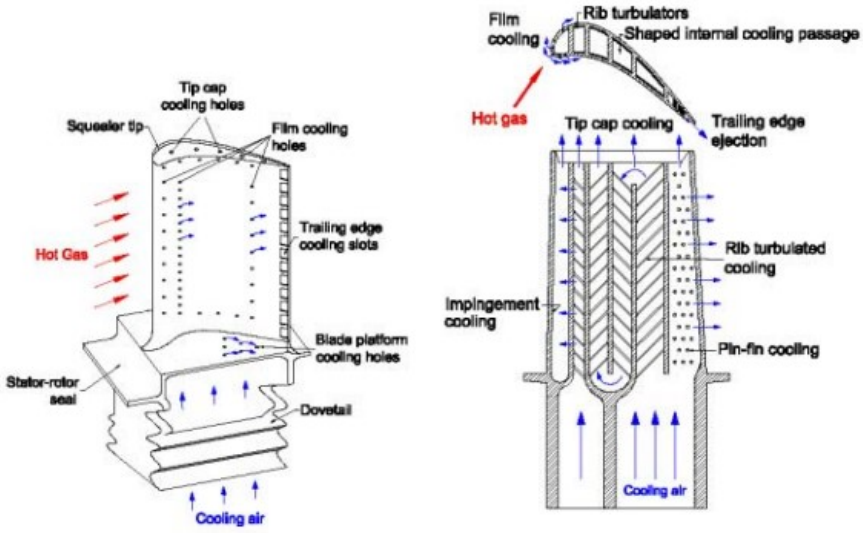

Figure 1.16 – Typical airfoil cooling design for a modern high-pressure gas turbine blade [38]

Impingement cooling consists of ejecting the coolant flow which then impacts the surface considered. The heat transfer intensification is due to the decrease of the boundary layer thickness in the vicinity of the stagnation area. The main disadvantage of this technique is that it can weaken the metal structure, therefore it is generally used near the leading edge of the blade [39].

In order to increase the internal heat transfer, a higher turbulence level and a higher surface are needed in the region of interest; for these reasons, an array of short cylinders (pin-fins) are generally used, especially near the trailing edge of the blade. The distribution arrangement is of fundamental importance in order to obtain major benefits from this configuration [39].

An arrangement including the two previous techniques is depicted in Figure 1.17.

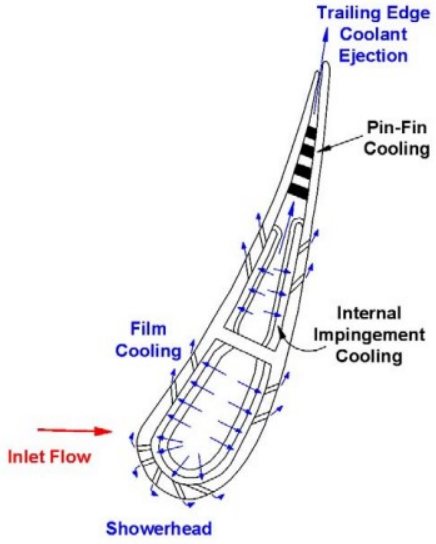

Figure 1.17 – Turbine vane cross-section with impingement and TE pin-fins [39]

Another technique adopted in order to increase the internal heat transfer is through the use of multi-pass channels which increase the surface and ribs or turbulence promoters which increase both the surface and the turbulence level (Figure 1.18). The fluid then separates and re-attaches downstream with a thinner boundary layer, causing the heat transfer to increase [40].

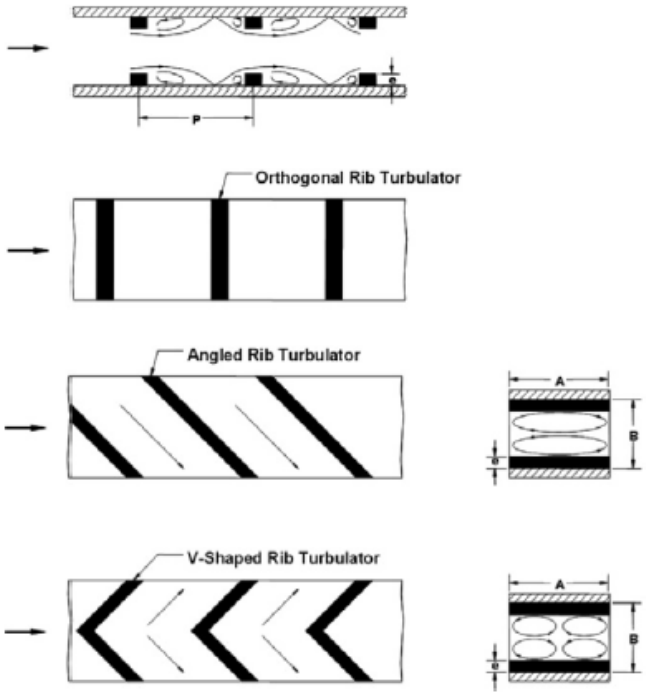

Figure 1.18 – Orthogonal, angled and V-shaped rib-induced secondary flow [40]

Regarding external cooling techniques, film cooling will be treated more in deep in chapter 4.1 -

1.5 - Additive manufacturing

This chapter illustrates the basic principles and cutting-edge technologies in the fields of additive manufacturing. No other manufacturing processes are investigated and considering the scope of the thesis, especially regarding the gas turbine vane analysed later, this manufacturing technique deserves several considerations.

Regarding materials, huge efforts have been undertaken nowadays trying to develop new techniques, especially in the field of additive manufacturing. The advantage of this technique is the capability to reproduce advanced and complex geometry that cannot be manufactured with conventional manufacturing techniques. For instance, looking at Figure 1.16, this concept is surely clearer. Furthermore, the capability to realize multi-material arrangements, lattice structures, and fully functional components has allowed this technology to grow exponentially over the last two decades [41]. Moreover, there are additional benefits when dealing with additive manufacturing, such as flexibility usage, the on-demand manufacturing and last but not least lower scrap metal [42]. Focusing on gas turbine applications and related components, the benefits continue with the capability to manufacture a specific component with specific classified material composition [43], in particular for those component operating at extremely high temperatures, and with the repairing and overhaul of the most expensive components [44] [45] [46].

Several metal additive manufacturing techniques are available in the industry and the three most relevant ones are Laser Sintering, Laser Melting and Laser Metal Deposition [47]. Generally, the technology can be classified following different aspects, including the form of metallic materials adopted. According to this classification, three techniques can be investigated: Powder bed, Powder feed and Wire feed [48]. Power bed additive manufacturing (Figure 1.19) consists in solidifying the metal powder layer upon layer. A layer is supplied by the powder delivery system, then spread by the roller or rake, and finally melted by an external energy source, for instance, a laser beam [49]. Powder feed (Figure 1.20) is slightly different: although the part is built layer by layer like the previous technology, here the metal powder is directly ejected through the nozzle feeder [50]. Wire feed technology (Figure 1.21), instead, uses metallic wires in conjunction with an external source of energy in order to build the final part.

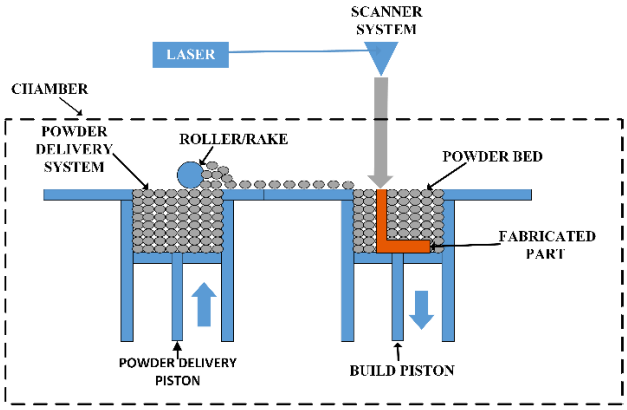

Figure 1.19 – Powder bed AM technique [48]

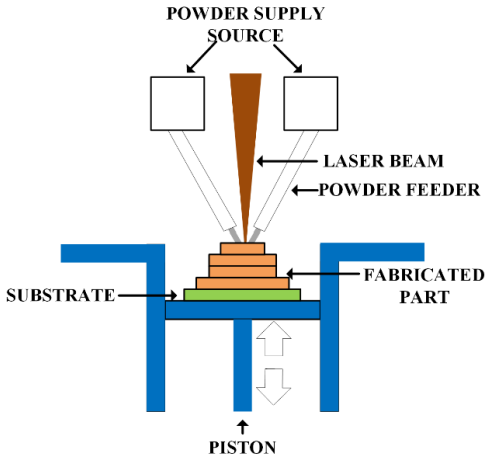

Figure 1.20 – Powder feed AM technique [48]

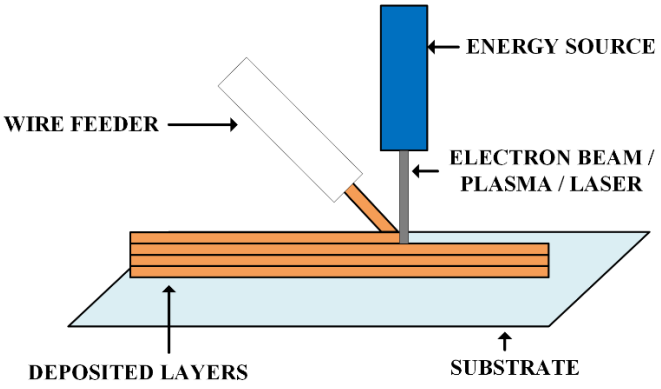

Figure 1.21 – Wire feed AM technique [48]

1.6 - Thesis structure

Given the generic nature of this research field, it was decided to provide in the first chapter a generic introductory overview of uncertainty, the main uncertainties affecting machines and a schematic procedure for carrying out an uncertainty quantification analysis aimed at showing the objectives and capabilities of this type of study. Furthermore, a description of heat transfer basics, as well as the main cooling systems adopted nowadays for gas turbine hot components and the different techniques used for additive manufacturing is provided.

The second chapter will provide the theoretical and mathematical bases for the correct definition of the various techniques and methodologies. A quick overview of the software that allows the final user to carry out this type of study, with particular attention to the one used in this study. Subsequently, a literature review will be carried out.

The third chapter will show the first application of these techniques to a one-dimensional fluid network solver, which solves the heat transfer on a combustor liner. A brief introduction to aeronautical combustors will be reported to better understand the problem from the correct physical point of view and the 1-D code used to validate the different UQ methodologies will be described. Finally, the different results obtained will be compared.

The fourth part of the thesis will focus on the application of UQ techniques to a CFD simulation; in particular it is applied to the film cooling of a real gas turbine blade. Also in this case a brief introduction to the problem will be reported, as well as the hypotheses at the base of the simulation and the numerical setup used. Finally, the results obtained will be analysed and compared with the experimental ones already carried out by previous studies.

The last part will be devoted to conclusions and possible future developments related to this type of activity.

2 - Uncertainty Quantification

In the previous chapter, a generic treatment has been provided to set up an uncertainty quantification analysis; in this chapter, the theoretical bases that allow its use and the description of the various methodologies are reported.

UQ techniques can be divided into two main groups: intrusive or non-intrusive. The former acts on the source code of the solver while the latter imposes an input uncertainty only on the input parameters and evaluate how these propagate within the code itself; in fact, through a finite number of deterministic numerical realizations of the code under investigation, the statistics of the output quantities are estimated.

This type of study does not require any variation of the solver, which can be considered a black box that associates each realization of the input parameters sampled to the corresponding outputs of the model. The non-intrusive analyses allow obtaining probabilistic results from already existing deterministic codes whether it is a commercial or open source software. This aspect allows to carry out UQ analysis on any numerical model, without any limitation related to the complexity of the same.

The main drawback of these techniques is that they require a number of deterministic simulations that depends on the number of uncertain variables considered and the level of approximation chosen; this aspect makes the non-intrusive analyses expensive from the computational point of view, a condition that worsens, therefore, with the growth of the computing resources required by the deterministic simulations to be solved. Such critical issue can be partially eliminated with the possibility to carry out deterministic simulations in parallel, working only on the deterministic code, and to carry out the UQ analysis, which, in fact, requires only the data to be processed a posteriori.

Considering that often computational fluid dynamics analyses are carried out with commercial codes, the work has been focused only on non-intrusive techniques; an evaluation of the propagation of uncertainty between upstream and downstream of numerical codes has been carried out, without acting on the source codes, which is why the theoretical aspects of only these techniques are reported.

2.1 - Probability theory

It is considered a continuous function $X(\omega) \in \{0,1\}$ defined on the probability space $(\Omega, \mathcal{B}, P)$, in which Ω is the results space, $\mathcal{B}$ are the sets of events and P is the probability value.

X is a function that assigns to each result ω of the measurement space (Figure 2.1) an integer $x \in \mathbb{R}$ and for each event $\mathcal{A}_i \in \mathcal{B} \subseteq \Omega$ in an interval $\mathcal{B}_i \subseteq \mathbb{R}$.

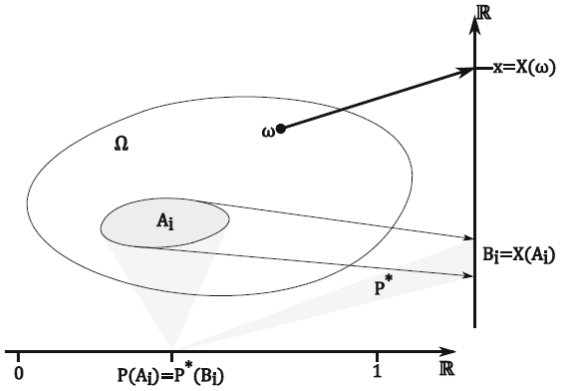

Figure 2.1 – Function X(ω) [51]

The interval $\mathcal{B}_i$ is one of the infinite numerable sets that make up the Borel[1] field $\mathcal{B}^*$ in $X(\Omega) \subseteq \mathbb{R}$.
The impossible event $\emptyset \in \Omega$ is associated with the empty set of real numbers, while the certain event Ω is defined in the range $X \subseteq \mathbb{R}$. In other words, the random variable $X(\omega)$ assumes the value $x \in \mathbb{R}$ with a probability defined in $X(\Omega) \subseteq \mathbb{R}$ from the probability $P(\omega)$ that $\omega \subseteq \Omega$ will occur. In conclusion, a random variable is a transformation:

$$(\Omega, \mathcal{B}, P) \xrightarrow{X} (\Omega, \mathcal{B}^*, P^*) \qquad \text{Eq. 2-1}$$

This transformation is applied to each element $\omega \in \Omega$ and assigns each pair of real numbers $(x, P^*(x)) = X(\omega)$.

2.1.1 - Probability and distribution

The probability is used to indicate the occurrence of a given event; this concept is based on empirical evidence and the theoretical justification is to be found in the theorem of J. Bernoulli on the law of large numbers [52].
The probability distribution function of a random variable $X(\omega)$, on the space of probability $(\Omega, \mathcal{B}, P)$, is defined as follows:

$$F_x(x) = P(X(\omega) \leq x) \qquad \text{Eq. 2-2}$$

$F_x(x)$ is called Cumulative probability distribution (CDF) of $X(\omega)$ and defines the sum of the probabilities that the random variable $X(\omega)$ assumes values less than or equal to value x (Figure 2.2).

[1] Borel field or σ-Algebra is the collection of Ω subassemblies meeting the following conditions:

- It is not an empty set: $\emptyset \in \mathcal{B}$ and $\Omega \in \mathcal{B}$
- If $\mathcal{A} \in \mathcal{B}$ then $\mathcal{A}^c \in \mathcal{B}$
- If $\mathcal{A}_1, \mathcal{A}_2, \ldots . \mathcal{A}_n \in \mathcal{B}$ then:

$$\bigcup_{i=1}^{\infty} \mathcal{A}_i \in \mathcal{B} \quad and \quad \bigcap_{i=1}^{\infty} \mathcal{A}_i \in \mathcal{B}$$

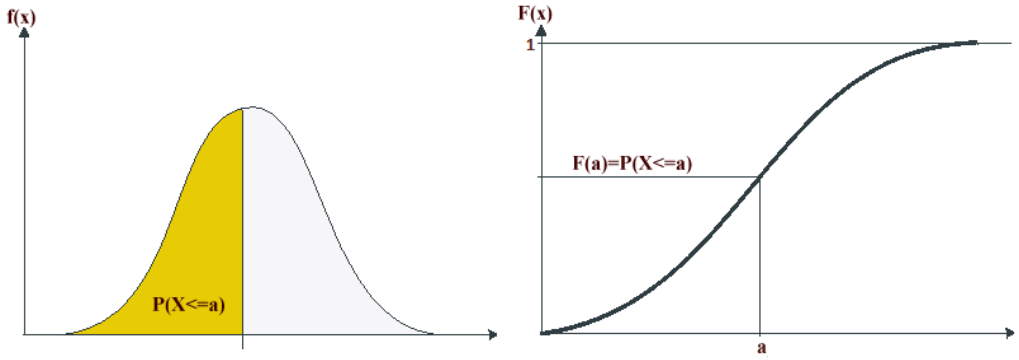

Figure 2.2 – Probability and cumulative functions for Gaussian distribution

By definition, the cumulative probability distribution cannot assume negative values and is non-decreasing monotonous between 0 and 1.

The main properties of probability are the following, given two events $A, D \in \mathcal{B}$:

1. $P(A \cup D) = P(A) + P(D) - P(A \cap D)$,
2. $P(A \cup D) = P(A) + P(D)$, if A and D mutually exclusive events
3. $P(\Omega) = 1$, certain event; $P(\emptyset) = 0$, Impossible event
4. $P(\bar{A}) = 1 - P(A)$

2.1.2 - Continuous random variable

The definition of probability presupposes the existence of an appropriate function $f(x)$, whose integral in a fixed generic range (a, b) provides the probability that the continuous random variable X assumes values belonging to the interval (a, b); if the integral is reduced to only one point, this is null.

Therefore, if X is a continuous random variable, the probability that assumes a fixed value is always zero.

$$P(X = x) = 0, \quad \forall x \in \mathbb{R} \qquad \text{Eq. 2-3}$$

In the case of a continuous random variable, the probability that X is within the continuous range (a, b), where a and b are constant and with $a < b$; is defined as follows:

$$P(a < X < b) = \int_a^b f(x)dx \qquad \text{Eq. 2-4}$$

The probability density function of a continuous random variable shall meet the following conditions:

- $f(x_i) \geq 0, \quad \forall x \in \mathbb{R}$ Eq. 2-5
- $\int_{-\infty}^{\infty} f(x)dx = 1$ Eq. 2-6

The probability distribution function of the continuous random variable X is defined with the following equation:

$$F(x) = P(X \leq x) = \int_{-\infty}^{x} f(x)dx \qquad \text{Eq. 2-7}$$

This definition implies that $f(x)$ is integrable; by the definition of $F(x)$, it turns out that this is a continuous function; therefore, in all the points where $f(x)$ is continuous, the derivative of the distribution function $F(x)$ is precisely the density of probability $f(x)$.

$$\frac{dF(x)}{dx} = f(x) \qquad \text{Eq. 2-8}$$

2.1.2.1 – Gaussian distribution

The normal or Gaussian distribution is very important in manufacturing processes and measurements because it describes the distribution of random errors; for this reason, it is also called the law of errors.
Different phenomena in nature can be described by means of a normal distribution, and it is also suitable for the approximation of numerous discrete distributions.
The density of the normal probability, or normal or Gauss distribution is defined by the following equation.

$$f(x) = \frac{1}{\sigma\sqrt{2\pi}} e^{-\frac{1}{2}\left(\frac{x-\mu}{\sigma}\right)^2} \qquad -\infty < x < \infty \qquad \text{Eq. 2-9}$$

Where μ and σ are parameters with $\sigma > 0$. It can be proved that μ and σ are respectively the mean value and the standard deviation of the random variable X distributed according to normal distribution.
The normal distribution $f(x)$ is defined on the whole axis of the real numbers and always assumes positive values; it is symmetrical with respect to the straight line $x = \mu$, that is, with respect to the average value of the distribution, which also coincides with mode and median[2].

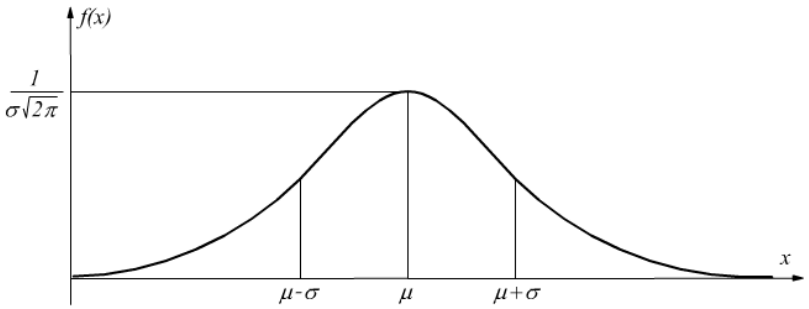

Figure 2.3 – Normal distribution

The distribution has a bell shape, as reported in Figure 2.3. Its maximum value is inversely proportional to σ; in addition, the standard deviation defines the distance of the inflection points from the mean value as they

[2] The median corresponds to the value that separates the underlying region from the probability distribution curve in two parts of equal area equal to $\frac{1}{2}$.

have abscissa respectively $\mu \pm \sigma$. Since the distribution represents the trend of the density function of a random variable, the area underlying the entire curve has unitary value. Each pair of values μ and σ uniquely identifies a normal distribution, i.e. for each pair, a different normal curve is defined (Figure 2.4).

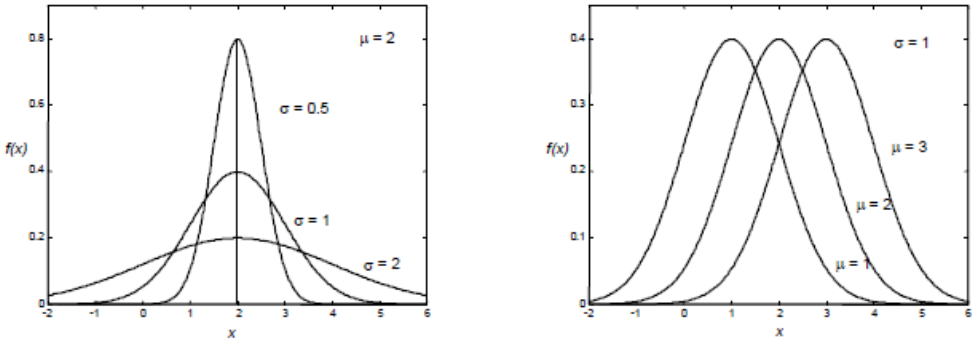

Figure 2.4 – Normal distributions with different mean value and standard deviation

The variation of σ with the same average value involves a greater width of the bell, while a variation of μ with the same standard deviation, only involves a translation of the curve.
The normal distribution or allocation function is given by the following equation.

$$F(x) = P(X \leq x) = \frac{1}{\sigma\sqrt{2\pi}} \int_{-\infty}^{x} e^{-\frac{1}{2}\left(\frac{t-\mu}{\sigma}\right)^2} dt \qquad -\infty < x < \infty \qquad \text{Eq. 2-10}$$

2.1.2.2 – Standardised normal distribution

The most important curve of the family of normal distribution is the standardized curve; in order to obtain this distribution, given the variable X normally distributed with mean value μ and variance σ^2, the random variable Z, called the standardised variable, is introduced.

$$Z = \frac{X - \mu}{\sigma} \qquad \text{Eq. 2-11}$$

This transformation allows to centre the distribution in zero, this distribution, in fact, has an average zero value and a unitary variance, which is why it is indicated by the diction $\mathcal{N}(0,1)$.
The probability distribution of the standardised normal variable Z is given by:

$$f(z) = \frac{1}{\sqrt{2\pi}} e^{\frac{z^2}{2}} \qquad -\infty < z < \infty \qquad \text{Eq. 2-12}$$

The standardised normal allocation function is defined as follows:

$$F(z) = P(Z \leq z) = \frac{1}{2\pi} \int_{-\infty}^{z} e^{-\frac{t^2}{2}} dt \qquad \text{Eq. 2-13}$$

The area beneath the curve in the range $\mu \pm \sigma$ is equal to 68,3%, the one in the range $\mu \pm 2\sigma$ is around 95,4%, while in the range $\mu \pm 3\sigma$ is approximately 99,7% (Figure 2.5).

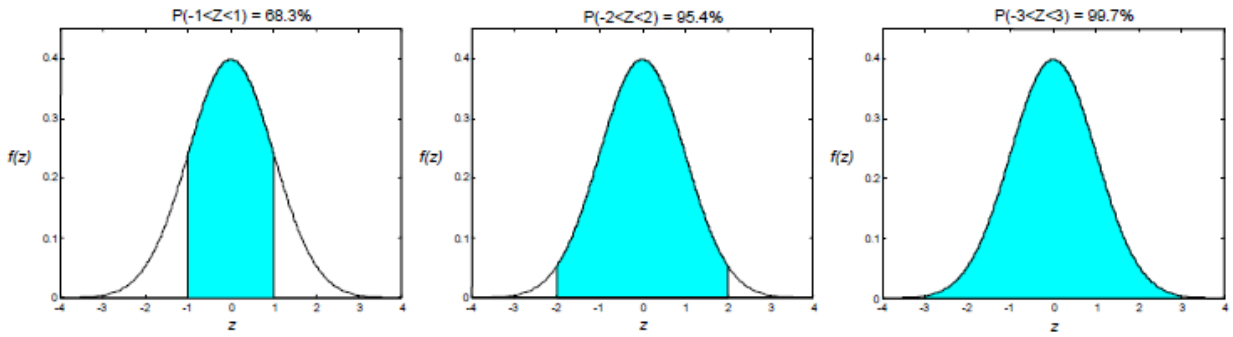

Figure 2.5 – Standardised normal distribution intervals

2.1.2.3 – Uniform distribution

Given two numbers a and b, with $a < b$, the continuous random variable X has a uniform distribution with parameters a and b, if its probability density is constant over the whole range considered and equal to:

$$\begin{cases} \frac{1}{b-a} & a \leq x < b \\ 0 & elsewhere \end{cases} \qquad \text{Eq. 2-14}$$

The uniform distribution function has the following expression:

$$F(x) = P(X \leq x) = \begin{cases} 0 & x \leq a \\ \frac{x-b}{b-a} & a < x < b \\ 1 & x \geq b \end{cases} \qquad \text{Eq. 2-15}$$

2.1.3 - Statistical moments

The most important characteristics of a distribution associated with a random variable are the mean value or expected value, variance, and moments of higher degree such as "skewness" and "kurtosis", which characterize the form of the distribution itself.

The average or expected value of a random variable X with probability density $f(x)$ is given by:

$$\mu = \mathbb{E}[X] = \int_{-\infty}^{\infty} x f(x) dx \qquad \text{Eq. 2-16}$$

The variance of X is defined as follows:

$$\sigma^2 = var(X) = \int_{-\infty}^{\infty} (x-\mu)^2 f(x) dx \qquad \text{Eq. 2-17}$$

The square root of the variance is called the standard deviation. The statistical moments are defined with respect to the average value by means of the following general formulation [51]:

$$\mathbb{E}[X^m] = \int_{-\infty}^{\infty} x^m f(x) dx \qquad \text{Eq. 2-18}$$

In which m is the degree of the moment.

The moments centered on the mean value are often used $\mathbb{E}[(X-\mu)^m]$. Since the central moments are zero up to the third degree, they are interesting for $m \geq 3$.

The third moment, called asymmetry ($skewness$, sk) or Pearson's asymmetry coefficient, provides an index of symmetry of the distribution. In particular, for positive asymmetry the distribution will have a tail to the right, while for negative asymmetry the tail will be turned to the left (Figure 2.6).

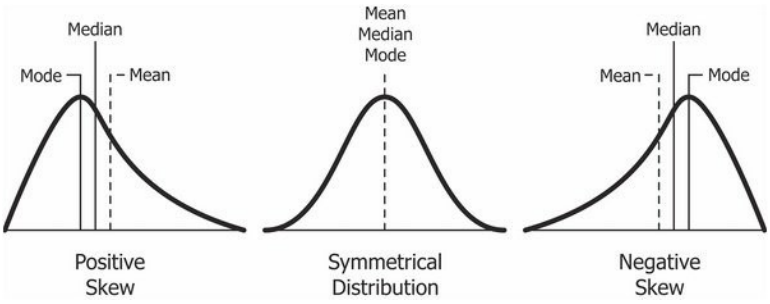

Figure 2.6 – Non-symmetric distribution

The fourth degree moment, called kurtosis, like the previous moment, gives an indication of the shape of the distribution; in particular, it defines the size of the tails, measuring their "thickness" according to the flattening of the distribution itself.

In other words, it indicates how much distribution is collected around the average value: a positive kurtosis implies a more concentrated distribution around the average and a higher fashion value, while a negative kurtosis implies a flatter distribution with more marked tails (Figure 2.7).

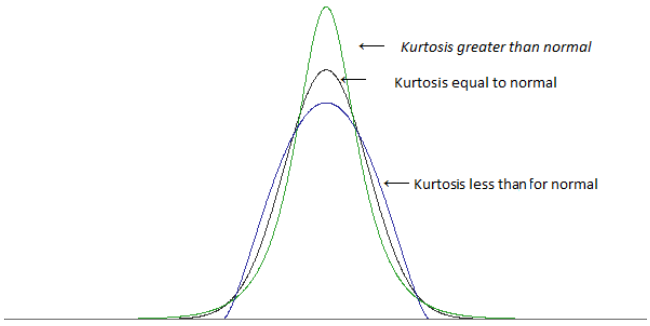

Figure 2.7 – Different Kurtosis PDF

2.2 - Stochastic processes

In physical systems, a random variable may vary continuously or discreetly with respect to physical space and/or time. Stochastic processes are used to study the evolution of random variables as a function of time and space; they are modelled as follows:

$$(X_t, t \in T) = (X_t(\omega), t \in T, \omega \in \Omega) \quad \text{Eq. 2-19}$$

defined on the probability space Ω.
If T, which can represent time or space, identifies a continuous interval then X will be a continuous process, on the contrary if T is a discrete interval also the process will be discrete.
A stochastic process can be considered as a function of two variables.

- Given the index t, it is an aleatoric variable:

$$X_t = X_t(\omega), \qquad \omega \in \Omega \quad \text{Eq. 2-20}$$

- Given a probability $\omega \in \Omega$, is a function of the index:

$$X_t = X_t(\omega), \qquad t \in T \quad \text{Eq. 2-21}$$

To simplify the treatment random vectors are introduced.

$$(X_{t1}, X_{t2}, \ldots, X_{tn}), \qquad t_1, t_2, .., t_n \in T \quad \text{Eq. 2-22}$$

These allow to consider a stochastic process of finite size but define the distribution of X_t.
A stochastic process $X_t, t \in T$, can be defined as a set of random vectors; therefore the definitions of the matrices of mean value, variance, and covariance for the random vector to the stochastic process can be extended and these quantities can be considered as functions of $t \in T$.
The equation of the expected value is given by:

$$\mu_X(t) = \mu_{X_t} = \mathbb{E}[X_t], \qquad t \in T \quad \text{Eq. 2-23}$$

The covariance function of X is defined as follows.

$$Cov_X(t,s) = cov(X_t, X_s) = \mathbb{E}[(X_t - \mu_X(t))(X_s - \mu_X(s))], \qquad t, s \in T \quad \text{Eq. 2-24}$$

The variance function of X is:

$$\sigma_X^2(t) = Cov_X(t,t) = var(X_t), \qquad t \in T \quad \text{Eq. 2-25}$$

The variance defines the deviation of the distribution from the expected value, while covariance provides an estimate of how much the dependence of two factors affects the random variable.

2.2.1 - Convergence in distribution

Given the sample $\{X_n\}$, this converges in the distribution or converges weakly in the random variable X, if for all continuous and limited functions f, the following conditions are applicable:

$$\mathbb{E}[f(X_n)] \to \mathbb{E}[f(X)], \qquad n \to \infty \qquad \text{Eq. 2-26}$$

2.2.1.1 – Central limit theorem

If $X_1, X_2, \ldots, X_n$ are independent random variables having the same distribution, with $\mathbb{E}[X_i] = \mu$ and $var(X_i) = \sigma^2 < \infty$. Then:

$$\bar{X} = \frac{1}{n}\sum_{i=1}^{n} X_i \qquad \text{Eq. 2-27}$$

$$U_n = \sqrt{n}\left(\frac{\bar{X} - \mu}{\sigma}\right) \qquad \text{Eq. 2-28}$$

So the distribution U_n converges into a standardised normal distribution $\mathcal{N}(0,1)$ for $n \to \infty$.
This theorem implies that the average value of a set of random variables $\{X_i\}_{i=1}^{n}$ converges with the growth of n to a Gaussian distribution $\mathcal{N}\left(\mu, \frac{\sigma^2}{n}\right)$ in which μ and σ^2 are respectively the mean value and the variance of the set of random variables.

2.3 - Theory of approximation

In this paragraph the concepts underlying the theory of approximations are reported and orthogonal polynomials will be introduced briefly; more detailed information can be found in the following textbooks [53], [54], [55].

2.3.1 - Orthogonal polynomials

A generic polynomial of degree n may be expressed with the following equation.

$$Q_n(x) = a_n x^n + a_{n-1}x^{n-1} + .. + a_1 x + a_0\,, \qquad a_n \neq 0 \qquad \text{Eq. 2-29}$$

Where a_n is the main coefficient of the polynomial and is called the "leading coefficient"; dividing by this coefficient the polynomial in monic form is obtained.

$$P_n(x) = \frac{Q_n(x)}{a_n} = x^n + \frac{a_{n-1}}{a_n}x^{n-1} + .. + \frac{a_1}{a_n}x + \frac{a_0}{a_n} \qquad \text{Eq. 2-30}$$

A set of polynomials $\{Q_n(x), n \in \mathcal{N}\}$ is called orthogonal when their internal product $\langle Q_n Q_m \rangle$ is void every time $n \neq m$.

In other words, the following condition applies:

$$\langle P_n P_m \rangle = \int_a^b P_n(x) P_m(x) \omega(x) dx = \gamma_n \delta_{mn} \qquad n, m \in \mathcal{N} \qquad \text{Eq. 2-31}$$

In which $\omega(x)$ is the probability density (therefore its integral over the whole range is unitary), δ_{mn} is the Kronecker Delta[3] and γ_n is a positive constant called the "normalization constant" because for $\gamma_n = 1$ the polynomials are also ortho-normal.
Orthogonal polynomials meet the following differential equation:

$$g_2(x) P_n'' + g_1(x) P_n' + a_n P_n = 0 \qquad \text{Eq. 2-32}$$

In which g_1 and g_2 are independent functions of n, while parameters a_n are constant and depend only on n. Most orthogonal polynomials can be expressed as hypergeometric series, according to the Askey's scheme [56].

Distribution	Density function	Polynomial	Weight function	Support range
Normal	$\frac{1}{\sqrt{2\pi}} e^{\frac{-x^2}{2}}$	Hermite $He_n(x)$	$e^{\frac{-x^2}{2}}$	$[-\infty, \infty]$
Uniform	$\frac{1}{2}$	Legendre $P_n(x)$	1	$[-1, 1]$
Beta	$\frac{(1-x)^\alpha (1+x)^\beta}{2^{\alpha+\beta+1} B(\alpha+1, \beta+1)}$	Jacobi $P_n^{(\alpha,\beta)}(x)$	$(1-x)^\alpha (1+x)^\beta$	$[-1, 1]$
Exponential	e^{-x}	Laguerre $L_n(x)$	e^{-x}	$[0, \infty]$
Gamma	$\frac{x^\alpha e^{-x}}{\Gamma(\alpha+1)}$	Generalized Laguerre $L_n^{(\alpha)}(x)$	$x^\alpha e^{-x}$	$[0, \infty]$

Figure 2.8 – Askey's scheme for different polynomials [57]

Polynomials reported in Figure 2.8 are optimal polynomial bases for different probability distributions; this is because they are orthogonal to the weighting functions, which correspond to the distribution functions themselves.

2.3.1.1 – Legendre's polynomials

Legendre's polynomials (Figure 2.9) are an orthogonal basis for the distribution of uniform normalized probability in the interval $[-1,1]$.

$$Le_n(x) = \frac{1}{2^n} \sum_{l=0}^{n/2} (-1)^l \binom{n}{l} \binom{2n-2l}{n} x^{n-2l} \qquad \text{Eq. 2-33}$$

These polynomials are even when n is even and odd otherwise.
Legendre's polynomials satisfy the following condition of recurrence:

$$Le_{n+1}(x) = \frac{2n+1}{n+1} x Le_n(x) - \frac{n}{n+1} Le_{n-1}(x) \qquad \text{Eq. 2-34}$$

[3] Kronecker delta $\delta_{nm} = \begin{cases} 0 & n \neq m \\ 1 & n = m \end{cases}$

In which the first two polynomials are given by $Le_0(x) = 0$ and $Le_1(x) = 1$.

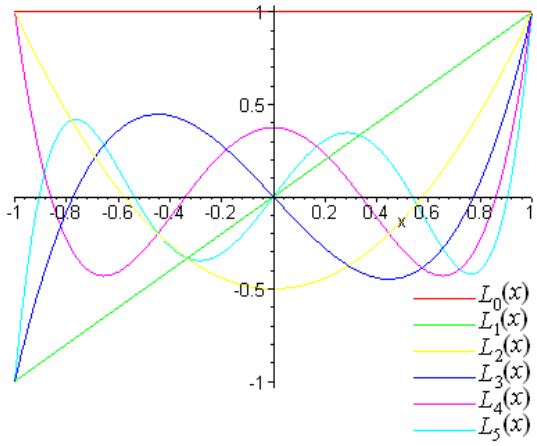

Figure 2.9 – Graphic representation of the first 6 Legendre's polynomials

2.3.1.2 – Hermite's polynomials

Hermite's polynomials (Figure 2.10) are an orthogonal base for the Gauss distribution. Their explicit form is given by the following relation.

$$He_n(x) = n! \sum_{m=0}^{n/2} (-1)^n \frac{1}{m!\, 2^m\, (n-2m)!} x^{n-2m} \qquad \text{Eq. 2-35}$$

Hermite's polynomials are recursive according to the report:

$$He_{n+1}(x) = xHe_n(x) - nHe_{n-1}(x) \qquad \text{Eq. 2-36}$$

The first two Hermite's polynomials are $He_0(x) = 1$ and $He_1(x) = x$.

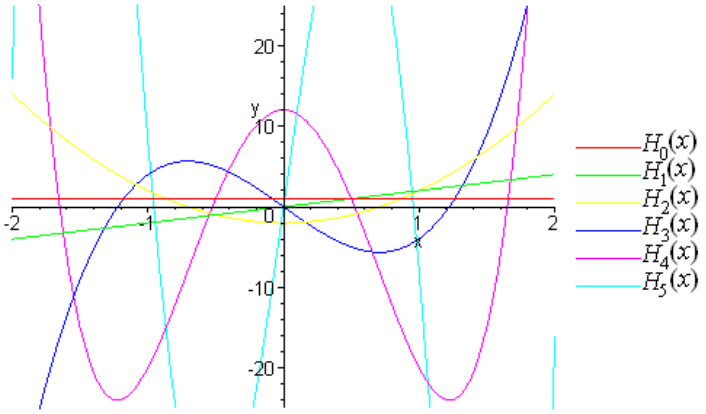

Figure 2.10 – Graphic representation of the first 6 Hermite's polynomials

2.3.2 - Polynomial interpolation

The objective of polynomial interpolation is to construct a polynomial that approximates a function of which only a few discrete points are known. More precisely, given $m+1$ pairs of points (x_i, y_i), the problem is to find a function $G = G(x)$ such that $G(x_i) = y_i$ for $i = 0,1,..,m$; where points y_i that the function G interpolates in nodes x_i are known.

Consider $N+1$ pairs of points (x_i, y_i), the interpolating polynomial $Q_M \in \mathbb{P}_M$ must be defined as follows:

$$Q_M(x_i) = a_M x_i^M + .. + a_1 x_1 + a_0 = y_i\,, \qquad i = 0,1,..,N \qquad \text{Eq. 2-37}$$

The points $\{x_i\}$ are the interpolation nodes; if $N \neq M$ the problem is over or under-determined.

For $N = M$, given $N+1$ different points $x_0, x_1, \ldots, x_N$ and $N+1$ corresponding values of $y_0, y_1, \ldots, y_N$, then there is only one polynomial $Q_N \in \mathbb{P}_M$ for which $Q_N(x_i) = y_i$ for each $i = 0,1,..,N$.

Let $f(x), x \in I$ be a known function and $Q_N f(x)$ its interpolating polynomial of degree N, built using the values $f(x)$ in $N+1$ different points.

It is assumed I_x as the minimum interval containing all the $N+1$ interpolating nodes $x_0, x_1, \ldots, x_N$; then the interpolation error at the point x is given by:

$$E_x(x) = f(x) - Q_N(x) f(x) = \frac{f^{N+1}(\xi)}{(N+1)!} q_{N+1}(x) \qquad \text{Eq. 2-38}$$

In which $\xi \in I_x$ and $q_{N+1} = \prod_{i=0}^{N+1}(x - x_i)$ is the nodal polynomial of degree $N+1$.

Let $\{Q_n(x)\}_{x \in \mathbb{N}}$, with $x \in I$, be an orthogonal polynomial; for each $n \geq 1$, Q_n has exactly n real and distinct zeros in the range I.

This result implies several properties for the zeros of interpolating polynomials, including two interpolating polynomials of degree n and $n-1$, Q_n and Q_{n-1}, that do not have common zeros; it is also possible to demonstrate that between two successive zeros of Q_{n-1} there is only one zero of Q_n.

2.3.3 - Stochastic systems

Given a deterministic model that describes the physical phenomenon it is necessary to correctly set up a stochastic model to study the effect of the uncertainty in the inputs of the system; upstream of the simulations, the key step consists in correctly characterizing the random inputs. The objective is to reduce the space of infinite probability in a space with finite dimension: this is done by parameterizing the space with a finite number of random variables.

The mathematical models of UQ require a set of random variables independent of each other. In other words, the critical phase for the stochastic formulation of the problem consists in correctly characterizing the space of probability defined by the random inputs of the physical system with a finite number of mutually independent random variables. The condition of independence of the variables is particularly complex in the field of application under investigation; regarding gas turbine heat transfer there are many factors that come into play and it is even more complicated to identify two or more variables totally independent of each other.

From a purely theoretical point of view this condition is not so stringent, and most of the software that perform UQ analysis have already implemented a procedure for the treatment of variables that are not independent of each other.
The procedure that allows passing from distributions of correlated variables between them to independent variables happens through a transform $\xi = T(x)$ generally non-linear.
This procedure is purely mathematical and is carried out autonomously by the software, which is why it is omitted from the treatment in this thesis; for a complete study of the subject please see [51], [4] and [58].

2.4 - Uncertainty quantification methodologies

This section describes the techniques for performing non-intrusive uncertainty quantification analyses.
Those methods that allow to approximate an output of a model involved by random variables, parameterized on a finite set of independent random variables $X(\omega)$, defined on a space of probability $(\Omega, \mathcal{B}, P)$ and having a probability density of $f_X(x)$ are defined.

2.4.1 - Sampling based methods

2.4.1.1 - Monte Carlo

This algorithm is very popular for stochastic simulations because it is simple, flexible and its convergence is not dependent on the number of input random variables of the system.
The Monte Carlo method consists in generating a sample of independent input variables x using a random number generator, run the evaluations required and calculate the statistics on the outgoing quantity of interest.
Since the condition of independence among the variables x_i is valid, it is sufficient to go back to their probability value ω_i from their respective distributions $f(x_i)$ previously fixed.
Let x_i be the generic element of the generated sample and let $y^i \equiv y(x_i)$ be the corresponding output value then its average value is given by:

$$\bar{y}(x) = \frac{1}{N}\sum_{i=1}^{N} y(x_i) \approx \mathbb{E}(y) \qquad \text{Eq. 2-39}$$

In which N indicates the number of simulations performed, coinciding with the sample size. The estimation of the error committed is obtained directly from the application of the theorem of the central limit: in fact, since the variables are independent and identically distributed, the function $\bar{y}(x)$ converges for $N \to \infty$ to a normal distribution $\mathcal{N}(\mathbb{E}(y), \frac{\sigma_y^2}{N})$, in which the standard deviation is defined as $\frac{\sigma_y}{\sqrt{N}}$ and σ_y is the standard deviation of the exact solution.
Although this method is widely used it suffers from a low convergence rate, this implies that the error made decreases with the size of the sample, therefore with the number of simulations performed.
The convergence rate or the error committed is in the order of $o\left(\frac{1}{\sqrt{N}}\right)$, this means that for an increase in accuracy of a 10^{-2} factor, 10^4 additional evaluations are required.

Although the Monte Carlo method is rather expensive, the fact of having the convergence rate invariant with respect to the size of the random space, defined by the number of variables, is a property that makes it unique: no other methodology has this peculiarity and this is could be useful for a large number of input variables.

2.4.1.2 – Sampling methods

In order to speed up the convergence rate of the Monte Carlo method, the choice of the sample can be varied. In particular, one of the most used technique is the Latin Hypercube Sampling strategy (LHS).
This sampling technique proposed by Helton [59] consists in dividing the distributions of each input parameter into intervals, the number of segments is equal to the number of samples and these will divide the distributions into portions having all the same area, therefore all equally possible (Figure 2.11). The points are then randomly selected within each area.

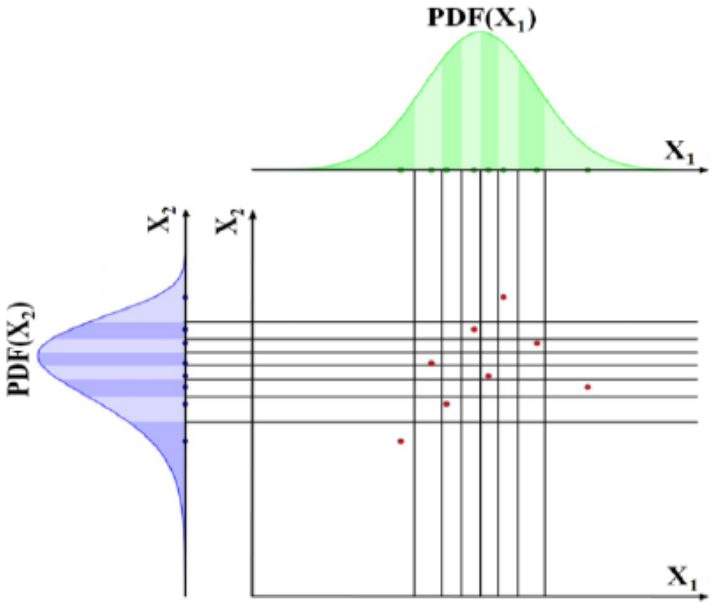

Figure 2.11 – LHS sampling for two variables

With this sampling strategy it is possible to exploit the advantages of the MC method but with a committed error order reduced to $o\left(\frac{1}{N}\right)$.
The advantage in terms of speed of convergence of this method is that a smaller number of points far from the mean value of the distribution of the inputs are selected; by dividing the probability distribution function is different sector, the number of points having a smaller probability of occurrence are surely taken at least once, depending on the number of points selected.

2.4.2 - Stochastic expansion methods

Since the systems are often very complex, the most used approach is to realize a simpler model, called surrogate model that can approximate the real starting model.

These methods are based on the spectral decomposition of the stochastic process through correlation functions; more precisely, the set of orthogonal polynomials, of the Askey's scheme, is used as an orthogonal base to approximate the functional link between the output of the stochastic system under examination and each of its random variables.

There are two approaches to the basis of stochastic expansion: the polynomial chaos expansion (PCE), which uses the bases of orthogonal polynomials and the stochastic collocation (SC) method which uses the bases of interpolating polynomials. Both methods allow to obtain the functional relation that links the output of the studied system to the incoming random variables.

2.4.2.1 - Polynomial Chaos

The polynomial chaos expansion of a generic response function R takes the following form:

$$R = a_0 B_0 + \sum_{i_1=1}^{\infty} a_{i1} B_1(\xi_{i_1}) + \sum_{i_1=1}^{\infty} \sum_{i_2}^{i_1} a_{i_1 i_2} B_2(\xi_{i_1} \xi_{i_2}) + \sum_{i_1=1}^{\infty} \sum_{i_2=1}^{i_1} \sum_{i_3=1}^{i_2} a_{i_1 i_2 i_3} B_3(\xi_{i_1}, \xi_{i_2}, \xi_{i_3}) + \dots \quad \text{Eq. 2-40}$$

In which the size of the independent random vector ξ_i is unlimited and each additional set of nested summations indicates an additional order of polynomials in the expansion.

Changing the indexing to order, with a term-based one, a reduced formulation can be found:

$$R = \sum_{j=0}^{\infty} \alpha_j \psi_j(\xi) \quad \text{Eq. 2-41}$$

In Eq. 2-41 there is a univocal correspondence between the coefficients a_i and the coefficients α_j and between polynomials $B_n(\xi_{i_1}, .., \xi_{i_n})$ and $\psi_j(\xi)$.

Terms $\psi_j(\xi)$ are multivariate polynomials involving the products of one-dimensional polynomials derived from a single random variable; a multivariate polynomial may be indicated with the following equation:

$$B_n(\xi_{i_1}, .., \xi_{i_n}) = \psi_j(\xi) \prod_{i=1}^{n} \psi_{t_i^j}(\xi_i). \quad \text{Eq. 2-42}$$

In which with the diction t_i^j indicates the term of multi-index expansion.

When the input variables have different distributions, therefore polynomial bases of different families, the given definition remains valid but the one-dimensional polynomials of the different distributions must be considered. In practice, Eq. 2-41 is always truncated with a finite number of random variables and a fixed polynomial of degree P.

$$R = \sum_{j=0}^{\infty} \alpha_j \psi_j(\xi) \approx \sum_{j=0}^{P} \alpha_j \psi_j(\xi) \quad \text{Eq. 2-43}$$

The polynomial can be truncated in two ways: by fixing the total order of the polynomial, or by defining the maximum order of the polynomial bases; this aspect plays a fundamental role as it defines the number of simulations to be carried out, so that it directly affects the computational costs.

- The final interpolating polynomial includes a complete polynomial base up to a specified total order.

In this case, the number of terms N_t of the expansion with total order p involving n random variables are given by the following relation:

$$N_t = 1 + P = \frac{(n+p)!}{n!\,p!} \qquad \text{Eq. 2-44}$$

This type of approach is called "**total or fixed order expansion**".
When searching for the functional link between the output parameter and two random variables ($n = 2$) with a polynomial of order two ($p = 2$), the total number of terms and therefore the number of simulations to be performed are six.

The other type of approach is called "**tensor-product expansion** "; in this case the limits to the order are not defined on the final polynomial but on the bases of the polynomial and all the combinations of the individual one-dimensional polynomial are included.
The number of total evaluations is given by:

$$N_t = 1 + P = \prod_{i=1}^{p}(p_i + 1) \qquad \text{Eq. 2-45}$$

This technique allows imposing different polynomial orders for the various bases of the input variables; in other words, it allows to impose heterogeneous problems, properties that do not have the method of total order expansion.

$$Total\ order\ Expansion\ =\ 2$$

$$\begin{aligned}
\Psi_0(\xi) &= \psi_0(\xi_1)\,\psi_0(\xi_2) &&= 1\\
\Psi_1(\xi) &= \psi_1(\xi_1)\,\psi_0(\xi_2) &&= \xi_1\\
\Psi_2(\xi) &= \psi_0(\xi_1)\,\psi_1(\xi_2) &&= \xi_2\\
\Psi_3(\xi) &= \psi_2(\xi_1)\,\psi_0(\xi_2) &&= \xi_1^2 - 1\\
\Psi_4(\xi) &= \psi_1(\xi_1)\,\psi_1(\xi_2) &&= \xi_1\xi_2\\
\Psi_5(\xi) &= \psi_0(\xi_1)\,\psi_2(\xi_2) &&= \xi_2^2 - 1
\end{aligned}$$

$$Tensor - product\ Expansion\ =\ 2$$

$$\begin{aligned}
\Psi_0(\xi) &= \psi_0(\xi_1)\,\psi_0(\xi_2) &&= 1\\
\Psi_1(\xi) &= \psi_1(\xi_1)\,\psi_0(\xi_2) &&= \xi_1\\
\Psi_2(\xi) &= \psi_2(\xi_1)\,\psi_0(\xi_2) &&= \xi_1^2 - 1\\
\Psi_3(\xi) &= \psi_0(\xi_1)\,\psi_1(\xi_2) &&= \xi_2\\
\Psi_4(\xi) &= \psi_1(\xi_1)\,\psi_1(\xi_2) &&= \xi_1\xi_2\\
\Psi_5(\xi) &= \psi_2(\xi_1)\,\psi_1(\xi_2) &&= (\xi_1^2 - 1)\xi_2\\
\Psi_6(\xi) &= \psi_0(\xi_1)\,\psi_2(\xi_2) &&= \xi_2^2 - 1\\
\Psi_7(\xi) &= \psi_1(\xi_1)\,\psi_2(\xi_2) &&= \xi_1(\xi_2^2 - 1)\\
\Psi_8(\xi) &= \psi_2(\xi_1)\,\psi_2(\xi_2) &&= (\xi_1^2 - 1)(\xi_2^2 - 1)
\end{aligned}$$

Figure 2.12 – Total-order expansion (left); tensor-product expansion (right) [57]

From Figure 2.12 it is evident that with the two different truncation methods a different type of approximation is obtained.
The imposed total order approach overlooks a significant part of the polynomial coverage of the tensor product approach, which is why, unless a very small number of variables is involved, the fixed total order method requires fewer evaluations (Figure 2.13).

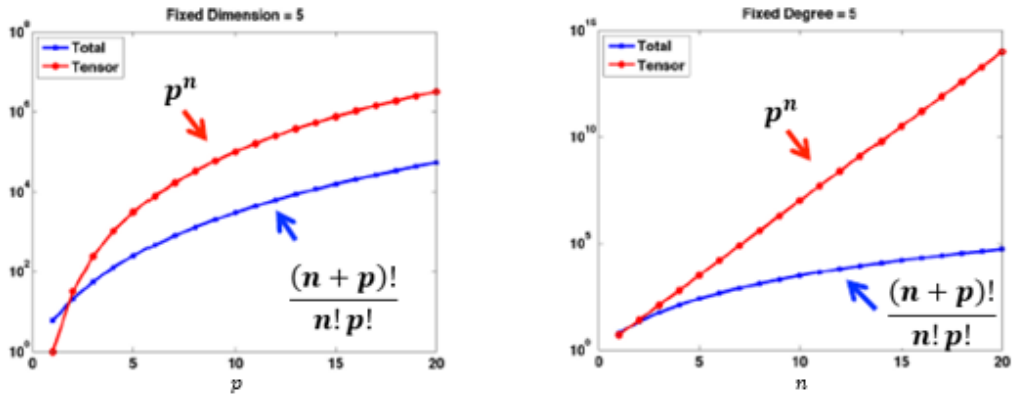

(a) (b)

Figure 2.13 – Number of evaluations required for different order (a) and variables (b) [57]

As far as the validation of uncertainty quantification methodologies is concerned, the work taken as reference by all the other articles in the literature is the one carried out by Eldred [60]. This shows that the number of evaluations required for the total order method imposed is higher than that one defined by Eq. 2-44; the author shows how it is necessary to oversample, at least twice the minimum number required, in order to obtain a more robust and accurate analysis response.

$$N_t = 1 + P = \frac{(n+p)!}{n!\,p!} \quad \Rightarrow \quad N_{t_{eff}} \geq 2N_t \qquad \text{Eq. 2-46}$$

As will be reported later, this expediency is implemented in all the works in the literature and in the next chapter it will be clear that was also necessary for this study as well in order to obtain reasonable results.

2.4.2.2 – Stochastic collocation

The stochastic collocation expansion is made by the sum of a set of multidimensional interpolating polynomials for the collocation points and a polynomial that interpolates the results on the adjacent points that can be made up of some components of the gradient of the function between the points themselves.
For the evaluation in the interpolating points, Lagrange polynomials are used, which interpolate a set of points with a functional one in the following form:

$$L_j = \prod_{\substack{k=1 \\ k \neq j}}^{m} \frac{\xi - \xi_k}{\xi_j - \xi_k} \qquad \text{Eq. 2-47}$$

The one-dimensional interpolation of the response function R, for a portion l containing m^l points is given by the following expression:

$$R(\xi) \cong \sum_{j=1}^{m_l} r(\xi_j) L_j(\xi) \qquad \text{Eq. 2-48}$$

The approximation given here reproduces the values of the response $r(\xi_j)$ at the interpolation points and it interpolates between these and other points.
For multidimensional interpolations the formulation remains similar, with the difference that the limit of the summation will be the number of the collocation points in the portion of space considered.

Hermitian polynomials are used for the interpolation of point values with gradients.

2.4.3 - Spectral projection

The main difference between the polynomial chaos expansion and the stochastic collocation is that for the first method the coefficients of the interpolating polynomial must be estimated starting from known polynomial bases, while for the stochastic collocation the interpolating polynomial must be found from known coefficients.
For polynomial chaos approach the polynomial coefficients can be found by a spectral projection method or by linear regression.
The first approach implies the numerical integration on the points that can be randomly sampled, or on special calculation grids that optimize the procedure. The most used grids are Gauss quadrature grids and Smolyak's sparse grids. Stochastic collocation, since it requires a structured data set for multidimensional interpolation of both point values and gradients, does not allow random sampling, but only the above-mentioned grids. The spectral projection consists in projecting the output of the system on each polynomial base by means of tensorial products, then the conditions of orthogonality are imposed in order to obtain the polynomial coefficients. Starting from Eq. 2-41, by carrying out an internal product with ψ_j from both sides and by isolating the polynomial coefficients, the following equation is obtained:

$$R \approx \sum_{j=0}^{P} \alpha_j \psi_j(\xi) \Rightarrow \alpha_j = \frac{\langle R, \psi_j \rangle}{\langle \psi_j, \psi_j \rangle} = \frac{1}{\|\psi_j^2\|} \int_{\Omega} R \psi_j \rho(\xi) d\xi \qquad \text{Eq. 2-49}$$

Each internal product involves a multidimensional integral on the space in which the weight function is defined $\rho(\xi)$; since this is a probability, the integral is defined in an interval of the space of probability. It is pointed out that the internal product of two quantities defined as positive coincides with the norm, so the denominator of the equation is the squared norm of the orthogonal polynomial multivariate, in which its structure depends on the type of distribution and its shape is that shown in the Askey's scheme. The integral approach is equivalent to calculating the mean value of the response function for each polynomial base; the first coefficient of the polynomial is, in fact, the mean of the response obtained at the exit of the code. The random sampling from a calculation point of view does not exist, this is generated with special algorithms that generate pseudo-random numbers; in practice, however, this type of generation is not an effective system for estimating the moments of the response function.
In accordance with what has already been described in the paragraph on the Monte Carlo method, a sampling method based on the LHS algorithm, which is the standard for this type of application, is more efficient. Subsequently, the sampling grids, which can be used for both PCE and SC methods, are described.

2.4.3.1 – Gauss quadrature grid

With this grid the integral of the Eq. 2-49 is solved using one-dimensional quadrature rules; with this approach the polynomial zeros are chosen in order to verify the condition of orthogonality with the weight functions.

Let us assume that $\{\xi_1^i, .., \xi_{mi}^i\} \subset \Omega_i$ is a sequence of abscissae by quadrature on Ω_i and $f \in C^0(\Omega_i)$, then it is possible to introduce a sequence of one-dimensional quadrature operators.

$$\mathcal{U}^i(f)(\xi) = \sum_{j=1}^{m_i} f(\xi_j^i)\omega_j^i \qquad \text{Eq. 2-50}$$

With $m_i \in \mathbb{N}$.

The newly introduced equation allows for the correct integration of any polynomial of less than $2m_i - 1$, for each $i = 0,1,..,n$.

Once a certain polynomial order p is set, the assessments of the highest order coefficient include an integrand function of a minimum order of $2p$ (ψ of order p modelling the response function R with order p) in each dimension, for which, in order to obtain a good accuracy of the coefficients, a minimum order $p + 1$ of Gauss quadrature is required.

The formulation for the multidimensional case is defined by a complete tensor product:

$$\mathcal{Q}_i^n f(\xi) = (\mathcal{U}^{i_1} \otimes .. \otimes \mathcal{U}^{i_n})(f)(\xi) = \sum_{j_1=1}^{m_{i_1}} .. \sum_{j_n=1}^{m_{i_n}} f\left(\xi_{j_1}^{i_1}, .., \xi_{j_n}^{i_n}\right)\left(\omega_{j_1}^{i_1} \otimes .. \otimes \omega_{j_n}^{i_n}\right) \qquad \text{Eq. 2-51}$$

This type of formulation requires $\prod_{j=1}^{n} m_{ij}$ evaluation functions.

When the number of input random variables is reduced, this approach is very efficient as it requires minimal computational effort. However, as the size increases, this method presents always a lower efficiency; this is due to the fact that the number of points to be evaluated increases exponentially with the number of input variables. By imposing the same polynomial order for all variables, $m_{ij} = m$, the previous equation requires a number of assessments equal to m^n.

2.4.3.2 – Smolyak sparse grid

When the number of variables is moderately high and the sampling on the Gauss quadrature grid becomes too expensive, it is possible to use the Smolyak grid [61].

This approach allows to drastically reduce the collocation points while maintaining a high level of precision (Figure 2.14 and Figure 2.15). The number of points required by this method is obtained from the following relationship, expressed for simplicity in a reduced form:

$$\mathcal{A}(w,n) = \sum_{l+1 \le |i| \le l+n} (-1)^{l+n-|i|} \binom{n-1}{l+n-|i|} \cdot (\mathcal{U}^{i_1} \otimes .. \otimes \mathcal{U}^{i_n}) \qquad \text{Eq. 2-52}$$

In the formula n which is the number of input variables and l which is the parameter that indicates the Smolyak level and it is independent of the number of variables considered.

This formula results in a linear combination of the Gauss formula (last factor of the summation) with a factor that reduces the number of points.

	$d=2$	$d=3$	$d=4$	$d=5$	$d=6$	$d=7$
Tensor Gauss	25	125	625	3125	15625	78125
Smolyak Gauss	17	31	49	71	97	127

Figure 2.14 – Points required with the Gauss grid (5th order) and Smolyak (1st level) [51]

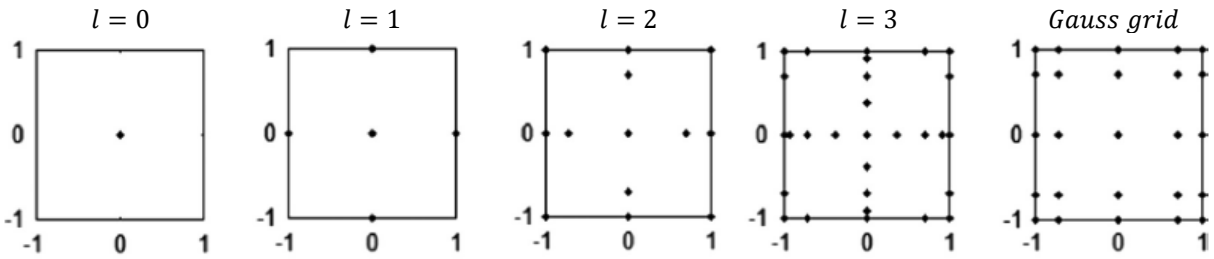

Figure 2.15 – Visual comparison for different levels of Smolyak and Gauss for a two variables problem [51]

It is important to underline how, for problems with reduced number of variables and limiting the polynomial order, the most efficient approach in terms of computational expenditure remains the one defined by the use of the Gauss tensorial grid.

2.4.4 - Linear regression

The interpolating polynomial can be obtained without using integral formulations but from the solution of the linear system defined by the set of polynomial coefficients that best approximate the response function R.

$$\psi\alpha = R \qquad \text{Eq. 2-53}$$

In this case, the sampling can be carried out either on a structured grid (Gauss or Smolyak), with the carefulness to maintain a sampling order higher than the polynomial order to avoid selecting the zeroes of the polynomial base, or on a non-structure grid as for pseudo-random sampling. In both cases in each row of the matrix ψ there are N_t multidimensional polynomial terms evaluated at a given point.

$$\begin{bmatrix} \psi_0(\xi_1) & \cdots & \psi_{N_t}(\xi_1) \\ \vdots & \ddots & \vdots \\ \psi_0(\xi_n) & \cdots & \psi_{N_t}(\xi_n) \end{bmatrix} \begin{pmatrix} \alpha_0 \\ \vdots \\ \alpha_{N_t} \end{pmatrix} = \begin{pmatrix} R(\xi_1) \\ \vdots \\ R(\xi_{N_t}) \end{pmatrix} \qquad \text{Eq. 2-54}$$

When:

- $n = N_t$ the system is solved directly
- $n > N_t$ the system is over-determined and it is resolved by minimum squares approaches
- $n < N_t$ the system is under-determined and it is solved with decomposition and elimination algorithms

2.4.5 - Analytics moments

The statistical moments previously defined are obtained differently using the methods of polynomial expansion. Mean value and covariance of polynomial expansions can be defined in closed form and provide the exact moments of the response functions.

$$\mu_i = \langle R_i \rangle \cong \sum_{k=0}^{P} \alpha_{ik} \langle \psi_k(\xi) \rangle = \alpha_{i0} \quad \text{Eq. 2-55}$$

$$cov_{ij} = \langle (R_i - \mu_i)(R_j - \mu_j) \rangle \cong \sum_{k=1}^{P} \sum_{l=1}^{P} \alpha_{ik}\, \alpha_{il} \langle \psi_k(\xi) \psi_l(\xi) \rangle = \sum_{k=1}^{P} \alpha_{ik} \alpha_{jk} \langle \psi_k^2 \rangle \quad \text{Eq. 2-56}$$

Similar formulations are obtained for stochastic collocation.

$$\mu_i = \langle R_i \rangle \cong \sum_{k=0}^{N_P} r_{ik} \langle L_k(\xi) \rangle = \sum_{k=1}^{N_P} r_{ik} \omega_k \quad \text{Eq. 2-57}$$

$$cov_{ij} = \langle R_i R_j \rangle - \mu_i \mu_j \cong \sum_{k=1}^{N_P} \sum_{l=1}^{N_P} r_{ik}\, r_{il} \langle L_k(\xi) L_l(\xi) \rangle - \mu_i \mu_j = \sum_{k=1}^{N_P} r_{ik} r_{jk} \omega_k - \mu_i \mu_j \quad \text{Eq. 2-58}$$

Expressions for asymmetry and kurtosis are obtained by direct numerical integration of the response function.

$$sk = \gamma_{1i} = \langle \left(\frac{R_i - \mu_i}{\sigma_i} \right)^3 \rangle \cong \frac{1}{\sigma_i^3} \left[\sum_{k=1}^{N_P} (r_{ik} - \mu_i)^3 \omega_k \right] \quad \text{Eq. 2-59}$$

$$Ku = \gamma_{2i} = \langle \left(\frac{R_i - \mu_i}{\sigma_i} \right)^4 \rangle - 3 \cong \frac{1}{\sigma_i^4} \left[\sum_{k=1}^{N_P} (r_{ik} - \mu_i)^4 \omega_k \right] - 3 \quad \text{Eq. 2-60}$$

2.5 - UQ software

The number of software and libraries for the uncertainty quantification is already considerable and will continue to grow over the years; in the literature, many highly custom programme performing uncertainty quantification analysis can be found. Moreover, calculation tools have been developed in the MATLAB environment and function libraries written in C/C++ and Python programming languages can be found as well.

This section describes the software used for the development of the workpiece and gives an overview of the other programs that are most interesting for this type of analysis.

2.5.1 - DAKOTA

The software used for the development of the entire work was DAKOTA [57]: a multidisciplinary executable capable of performing, in addition to UQ analysis, experimental test design, sensitivity analysis, reliability studies, parameter estimation and which has optimization algorithms incorporated, including multi-objective ones; it was developed by the "Sandia National Laboratories" and is completely open-source.
The software has the advantage of interfacing, potentially, with any other solver from which it receives data for subsequent statistical processing; moreover, the interface with Python environments for the pre-processing of the data is directly provided.
The software needs a first input, in the form of a text file, in which the type of analysis, the distributions of the input variables, the interface and the number of response functions to be analysed are specified; at this point, the simulation cycle begins. For each sample input, DAKOTA, through the interface, launches the third-party software and quantities of interest are then obtained; the procedure is repeated for the number of simulations required, depending on the type of analysis. The block diagram of the procedure is shown in Figure 2.16. Once all the evaluations have been completed, the statistics of the parameter studied are provided at the output.

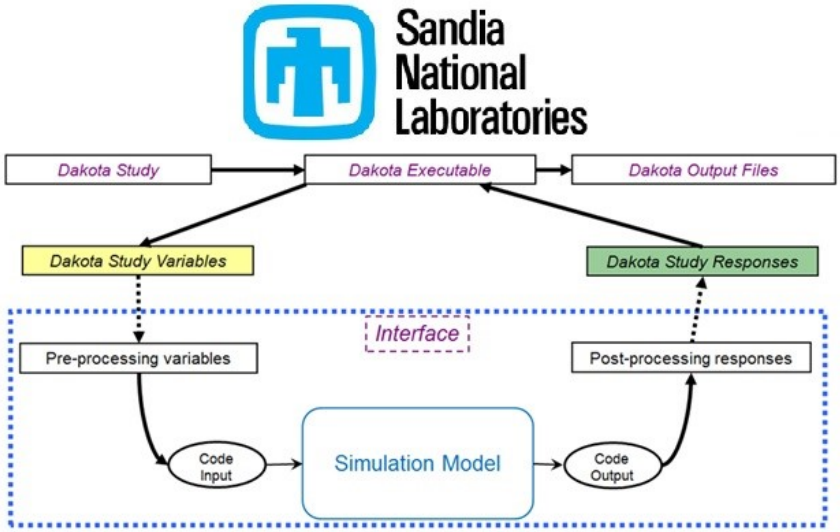

Figure 2.16 – General UQ analysis procedure using DAKOTA [57]

In terms of output, the software provides the four statistical moments for each response functions; the discretization of the functions and the number of output quantities must be specified in the input file. The data coming out from the software are in the form of text files; this aspect is rather critical in terms of data processing: in fact when the number of "response functions" increases, the size of the output file is too big and it cannot be processed directly; for this reason it is necessary to use reading and processing scripts to obtain the results in graphic terms. It was decided not to include input and output files in this work as not to weigh the writing down: all the relevant information are provided in the body text and in Chapter 3.2.2 -.
This executable was chosen because it is open-source, easily interfaced with other software and because it does not only perform UQ analysis but also combines it with sensitivity analysis; moreover, as already mentioned, it can also be used for optimization studies.

From the point of view limited to uncertainty quantification, DAKOTA is not the most complete software (Figure 2.17), but it represents a tool that allows fluctuating in different fields, which, for turbomachinery and heat transfer application, could simplify the procedure of design and optimization in every aspect.
The strength of this executable, which in fact has been preferred over other software, is its simplicity; it elaborates text files suitably formatted, in which the different methodologies and set up to be carried out are specified through keywords. It presents special commands to manage any errors or particular operation of the software to which it is interfaced with; in this way it can independently solve situations where the result obtained is incorrect or when the software interfaced to DAKOTA presents sudden crashes. It also is well suited to the analysis of data already in the possession of the user, or it allows the processing of data already acquired stand-alone. In this configuration it is possible to import a certain set of points as sample input; in CFD simulations this aspect is particularly interesting, in fact the simulations can be priory performed and then the analysis of UQ can be carried out a posteriori, only after verifying the results obtained.

2.5.2 - Python libraries

- OpenTURNS [62] is a C++ library then also translated into Python language; it is very similar to DAKOTA in terms of computing capacity but, currently, has not implemented any method for numerical integration and has no optimization packages.
  It should be noted that this toolbox was funded by a consortium formed by industrial leaders in the aeronautical sector such as Airbus and ONERA; this is to highlight once again how much uncertainty quantification analysis plays an increasingly central role in the aeronautical field.
- Chaospy [63] is a library completely written in Python for UQ analysis. In the article cited, the authors show detailed comparisons between the various capabilities of the newly introduced software. This is the most complete library in terms of distributions assignable to the different inputs of the problem, it also shows how OpenTURNS is more developed than DAKOTA in mathematical terms, to make the input variables independent and also has a greater number of sampling methods.

Chaospy is the basis of another Python library, "Uncertainpy" [64] developed in the field of neural networks by the University of Oslo.

Feature	Dakota	Turns	Chaospy
Distributions	11	26	64
Copulas	1	7	6
Sampling schemes	4	7.5	7
Orthogonal polynomial schemes	4	3	5
Numerical integration strategies	7	0	7
Regression methods	5	4	8
Analytical metrics	6	6	7

Figure 2.17 – Main characteristics of different software [63]

2.5.3 - MATLAB environment

UQ analyses can be carried out in the MATLAB environment using an extension created by the ETH Zurich, called "UQLab" [65]. Although the tool's capabilities are similar to those of the other software mentioned above, the need for the license makes the software more suitable for research environments, limiting its use in industrial applications. This module has more critical issues than the other codes just described in the interface with other software, the absence of optimization methods restricts the use of the activities of UQ.

2.6 - Sensitivity analysis

Since DAKOTA carries out sensitivity analyses independently whenever a spectral method is used, it is considered appropriate to describe this type of procedure, even though it is not the main focus of the thesis work.

This type of analysis allows to estimate, in mathematical terms, through the Sobol's indices [37], how much a particular input random variable affects the output quantity considered. This characteristic is very interesting in the field of heat transfer in turbomachinery because there are a large number of factors and physical phenomena that could affect the results.

The mathematical procedure is based on the decomposition of the variance from which two different indices are obtained, one due strictly to the input variable considered, indicated with S_i, and called main Sobol's index; the other, indicated by S_{T_i}, takes into account all the effects due to the interaction between the variable considered and the others; for this reason, it is defined as total Sobol's index.

The main index corresponds to that fraction of uncertainty of the output Y which is generated solely by the presence of the variable x_i under consideration; the main indices of the first order are defined as the ratio between the variance of the expected value conditioned by the variable considered and the variance of the output variable.

$$S_i = \frac{Var[E(Y|x_i)]}{Var(Y)} \qquad \text{Eq. 2-61}$$

Considering also the main indices of greater order (interaction) that define how much the variation of a variable is related to another one on the output of the system, the following property can be obtained, valid for the principal Sobol's indices:

$$\sum_{i=1}^{n} S_i + \sum_{j<i}^{n} S_{ij} = 1 \qquad \text{Eq. 2-62}$$

In which n is the number of random variables used for the analysis.

The total Sobol's index takes into account all the interactions that concern a given variable and they are defined as follows:

$$S_{T_i} = \frac{E[Var(Y|x_i)]}{Var(Y)} = \frac{Var(Y) - Var[E(Y|x_i)]}{Var(Y)} \qquad \text{Eq. 2-63}$$

The definition of the total Sobol's indices necessarily implies the following condition:

$$\sum_{i=1}^{n} S_{T_i} \geq 1 \qquad \text{Eq. 2-64}$$

In this thesis it has decided not to report the equations by which DAKOTA analytically calculates the Sobol's indices, for the complete treatment of the subject please refer to the article of Tang et al. [66].

2.7 - Bibliography

As already mentioned, the propagation of uncertainty within the numerical codes used for turbomachinery application is relatively recent, nevertheless, there are works in the literature that deal with different aspects related to heat transfer in turbomachinery applications.

It has already been mentioned that the first work regarding comparison and validation of UQ methods was carried out by Eldred [60]; this article shows how the residuals of a CFD analysis vary with the variation of the mathematical approach used.
The treaty shows that the performance of PCE and SC is much more effective than the Monte Carlo method.
A comparison is then made between the main methods of UQ, the polynomial chaos expansion and stochastic collocation, which shows that they have similar performance; the author says that for an equal number of points sampled the two different methods give approximately the same results.
For Eldred, the main advantage of the PCE method compared to the SC is the possibility to carry out the sampling also on unstructured grids.
In terms of computational costs, for a low number of uncertain variables, the best method is linked to the tensorial product on the Gauss grid; as the size increases, Smolyak grids are increasingly advantageous, allowing high accuracy with a reduced number of evaluations.
Another important result reported by the author is the one related to the PCE method with fixed total order, for which there is the need to use an oversampling in order to obtain an accurate response.

As far as the applications of UQ to the heat transfer in turbomachinery are concerned, there are not so many works currently in the literature and they cover different problems: from the most classic issues related to the cooling of components at high temperature to emissions due to new types of combustion to more complex issues such as the phenomena of thermal-acoustic stability inside the combustor or applications for the study of turbulent flames with LES simulations.
The UQ studies applied to CFD that one can find in the literature are characterized by having a limited number of uncertain variables, three at most, generally; this is due to the high increase in the computational cost that occurs with the increase in the number of variables, a problem known as curse of dimensionality.
The studies in which a higher number of inputs are considered are applied to low-fidelity codes that allow a high amount of information to be obtained with reduced computational efforts.
The study carried out by Durocher et al. [67] assesses the impact of atmospheric carbon compounds on the emissions of a combustor, in particular, changes in hydrocarbon (CH) concentrations are estimated, of nitrogen oxides (NO_x) output and flame speed, with a one-dimensional simulator called "Cantera" [68].

In this study validation of the PCE methods and of the relative calculation grids with the Monte Carlo method is carried out; the uncertain variables considered are the kinetic coefficients that govern the chemical reactions that take place in the combustor. The author evaluated the impact of nine reactions on the quantities of interest, those with the highest kinetic coefficients and considered them uniformly distributed.
The specific analyses carried out and the results obtained from the simulations are reported in terms of mean value and standard deviation in Figure 2.18; the uncertain variables are eight because one same factor act on two different reactions.

Method	CH peak (ppm)		NO_x (ppm)		S_u (m/s)	
	Average	Std. Deviation	Average	Std. Deviation	Average	Std. Deviation
MC-LHS (4000 points)	1.563	1.494	22.43	8.107	0.3384	0.02967
1^{st}-order total-order (9 points)	1.539	1.144	21.16	6.029	0.3399	0.02821
2^{nd}-order total-order (45 points)	1.568	2.000	22.49	11.54	0.3405	0.03547
2^{nd}-order total-order (180 points)	1.543	1.438	22.34	7.975	0.3402	0.03169
2^{nd}-order tensor-product (6561 points)	1.539	1.382	22.37	7.833	0.3400	0.02764
l_2 sparse grid (161 points)	1.548	1.394	22.45	7.890	0.3464	0.03017

Figure 2.18 – Analyses and results carried out by Durocher et al. [67]

The results obtained by Durocher et al. [67] reflect what was stated in [60]: in order to obtain more accurate analyses, the total order PCE methodology requires over-sampling, and for this application the authors carried out samples three times as high as required.
It can be seen that the Gauss tensor product method is also less efficient than the Monte Carlo method, which required four thousand evaluations to reach convergence, although no data on the actual convergence of the method has been reported.
Another aspect is the efficiency shown by the Smolyak grid which, overall, finds the best agreement with the MC method.
The study showed that the one-dimensional solver, subject to nine uncertain parameters, produces a variation of 400% in the output quantities with respect to the nominal values, while the band of uncertainty obtained from experimental tests is 20%, which shows that the solver must be implemented with more accurate chemical mechanisms.
Also in the field of combustion, a UQ study on a CFD analysis with LES approach was carried out by Mueller et al. [69]. This article assesses the uncertainty associated with modelling chemical kinetics for an unmixed turbulent flame. The uncertain variable considered is the coefficient of "reaction rate", the probability distribution is imposed by the authors as log-normal and sampled with LHS method. The technique used for UQ analysis is stochastic expansion through polynomial chaos.
The author reports the temperature and mass fraction of carbon monoxide (y_{CO}) for the different mixture fractions (Z) in which, for both quantities is also reported the confidence interval of the 99% (Figure 2.19).

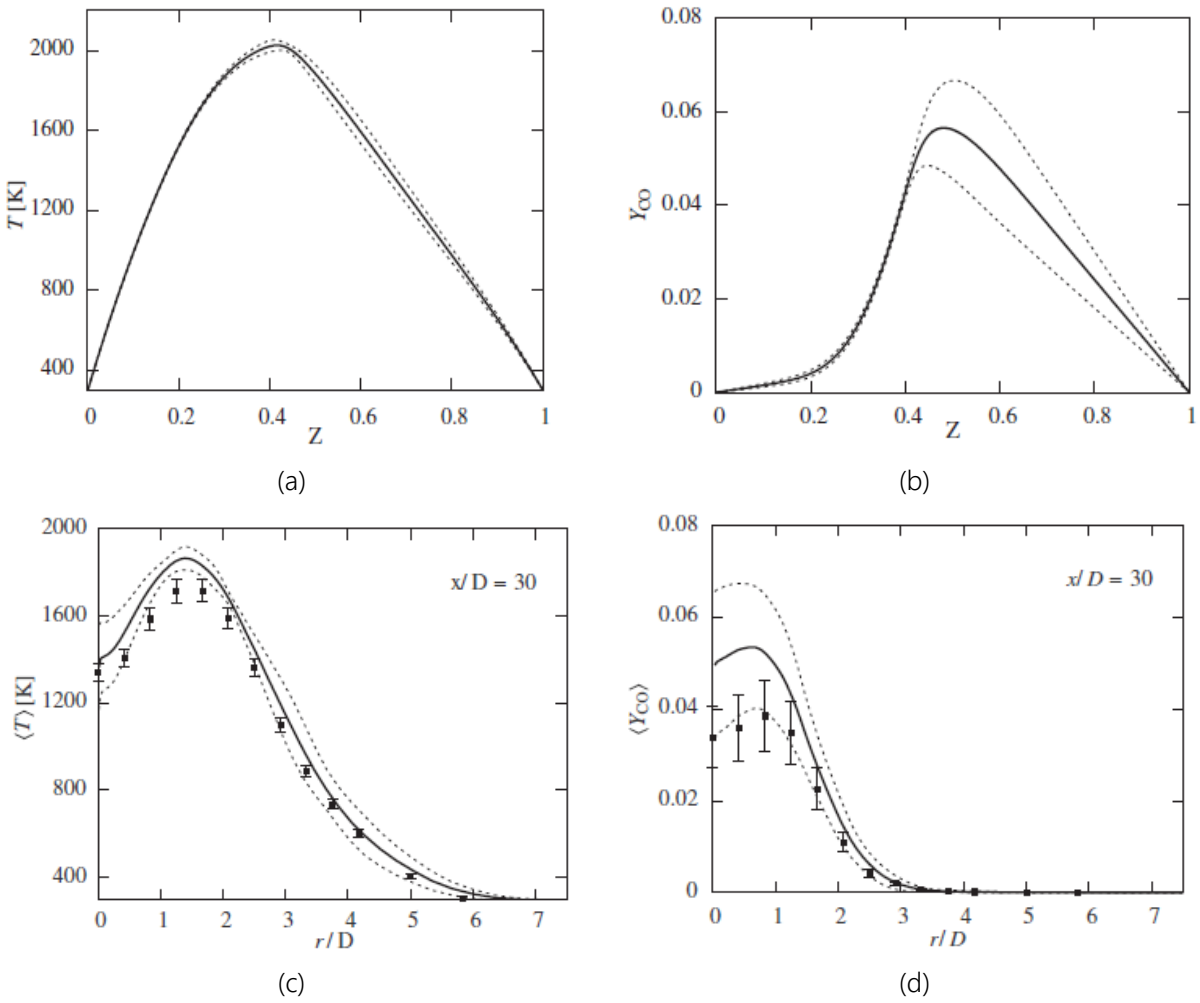

Figure 2.19 – (a) Confidence interval of 99% for temperature as a function of mixture fraction; (b) Confidence interval of 99% for the mass fraction of CO; (c) Comparison of average over-time radial temperature profile; (d) Comparison of average radial fraction profile by mass of CO [69]

In the study, a comparison between the values numerically and experimentally obtained (the latter, acquired from previous studies) is made, along with the relative error bands. The average radial profiles of temperature and mass fraction of CO are compared.

From the previous figure it can be noticed how the experimental results are overestimated by the LES simulation; but also how, considering the uncertainties both numerical and experimental, especially for the y_{CO} there is a good agreement. The author, considering the results, decided to validate the combustion models used.

In the field of heat transfer, one of the most important theme is the film cooling for turbine blades; the most studied uncertain variables are those related to the boundary conditions that occur inside the machine. This theme is treated by D'Ammaro [70]; in his study the pressures of the main flow and that of the flow that generates the film are assumed as uncertain variables, both considered distributed according to a normal distribution.

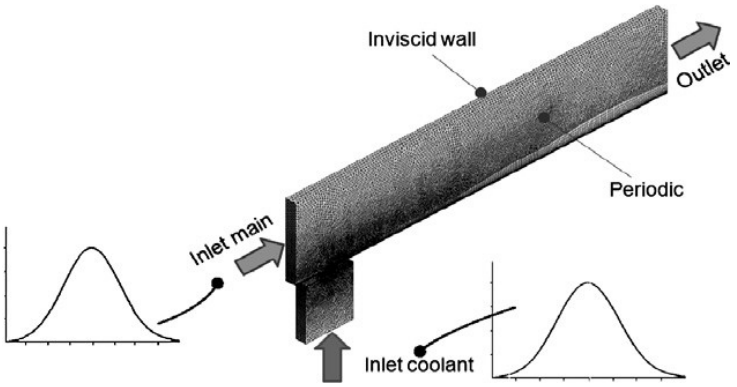

Figure 2.20 – Test case analysed by D'Ammaro et al. [70]

Simulations were carried out on a simplified geometry with RANS approach (Figure 2.20) with reduced domain: there is only one film cooling hole and a plenum from which the flow that will form the film and the fluid domain affected by the main flow comes out; in this study the real geometry of the blade is not considered; instead, the blade surface is approximated like a flat plate.
A comparison between the MC method (242 simulations) and the stochastic expansion method is carried out for two different total orders of the PCE procedure, two and four; for the latter case instead of carrying out the required simulations only, according to Eq. 2-44, about twice as often the simulations are performed to obtain a more precise solution. The results obtained in [70] are reported in Figure 2.21.

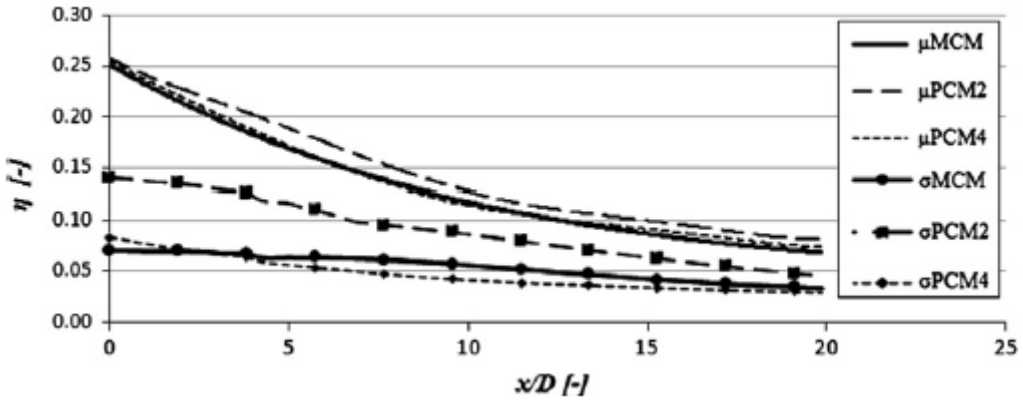

Figure 2.21 – film cooling effectiveness for MC approach and PCE 2nd and 4th order [70]

The probability distributions of the pressures are imposed in order to obtain a variation up to 100% on the main flow pressure and 20% on that of the coolant.
From the graph, it is clear that the polynomial of 2nd order does not give a reliable result while the polynomial of 4th order, which however requires a number of simulations ten times lower than the Monte Carlo method, is in total agreement with the solution predicted by the MCM.

A similar work to the one just mentioned is that of Babaee [71], in which the influence of the uncertainty of the blowing ratio on the film cooling effectiveness is evaluated. The particularity of this study is that the turbulence is not modelled but completely resolved: in fact, DNS (*Direct Numerical Simulation*) simulations are carried out. The geometric domain is similar to the case already described above.

The author validates the computational results with those experimentally obtained by comparing the axial velocity at different heights of the duct, and they ended up with an excellent agreement between the two approaches. In terms of UQ analysis the polynomial chaos expansion is explored with a total order of three; the only uncertain parameter, the blowing ratio, is modelled with a normal distribution $\mathcal{N}(0.3, 0.01)$.

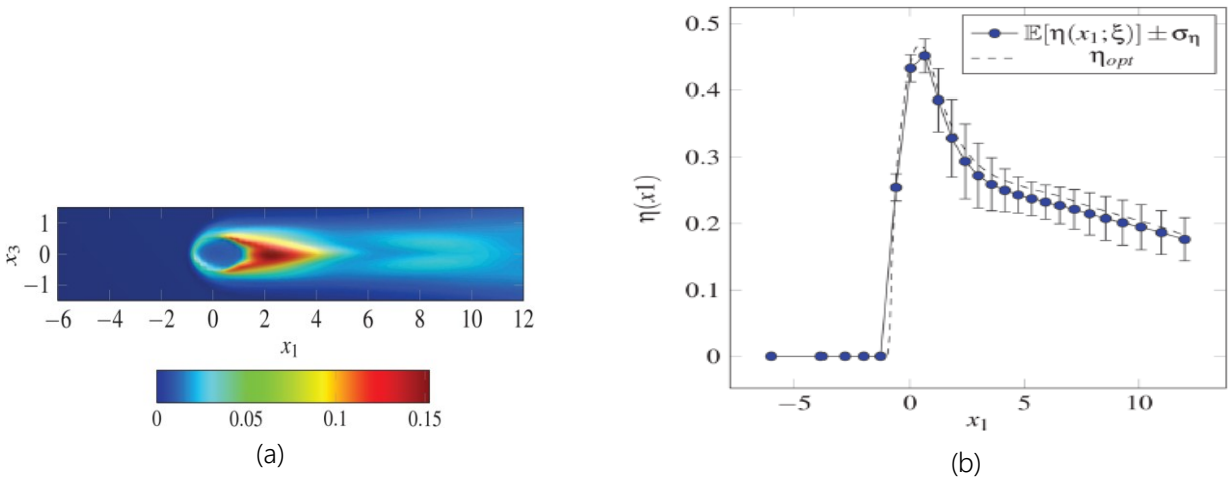

Figure 2.22 – Evolution $\sigma_T/\mathbb{E}(T)$ for different BR (a); Effectiveness and relative uncertainty (b) [71]

The study shows that the input uncertain considered produces the maximum excursion in terms of film cooling effectiveness immediately downstream of the hole (Figure 2.22a), although the average protection in this area is good, this portion of the blade is subject to a considerable temperature excursion range.

There are works in literature that evaluate the impact of geometric uncertainties on the film cooling effectiveness; the first study related to these issues with a probabilistic approach was carried out by Montomoli et al. [72] in which the effect of the fillet radius at the base of the cylindrical section of the hole is evaluated. The test case is similar to the studies described above, i.e. a plenum with a single film cooling hole and a flat plate, the variable considered is the variation of the ratio between the curvature radius of the fillet and the diameter of the hole; four cases are studied within the range defined by the ideal case without fillet ($r/D = 0\%$) up to a maximum value of 5%, with a pitch of 1.25%.
In this study, no stochastic expansion techniques or sampling techniques on particular grids are used, instead, different variations of Mach number and pressure drop are imposed for the various fillet radii dispersed according to a Gaussian distribution. At the end of the simulations the probability distributions of the pressure loss coefficient C_d and the film cooling effectiveness η are constructed.

Regarding film cooling, a real UQ analysis based on the geometric parameters of the hole was carried out by Shi et al. [73]; in this article three uncertain parameters are set: the diameter of the cylindrical section of the hole, assumed with normal distribution $\mathcal{N}(7.75, 0.775^2)$, which implies a variation of the 10% with respect to the nominal diameter; the fillet radius, discretized in four values of r/D in the interval $0 \div 10\%$ uniformly distributed and the countersink angle of the end part of the hole, also uniformly distributed in the range $0° \div 0.8°$.

An analysis is carried both with the Monte Carlo method and with the polynomial chaos expansion. The output quantities of the CFD analysis were the discharge coefficient C_d and the film cooling effectiveness η; for the latter, results are obtained in total agreement with the articles already mentioned, i.e. the maximum dispersion of the film occurs near the edge of the hole (Figure 2.23a). The author also reports a comparison between the discrete probability obtained from Monte Carlo simulations with the continuous distribution obtained from the PCE (Figure 2.23b), showing how the latter perfectly underlies the other.

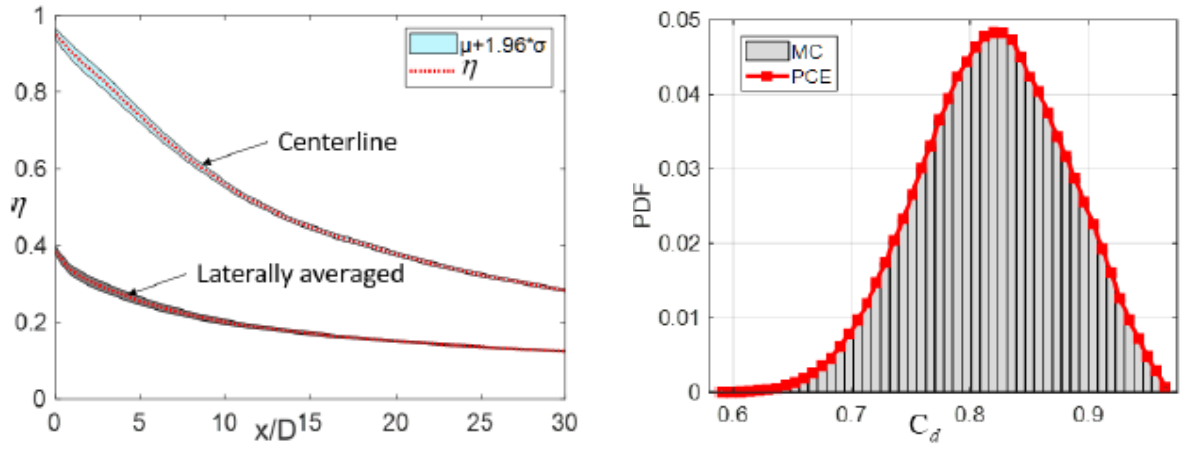

(a) (b)

Figure 2.23 – (a) Effectiveness on the centreline and spanwise average in 95% confidence interval; (b) Comparison of probability distribution of C_d. Shi et al. [73]

As previously introduced, a UQ study was carried out to assess the impact of uncertainties related to the thickness of TB, the tangential position of the hot core from the burner, and the intensity of the turbulence on the blade temperature of the first nozzle [26].
All variables considered are distributed according to a Gaussian distribution. The test case and uncertain variables are reported in Figure 2.24.

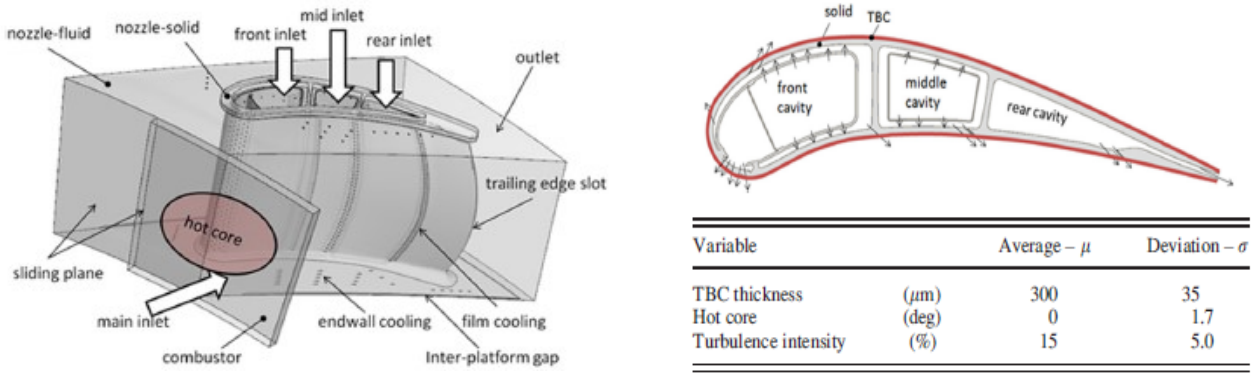

Variable		Average – μ	Deviation – σ
TBC thickness	(μm)	300	35
Hot core	(deg)	0	1.7
Turbulence intensity	(%)	15	5.0

(a) (b)

Figure 2.24 – (a) 1st stage nozzle analysed; (b) Probability distribution [26]

The author used the methodology of the polynomial chaos expansion by imposing a total order to two. Since there are three random variables considered, with the chosen polynomial order, ten simulations would be necessary; in order to increase the accuracy of the solution, an oversampling is performed and twenty-seven simulations are carried out. From the uncertainty propagation analysis the temperature trend on the blade surface is obtained, including the probability distribution (Figure 2.25a). The author provides a histogram showing the weight of the uncertainty of the individual variables on the temperature (Figure 2.25b).

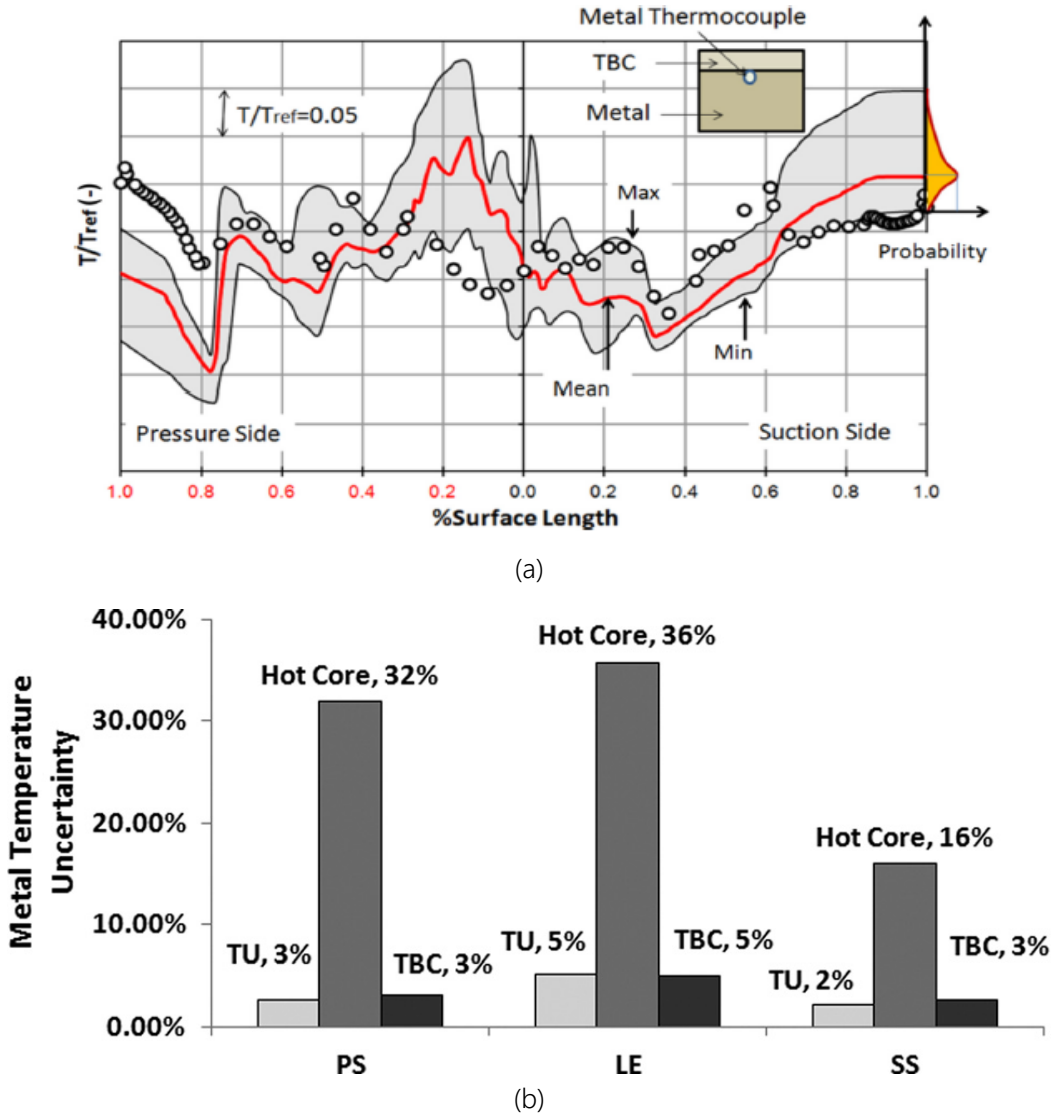

Figure 2.25 – (a) Blade temperature distribution; (b) Sensitivity analysis [26]

In Figure 2.25a it can be noticed how the experimental data are almost contained within the band of uncertainty of the computational results and, therefore, how the two approaches are in agreement; in the last part of the pressure side this phenomena does not occur: this discrepancy, according to the author, is to be attributed to the real shape of the "hot streak" that does not result symmetrical as hypothesized. Instead, it could present pronounced asymmetry towards the side of the nozzle. From the sensitivity analysis,

it is clear that the position of the "hot core" has a dominant influence with respect to the other two variables in each position of the blade.

3 - UQ analysis on low-order-code

3.1 - Aeronautical combustors

The combustor is the component of the machine in which the combustion takes place. The exothermic reaction allows the potential energy contained in the fuel to be converted into enthalpy, which will then be converted into mechanical energy by the turbine. It is clear that the performance of the entire machine is dependent on its proper operation.

The layout of the combustor is such as to guarantee the correct fluid-dynamic and chemical conditions to obtain a stable and efficient combustion (Figure 3.1). To ensure stoichiometric combustion and, at the same time, correct cooling of the surfaces, the combustor is divided into two volumes: one in which the flame bounded by the liner develops and one in which only air circulates, between the casing and the liner.

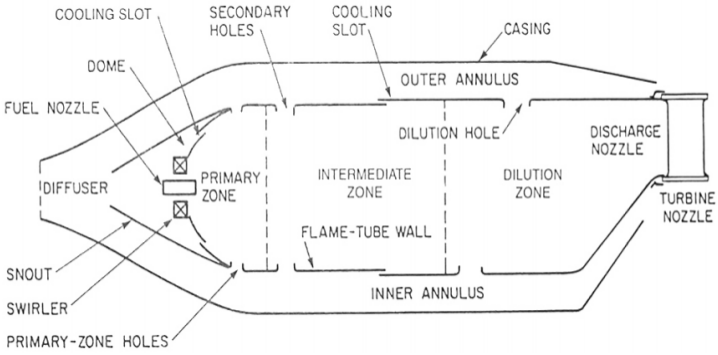

(a) Cross-sectional view of a combustor

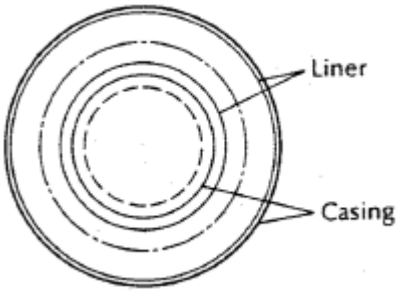

(b) Annular combustor

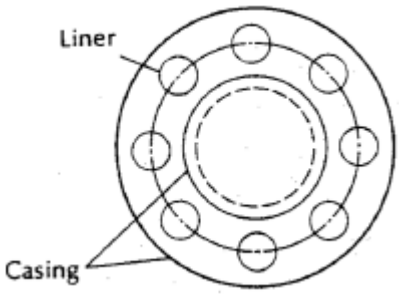

(c) Can annular combustor

Figure 3.1 – General layout of an aeronautical combustor [74]

The most used configurations in the aeronautical field are basically two, both developed starting from the tubular combustors that are too heavy for this type of applications: the annular section combustor provides a light and compact solution, has minimal pressure losses but the surfaces of the liner are subject to high heat loads (Figure 3.1b); while can annular configurations (Figure 3.1c) have cylindrical liners inside an annular case, allow a better control of the flame compared to the previous ones while maintaining a reduced size, but they are heavier and more expensive.

The research on combustors stems from the need to respect the emission limits, during the take-off and landing phase, set by ICAO-CAEP [75] which define the limits within which an engine can be certified (Figure 3.2).

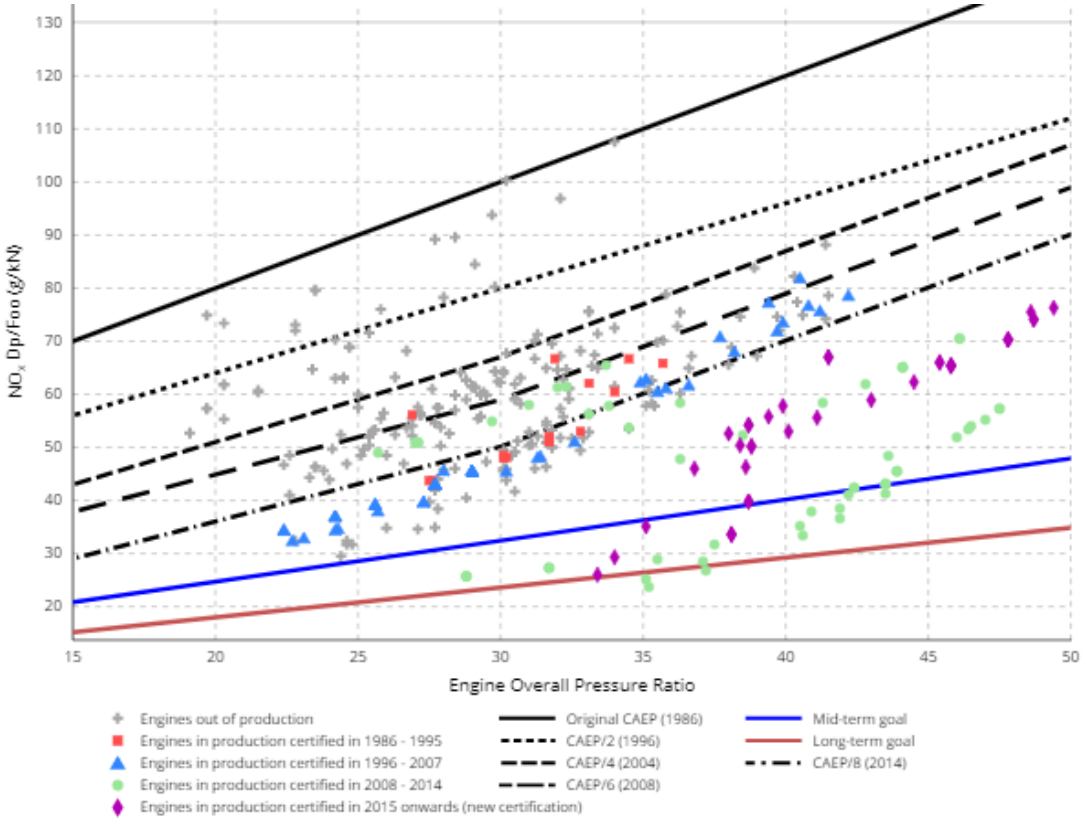

Figure 3.2 – NO_x emission limits for engines with thrust greater than $89kN$ [75]

The objectives set by the European project "Clean Sky 2" [76] (Figure 3.3), currently underway, push research towards new generation combustors in order to develop a stable, but at the same time low environmental impact combustion, to meet the abatement of pollutants summarized in the following figure.

	CLEAN SKY 2008-2017	CLEAN SKY 2 2014-2024	FLIGHTPATH 2050
-CO_2	-26%	TO -20% -30%	-75%
-NO_x	-60%	TO -20% -30%	-90%
NOISE	TO -50% -75%	TO -20% -30%	-60%

Figure 3.3 – European project Clean Sky objectives [76]

3.1.1 - RQL combustors

The research has led to the development of RQL (Rich-burn/quick-Quench/Lean-burn) combustors that represent the standard for low emission engines of NO_x.

In these combustors it is possible to limit polluting emissions, through the control of the local fuel-air ratio; in particular, there is an area with $\phi = 1.2 \div 1.6$ in the primary zone, which guarantees a high stability of the flame (combined with the recirculation of hot gases through the swirled flow) and a low temperature; subsequently there is a strong input of primary air, which involves a rapid cooling and the achievement of lean mixture conditions ($\phi = 0.5 \div 0.7$) (Figure 3.4).

The diffusive flame is fed by 30% of the air exiting the combustor while the remaining 70% is used to control the diffusive process, the temperature profile at the burner outlet and to feed the cooling systems.

The purpose of the whole procedure is to reduce to a minimum the presence of stoichiometric conditions inside the combustor, to which the maximum emissions are associated.

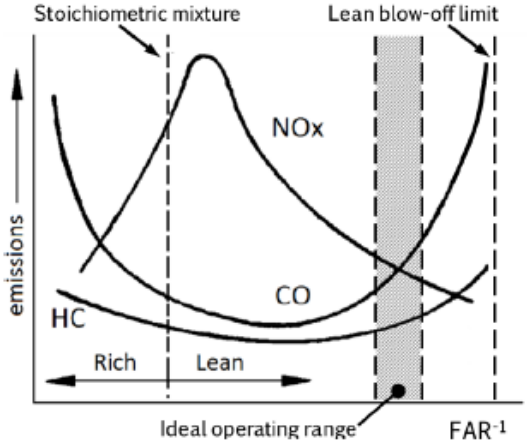

(a)

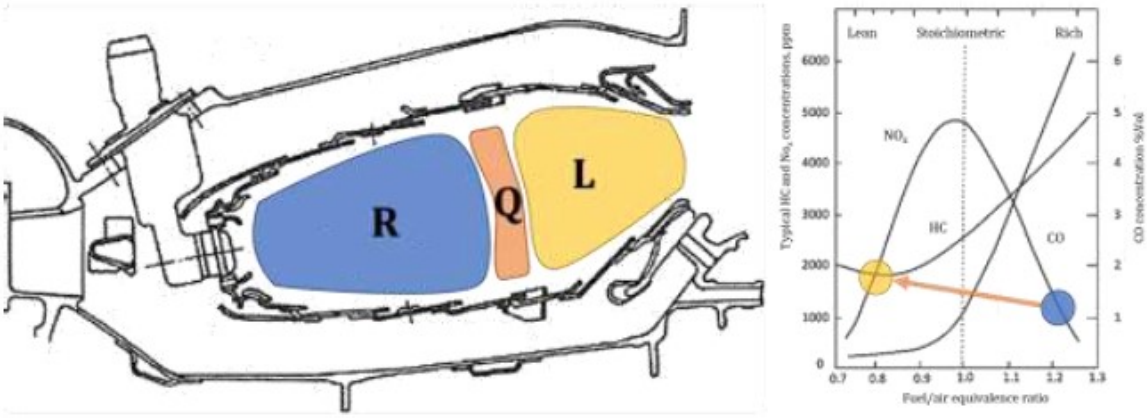

(b)

Figure 3.4 – (a) Emissions as a function of Φ. (b) RQL combustor conditions [74]

3.1.2 - Lean combustors

In order to further reduce emissions of NO_x lean premixed flame burners are being studied. They are based on the concept of global control of the total equivalence ratio, keeping it mainly lean, which is why these types of combustors are more complicated than the previous ones, as they suffer from problems of flame stability. They consist of a primary zone in which a pilot flame with a slightly lean, almost stoichiometric equivalence ratio is exploited, ensuring stable combustion and reduced emissions of CO and hydrocarbons, while the rest of the chamber is kept in lean conditions (Figure 3.5).
To ensure the conditions listed above, the fuel must enter the chamber already completely evaporated so that the injectors play a fundamental role.

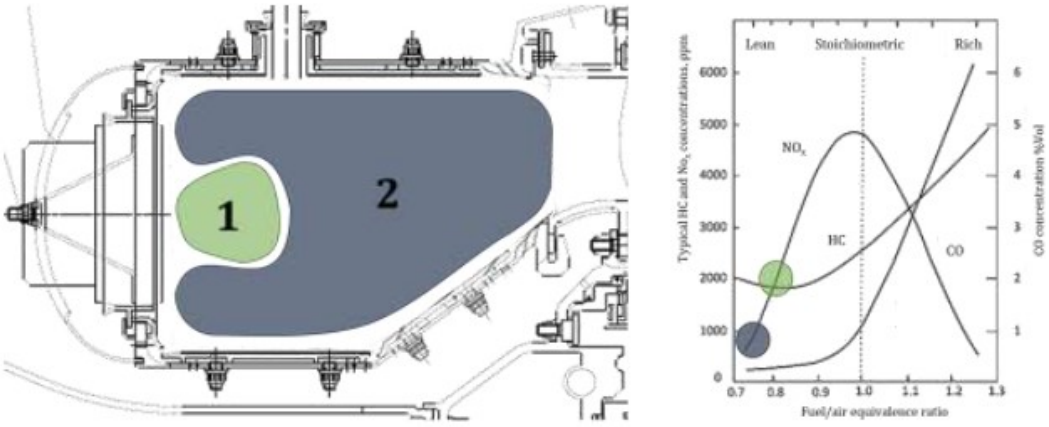

Figure 3.5 – Lean combustor performance

Although the thermal loads on the liner walls are lower, cooling for this type of combustor is critical because the available air is limited (Figure 3.6), since most of it is used to maintain lean conditions in the chamber [77].

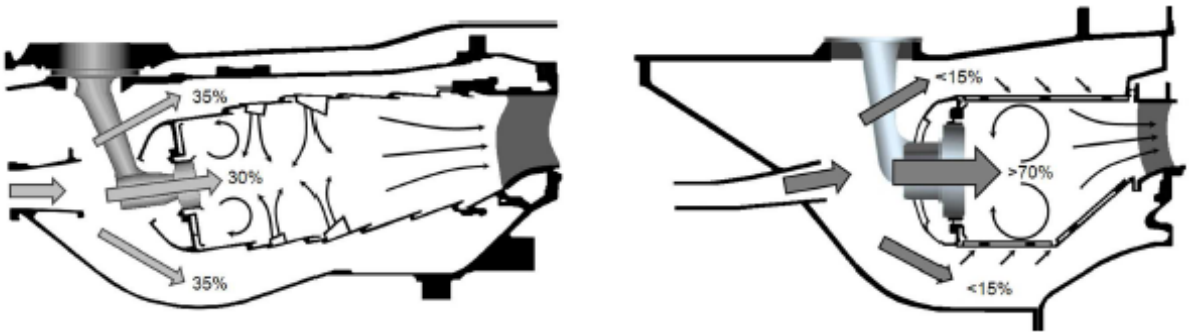

(a) (b)

Figure 3.6 – Air splitting for RQL (a) and Lean (b) [78]

3.1.3 - Combustor cooling

With the increase in the maximum temperature and the need to reduce polluting emissions, the cooling the combustor walls requires increasingly demanding solutions. For nickel-based alloys, the maximum operating temperature must not exceed $1300K$, with flame temperatures generally higher than $2000K$ [74].
The cooling systems of the liner walls play a key role in the durability of the combustor; the main methodologies are reported by Cerri et al. [79] and are shown in Figure 3.7.

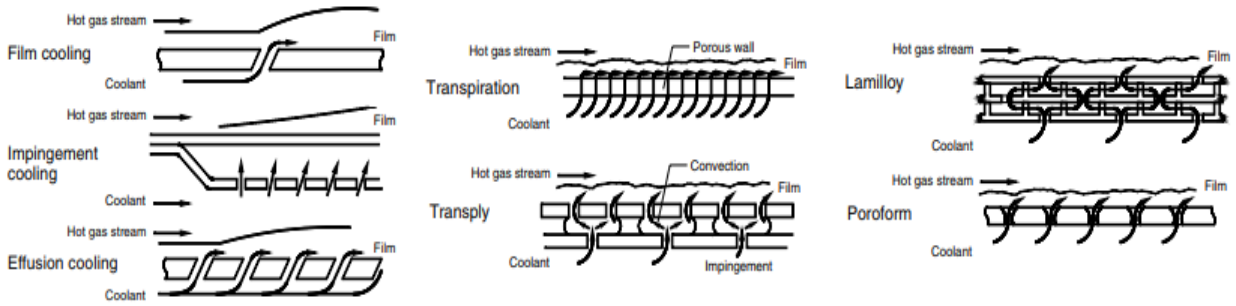

Figure 3.7 – Main cooling techniques: convective and transpiration [79]

With the growing need to limit the flow of refrigerant fluid in order to control combustion in the chamber, the current trend is to use effusion cooling to protect the liner wall. This cooling technique allows avoiding the high quantity of air that only film/slot cooling would require and the reliability problems linked to the cooling techniques by transpiration using porous materials. It consists of a series of inclined cylindrical holes with a small diameter, similar to those of film cooling, but closer together, ensuring more uniform protection (Figure 3.8). Since the holes are characterized by a high length/diameter ratio, there is a high heat removal due to the sink effect [80]. Effusion cooling protection only begins after the first holes, which is why the initial area of the liner is usually protected by a slot from which the cooling air escapes.

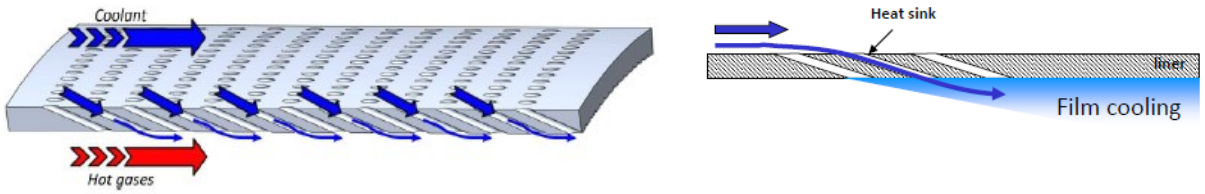

(a) (b)

Figure 3.8 – (a) Effusion cooling (b) Heat removal and protection

The effusion cooling is a cooling technique studied for at least 50 years; in the literature there are many works that assess the efficiency in different operating conditions. The first studies concern the influence of spacing and hole diameter on the global coverage [81]. Krewinkel [82] reports a review of the main studies carried out on this cooling procedure; the efficiency is evaluated varying the blowing ratio (BR) [83] (Figure 3.9a) and varying the inclination angle of the hole [84] (Figure 3.9b).

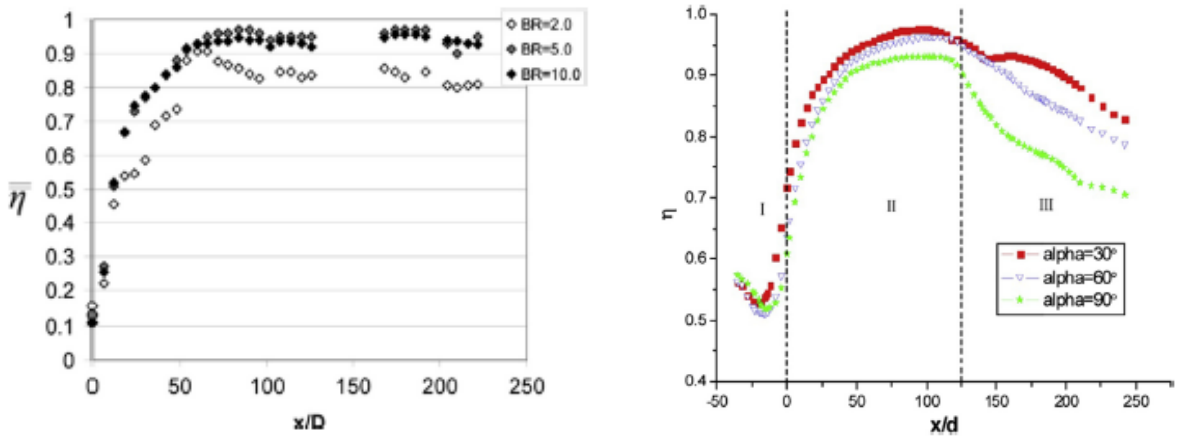

(a) Effectiveness for different BR

(b) Effectiveness for different inclination angle

Figure 3.9 – Krewinkel results [82]

In [85], an experiment is conducted to quantify the influence of the velocity ratio (VR) and the effect of the Reynolds' number (Re) on the film cooling effectiveness.

Andreini et al. [86] carries out an extensive study in which they assess the influence of the blowing ratio (BR), of the density ratio (DR) and of the turbulence level (Tu) on the main stream (Figure 3.10); the same author in [87] carries out a numerical study to quantify the pressure losses associated with effusion cooling.

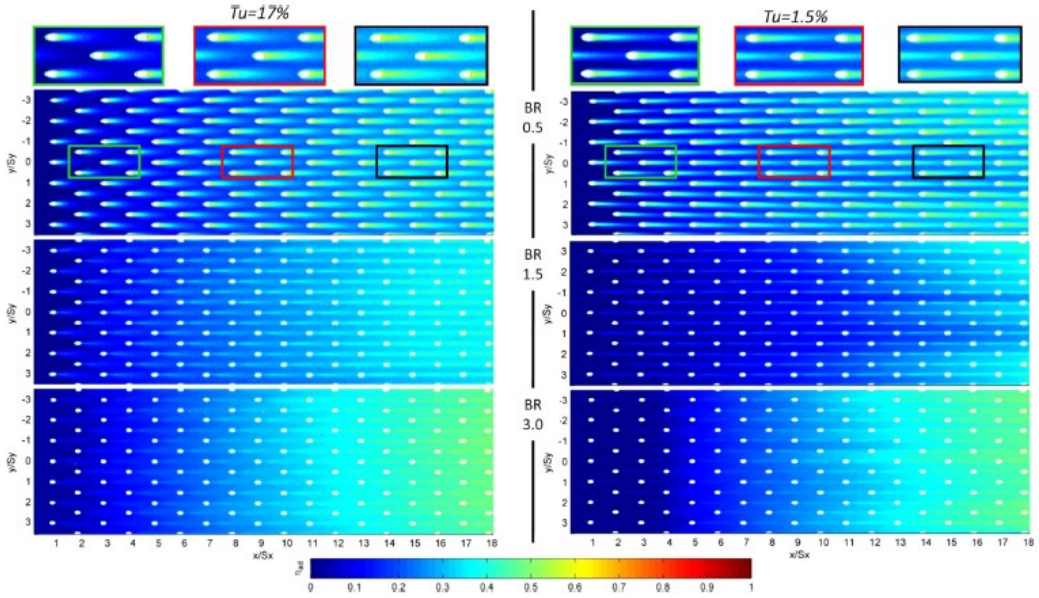

Figure 3.10 – Adiabatic effectiveness with varying BR and Tu [86]

Scrittore et al. [88] carries out an experimental study to investigate the flow motion field near a dilution hole; a similar evaluation was carried out, using CFD, by Tarchi et al. [89], quantifying the effect that the recirculation area has on the effectiveness of the system.

3.2 - LEMCOTEC project

The combustor considered for the UQ analysis was the one developed for the European project LEMCOTEC (Low EMission COre-engine TEChnologies) which ended in June 2017. The main objectives of the European project were focused on the development of a new engine with greater thermal efficiency, with a high overall pressure ratio (OPR) up to 70, which results in a reduction of the CO_2 emitted. The increase in TIT due to the higher OPR inevitably leads to an increase in NO_x emissions; therefore, research focused on the development of new lean combustion techniques to compensate for this phenomenon.

The combustor is of the lean type, has an annular structure and develops combustion in lean mixture conditions guaranteed by a particular injection system, in which the stability of the flame is ensured by the staging of the fuel with a pilot injection by an atomizer. Part of the primary air is used for the cooling of the swirler and the dome, the latter cooled by jets of impingement, the remaining feeds the annuli for the cooling of the liner walls protected in the first part with a slot and for the major zone by effusion cooling.

The LEMCOTEC combustor can be considered as the successor to the one developed by GE Avio during the NEWAC programme (Figure 3.11a); the new combustor has an optimised structure and cooling system to minimise pollutant emissions and improve the life of the component itself.

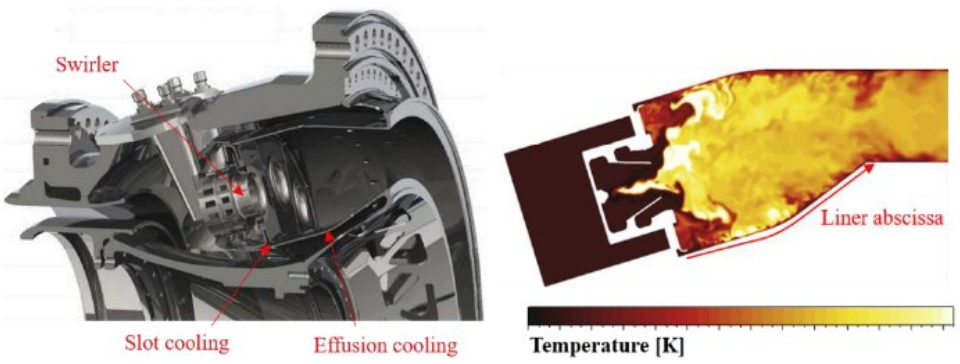

(a) (b)

Figure 3.11 – (a) NEWAC combustor (GE Avio) (b) Temperature distribution for the approach condition estimated by Bertini et al. [90].

The validation of the project was carried out, in part, through experimental tests carried out at CIAM (Central Institute of Aviation Motors) for the conditions of Idle, Approach and Cruise; the working conditions at Take-Off were simulated by Bertini et al. [77] and [90]. The points tested are shown in Figure 3.12.

Test point	P30 bar	T30 K	FAR ‰	P/T %	Active injectors
Idle (ICAO 7)	5.4	518	14.5	100	9
Approach (ICAO 30)	13.5	655	17.2	70,90,100	18
Cruise (ICAO 85)	13.5	655	28.3	5,10,20	18
Take-Off (ICAO 100)	19.0	840	28.3	5,10,20	18

Figure 3.12 – Conditions tested at CIAM and simulated (Take-Off) of the LEMCOTEC combustor [77]

3.2.1 - One-dimensional approach

One-dimensional codes are simulation tools that are based on simplified approaches: they allow rapid results to be obtained by providing a one-dimensional calculation, which is why these are ideal in the preliminary design phase. This is the main reason why it was decided to use this type of approach in order to carry out a first UQ study; with the aim to validate methods and sampling grids, a simplified procedure is more suitable as a large number of discrete evaluations are required. The code used in this study is called Therm-1D [91] and is intended for the preliminary design of the cooling system of the combustor, both to define a preliminary arrangement of the cooling system, and to assess the performance under different operating conditions.

This tool is able to predict the temperature of the walls and the thermal loads on different liner positions, coupling a fluid network solver, well tested and developed internally at the DIEF of the University of Florence, with a standard heat transfer model based on the methodology proposed by Lefebvre [74].

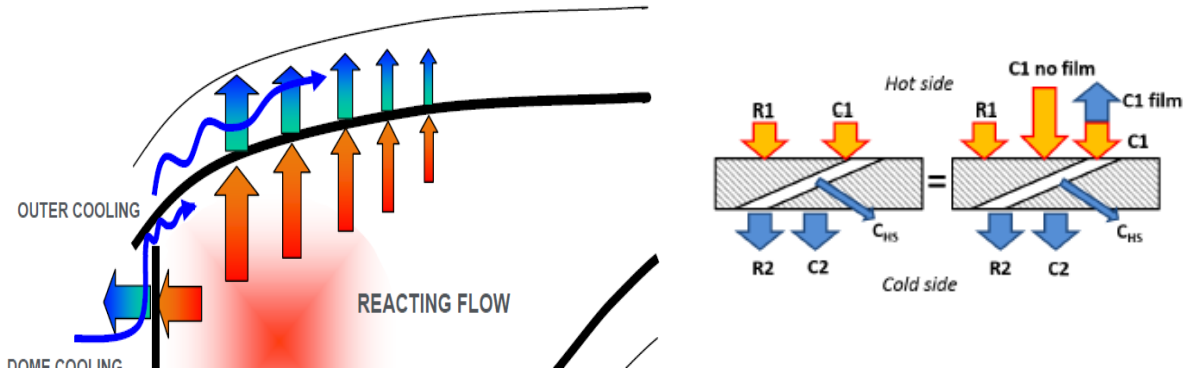

(a) (b)

Figure 3.13 – (a) Heat transfer in the combustor [74] (b) 1D thermal flux scheme [92]

In Figure 3.13 the convective thermal loads have been indicated with C_i, the radiative ones with R_i, while C_{HS} indicated the contribution of heat removal for the sink effect.

The thermal balance of a single liner element will be obtained by imposing the equality of the internal and external heat flows, which in turn will be equal to the radial conductive thermal load.

$$C_1 + R_1 = C_2 + R_2 + Q_{HS} = K_{1-2} \qquad \text{Eq. 3-1}$$

For combustors operating in lean conditions, sink effect heat removal plays a key role in total cooling ($\approx 45 \div 60\%$), while the thermal radiative load on the cold side produces a contribution lower than the 10% [92].

The influence of the convective load on the cold side, in some areas of the liner, can make a greater contribution than the protection due to the film, but this effect decays along the advancement of the annulus: the reduction in mass flow rate of the coolant affects more than the greater discharge coefficient that occurs in the terminal holes of the liner, causing an overall reduction in the heat transfer coefficient.

3.2.2 - Therm-1D

The Therm-1D procedure solves the conjugated fluid-wall calculation by imposing the condition of the radial thermal equilibrium of the liner, neglecting the heat transfer in circumferential and axial direction.
The whole procedure is carried out in an iterative way by different sub-codes and is outlined in Figure 3.14.

Geometric inputs and boundary conditions

⇩

Start the external iterative cycle

- **ICONS1d**
  - Solves coolant flow network
  - Assess convective load gas side
- **MESH1d**
  - Defines the mesh

Start the internal iterative cycle

- **COWL**
  - Assess radiative load gas side
- **THERM1D**
  - Solves the conduction

End of the internal iterative cycle

End of the external iterative cycle

⇩

Liner wall temperature gas side
Liner wall temperature coolant side

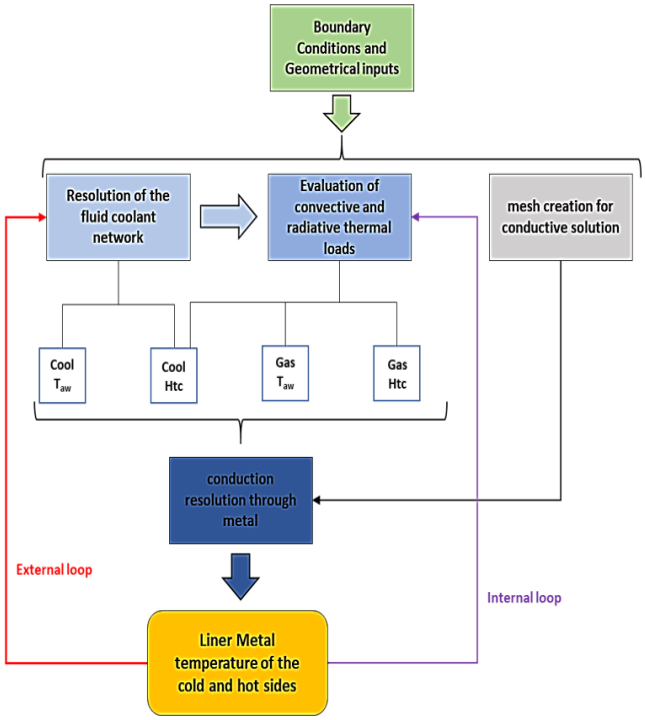

Figure 3.14 – Therm-1D procedure

The Therm-1D code uses the output files generated by ICONS1D and COWL as boundary conditions for the resolution of the one-dimensional heat conduction equation (Eq. 3-1) by which it determines the equilibrium temperature of the liner wall in each node of the calculation domain.
To speed up convergence, in addition to the external iterative cycle, there is an internal iterative cycle that involves the evaluation of radiative loads, whose sensitivity to temperature is much more pronounced than that of convective loads. Once the iteration has reached convergence, it is possible to establish the temperature of the liner and therefore evaluate the efficiency of the cooling system.

The procedure requires a certain set of input files in order to carry out correctly the whole routine; the main files are linked to the geometric discretization of the combustor, to the definition of the cooling techniques and to the thermal-fluid-dynamic conditions of the hot gas; in fact, the gas define the operating conditions of the machine. The main input files are described below. As already mentioned in Chapter 2.5.1 -it was decided not include input and output files in the annex as not to weigh the writing down: all the relevant information are provided below.

- Mod.dat It discretizes the combustor and the cooling techniques to which it is subjected, in simplified interconnected models, among which the continuity of the flow rates and the equality of temperature and pressure are imposed; moreover, it adds a set of correlations that characterize the specific fluid-dynamic behaviour of the single model.
  The code allows different types of operation, depending on the boundary conditions imposed:
  1. Imposed massflow rate: all inlet sizes are fixed, such as flow rate, total pressure, and total temperature; the code calculates how the various flow rates are distributed in the points of interest of the system and the pressure with which they are discharged.
  2. Imposed pressure: total pressures are imposed at each input point, and static pressures at each output point; the iteration provides the distribution of flow rates along the network.
  3. Mixed mode: the code requires the flow rate values at the inlet and the static pressure values at the outlet; the total pressures at the inlet are calculated in an iterative manner by the code.
- Geometry.dat Allows the user to define the geometry and structure of the combustor; it is in this file that one specifies the number of fluid domains, liners and their conditions of heat transfer. Each liner is characterized in terms of cylindrical coordinates. The code also allows the inclusion of a possible cover by TBC.
- SC1_lin.dat Defines the type of cooling system, discretizing it into cylindrical coordinates; the number of rows of holes and their dimensions are defined. This file contains the generic parameters for both the geometrical quantities and the heat transfer.
- Gas.xxx Here the characteristics of the hot gas are specified, in terms of temperature, temperature at which the radiation takes place, pressure, density, and speed; in fact, these are the conditions that define the operating conditions of the machine.
- Mesh.dat Allows the user to set the number of points in which to calculate the liner temperature.
- Therm1D.dat Here convergence criteria for iterative cycles are defined.
- Tunehext.xxx Allows tuning of the external heat transfer coefficient by means of an additive coefficient and a multiplicative factor.

3.3 - Uncertainty quantification analysis

The uncertainty quantification analysis was carried out with a double purpose, the first objective was to verify the accuracy of the uncertainty propagation methods and the relative sampling grids, comparing the spectral methods with the Monte Carlo method and verifying how much the polynomial order affects the final interpolating solution. The second aim was to carry out a further validation of the one-dimensional code used in order to assess which are the aspects that most affect the response of the system.

In the following chapters, the applicative part of the thesis work is reported: the description of the fluid network used, all the assumptions made for the choice of the uncertain variables and their relative distribution, the procedure performed to interface the network solver with DAKOTA and the post process for the subsequent data processing.

3.3.1 - Test case

The UQ analysis was carried out on the fluid network relating to the inner liner of the LEMCOTEC combustor supplied by GE Avio Aero. The network under examination has only two regions, one of the main flow and one, between the liner and the casing, affected by the cooling fluid (Figure 3.15). The network has been supplied without slot cooling modelling, which effect is simulated by imposing a lower hot gas temperature than the real ones in the initial part of the liner. As it can be seen from the results section, this modelling will be highly impacting in terms of liner wall temperature for this part of the liner.
The initial fluid network was provided under Max Take-Off conditions; given the absence of experimental points in these conditions it was decided to analyse the Approach conditions, as both the experimental data and those obtained by numerical methods are available.
Despite the availability of the full 3D conditions found through CFDs in Bertini's work previously cited [90], it was preferred, under GE Avio Aero's indication, to use specific equations in order to scale the physical quantities with a simplified approach, according to the standard procedures of the industrial partner. In this way, acting on the file gas.xxx, the fluid network was brought back from the conditions of the Max Take-Off to those of the Approach.
The conditions imposed on the various planes of the model were obtained from the experimental tests carried out at CIAM, performed under different operating conditions of the machine. The tests show the pressures at plane 31 and 36 of the combustor.
As far as the cooling system is concerned, the outlet flow rate has been set, as the bleeding flow rate is fixed in the actual operation; in other words, the effusion cooling has been modelled as operating with the pressure drop, actually measured, and with the outlet flow rate set equal to the bleed one. From the point of view of the code, this last condition has been realized imposing the output flow rate, equal to the bleed flow rate, to the last row of effusion holes.

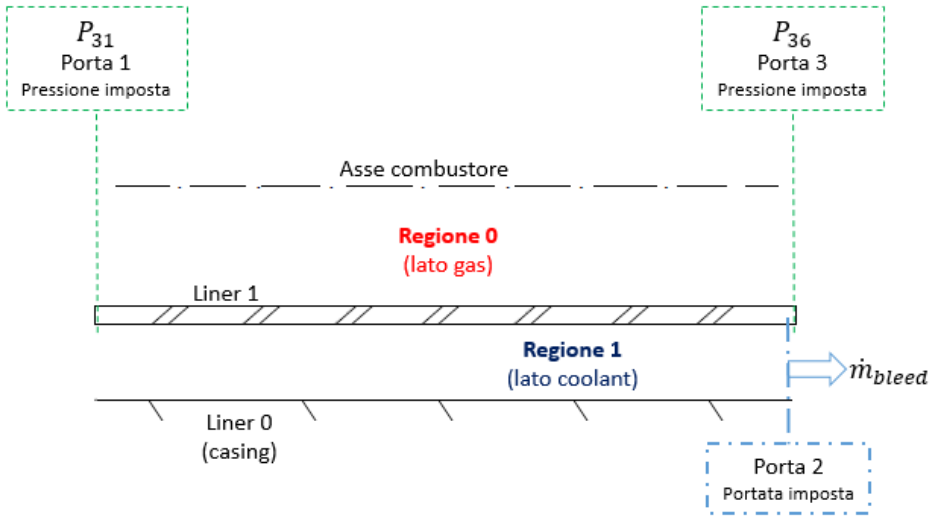

Figure 3.15 – Flow network discretization

The liner was discretized with a one-dimensional mesh having 712 nodes, the output size studied is the wall temperature of the liner.

3.3.2 - Uncertain variables and simulations

A total of four types of macro-analysis were carried out. In the first one, the influence of the uncertainty of two geometric parameters was evaluated, another was conducted for the three heat transfer tuning factors of the code and in the third one, the uncertainties of the quantities defining the boundary conditions inside the machine were considered. For all three analyses the liner wall temperature was evaluated as the output variable. The last and final analysis carried out contains all the previous random variables (seven) and was performed to assess the behaviour of the Smolyak sparse grids.

The first analysis of uncertain geometric factors was the one used to verify the correct number of samples to ensure the convergence of the Monte Carlo method, the sensitivity of the final interpolating polynomial to the various polynomial orders, and the relative sampling methods.

The LHS sampling technique has always been used for both the Monte Carlo method and the fixed-order polynomial chaos expansion method. It has been demonstrated that for this spectral expansion method it is necessary to over-sample by a factor of at least two with respect to the number of evaluations required, and this has been done by default for the other analyses under examination.

As will be shown below, the stochastic collocation method provides the same results as the polynomial chaos expansion with tensor product, which is why this method was carried out only for geometric analysis.

For all the analyses mentioned, a Monte Carlo simulation was also carried out in order to validate the results obtained by stochastic expansion methods.

In Table 3.1 a summary of the simulations carried out is provided, divided by type of analysis, by UQ methodology and providing the number of evaluations required. The selection of the collocation points was made according to what already described in Chapter 2.4.3 -and 2.4.4 -.

Table 3.1 – Different analyses carried out

		Geometric	HTC	Boundary Conditions	Overall
Monte Carlo		10-100-1000	1000	1000	50 -100-250-500-1000
Tensor product 1		4	8	4	128
Tensor product 2		9			
Tensor product 3		16			
Total order 2	CR=1	6			
	CR=2	12	20	12	72
Total order 3	CR=1	10			
	CR=2	20			
Total order 4	CR=1				
	CR=2	30			
Stochastic coll 1		4			
Stochastic coll 2		9			
Stochastic coll 3		16			
Smolyak level 1					15
Smolyak level 2					128
Smolyak level 3					807

3.3.2.1 – Geometric analysis

For this type of analysis two uncertain variables have been considered, the first, purely geometric, is the inclination angle α of the effusion cooling hole (Figure 3.16).

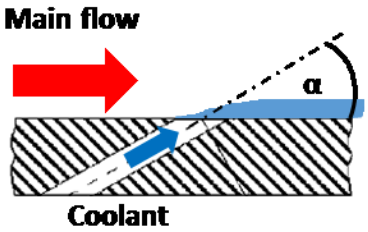

Figure 3.16 – Inclination angle

The second variable considered is the discharge coefficient, C_d; this is not properly a geometric parameter but it is an index of how much the flow actually disposed of by the hole tends to the ideal isentropic one; through this factor, it is included in the fluid dynamic behaviour the real geometry of the hole and therefore of the manufacturing process by which it is realized.

$$\dot{m} = C_d \dot{m}_{is} \Rightarrow C_d = \frac{\dot{m}}{\dot{m}_{is}} \qquad \text{Eq. 3-2}$$

In which

$$\dot{m}_{is} = P_0 \left(\frac{P}{P_0}\right)^{\frac{\gamma+1}{2}} \sqrt{\frac{2\gamma}{(\gamma-1)RT_0}\left[\left(\frac{P_0}{P}\right)^{\frac{\gamma-1}{\gamma}} - 1\right]} \frac{\pi}{4} D_h^2 \qquad \text{Eq. 3-3}$$

Both parameters are contained in the input file "SC1_lin.dat".

In order to carry out the sampling on the input variables, DAKOTA requires the relative probability distributions; as previously stated, this step is critical because there are no data available in the literature and performing tests and measurements to define how a given parameter is distributed is expensive and difficult to implement. For this reason, the distributions have been hypothesized basing the choices on the works currently present in the literature and according to the industrial partner.

From the bibliographic review, it is clear that the most common and reasonable trend is to impose a normal distribution to the uncertainties of geometric nature that depend on a manufacturing process; reason for which both the considered variables have been assumed with Gaussian distribution.

For the distribution limits of α the work of Bunker [2] has been taken as a reference, reported in the introductory chapter in Figure 1.7, in which a tolerance of $\pm 5°$ on the inclination angle is considered for a film cooling hole with respect to a mean value of $30°$. Although the cooling system is not the same, it was decided to use this parameter because of the high affinity between film and effusion cooling and the absence of data for this type of application of the system considered.

The uncertainty was modelled with a truncated normal distribution $\mathcal{N}(30°, 2.5°)$, whose extreme values $(25°, 35°)$ are located at a distance 2σ from the mean value.

With no direct information on the variation of the C_d it has been decided by analogy to impose the limit values of the normal distribution with a variability equal to 2σ with respect to the mean value.

The characteristics of the distributions, imposed for the geometric variables, are summarized in Table 3.2.

Table 3.2 – Geometric variables probability distribution

	$\boldsymbol{\mu}$	$\boldsymbol{\sigma}$	$\boldsymbol{Lim_{up}}$	$\boldsymbol{Lim_{low}}$	$\boldsymbol{Distribution}$
$\boldsymbol{\alpha}$	30°	2.5°	35°	25°	$Normal$
$\boldsymbol{C_d}$	0.7	0.05	0.8	0.6	$Normal$

3.3.2.2 – Heat transfer tuning factors analysis

In this analysis, the three heat transfer tuning factors were considered as uncertain variables: hot gas side (HTC_{hot}), coolant side (HTC_{cold}) and the one inside the hole related to the sink effect ($Fatht$).
The study was conducted in order to assess how much these uncertainties affect the final result; this aspect is interesting because these parameters are calibration factors that are imposed in order to achieve the correct heat transfer value, obtained from experimental tests or more accurate CFD simulations. Especially in the early stages of design, where most of the quantities involved are not yet defined, these factors could lead to inconsistent results with respect to the physical phenomenon investigated. A proper assessment of how much the response function may differ to changes in these parameters can lead to the definition of a possible range in which to vary the coefficients of heat transfer and speed up the whole design process.
The heat transfer factors of cold side and sink effect are contained in the input file "SC1_lin.dat", while the hot side one is in the "tunehext.xxx"; for this last parameter there is no single value, but one can specify both a multiplication factor and an additive coefficient.
Given the purposes of this analysis, in accordance with Durocher et al. [67], it has been defined a variable with uniform distribution for each of the three parameters. The three variables have been assumed as multiplicative factors, which increase or reduce the relative nominal heat transfer factor supplied by GE Avio Aero. All three distributions are centred around the unitary value; the limits of the distributions are fixed in order to obtain a variation of the 20% for the cold side and sink effect factors, while a variation of 30% for the factor acting on the heat transfer coefficient on the hot gas side has been imposed.
For uniform distributions DAKOTA requires only the entry of the upper and lower limit; these are summarized in Table 3.3.

Table 3.3 – Probability distribution for heat transfer tuning factors

	$\boldsymbol{Lim_{up}}$	$\boldsymbol{Lim_{low}}$	$\boldsymbol{Distribution}$
$\boldsymbol{HTC_{cold}}$	1.2	0.8	$Uniform$
$\boldsymbol{Fatht}$	1.2	0.8	$Uniform$
$\boldsymbol{HTC_{hot}}$	1.3	0.7	$Uniform$

3.3.2.3 – Boundary conditions analysis

The analysis has the objective to study the impact of the conditions that occur inside the combustion chamber on the considered response function. The uncertain quantities taken into consideration are the temperature of the gas, the radiative temperature with which the radiation is modelled, the type of mixture through FAR (Fuel-Air ratio) and the kinetic conditions of the gas.

The random variables considered were only two; in practice, the same procedure as the previous analysis was carried out: it was considered a single multiplier factor for the thermal conditions just listed including the FAR and another factor for gas velocity.
This type of approach has allowed to reduce the computational cost related to the type of analysis, since only two variables have been considered and not one for each named quantity, remembering that the number of simulations increases exponentially with the variables for spectral methods. Moreover, it allowed to avoid non-physical conditions by placing a multiplicative factor for each quantity: a non-real situation could have occurred in which the two temperatures could have had a contrasting trend, such as, for example, a growth of the radiative temperature with a simultaneous decreasing of the total temperature of the gas, due to a simultaneous sampling of a multiplicative factor and a reductive one for the quantities.
As far as the distributions are concerned, two normal distributions have been assumed; in the literature there are no works analogous to the cases analysed, for this reason a Gaussian distribution was chosen so as to be able to give greater probabilistic value to the nominal working conditions of the machine. In other words, it was considered to vary the boundary conditions with respect to the condition of maximum probability defined by the nominal working point. By defining the factor that multiplies the temperatures and the FAR with x_T and the factor affecting the velocity with x_v, the characteristics of the two distributions are defined as follows in Table 3.4.

Table 3.4 – Probability distribution for boundary conditions variables

	μ	σ	Lim_{up}	Lim_{low}	$Distribution$
x_T	1	0.05	1.1	0.9	$Normal$
x_v	1	0.25	0.5	1.5	$Normal$

3.3.3 - DAKOTA / Therm-1D interface

The distributions on which DAKOTA has to carry out the sampling procedure have been defined but it has not been yet specified how the interface between the executable and the fluid network solver occurs. Once the sampled data have been obtained, they must be replaced within the correct input files of Therm-1D; this procedure is carried out by a specific script, written in Python language, provided by Sandia Laboratories, called “dprepro.py”.
Once the fluid network solver has completed the single evaluation for a given set of inputs sample, the results of the studied response function must be re-introduced into DAKOTA, so that DAKOTA, once all the evaluations have been completed, can calculate the statistics and generate the interpolating polynomials constituting the surrogate model, which are then interrogated to obtain the output results in the study.
This task is done by a Python script “read_Tw.py”, specifically created for this type of application, which executes the following commands: opens the correct output file of Therm-1D, which contains the response function, reads and then saves the results in a text file that will then be read by DAKOTA; the whole routine is summarized in Figure 3.17.
For simplicity, since the work was done on a Windows operating system, the actual interface called by DAKOTA is a batch executable "simulator.exe" which, in turn, calls the script "dprepro.py" to replace the

sampled points within the input files of Therm-1D; then after the simulation, calls the Python file "read_Tw.py", which reads the desired result and saves it, and then return them back to DAKOTA.
Since the dimensional results are not publishable, the reading file also performs the task of making them dimensionless: all subsequent graphs report a dimensionless temperature on the y-axis.

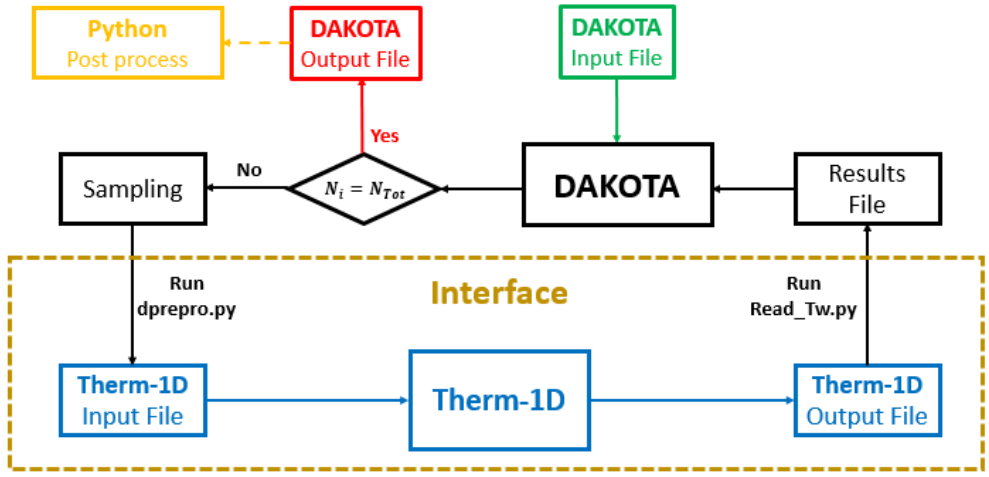

Figure 3.17 – UQ analysis diagram with Therm-1D

The subsequent processing of the DAKOTA output file, to extrapolate the desired quantities, was done with a Python script specifically created for this analysis. The script has been designed to perform a keyword reading of the output file in order to provide the user with the type of uncertainty quantification method adopted, the number of assessments made, the graphical trend of mean, maximum and minimum values (both for the values actually obtained by Therm-1D and those resulting from the surrogate model built by DAKOTA), the sensitivity analysis (only for stochastic expansion methods) and a possible reliability analysis under a particular imposed conditions. Another information obtained is a probabilistic map that links every temperature value that the liner can assume to the probability of occurrence of the event.

3.4 - Results

This section will provide and describe all the results obtained from the study of uncertainty quantification on the fluid network solver "Therm-1D".
Before showing the results of the analyses it is necessary to make a preface on the type of approach used and on the results obtained; for this reason the results obtained with a deterministic approach are shown in Figure 3.18.

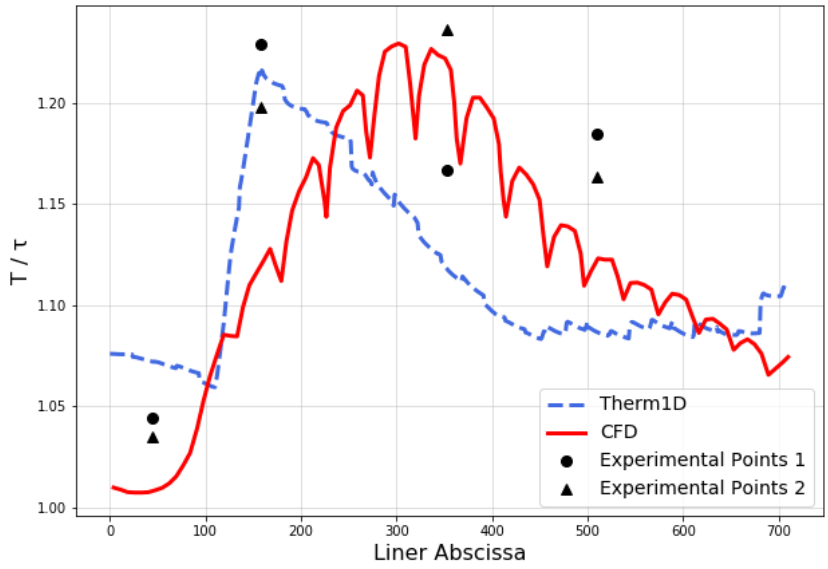

Figure 3.18 – Comparison among results: Therm-1D, Experimental test at CIAM, and CFD [77]

The one-dimensional approach is greatly influenced by the internal temperature range imposed in the input file "gas.xxx". As already mentioned, the temperature range has been defined according to GE Avio Areo's best practices; the temperature distribution of the gas inside the chamber has been imposed in order to model the effect of the slot cooling since it is not present in the fluid network supplied; this involves an initial trend of the liner wall temperature which does not depend on the behaviour of the solver itself, but is attributable to the temperature range of the hot gases imposed.

As expected, the trend of the liner wall temperature obtained by CFD simulation from Bertini et al. [77] has a greater agreement with experimental data than the one-dimensional approach.

From the results shown it can be seen how the maximum excursion between the two approaches is found in the initial section of the combustor and in the temperature rise ramp, which can be attributed to the slot cooling modelling.

With this assumption it is possible to better understand the result provided by the fluid network solver and proceed to the description of the results obtained with the uncertainty quantification analysis.

The parameter used as a reference was the liner wall temperature: mean value, maximum and minimum values, and standard deviation are measured both for the results obtained from the simulations carried out with Therm-1D and for those obtained from the surrogate model.

It should be stressed that uncertainty propagation analysis is a purely mathematical study. In fact, the interpolating polynomial obtained from the surrogate model does not provide the development of the wall temperature along the axis of the combustor; this is due to the fact that DAKOTA creates an interpolating polynomial for each response function; in other words, as many polynomials as response functions are obtained. It should be remembered that the liner is discretized in 712 points, so from the UQ analysis 712 polynomial expansions are obtained; the graphs provided below show the values of the T_w in the above points, obtained from the respective polynomials, so that there is no physical continuity between two contiguous curvilinear abscissae.

The results obtained with the spectral methods are validated with the Monte Carlo method, from which it is obtained a temperature value averaged over a number so that it can be assumed that the method is convergent.
With the aim of making a precise comparison among the methods, when the surrogate model was used, a further LHS sampling of 1000 points was performed in order to obtain the same sample size obtained with the MC method; thus, the results obtained were used to make the comparison among the various methods.
In order to obtain a probabilistic estimate linked to the temperature range provided by the UQ methods, a further procedure that exploits the non-parametric estimate of the probability density [93] based on sampled data on the surrogate model was carried out. This procedure allows obtaining an estimate of the continuous probability starting from the results obtained of T_w and has been preferred for the final comparison.

3.4.1 - Geometric analysis results

The sample size for the Monte Carlo method has been defined in order to be able to evaluate the convergence. All samples were taken with the LHS method in order to speed up convergence.
The tests were carried out for three sample sizes: 10, 100 and 1000 samples. It should be noted that, although the approach is simplified, a simulation of the solver Therm-1D takes a couple of minutes to perform the complete calculation on a high-performance personal computer, so a Monte Carlo simulation of 1000 samples requires a total computational cost of almost 36 hours.
The average values obtained from the Monte Carlo analysis are presented in Figure 3.19.

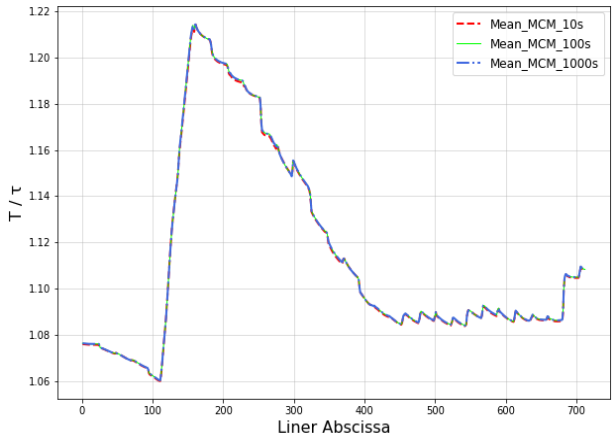

Figure 3.19 – Mean values of T_w

The Monte Carlo method is not affected by the sample size regarding the mean value, but the same cannot be said for the extreme values found for the different samples and for the standard deviation (Figure 3.20).
Considering the identical trend of the three mean values, in the graphs of Figure 3.20 (a) it was chosen not to show all the mean terms, in order not to complicate the reading of the graph.

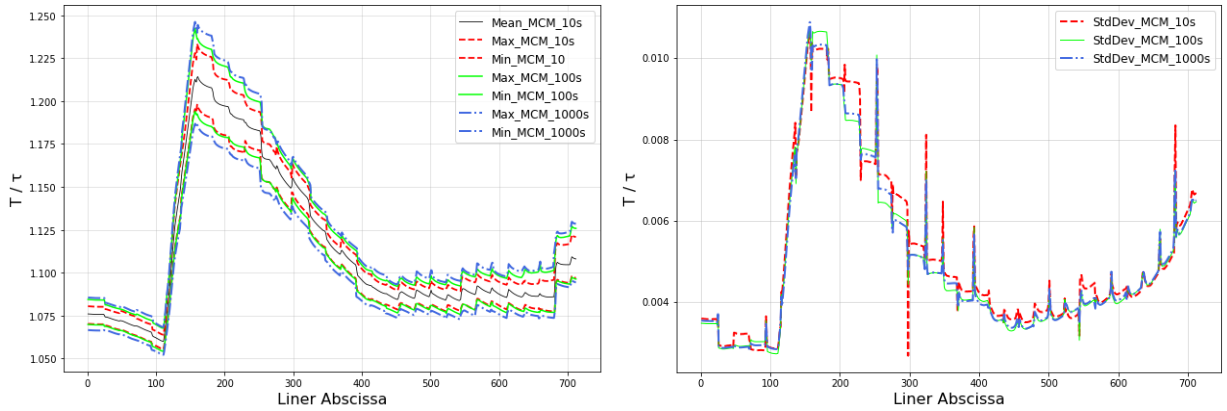

(a) (b)

Figure 3.20 – (a) Maximum and minimum values of T_w (b) Standard deviation

As the sample size increases, the gap between the minimum and maximum values increases: this phenomenon is explained by the type of sampling carried out. In fact, the LHS technique divides the initial distribution into areas of equal probability and then randomly samples a point within each area; this causes many more points to be considered in the analysis at the far end of the distribution, leading to an increase in the dispersion of the results.

The main differences between the sample sizes can be seen from the graph of the standard deviations; as expected, it can be noticed a greater difference of the minimum sample size compared to other sizes, indicating a lack of convergence.

In order to evaluate the convergence of the Monte Carlo method, larger sample sizes were evaluated, but given the high calculation times and the minimal differences, it was possible to see how the size of 1000 samples guarantees a good compromise between computational effort and convergence; for this reason it was decided to base the subsequent comparisons with this size.

Moving on to spectral expansion methods, the first comparison carried out is that one between the polynomial chaos expansion method based on the tensor product of the bases and the stochastic collocation method. The results obtained with the two methodologies are almost identical (Figure 3.21).

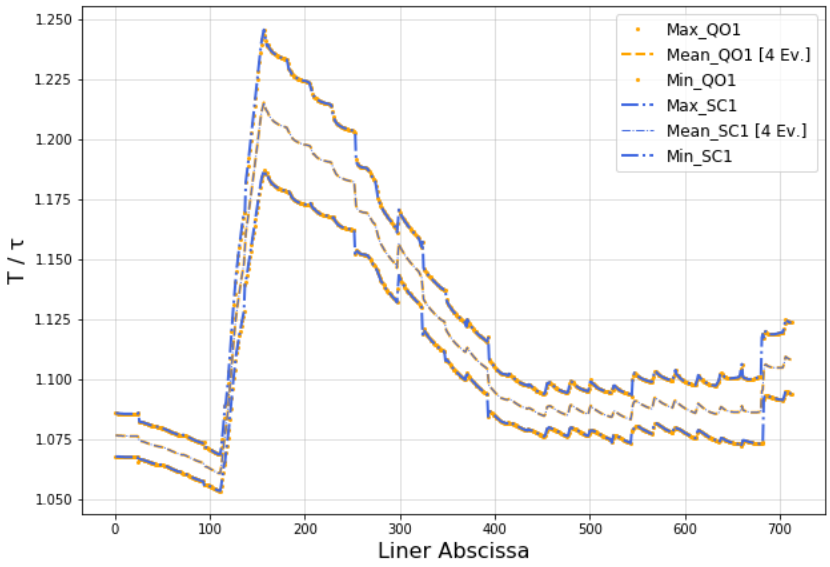

Figure 3.21 – Comparison PCE (quadrature order) and SC

In Figure 3.22 the change in liner temperature as the polynomial order increases for both methods is shown.

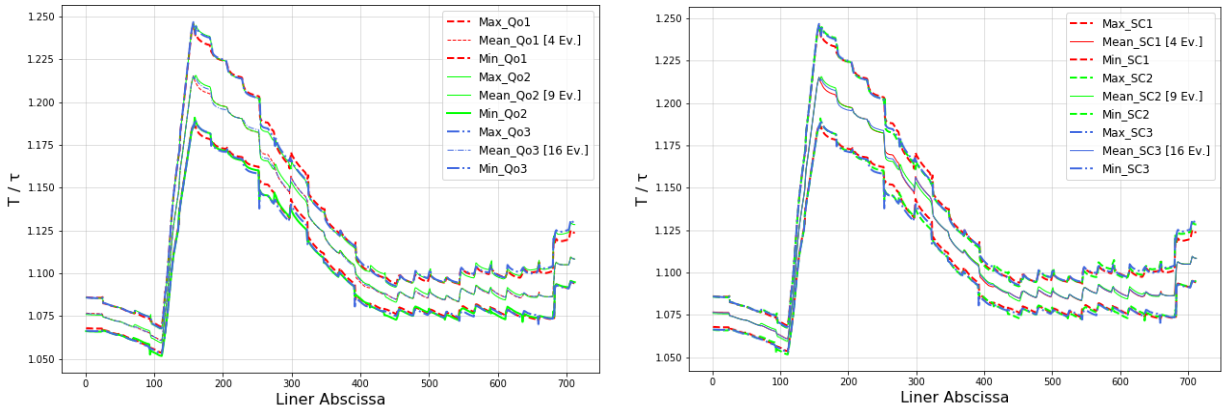

(a) (b)

Figure 3.22 – Order sensitivity for PCE quadrature order (a) and SC (b)

The results obtained are in accordance with Montomoli et al. [26], which declared a variation between the two methods of 0.6%.

Since the two methods provide the same result, both in terms of average and interval, the stochastic collocation method was not considered for the subsequent analyses and comparisons.

The last stochastic expansion methodology to be shown is that one of the PCE with total order imposed; in this case, the polynomial order coincides with the degree of the final interpolating polynomial.

In Figure 3.23 (a) the analysis with a polynomial order of two is reported, in which a sampling equal to the minimum required from Eq. 2-44 has been considered; in Figure 3.23 (b) the result obtained by carrying out twice the required sampling is provided. Results show clearly how the first analysis gives non-sense results.

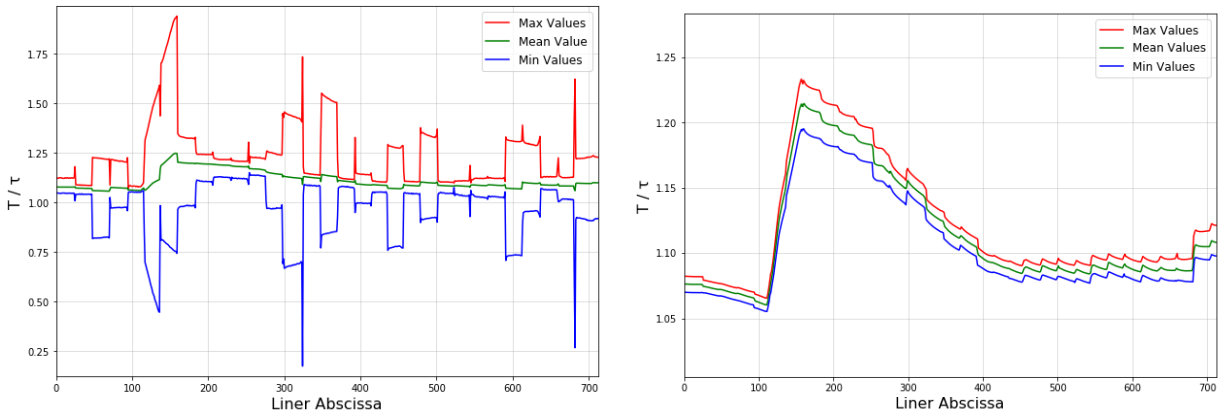

Figure 3.23 – PCE total order 2 without over-sampling (a) and with double over-sampling (b)

As already stated in [60], also for this analysis, operating with this methodology, an over-sampling is mandatory in order to obtain results comparable with the previous methods. For all subsequent analyses, carried out with this expansion technique, an over-sampling of a factor of two was carried out ($collocation\ ratio\ =\ 2$).

The results are then displayed when changing the polynomial order (Figure 3.24).

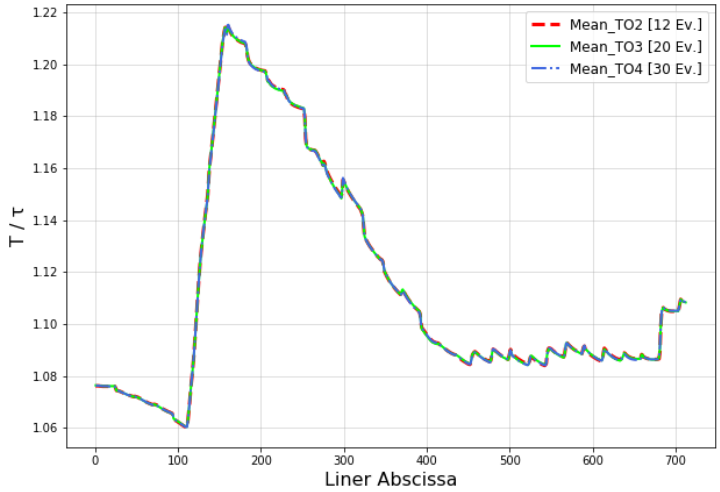

Figure 3.24 – Mean values for different orders of PCE with total order

It can be observed that the mean values are not sensitive to the polynomial orders studied.

In Figure 3.25 the trends in terms of maximum values, minimum values, and standard deviation are reported; these trends show that this method is the most sensitive to the polynomial order. In particular, it is noted that the polynomial of higher order has fluctuations with respect to those of lower order.

On the contrary to how one might think, a single increase in the polynomial order does not lead to any benefit in terms of approximation of the function considered, in contrast, it can lead to results with a lower degree of accuracy.

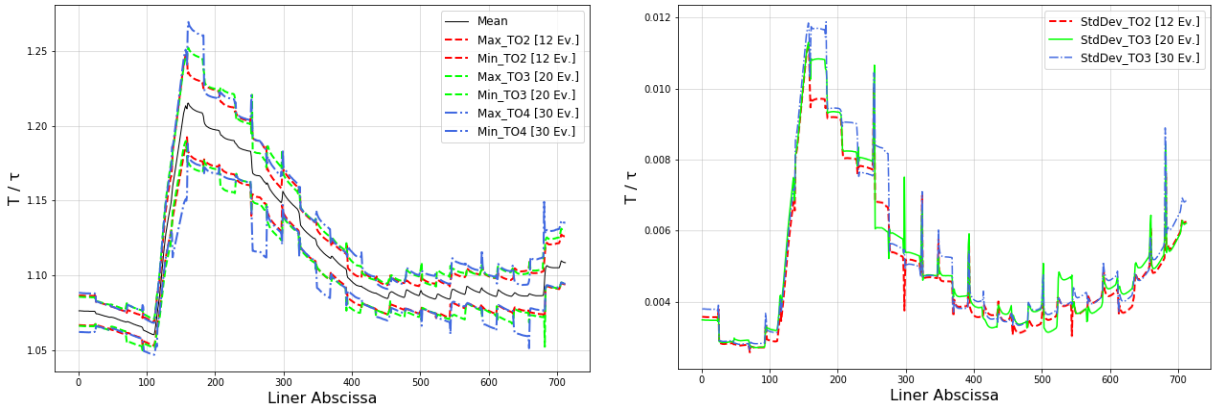

(a) (b)

Figure 3.25 – (a) Maximum and minimum values for PCE total order (b) Standard deviation

Combining these results with those of the following chart (Figure 3.26), in which the various methods of uncertainty quantification are compared, it is possible to conclude that this method has a good behaviour in predictive terms with the growth of the polynomial order only if this is coupled with an increase in the over-sampling, which therefore translates into higher computational costs. Comparing the results obtained with the Monte Carlo method and those obtained with stochastic methods (Figure 3.26), it is clear that the latter are much more efficient; in fact, a surrogate model obtained with only 4 simulations can predict both the average trend and the limit values of the metal temperature.

Subsequently, it will be shown that these will be able to predict also the probabilistic distribution with excellent results.

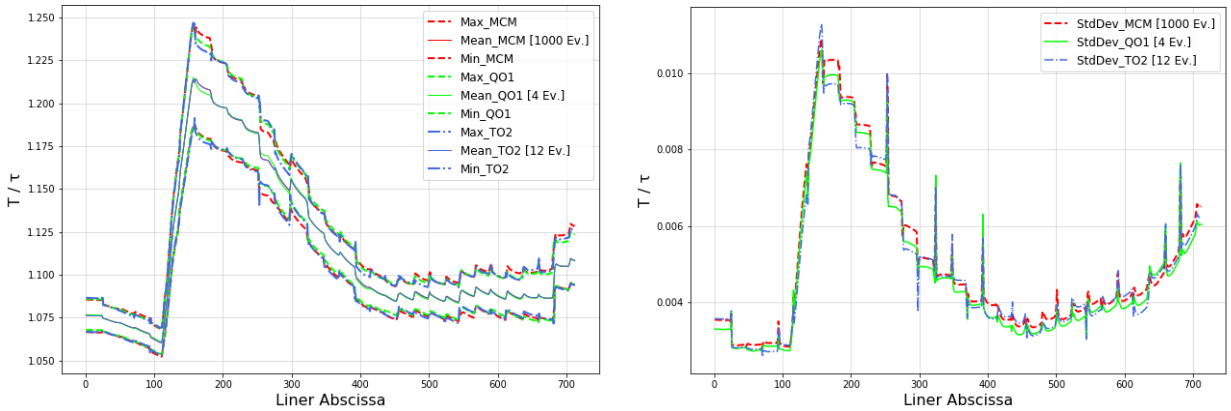

(a) (b)

Figure 3.26 – Comparison between MC and PCE for mean values (a) and standard deviation (b)

When the number of variables is low, the need to ensure over-sampling for the fixed-order PCE results in a higher computational cost than with the tensor-product method and, thus, also with the stochastic collocation method.

It should be emphasized that the results obtained in terms of the agreement between the Monte Carlo method and those of stochastic expansion are not generalizable in the absolute sense; the extreme efficiency that the polynomial chaos expansion presents is attributable also to the system studied.
Most likely, with a model having a response function with a highly non-linear trend, in order to obtain a good level of prediction, it would have been necessary to have a higher polynomial order and, therefore, a higher computational cost linked to the uncertainty quantification analysis.
As previously mentioned, another important result obtained from this type of analysis is that of evaluating in probabilistic terms the probability distribution associated with the temperature range achieved with the surrogate model. The estimation of the probability density obtained with the Monte Carlo method (1000 samples) and those obtained by sampling on the surrogate models of the two PCE methods, one based on the Gauss grid and the other with a fixed total order, which respectively require 4 and 12 simulations, are reported in Figure 3.27. The result obtained with the stochastic collocation is also reported (4 simulations). In this way, it is possible to observe the variation of the PDF of the wall temperature as a function of the non-dimensional abscissa of the liner.

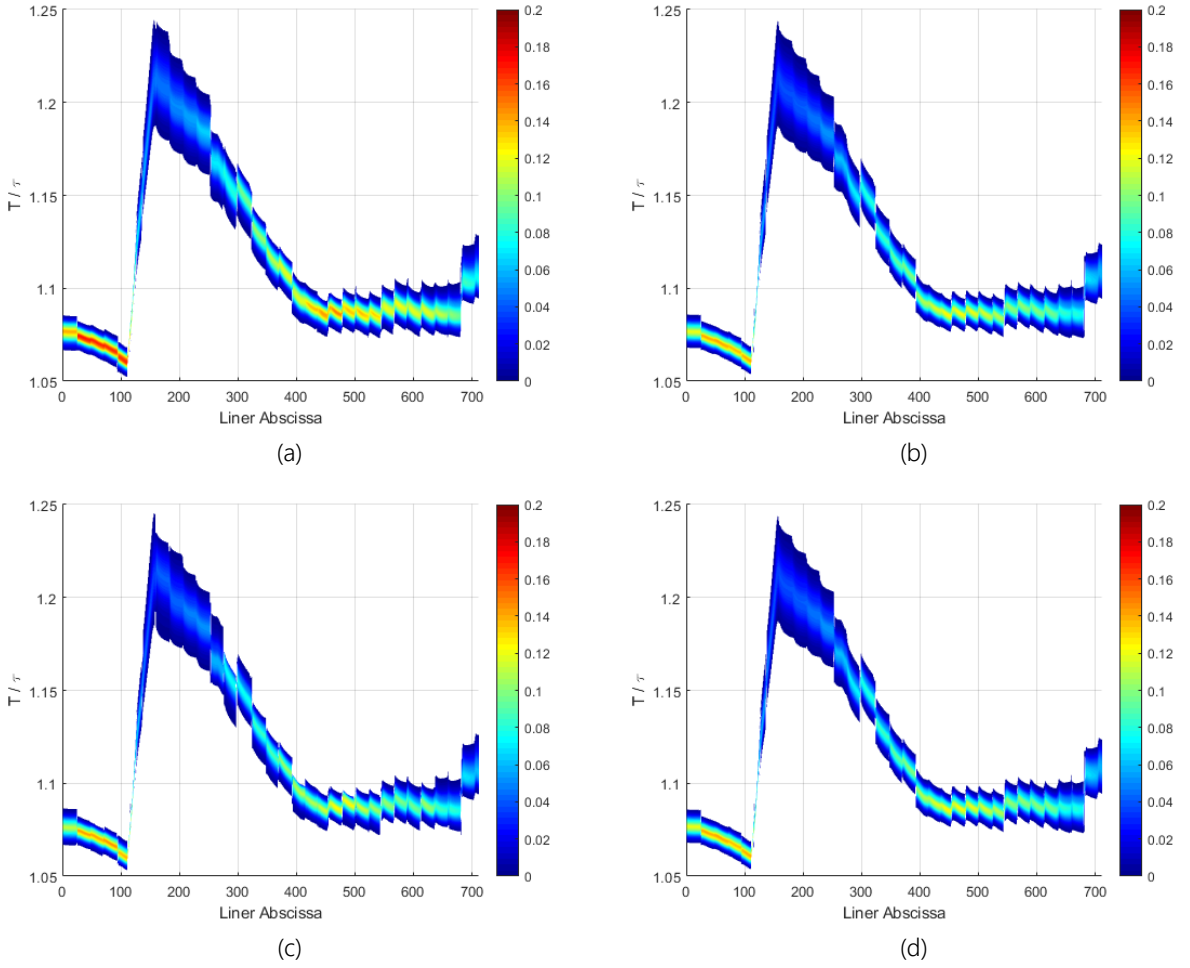

Figure 3.27 – Geometric analysis output probability: (a) MC (b) PCE tensor-product
(c) PCE total order (d) SC

It should be noted that these graphs are based on independent points, so it is not possible to have an indication of the axial development of the liner temperature; in other words each point has a probability of

occurrence that does not depend on the others. The correct use of this type of graph is to fix a coordinate of the liner and assess the probability to get a certain wall temperature because at each point of the liner there is a certain probability distribution that is independent of the previous and following one.
Overall, it can be seen that the methods are also in agreement with themselves in probabilistic terms. In all the regions of the liner there is a zone with a greater probability, associable to the modal value of the probability distribution. This assumption is not valid for the most critical condition in terms of wall temperature: where the maximum value is reached there is not a zone to which a higher probability of occurrence can be associated; this involves an almost equal probability (almost equal colour) of obtaining a value between the maximum and the minimum temperature, in which there is a range of variability of 30%.
In Figure 3.28 the sensitivity study is reported as a histogram. It revealed that the discharge coefficient has a generally greater influence on liner temperature than the angle of inclination of the effusion hole. Sobol's indices are reported in a cumulative graph.

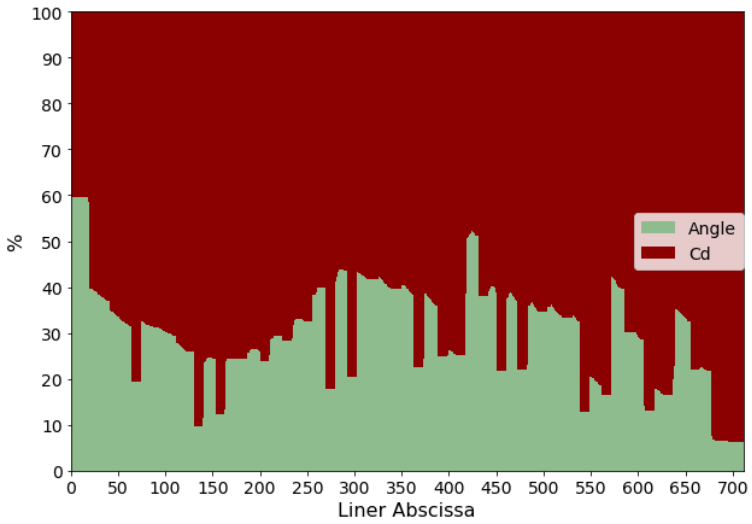

Figure 3.28 – Sensitivity analysis for geometric parameters

The study has shown that spectral expansion methods are in good agreement with the Monte Carlo method for reduced polynomial orders; this has allowed to conduct the remaining analysis of UQ with minimum polynomial orders and therefore, ensuring the lowest computational cost.
For the remaining analyses, only comparisons among methods will be provided.

3.4.2 - Heat transfer factor analysis results

The purpose of this analysis is to quantify how and which heat transfer tuning factor most influences the response function. The study shows a perfect agreement between the stochastic expansion methods with the Monte Carlo method, both in terms of temperature trend and standard deviation.
As further explained below, by comparing the various analyses, it appears that the uncertainties regarding the heat transfer coefficients have a greater impact on the liner temperature than the geometrical factors studied in the previous chapter. This can be seen from the fact that the latest analysis conducted has led to a greater range of temperature variability for each response function considered (Figure 3.29).

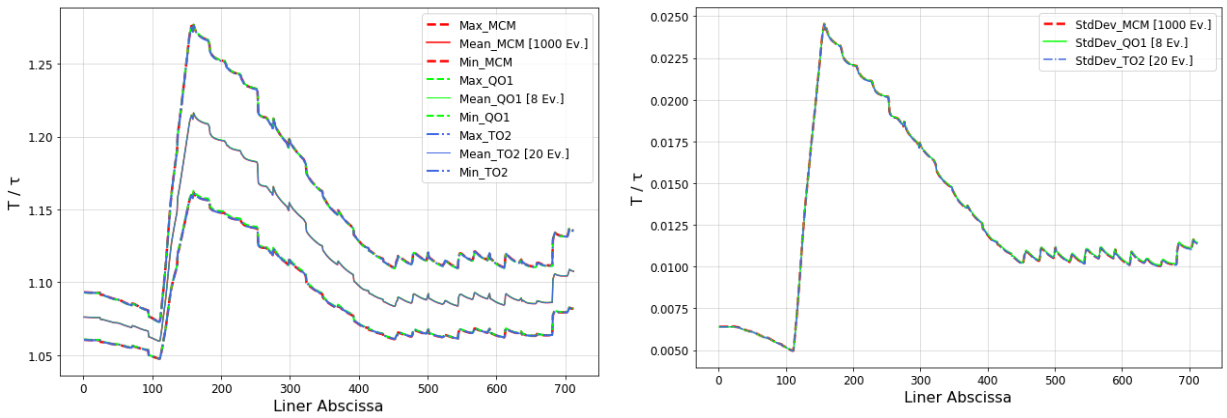

(a) (b)

Figure 3.29 – Comparison HTC analysis (a) Temperature (b) Standard deviation

From the sensitivity analysis using Sobol's indices reported in Figure 3.30, it appears that the heat transfer coefficient on the gas side has a predominant effect on the liner temperature.

In accordance with what has been stated in [92], the second major contribution is represented by the factor that acts on the heat transfer coefficient linked to the sink effect. The cold side heat transfer tuning factor has a limited influence on the liner wall temperature

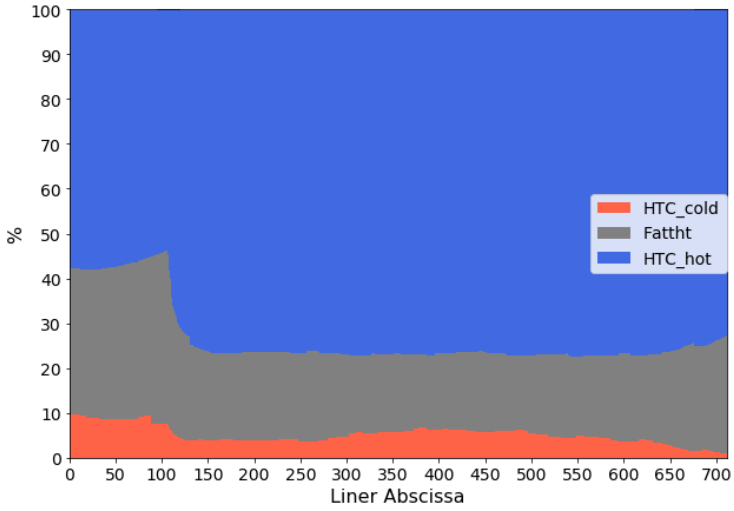

Figure 3.30 – Sensitivity analysis for heat transfer tuning factors analysis

The probability maps obtained for the four methods are provided below in Figure 3.31.

The results are analogous to those already described for the geometric analysis; from the graphical visualization of the data obtained it is highlighted the greater variability associated with the temperature range of the liner. As for the previous analysis, the maximum excursion occurs in those areas of the liner where the temperature peak is reached; in this area the uncertainty on the heat transfer factors leads to a maximum variability on the results of the 40%.

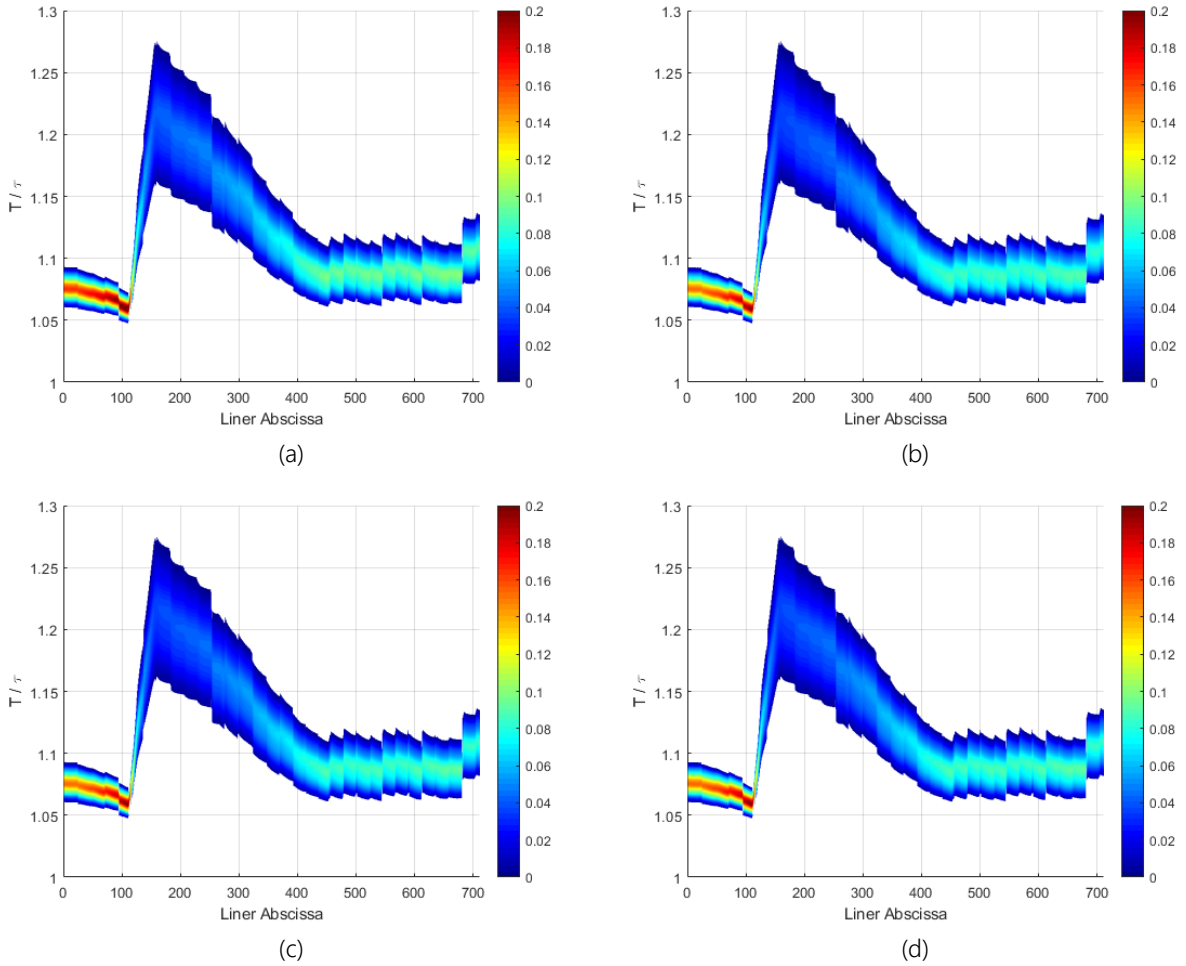

Figure 3.31 – Output probability for HTC analysis (a) MC (b) PCE tensor product (c) PCE total order (d) SC

3.4.3 - Boundary conditions analysis results

Also for this type of analysis, multiplicative factors that act on different quantities have been considered, all related to the boundary conditions that occur inside the combustor. In particular, one factor acts on the temperature of the hot gas, on the FAR and on the temperature at which the radiation occurs; the other factor acts on the velocity of the gas inside the chamber, which in practice influences two parameters of the fluid network: the velocity of the gas and the product density-velocity.

From the comparison of the UQ methods, the results are shown in Figure 3.32.

It is worth noting that in average terms both stochastic expansion methods present good agreement with the Monte Carlo method; as far as the standard deviation is concerned, the method based on the Gauss grid tends to differ from the other two.

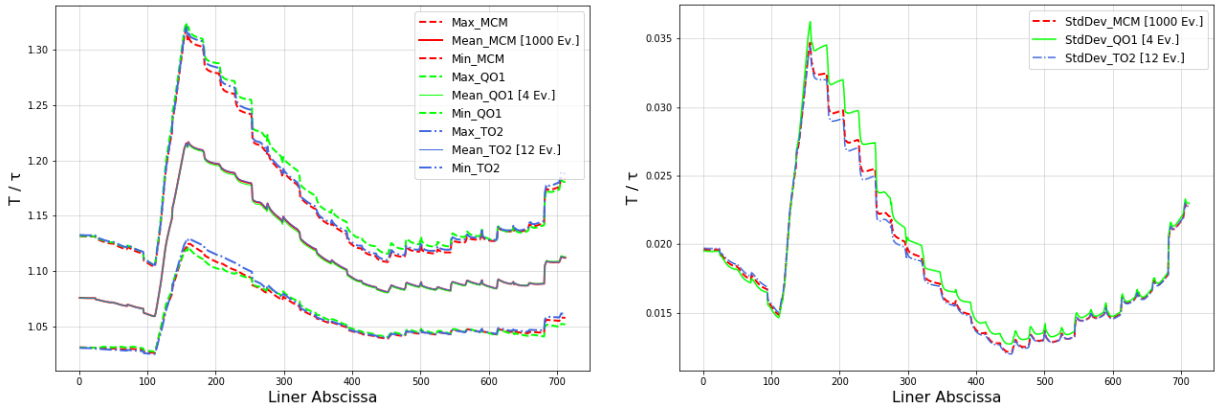

(a) (b)

Figure 3.32 – Boundary condition analysis comparison (a) T_w (b) Standard deviation

Sensitivity analysis using Sobol's indices (Figure 3.33) shows how the factor acting on thermal parameters has a greater impact in the first zone of the liner wall temperature compared to the kinetic variable, while the factor acting on kinetic terms takes on greater weight in the final region of the combustor. In the middle of the liner the situation is well balanced.

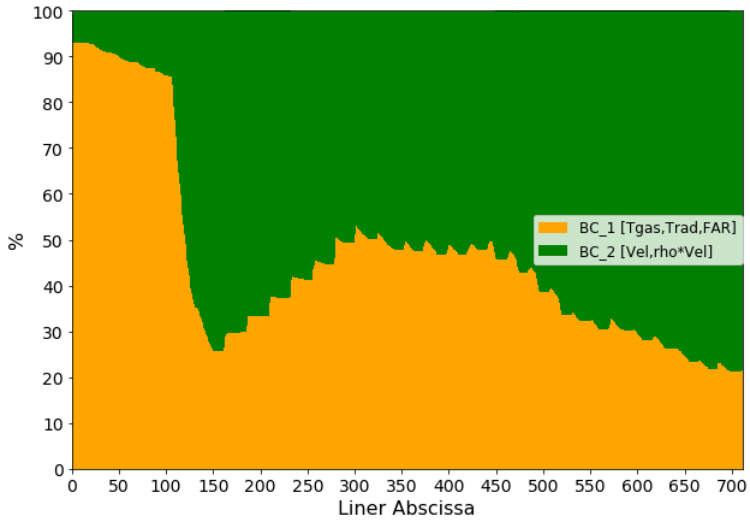

Figure 3.33 – Boundary conditions sensitivity analysis

This study confirms what has been hypothesized in the discussion of the results obtained by the deterministic approach (Figure 3.18) i.e. that the solution obtained by the fluid network solver is extremely dependent on the conditions that are imposed in the input file "gas.xxx".

It can be concluded that acting on the temperature of the internal gas to model the effect of the film cooling with the fluid network supplied by GE Avio Aero, in fact, is equivalent to impose a priori the temperature of the liner wall. This approach is correct; however, it is necessary to insert gas temperature values such as to make the liner wall temperature supplied by the fluid network solver coincide with the experimental data measured during the test phase. From the results obtained, the temperature inserted according to the indications provided by GE Avio Aero is not correct in order to obtain the experimental result hoped for with

a deterministic approach; however, it should be remembered that this aspect was not an objective of this work. The probability maps obtained with the different methods are reported in Figure 3.34.

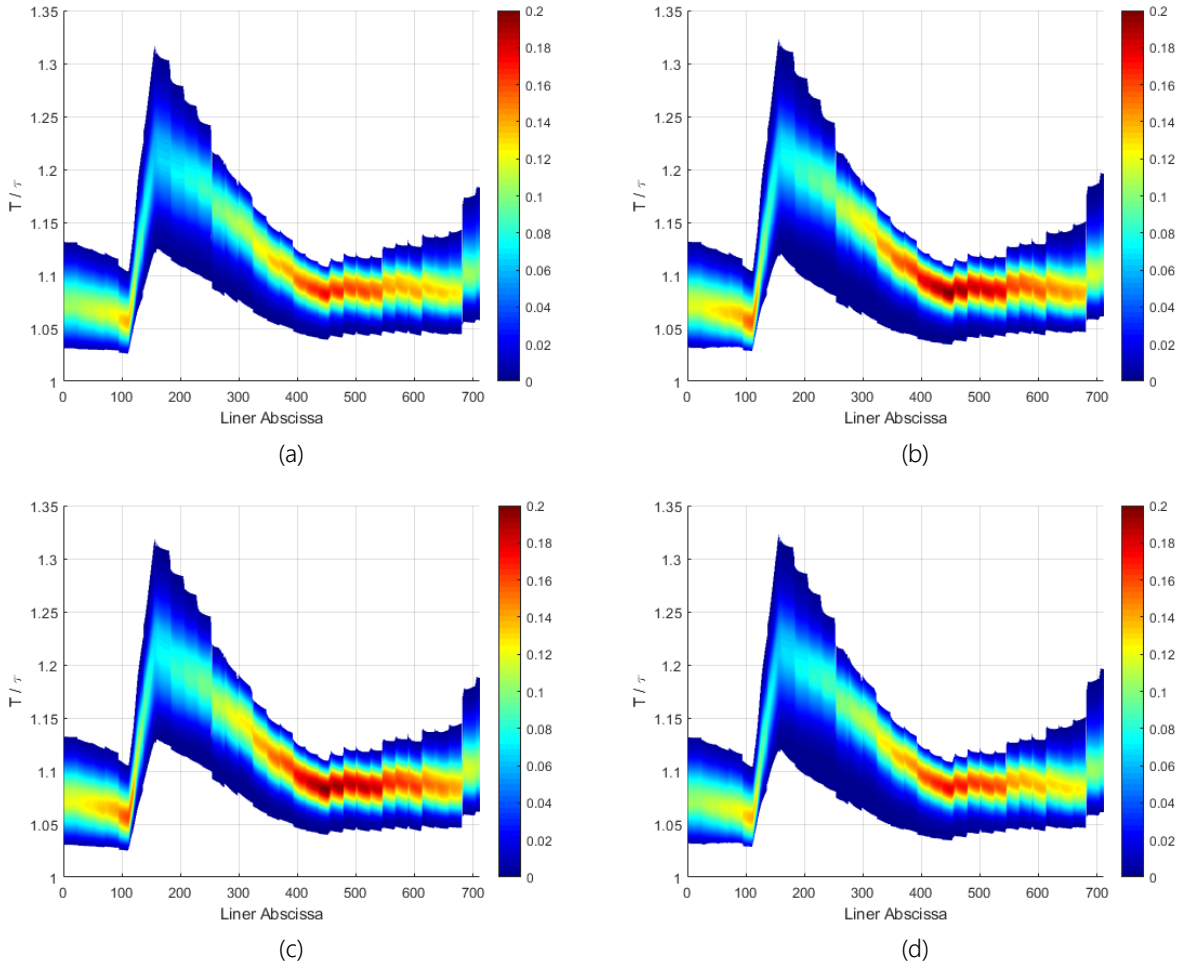

Figure 3.34 – Boundary conditions analysis output probability
(a) MC (b) PCE tensor product (c) PCE total order (d) SC

All four probabilistic approaches provide qualitatively the same result. It can be seen that this type of analysis involves the largest amplitude in terms of liner wall temperature. A variation of 20% on the temperature conditions of the hot gas inside the combustor causes a maximum variability of 54% on the liner wall temperature, which occurs, as in previous analyses, at the abscissae where the temperature peak is located. Contrary to what has been obtained from previous analyses, this study shows a zone with a higher probability in each zone of the combustor; it is underlined that this portion of the map is the one defined by the deterministic response of the fluid network.

Even if it was not part of the objectives of the work, the experimental points were also included in a dedicated graph (Figure 3.35); from visual comparison, it is evident that the one-dimensional approach with the boundary conditions provided does not succeed in predicting the trend of the liner wall temperature obtained experimentally. From the graph, it is evident that the methodology used, with the conditions already described of the fluid network, does not allow to obtain a probabilistic estimate that reflects the real trend of the liner temperature. It is underlined once again that for the two experimental tests there is the

possibility to obtain the temporal and axial development of the wall temperature, while similar considerations are not valid for the probabilistic estimate because for each discretized point of the liner a probability distribution is obtained and this is independent of the others.

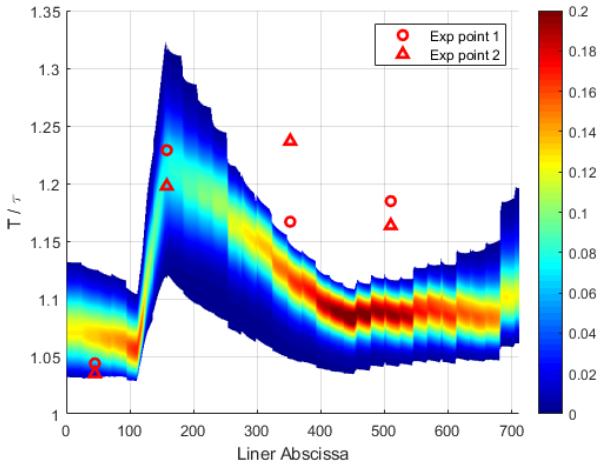

Figure 3.35 – Probabilistic map including experimental data

It is recalled that this type of graphs, such as those in which the minimum and maximum trend is shown (for example Figure 3.32), do not show the axial development of the liner wall temperature, but only the limit values within which this can occur; in other words, values beyond which no temperature condition linked to the specified operating point of the machine should occur are obtained, according to the fluid network model used and the uncertainty quantification analysis carried out,.

3.4.4 - Comparison among analyses

Before moving on to the validation of the Smolyak grid, a brief summary of the results obtained should be carried out. From the comparison of the results of the different analyses (Figure 3.36), it is more evident what has already been mentioned in terms of variability of the response function.

Regarding mean terms, each analysis gives the same result. The uncertainty about the boundary conditions produces the maximum variability of the response function analysed; after the peak temperature, the analysis produces a sudden decrease in the wall temperature: this is attributable to the different velocity field to which the burner has been subjected, as it was imposed an uncertain factor that affects the velocity of the gas, which in turn affects the convective heat transfer.

The boundary conditions produce a translation with respect to the mean value, as constant variations are imposed throughout the development of the combustor.

Heat transfer factors have a strong incidence in the central areas of the liner, where the heat transfer is higher, while in the initial and final areas of the combustor they do not make a very different contribution from the one due to the geometric factors of the holes.

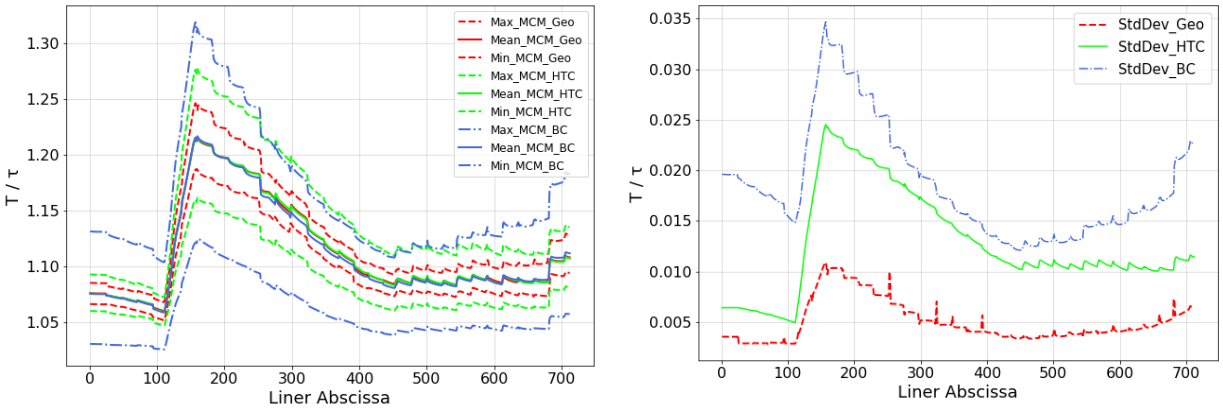

(a) (b)

Figure 3.36 – Comparison for (a) T_w (b) Standard deviation

3.4.5 - Overall analysis and Smolyak grid validation

For heat transfer on high temperature components in turbomachinery applications, it is not always possible to carry out studies with a small number of variables; for this reason an additional analysis has been conducted for the validation of the Smolyak grid, which has an excellent efficiency as the number of variables increase, whereas the other spectral methods, especially when the polynomial order is greater than three, require a huge computational costs.

The analyses carried out have been combined in a macro-study; this has been exploited, in addition to the validation of Smolyak grids, also to assess which are the parameters that affect the response function obtained by the fluid network solver.

In addition to the objectives listed above, a study is carried out on the sensitivity of the Smolyak grid to the level (Eq. 2-52), and for this reason three levels are considered: $l = 1$, $l = 2$ ed $l = 3$.

The more the level grows and the more the Smolyak grid tends to the Gauss one, for which the computational cost increases exponentially.

In Figure 3.37 the number of simulations for the different UQ method are provided. The figure summarizes all the conditions described above. Generally, the lowest computational cost would be guaranteed by the total order polynomial chaos expansion, but since this methodology requires sampling at least twice the minimum value required, the condition that requires the least number of evaluation is based on the Smolyak grid.

In this analysis, the seven variables previously analysed were evaluated at the same time.

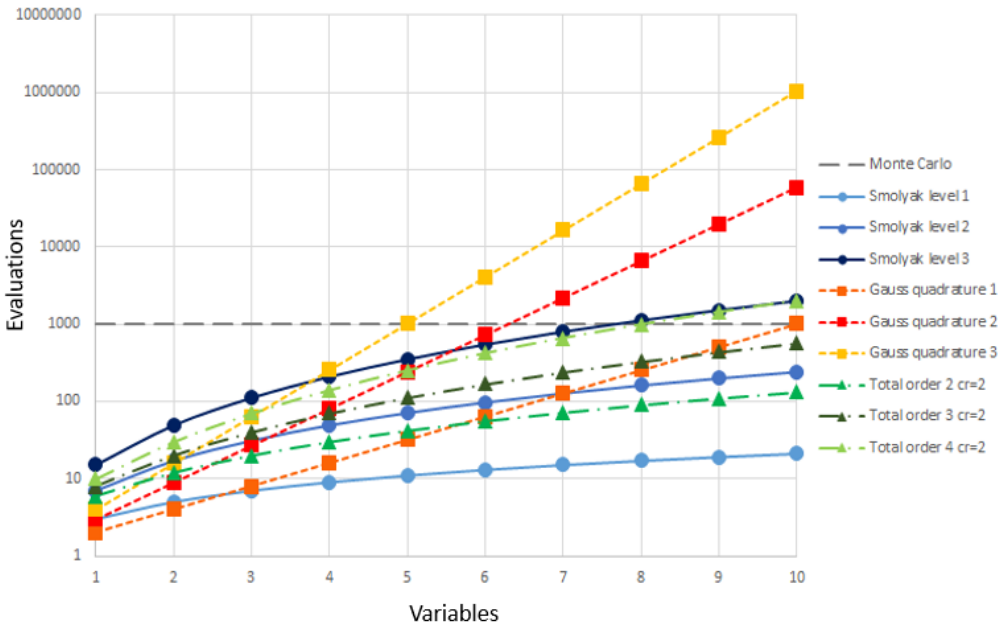

Figure 3.37 – Number of evaluations required by each method

For this study, the sensitivity of the Monte Carlo method to the size of the sample was re-evaluated and the results are shown in Figure 3.38. As for the previous analyses, also for this case the size of 1000 samples was considered a good compromise between the calculation time and the convergence of the solution.

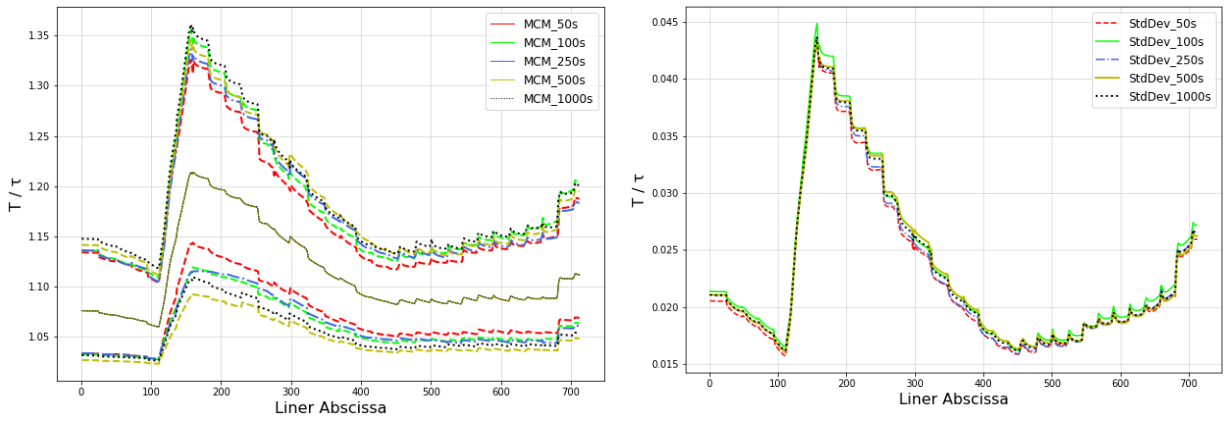

Figure 3.38 – Monte Carlo sensitivity analysis (a) T_w (b) Standard deviation

From the analysis it is clear that the trend is different from the one of the geometric parameters. The trend of minimum values obtained with the sample with 500 points is lower than that obtained with 1000, this may be due to the fact that some values of the sampled quantities have a greater weight for the one-dimensional code than others.

To further justify this trend, it should be remembered that the values of T_w graphically reported, are not to be intended as values of a single sample set: in fact, the maximum and minimum values obtained for each calculation point of the fluid network have been considered, so they are not physically contiguous values along the non-dimensional abscissa.

In conclusion, the points represented by the minimum line of the sample with 500 points may be due to a singularity, for which values are obtained lower than all the other points considered. In terms of standard deviation, the maximum excursions are due to smaller samples. Moving to the Smolyak grid, three levels were considered; in this way the behaviour of the method was evaluated for an extremely reduced number of evaluations, going from15 simulations for level one up to a number of simulations comparable to that of the Monte Carlo method: 800 simulations for level three. The results are shown in Figure 3.39.

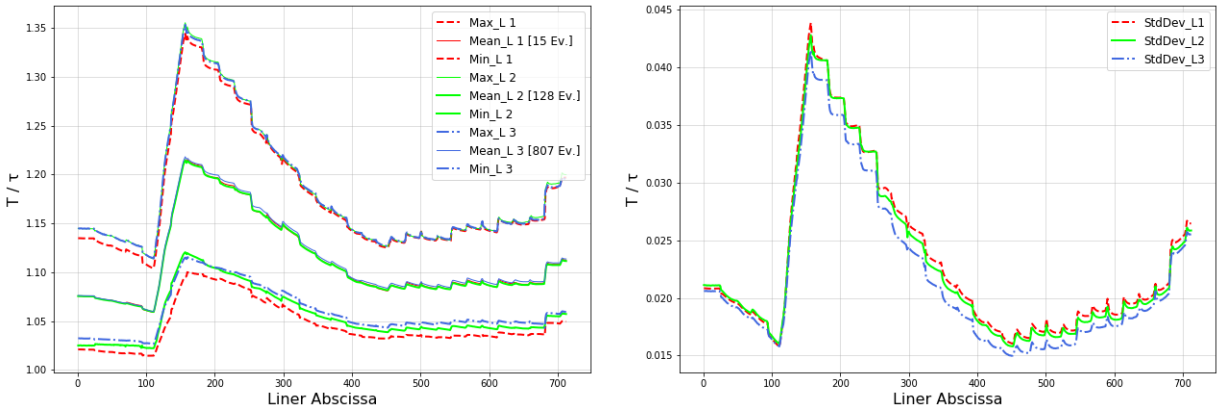

(a) (b)

Figure 3.39 – Smolyak grid order sensitivity (a) T_w (b) Standard deviation

From this analysis it is clear that the grid level does not affect the mean term; the lowest level, requiring only fifteen evaluations, does not have very different results from the other two, only a slight underestimation of the minimum values. The difference between this level and the others is less than 3%. In terms of standard deviation, the trend from the highest level is lower than the other two levels. For a more detail comparison, the methods of polynomial chaos expansion with Gauss grid and fixed order, respectively of order one and two, have also been evaluated. Figure 3.40 reports all the comparison of the methods.

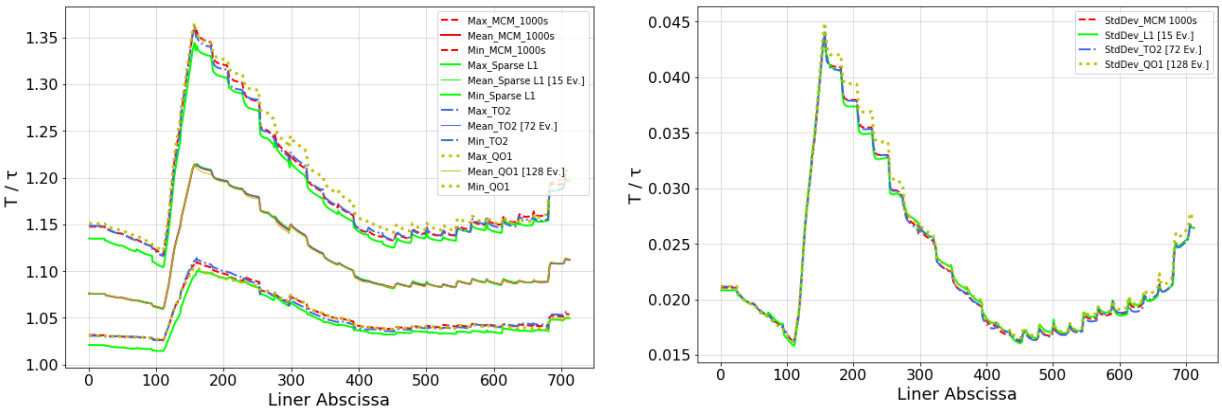

(a) (b)

Figure 3.40 – Comparisons (a) T_w (b) Standard deviation

The polynomial chaos expansion based on the Smolyak grid slightly underestimates both the maximum and minimum trends, but given the extremely low computational cost, it can be an important tool for applications where simulation requires more computational resources.
For completeness, in Figure 3.41 the probabilistic maps of the Monte Carlo method and the three cases for the polynomial chaos expansion are reported.

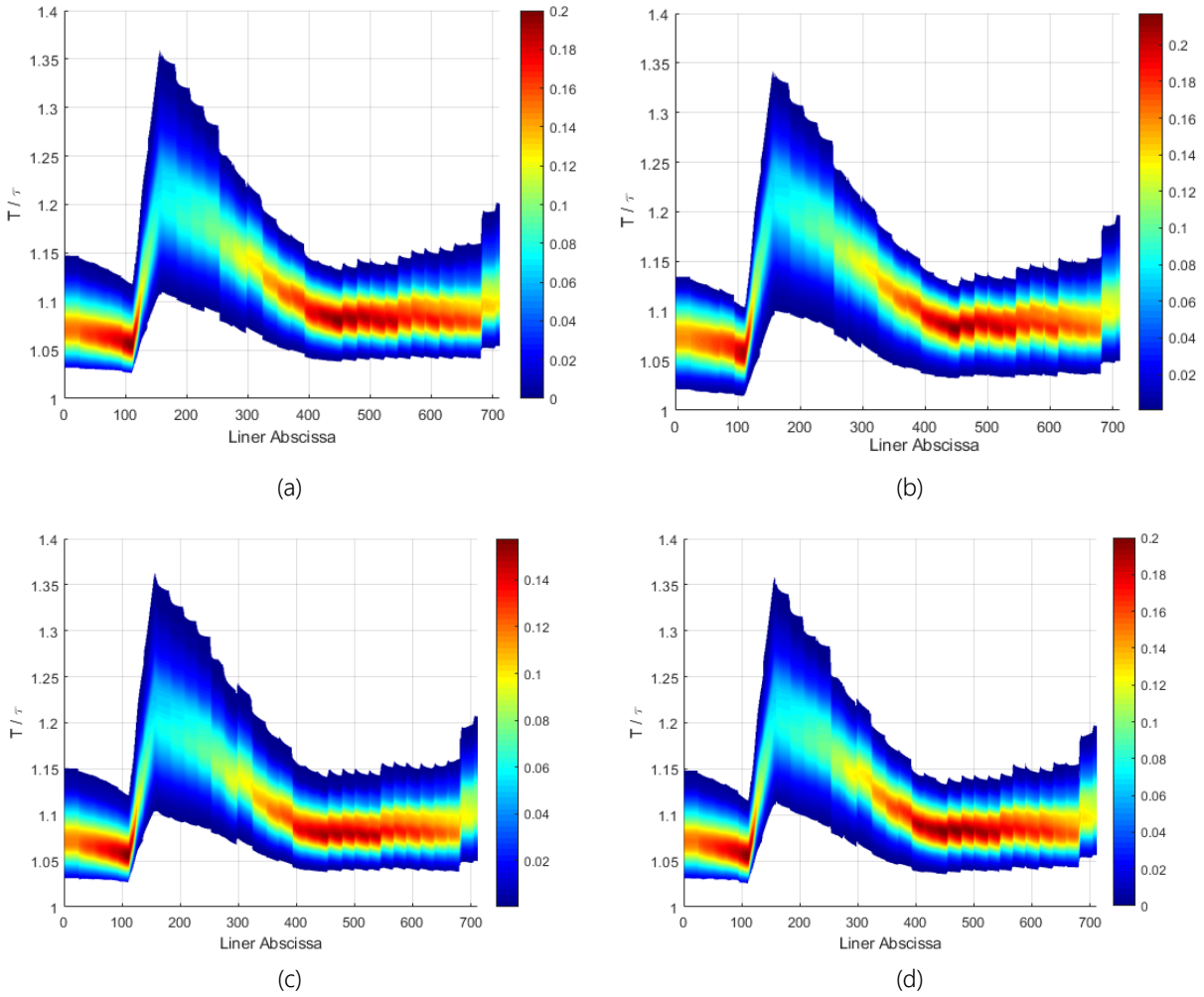

Figure 3.41 – Probabilistic maps (a) MC (b) PCE Smolyak (c) PCE Gauss (d) PCE total order

The results are analogous to what already described previously; from this kind of diagram it is possible to notice more clearly the slight underestimation of the T_w provided by the method based on the Smolyak grid. Another important consideration is focusing on the possible range of the output temperature: this range is the higher one, as expected if compared to the previous analyses, but the important result is the quantification of this uncertain considering all the variables. In fact, the range is slightly more extended than the one of the boundary conditions analyses, indicating that, of course, the output range has not a linear dependence over more analyses with parameters individually taken.
The sensitivity analysis provides very interesting information, the results are shown in Figure 3.42.

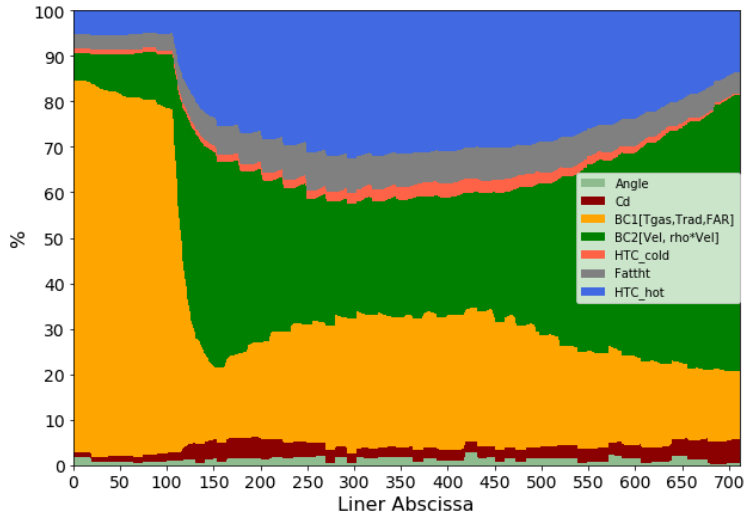

Figure 3.42 – Sensitivity analysis for the overall analysis

From the histogram it is clear that, excluding the initial part in which the results strongly depend on the temperature distribution of the gas set, in the central zone the variable that acts on the heat transfer coefficient inside the combustor assumes an importance approximately equal to the variables related to the boundary conditions; overall, these three quantities have the greatest weight on the response function.
In the last part of the component, the variable that has the greatest impact on the T_w is the one related to the temperature field.
The terms related to the geometry of the holes have a cumulative Sobol's index of less than 5% over almost the entire development of the liner, excluding the last part. Regarding heat transfer it can be concluded that the current modelling of the geometrical effects of the fluid network does not affect the response function; this behaviour is in accordance with what is reported in the study of Bunker [2] in which, although it is focused on film cooling and not properly on effusion cooling, the uncertainty related to the diameter of the hole and its inclination angle with respect to the direction "streamwise" have a medium-low influence on the heat transfer.

4 - UQ analysis applied to CFD

The second part of the thesis is based on the application of uncertainty quantification methodologies to computational fluid dynamics. The selected case study focuses on the evaluation of the impact of geometric uncertainties on the film cooling effectiveness evaluated on a gas turbine vane; this type of analysis was chosen because film cooling plays a fundamental role in the cooling system of the blade profile. In [17] is indicated that a variation of 10% in diameter or ratio L/D of the hole with respect to the nominal conditions may lead to a reduction in service life of more than 80%.
Some authors have already undertaken UQ studies for this type of application [70], [72] and [73], however, all of them have considered a simplified geometric domain with a flat plate and not on a real geometry. Therefore, the main contribution of this work is to try to evaluate and asses the uncertainties on a real gas turbine vane geometry.

4.1 - Film cooling

Film cooling is one of the most important cooling systems for turbine blades and vanes; the profile is generally provided with holes that allow the coolant fluid to flow from the internal cavity to the external surface; an example of film cooling blade configuration is given below in Figure 4.1.

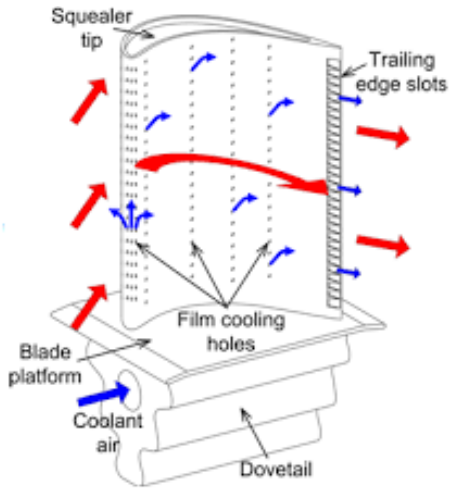

Figure 4.1 – Film cooling configuration [94]

The coolant flow creates a protective layer around the blade profile: since it is at a lower temperature than the main flow it reduces the amount of heat entering the blade. The adiabatic film cooling effectiveness is used as a parameter to quantify the degree of protection offered by the film; it is defined as follows in Eq. 4-1:

$$\eta = \frac{T_\infty - T_{aw}}{T_\infty - T_c} \qquad \text{Eq. 4-1}$$

In which T_∞ is the temperature of the main flow, T_{aw} is the wall temperature and T_c is the temperature of the coolant.

The reduction of the thermal flow entering the blade profile (q_f) is evaluated with respect to the case in the absence of film cooling (q_0); in fact, the local injection of the cooling jet leads to an increase in turbulence with a consequent increase in the heat transfer coefficient which could result in a condition for which the film cooling does not offer protection, instead it increases the heat load.

For this reason, the performance of the film in relation to heat reduction is evaluated in terms of reduction of the net heat flow (Net Heat Flux Reduction "$NHFR$").

$$NHFR = 1 - \frac{q_f}{q_0} = 1 - \frac{HTC_f(T_{aw} - T_w)}{HTC_0(T_\infty - T_w)} = 1 - \frac{HTC_f}{HTC_0}\left(1 - \frac{\eta}{\varphi}\right) \quad \text{Eq. 4-2}$$

In which φ represents the cooling efficiency defined as follows.

$$\varphi = \frac{T_\infty - T_w}{T_\infty - T_c} = \begin{cases} 0.6 \rightarrow Turbine \\ 0.8 \div 0.9 \rightarrow Combustor \end{cases} \quad \text{Eq. 4-3}$$

From this definition, it is clear that the film produces, in addition to protection, a reduction in the thermal load entering when $NHFR > 0$ or when this reduction is greater than the increase in the heat transfer coefficient.

It is also clear that the more the coolant jet remains attached to the surface of the blade, the longer is the duration of the protection offered by the film: this phenomenon is characterized by the blowing ratio (BR or M) (Figure 4.2) and defined by Eq. 4-4.

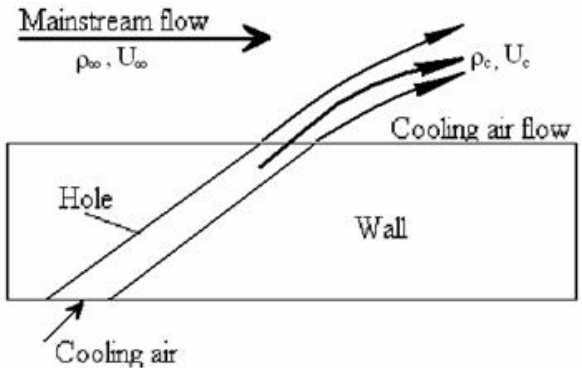

Figure 4.2 – Film cooling characteristics

$$BR = M = \frac{\rho_c V_c}{\rho_\infty V_\infty} \quad \text{Eq. 4-4}$$

As reported by Goldestein [95] for high blowing ratio $M > 1.5$ the coolant has a momentum capable of perforating the main flow and that does not adhere to the pallet; while for $M < 0.2$ the coolant flow rate is too low to ensure efficient coverage.

4.1.1 - Literature review

Film cooling plays a central role in the cooling system of the blade profile, for this reason, it is one of the most studied techniques: the different forms of hole, the inclination angle of the hole, the geometry of the hole matrix and various operating conditions have been evaluated in previous studies.
The first studies carried out by Goldestein [95] show the behaviour of the film when the blowing ratio varies for different distances from the hole (Figure 4.3).

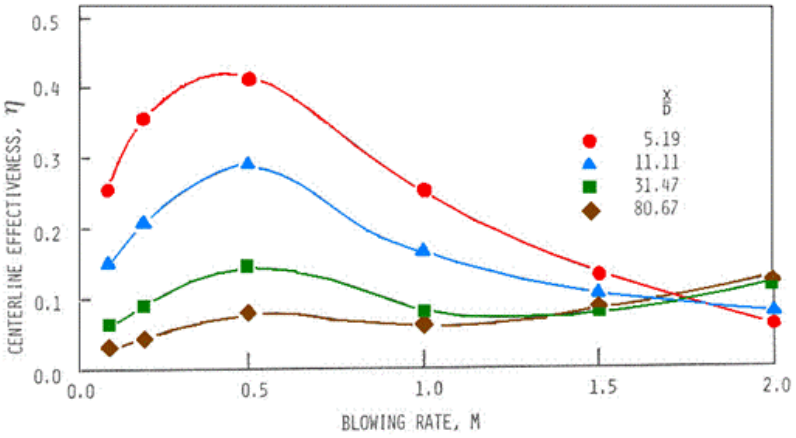

Figure 4.3 – film cooling effectiveness for a single hole for different distances and M [95]

Similar results have been obtained by Baldauf et al. [96], reported in Figure 4.4.

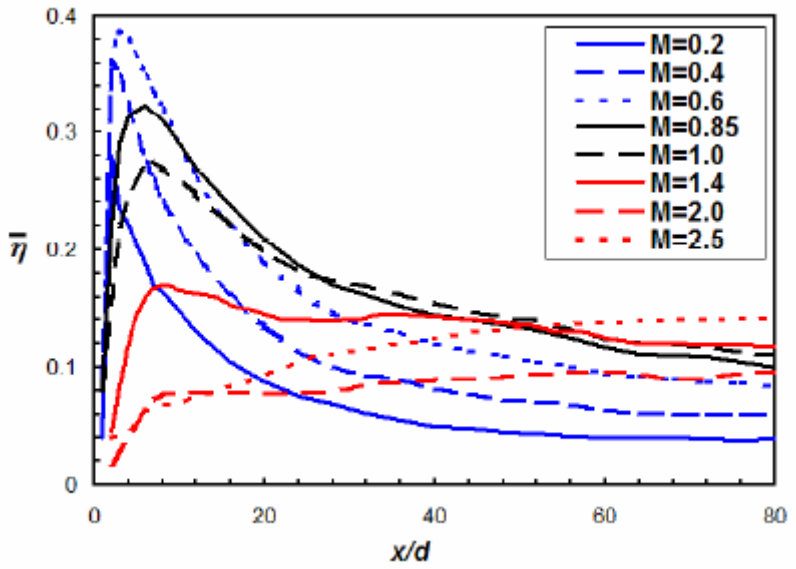

Figure 4.4 – mean film cooling effectiveness along streamwise direction for different M [96]

Goldestein et al. [97] evaluated the influence of the surface roughness of the blade on the film cooling effectiveness. In the study it was demonstrated that the behaviour of the film for a single hole, depending on the surface roughness, varies with the blowing ratio: for low M the surface roughness worsens the performance offered by the film by $10 \div 20\%$ compared to the case with smooth wall, while for high blowing ratios the surface roughness increases the performance up to $40 \div 50\%$; the enhancement of the film effect

is due to the greater turbulence that increases the mixing of the jet of coolant dissipating part of the energy unfavourable to the penetration of the main flow.

The continuous research on film cooling has allowed its development and a progressive performance increase. Over the years, the greatest increase has been due to the transition from the completely cylindrical holes to the flared ones (shaped), which still represent the standard configuration today. In the work carried out by Saumweber et al. [98] the comparison between the effectiveness obtained with cylindrical and shaped holes for two different levels of turbulence is shown (Figure 4.5); it can be seen how this geometry allows to reach higher and always increasing effectiveness values in the blowing ratio interval considered by the author.

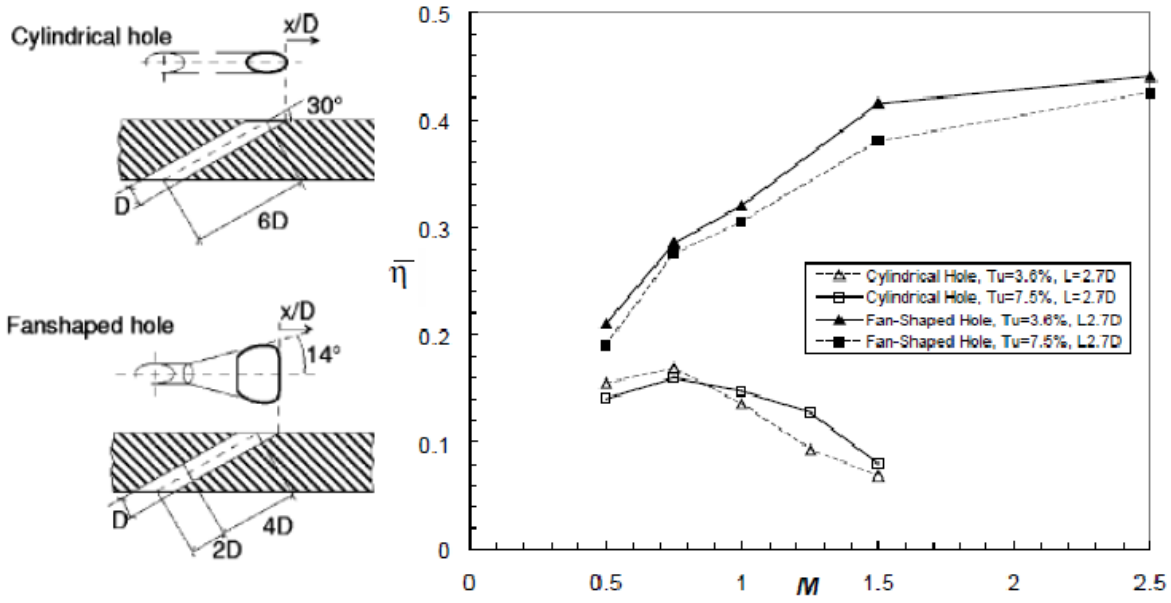

Figure 4.5 – Comparison between standard and shaped cooling holes [98]

The shaped holes are the subject of many works carried out by Bunker in [99], in which the results obtained by Takeishi et al. [100] are reported: a series of comparisons between standard shaped holes and with laidback angle are reported, including the variation of blowing ratio and turbulence level (Figure 4.6). The laidback angle consists in making a further countersink in the shaped section of the hole; this shrewdness allows to reduce the relative angle between the exit of the film and the surface: this configuration allows to reduce the separation of the coolant flow at the exit of the hole.

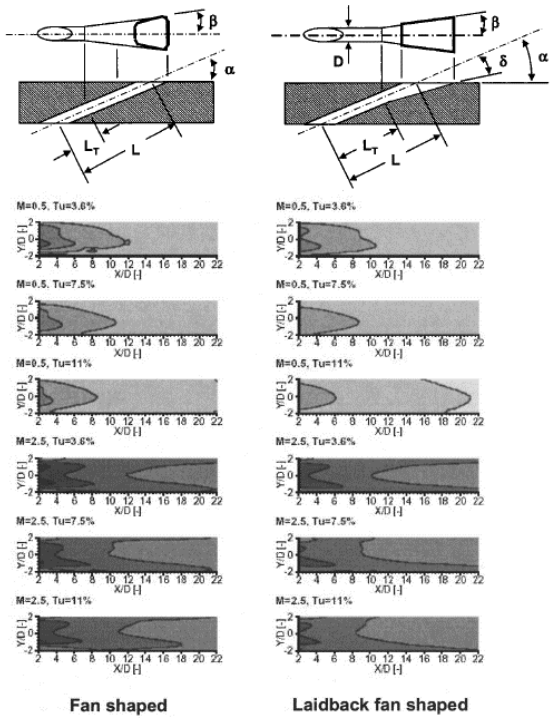

Figure 4.6 – Comparison of geometries for different operating conditions [100]

Ekkad and Han [101] carry out a literature review on the main studies related to film cooling for the last forty years. In the treatment, they focus on the effects related to the different density between the coolant and the main flow. The results obtained by Pedersen et al. [102] show, in Figure 4.7, how for increases in the density ratio there is a first increase in effectiveness for blowing ratio below 0.8 and a subsequent decrease in performance; a different trend is found for fluids with very high density, for which there is a continuous growth as the blowing ratio increases.

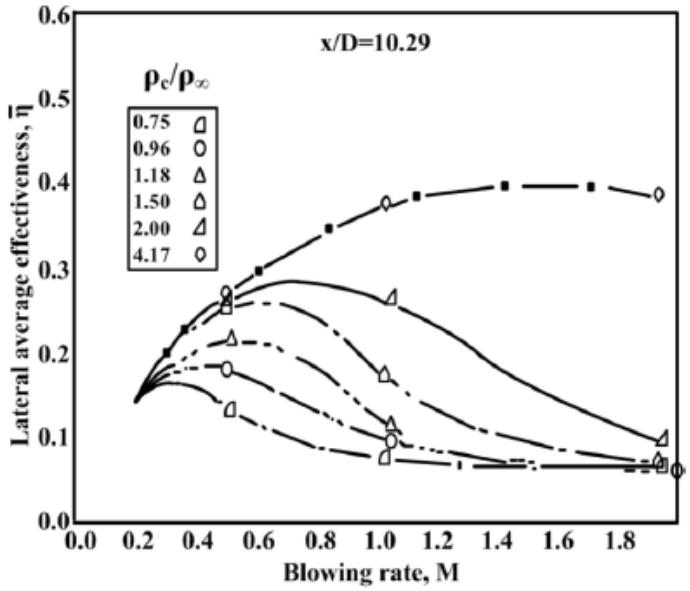

Figure 4.7 – Film cooling effectiveness performance varying density ratio [102]

Over the years, the idea of positioning the film cooling holes with a yaw angle with respect to the axis defined by the hole itself has been considered; the results obtained by Gao et al. [103], showed in Figure 4.8, indicate that the angled configuration ensures greater coverage of the wall of the blade profile.

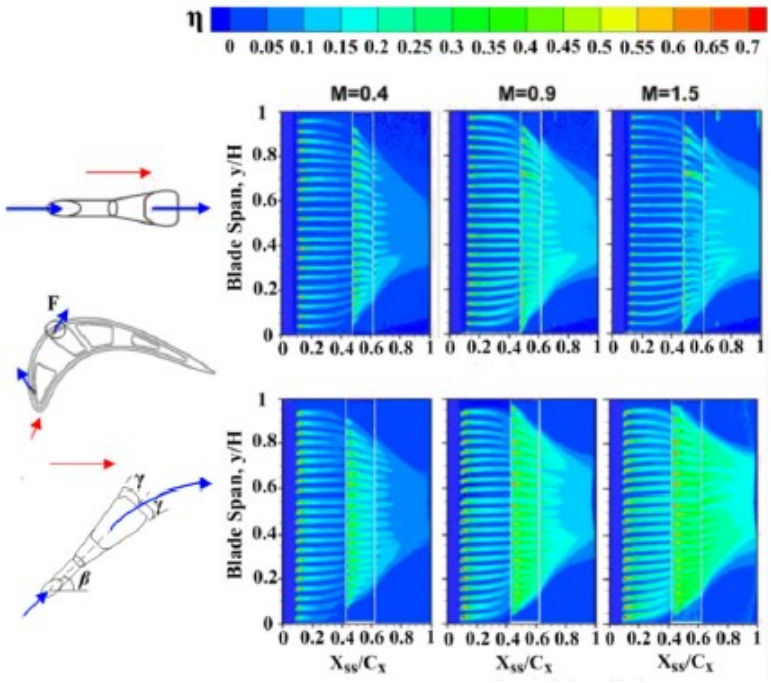

Figure 4.8 – Comparison between straight cooling holes (top) and angled (bottom) [103]

The effects related to the geometry of the shaped hole are evaluated in the work of Gritsch et al. [104] in which the performances of more than fifteen different hole geometries are compared. The authors point out that the geometry has a little influence on the flow coefficient, and therefore, on the pressure drops; as regards the film cooling performance, the parameters evaluated in the study have a relatively low impact, in fact, the authors additionally point out that a greater tolerance on the shaping can be tolerated if the manufacturing process used would require it.

One of the most studied geometrical configurations is the one related to the shaped hole "7-7-7" [105], in which the performances are evaluated with the variation of the blowing ratio. The same authors evaluate the effect of the turbulence level of the main flow in [106] and the effect of the roughness inside the hole [107]. In [108] the blockage due to the thermal barrier coating on the coolant is evaluated; while in [109] the impact of the hole length on film cooling performance is assessed.

In recent years, the impact of the manufacturing process used to produce the hole has been evaluated, as well as how the geometry obtained varies with respect to the design conditions and the respective variations in the performance of the film cooling associated with them.
Bohn and Krewinkel [110] evaluate the performance of the film cooling hole of the real geometry obtained by the EDM manufacturing process compared to the ideal geometric model (Figure 4.9).

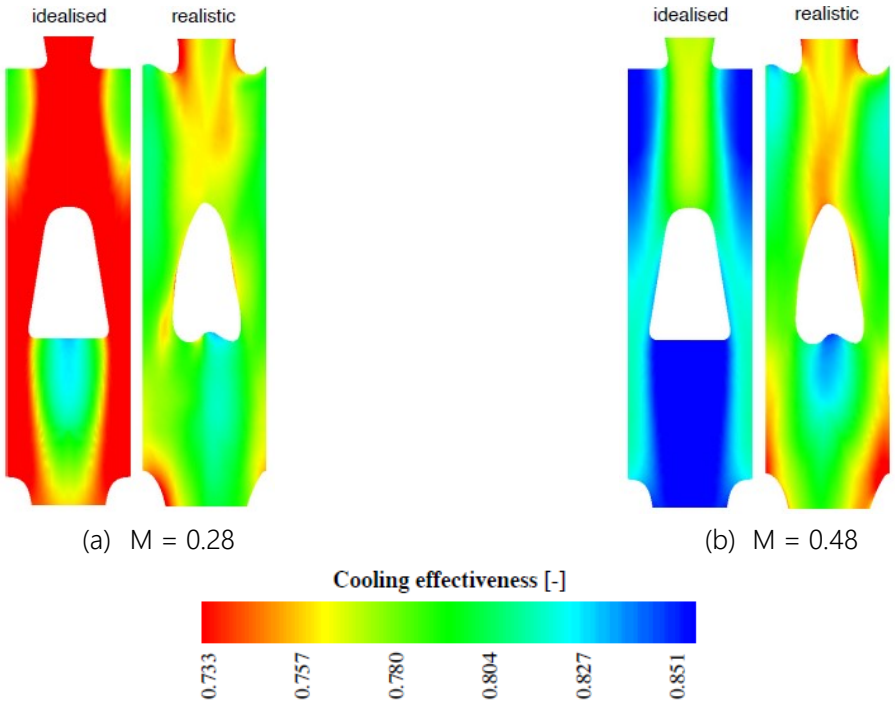

(a) M = 0.28 (b) M = 0.48

Figure 4.9 – Comparison of film cooling performance between ideal and real geometry at different BR [110]

Similar considerations on laser drilling are carried out by Jovanovic et al. [111]; the effects of geometric imperfections produce the same results as surface roughness: at high blowing ratios they can lead to an increase in protection near the hole.

Aghasi et al. [112] carry out a comparison between six different additive manufacturing processes for the production of film cooling holes for various blowing ratio conditions (Figure 4.10); also from this study it emerges that the surface roughness is the main factor influencing the film cooling performance.

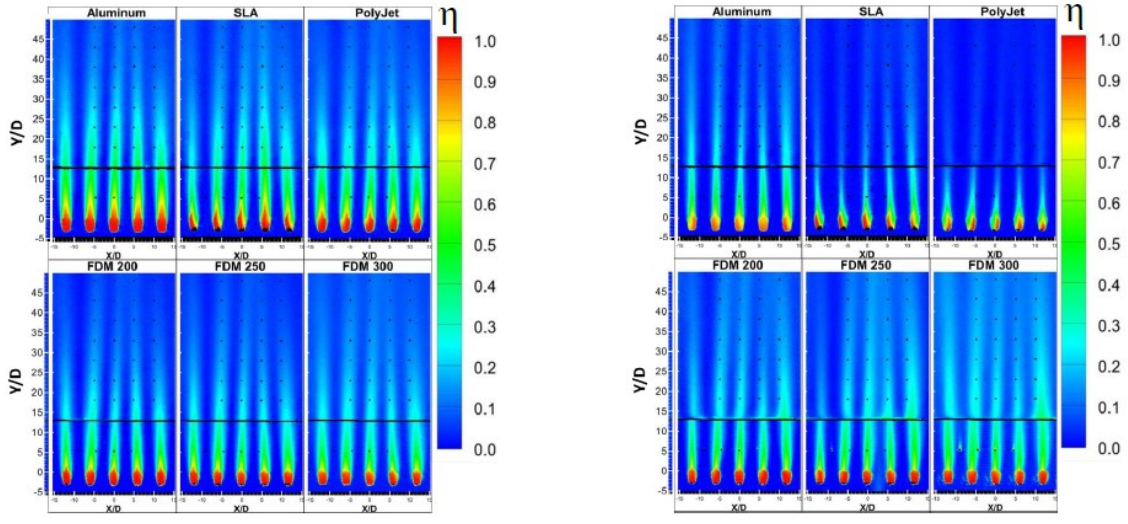

(a) M = 1.5 (b) M = 3.5

Figure 4.10 – Film cooling effectiveness for different additive manufacturing processes [112]

4.2 - Test case

A UQ analysis using computational fluid dynamics is carried out in order to assess the impact of geometric uncertainties on the film cooling effectiveness on a gas turbine vane. The suction side of a second stage turbine stator blade made in additive manufacturing with EDM-made standard shaped holes was considered. The aerodynamic profile considered has already been treated in previous studies; an initial work, both experimental and numerical, was carried out by Bacci et al. [113], in order to validate the conjugated heat transfer procedure between fluid domain, through CFD and solid domain, using FEM analysis from which the temperature distribution on the blade profile is obtained; RANS simulations have been used and the result numerically obtained has been compared with the measured experimental one. In this specific test case, the blade profile did not have a film cooling system but only a smooth internal cooling channel with "U" shaped bend (Figure 4.11).

Figure 4.11 – Internal convective cooling channel [113]

In [113] the CFD analysis was also carried out with the aim of optimizing the test rig, specifically designed to carry out the test campaign. The test rig thus defined, reported in Figure 4.12, was also used to carry out a second study, also carried out by Bacci et al. [114]; for this case film cooling performance is assessed.

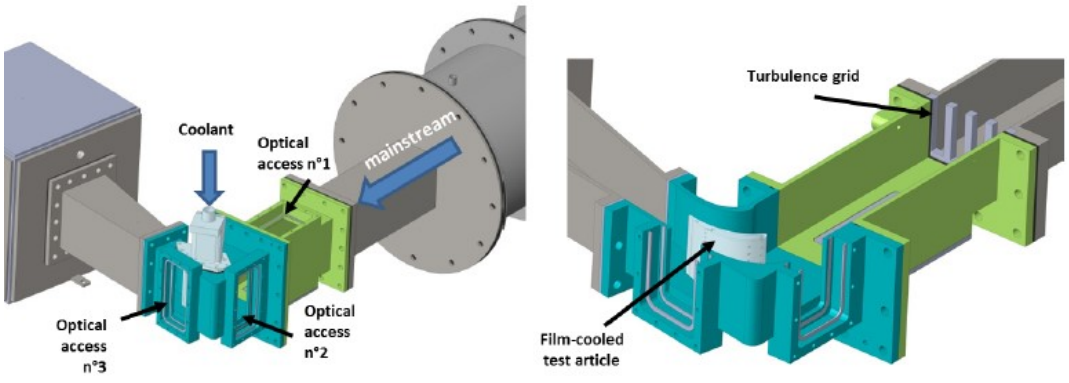

(a) (b)

Figure 4.12 – (a) test rig (b) blade optical accesses details [114]

This experimental test was conducted using the analogy between heat and mass transfer: the effectiveness of the film was measured with PSP (Pressure Sensitive Paint), special fluorescent paints sensitive to the partial pressure of oxygen.

4.2.1 - Mass transfer analogy

The development of the PSP measurement technique has allowed overcoming the problem of conductive heat transfer within the component during adiabatic wall temperature measurements; with this experimental technique the test is truly under adiabatic conditions, therefore, measurement is more accurate.
The physical principle at the base of the analogy is reported in Figure 4.13; in order to ensure the adiabatic wall condition it is necessary to ensure the condition of impenetrability of the wall itself.

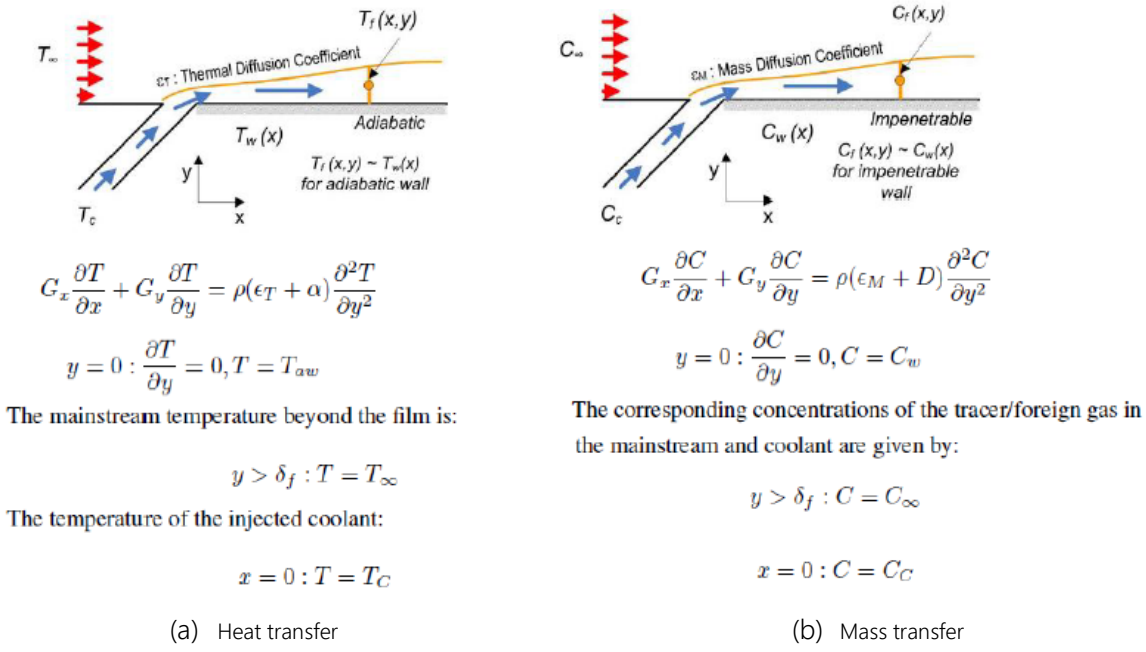

(a) Heat transfer (b) Mass transfer

Figure 4.13 – Analogy between heat (a) and mass transfer (b) [94]

When the Lewis number[4] is equal to 1, the film cooling efficiency is given by Eq. 4-5 and can be calculated using the oxygen concentrations contained in the different flows.

$$\eta = \frac{T_\infty - T_{aw}}{T_\infty - T_c} \equiv \frac{C_w - C_\infty}{C_c - C_\infty} = \frac{C_{O_{2_f}} - C_{O_{2_\infty}}}{C_{O_{2_c}} - C_{O_{2_\infty}}} \qquad \text{Eq. 4-5}$$

The coverage efficiency offered by the film is given by the difference in oxygen concentration contained in the film ($C_{O_{2_f}}$) and that one of the main flow ($C_{O_{2_\infty}}$), in relation to the difference between the oxygen

[4] Lewis number (Le): ratio between thermal diffusion (α) and mass transfer ($\mathcal{D}$) $\Rightarrow Le = \frac{\alpha}{\mathcal{D}}$

concentration in the coolant flow ($C_{O_{2_c}}$) and that one of the main flow; It is also stressed that there is no difference between oxygen concentration and partial pressure of oxygen, as they are identical.
The advantage of using the analogy is the usage of oxygen-sensitive luminescent paints, thanks to which, once the cameras have been calibrated, the oxygen concentration is measured in terms of the light intensity emitted by the painted surfaces. PSP emit luminescent radiation only if excited with ultraviolet radiation; moreover the emitted radiation is in the infrared field, which is why the test rig (Figure 4.14b) needs an exciting lamp and a camera with infrared filter for image recording and subsequent acquisition.

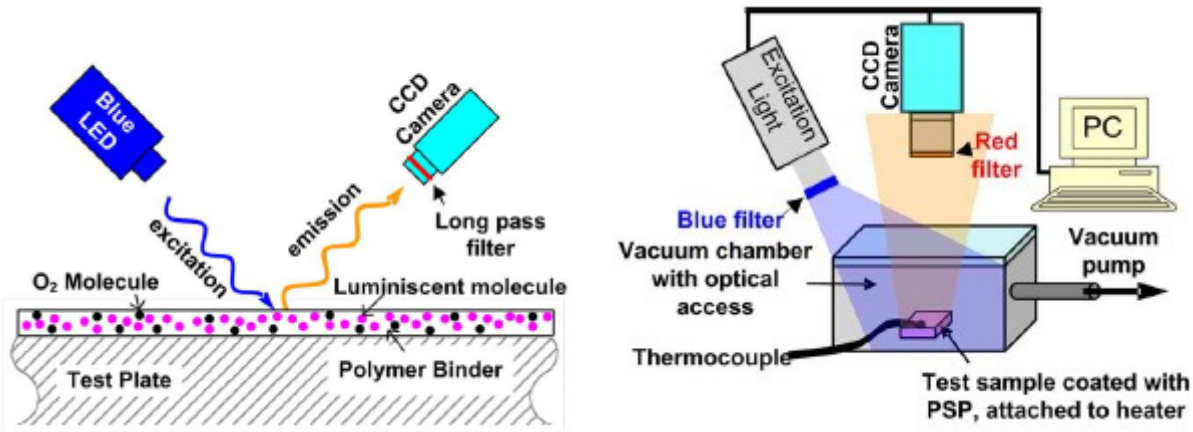

(a) PSP working principles (b) Test rig

Figure 4.14 – PSP measuring technique, principle of operation and components [94]

4.2.2 - Results

In order to validate the numerical procedure carried out subsequently, the experimental results obtained from Bacci's et al. [114] tests are here described and used as a reference for the comparison.
The objective of the experimental study was to measure the film cooling effectiveness through PSP on both the pressure side (PS) and suction side (SS) surfaces and compare it with that measured on a flat plate; the blade geometry on which the experimental tests [114] were carried out is reported in Figure 4.15.

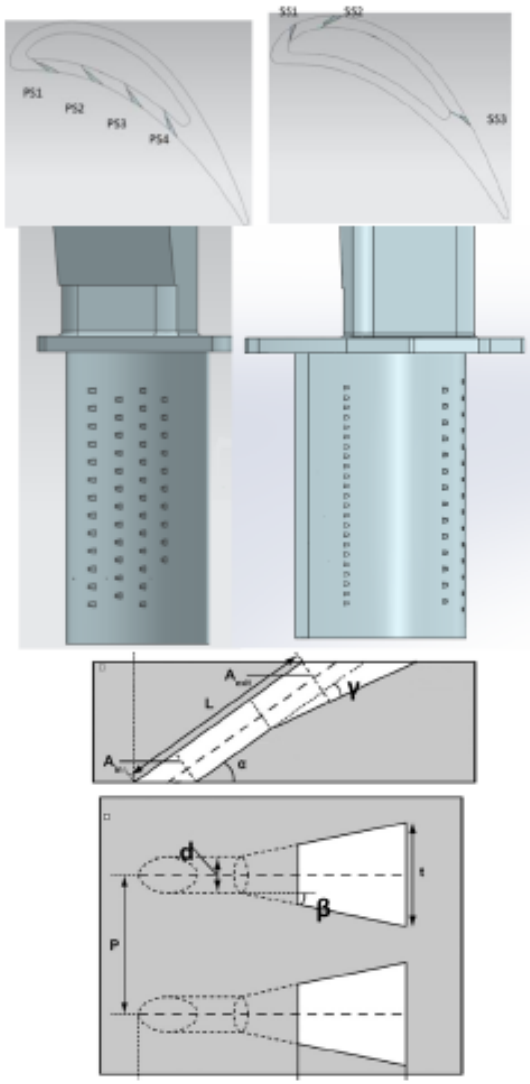

ROW PS1									
d	α	β	γ	s	t	p	n	AR	dist. LE
[mm]	[°]	[°]	[°]	[mm]	[mm]	[mm]			[mm]
0.6	35	10	10	3	2.33	7.80	13	7.05	12

ROW PS2									
d	α	β	γ	s	t	p	n	AR	dist. LE
[mm]	[°]	[°]	[°]	[mm]	[mm]	[mm]			[mm]
0.6	30	10	10	3	2.50	7.80	12	6.95	24

ROW PS3									
d	α	β	γ	s	t	p	n	AR	dist. LE
[mm]	[°]	[°]	[°]	[mm]	[mm]	[mm]			[mm]
0.6	30	10	10	3	2.50	7.80	13	7.04	36

ROW PS4									
d	α	β	γ	s	t	p	n	AR	dist. LE
[mm]	[°]	[°]	[°]	[mm]	[mm]	[mm]			[mm]
0.6	30	10	10	3	2.50	7.80	10	6.96	48

ROW SS1									
d	α	β	γ	s	t	p	n	AR	dist. LE
[mm]	[°]	[°]	[°]	[mm]	[mm]	[mm]			[mm]
0.6	45	10	10	3	2.00	7.30	15	7.23	9.76

ROW SS2									
d	α	β	γ	s	t	p	n	AR	dist. LE
[mm]	[°]	[°]	[°]	[mm]	[mm]	[mm]			[mm]
0.6	42.5	10	10	3	2.20	7.30	14	7.88	21.76

ROW SS3									
d	α	β	γ	s	t	p	n	AR	dist. LE
[mm]	[°]	[°]	[°]	[mm]	[mm]	[mm]			[mm]
0.6	35	10	10	3	1.64	4.40	23	4.07	68.31

Figure 4.15 – Geometrical detail of the vane considered [114]

Several tests were carried out as the blowing ratio varied and for a fixed density ratio; all the conditions tested are summarised as follows Figure 4.16.

CASCADE RIG		**FLAT PLATE**	
Mainstream		**Mainstream**	
Inlet total pressure [Pa]	125000	Inlet total pressure [Pa]	90300
Inlet total temp. [K]	300	Inlet total temp. [K]	300
Mass flow [g/s]	930	Mass flow [g/s]	250
Re inlet [-]	5.62E+05	Re [-]	9E+05
Re throat [-]	9.34E+05		
Mach throat [-]	0.54		
Coolant		**Coolant**	
BR [-]	1, 1.5, 2, 2.5	BR [-]	1, 2
DR [-]	2.5	DR [-]	2.5

Figure 4.16 – Operating conditions [114]

The density ratio $DR = 2.5$ was obtained using a mixture of gases consisting of N_2 and SF_6.

Part of the experimental results obtained by Bacci et al. [114] is reported in Figure 4.17. These represent the one-dimensional profile of the film cooling effectiveness averaged along the radial development of the blade ("spanwise" direction).

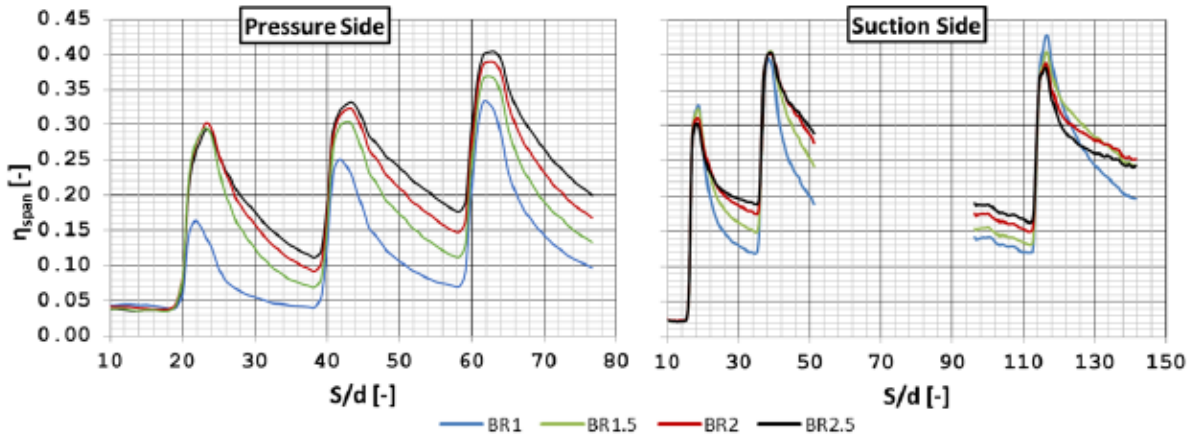

Figure 4.17 – Average film cooling effectiveness 1D profile [114]

The discontinuity in the results concerning the suction side is due to the fact that, given the reciprocal position between the holes of the first and last rows, it was not possible to measure both zones simultaneously with a single camera. Therefore, the results shown for the first two rows and for the last one are not simultaneous: for each condition tested two data acquisitions were carried out: one for the first two rows of holes and the other for the last row.

To obtain the 1D profiles of the film effectiveness, the data obtained from the experimental campaign were processed as follows: each pixel was associated with an effectiveness value based on the colour of the pixel itself, then an average along the "spanwise" direction was carried out in a sector defined by the coordinate h, which is the variable identifying the height of the portion of the vane considered. In particular, for the pressure side, the average is carried out in the interval $h/H = 10 \div 35\%$; while for the suction side the average was carried out in the portion defined by the range $h/H = 35 \div 65\%$.

4.3 - Numerical methodology

The first part of the activity focuses on the validation of a numerical procedure to be used as a baseline for the UQ analysis. A simulation using the analogy between heat and mass transfer was then carried out through the CFD software ANSYS Fluent. For the purposes of the study, it has been decided to take the film cooling effectiveness as a measure only for the test concerning the "suction side". The numerical work was based on further experimental results obtained by Bacci, similar to those carried out in [114], on behalf of an industrial partner, in which the CO_2 is used as a coolant. Eventually, the numerical approach will be based on this particular test case, so the numerical analysis will only cover the geometric parameters of the experimental case [114]; the characteristics of the holes taken into consideration are provided in Figure 4.15 and synthetically reproduced in Figure 4.18.

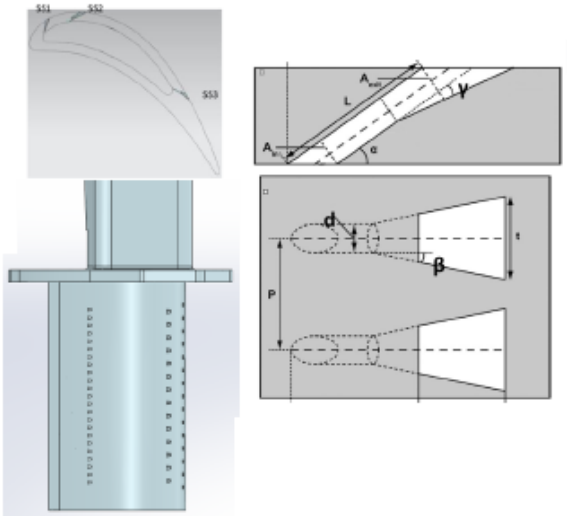

ROW SS1									
d	α	β	γ	s	t	p	n	AR	dist. LE
[mm]	[°]	[°]	[°]	[mm]	[mm]	[mm]			[mm]
0.6	45	10	10	3	2.00	7.30	15	7.23	9.76

ROW SS2									
d	α	β	γ	s	t	p	n	AR	dist. LE
[mm]	[°]	[°]	[°]	[mm]	[mm]	[mm]			[mm]
0.6	42.5	10	10	3	2.20	7.30	14	7.88	21.76

ROW SS3									
d	α	β	γ	s	t	p	n	AR	dist. LE
[mm]	[°]	[°]	[°]	[mm]	[mm]	[mm]			[mm]
0.6	35	10	10	3	1.64	4.40	23	4.07	68.31

Figure 4.18 – Geometric details of the shaped holes

In order to perform an analysis as faithful as possible to the experimental tests, the numerical study was carried out using the analogy between heat and mass transfer and a two-fluid air/carbon dioxide approach was adopted. Given the purpose of numerical activity, i.e. to carry out an evaluation of the propagation of uncertainties within the numerical code, it was decided to consider only one operating condition for the flow, i.e. the analyses were carried out for a single value of blowing ratio, in particular the study was carried out with a $BR = 1$. The results of the corresponding experimental test condition were used to make the comparison. It is emphasized that working in analogy, to derive the film cooling effectiveness, as introduced by Eq. 4-5, it is sufficient to calculate the carbon dioxide concentration on the surface wall under investigation. The fluid domain was taken from [114], and it is shown in Figure 4.19.

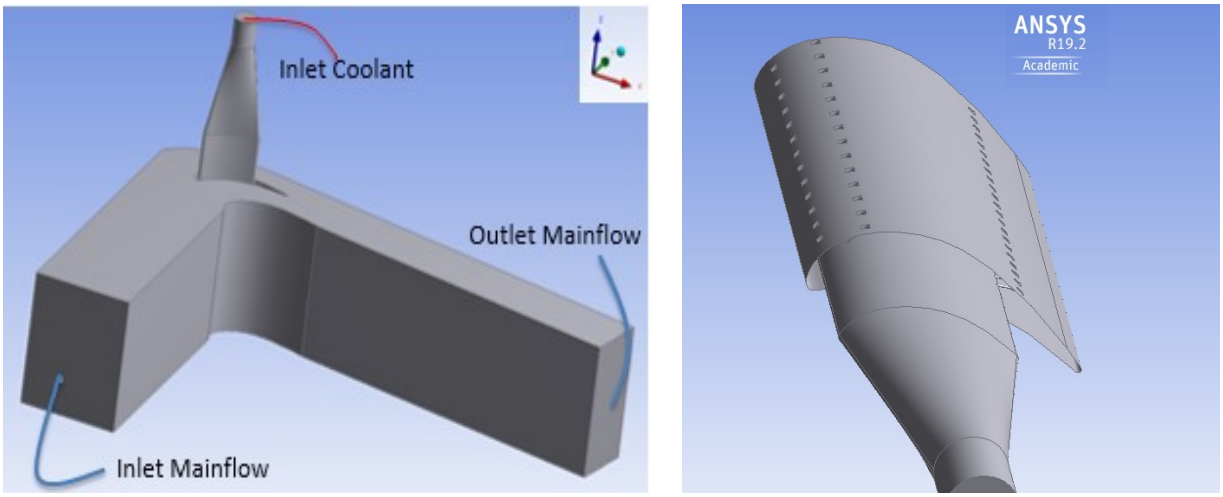

(a) (b)

Figure 4.19 – (a) Fluid domain (b) internal coolant channel

Considering that the UQ analysis requires a much greater computational effort than a classical deterministic approach, it was decided to reduce the fluid domain to save, where possible, computational resources. As

carried out also in [70], [71] and [73], the initial geometry has been reduced to a portion of the blade, while maintaining the real curvature of the surfaces. As for the works mentioned above, the fluid domain has been reduced to the minimum periodic geometry: this has allowed minimizing the volume being studied. The number of holes in the three rows of holes, reported in Figure 4.18, did not allow this reduction, because the number of holes in the first two rows (with the same pitch) and the last are prime numbers among each other; to overcome this problem it was decided to reduce the pitch between the holes in the third row by the minimum allowed in order to obtain a periodic geometry: two holes in the third row were brought closer together and the pitch was reduced by 15% with respect to the real geometry. The resulting portion of the aerodynamic profile thus obtained has a radial development $h/H = 7.3\%$ with respect to the real geometry. The domain is represented in Figure 4.20. From the figure it is clear that the coolant supply duct has a radial development double than the one considered for the aerodynamic profile: this configuration allows a better development of the flow starting from the inlet and consequently more uniform conditions; this choice will be further explained in the following chapter specifically dedicated to numerical setup.

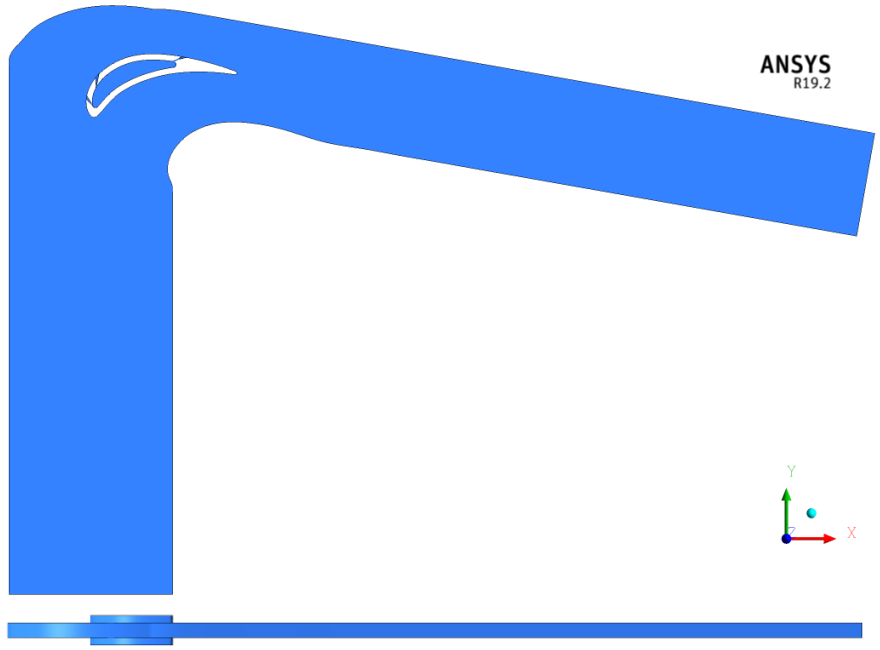

Figure 4.20 – Resulting portion of the fluid domain considered $h/H = 7.3\%$

Given the high distance of the aerodynamic profile with respect to the inlet and outlet sections, it was decided to further reduce the fluid domain by bringing the inlet and outlet of the main flow closer to the blade. By carrying out this modification, the decay of the total pressure was taken into account by applying the correct pressures, obtained from an analysis previously carried out on the initial fluid domain. The reduction of the length of the inlet and of the outlet channel is shown in Figure 4.21; in this case, it is compared with the initial geometry; the reduced geometry thus obtained was used to carry out the uncertainty quantification analysis.

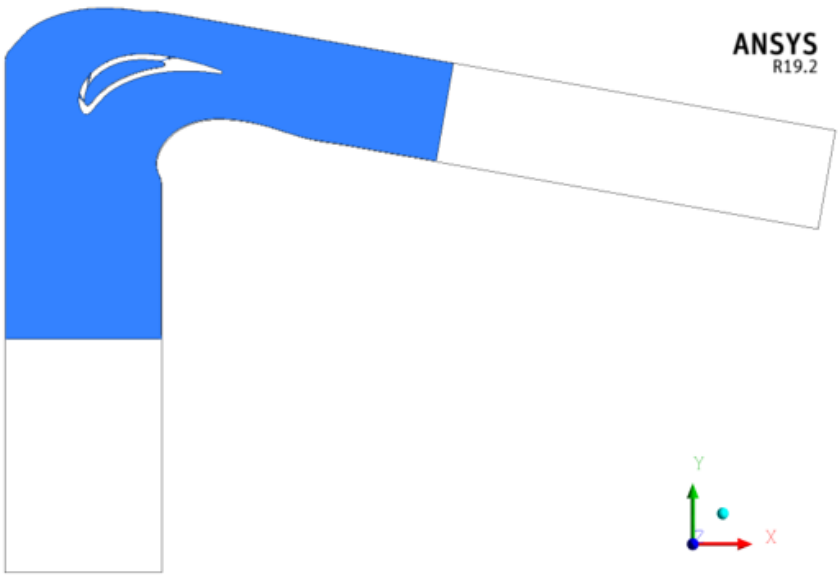

Figure 4.21 – Reduced fluid domain adopted for the UQ analysis

The validation of this procedure will be based on the film cooling effectiveness; a comparison will be made with the data experimentally obtained and will show the changes in the efficiency due to the reduction of the fluid domain, which depends on the reduced pitch in the third row. All the results just introduced will be shown in the next chapter, after describing the numerical setup.

4.3.1 - Numerical setup

Both steady and unsteady simulations are carried out: the first one using a RANS approach and explained in this chapter, the second one using a hybrid LES-RANS approach and explained in chapter 4.3.3 -. Since the purpose of the study is to carry out an uncertainty quantification analysis, the numerical investigation for the UQ study was conducted with a RANS approach ($Reynolds\ Averaged\ Navier-Stokes\ equation$); this approach gives, as a result, the variation of the average quantities, as each parameter in the study is averaged over time and the turbulence is only modelled through a turbulence model. This approach has been adopted because it requires a sensible lower computational effort than LES approaches ($Large\ Eddy\ Simulation$), which solving almost 70-80% of the turbulence length scale require a huge computational effort. In terms of results, a LES approach could represents the physical problem with a higher accuracy [115], but for the scope of the analysis (the UQ) and based also on the results provided soon it will be clear that the RANS approach is sufficient enough to accurately represent the experimental test.
The turbulence model used was the $k-\omega\ SST$ that guarantees robust behaviour both on the wall side and in the central zones of the fluid domain [3]; this model is the most adopted in the literature for heat transfer applications in which the effects of the behaviour of the flow on the wall are dominant [116], [117], [118]. As far as the spatial discretization is concerned, an approximation to the second order of all the quantities has been imposed. For the boundary conditions it has been chosen to impose a total pressure on the inlet of

both the main flow and the coolant flow, and static pressure at the outlet of the fluid domain; the conditions imposed are summarised in Table 4.1

Table 4.1 – Boundary conditions

$\boldsymbol{Inlet\ Mainflow}$	$\boldsymbol{P_0 = 135770Pa}$	$\boldsymbol{T_0 = 286.15K}$
$\boldsymbol{Outlet\ Mainflow}$	$\boldsymbol{P = 123279Pa}$	
$\boldsymbol{Inlet\ Coolant}$	$\boldsymbol{P_0 = 144760Pa}$	$\boldsymbol{T_0 = 286.15K}$

It was decided to impose this type of condition, as the purpose of the study was to evaluate the influence of the geometric uncertainties of the holes on the film cooling effectiveness, on the discharge coefficient and on the blowing ratio; it is also the most representative condition of the actual operation in the machine. Moreover, this type of boundary condition allowed to avoid further preliminary studies: since the fluid domain was reduced to a single blade portion, setting the coolant flow rate would have required a non-trivial and certainly not productive study thinking about geometrical discrepancies on the holes. Instead, by setting the pressure value at the inlet of the coolant supply duct, a most confident zone, the calculation of the correct mass flow is carried out internally by the solver during the analysis. From the analysis of the initial and complete fluid domain it was obtained the confirmation that the coolant supply duct acts a plenum, therefore, it is admissible to set the same total pressure on the whole section considered.
As far as the volume supply of coolant is concerned, it can be seen from Figure 4.20 that this has a greater thickness than the aerodynamic profile considered, in fact, an additional thickness of $p/2$ on both sides has been imposed. It was decided to study this configuration because it was preferred not to impose the conditions of periodicity in this area: the conditions imposed for the plenum were all "wall" unless the inlet section of CO_2: these properties are more representative of actual operation than periodicity properties. An enlarged domain with respect to that of the aerodynamic profile was therefore considered to ensure a coolant flow developed downstream of the inlet section before entering the film cooling holes. A detail of the inlet area of coolant flow and of the portion of the aerodynamic profile studied is reported in Figure 4.22.

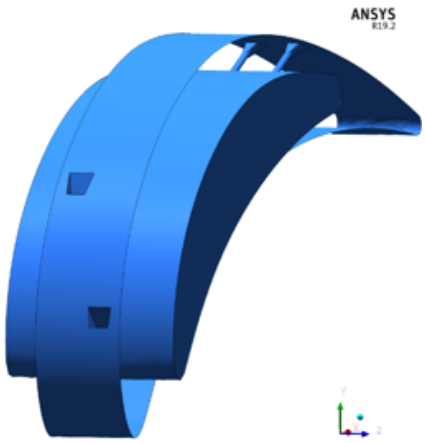

Figure 4.22 – Inlet plenum for CO_2 and the portion of the aerodynamic profile considered in the analysis

All boundary conditions imposed on the various sections of the domain are listed in Figure 4.23, where only one of the two surfaces with periodicity conditions is reported to make the image clearer.

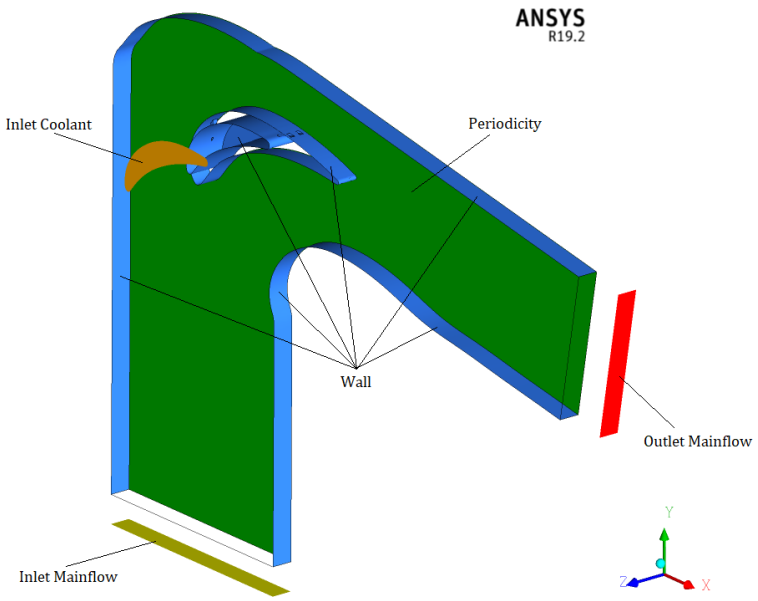

Figure 4.23 – Boundary conditions imposed form the simulation

The domain was discretized with tetrahedral elements; ten prismatic layers of elements were arranged on the wall; the general dimension of the elements was set to $8 \cdot 10^{-3} mm$; only on the "suction side" surface finer elements were placed with the sizing of $5 \cdot 10^{-4} mm$ in order to better reproduce the objective zone. A sensitivity study was carried out on the calculation grid: three meshes were compared, in which the size of the elements was varied by a scale factor of 1.5; in this way, a coarser grid and a finer one were obtained. The y^+ is approximately 1 for the coarse mesh and well below 1 for the fine mesh. The characteristics in terms on number of elements of the three meshes are reported in Table 4.2.

Table 4.2 – Mesh sensitivity details

	Coarse	***Medium***	***Fine***
Elements	2.06 M	3.18 M	4.33 M
Nodes	635 k	972 k	1.33 M

The comparison between the results obtained with the different calculation grids is shown in Figure 4.24 below; the term of comparison used was the one-dimensional profile of the film cooling effectiveness averaged along the "spanwise" direction.

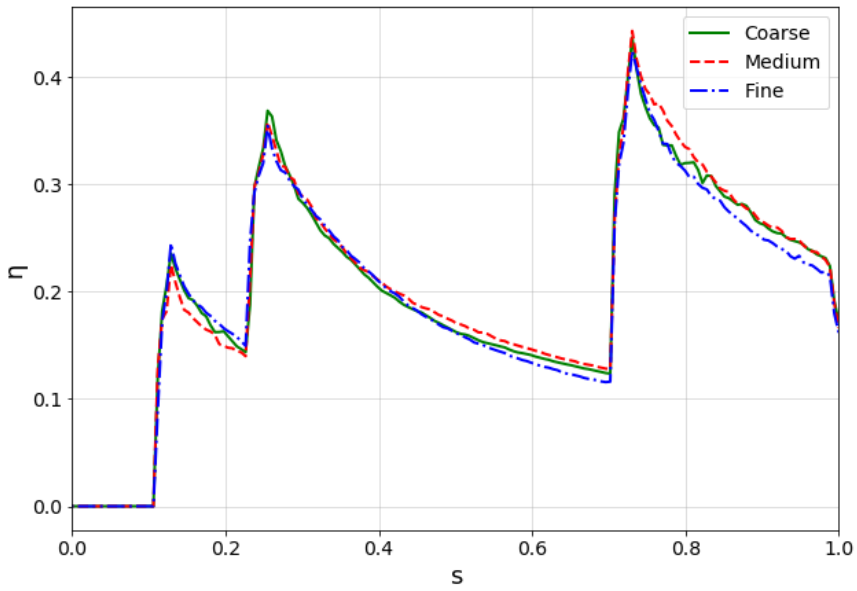

Figure 4.24 – Mesh sensitivity results

The comparison of the results shows that the calculation grid does not have a great influence, although the coarse grid produces results more similar to the fine grid, it was decided to use the mesh medium as it guaranteed a good compromise between computational costs and geometric discretization. As can be observed in Figure 4.25 the coarse calculation grid is not able to represent the holes correctly; the medium mesh, on the other hand, despite the smaller number of elements compared to the fine one, does not present any particular criticality in approximating the geometry.

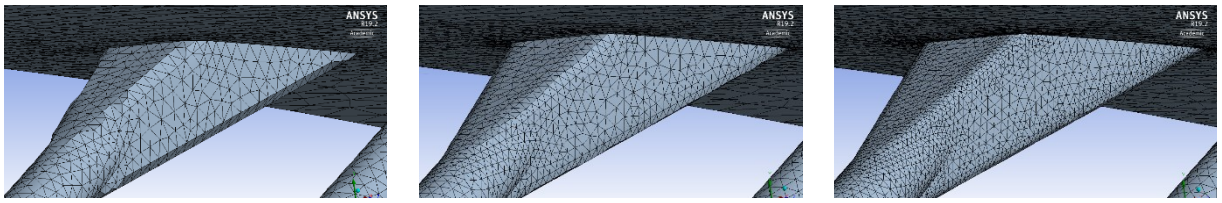

(a) Coarse (b) Medium (c) Fine

Figure 4.25 – Mesh details

4.3.2 - Results validation

In this chapter, the results of this first numerical activity are reported which are the basis for the uncertainty quantification analysis. The results obtained are compared with the experimental data in order to validate the procedure implemented and proceed with the further objective of the study.

The results of the numerical analysis have been appropriately processed in order to carry out the correct comparison with the experimental data. A special macro-function has been created to allow the export of the values of the CO_2 concentration on the blade portion under investigation; this area was discretized by means of 50 two-dimensional profiles. The efficiency values obtained are not ordered with respect to the streamwise direction of the blade, so they were processed through a Python code, written specifically to

perform the following actions: sort the data vectors of each individual profile with respect to the non-dimensional abscissa, interpolate them in order to obtain a common dimension to all the vectors, and finally, perform an average in the spanwise direction to find, in a manner similar to what was done in the experimental activity of Bacci et al. [100], the one-dimensional profile of the film cooling effectiveness.
First of all, it was preferred to show the numerical results obtained considering the whole geometry, reported in Figure 4.19, which is the same as in the experimental test case.
The comparison between the numerical and experimental results are reported in Figure 4.26.

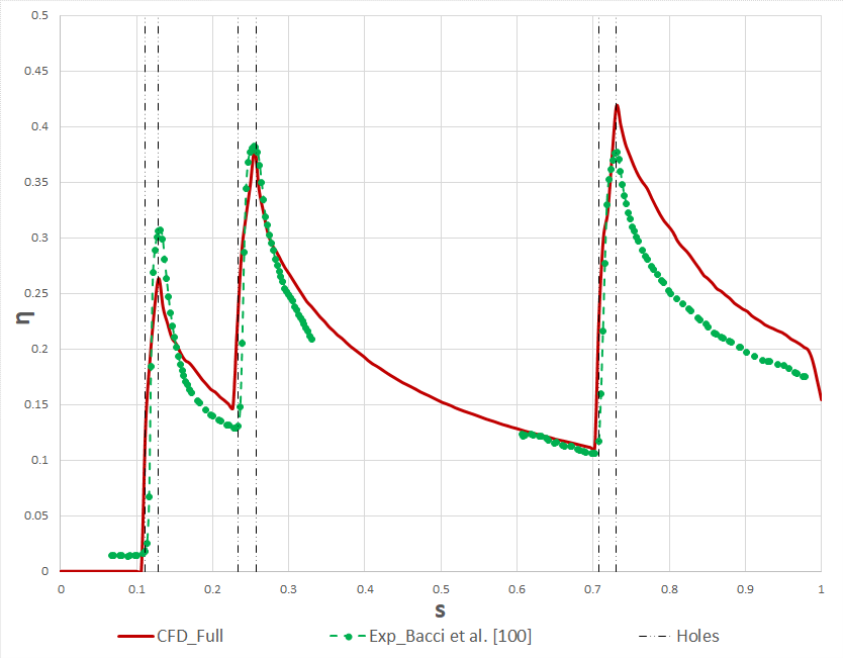

Figure 4.26 – Comparison between numerical and experimental results of Bacci et al. [114]

From the comparison, it is clear that the first two holes have a good agreement with the experimental data while for the last row of holes the numerical data overestimates by 5-10% the effectiveness measured experimentally by Bacci et al. [114]. Near the exit of the holes it can be noticed how the experimental result presents a peak with a more gentle variation in slope: this is due to the process that has undergone the data acquired in the laboratory. In fact, in the image obtained by the camera, the areas affected by the exit sections of the holes have the effectiveness very close to the unit, as there is the maximum concentration of CO_2. Near the leading edge of the hole there are high values of effectiveness, therefore, there will be a high number of pixels affected by a high concentration of coolant so that the change of slope immediately after the peak will be less intense. In the numerical analysis the opposite happens: since the data are measured on the nodes of the elements of the various profiles and since the area inside the hole does not belong to the blade profile, in this area there will be a null concentration of CO_2. This aspect involves a strong discontinuity of effectiveness at the exit edge of the hole, which in turn causes a much more intense variation in slope, with the peak of η located right at the end of the film cooling hole. For the data processing carried out, an interpolation grid is defined and points are formed within the area inherent in the holes due to the interpolation of the data of the various two-dimensional profiles made necessary to carry out the "spanwise" average on the aerodynamic profile and in order to have data vectors of the same size and then average

the values of CO_2 with the same non-dimensional abscissa. For this reason the values numerically obtained that define the rising line are not properly significant: because they do not derive from the CFD simulation carried out but from the post-process suffered by the data.

From the comparison it results that a numerical approach based on the analogy between heat and mass transfer produces reliable results, except for an overestimation of 10% in the last row of holes under examination; this overestimation, however, is considered attributable to the $RANS$ approach used rather than the methodology itself.

The following figure shows the comparison with the results obtained using the reduced geometry using the periodicity condition.

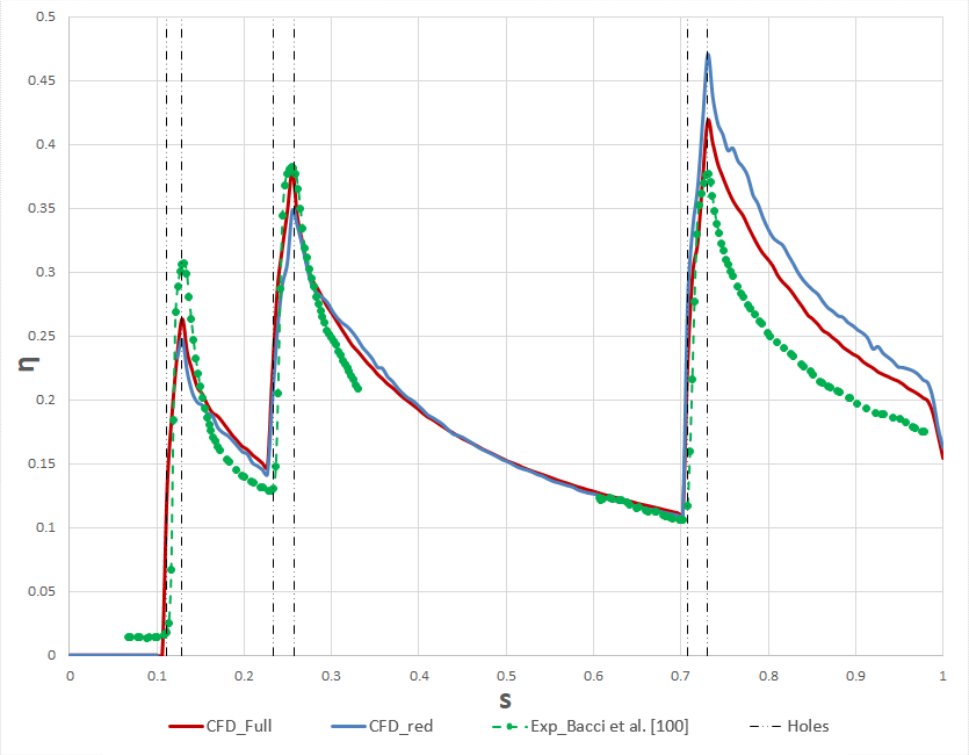

Figure 4.27 – Reduced domain results validation

Compared to the complete geometry, the reduced one has a greater efficiency downstream of the third row of holes: this was predictable, having slightly reduced the pitch between the holes in order to exploit the periodicity. This geometric modification led to an increase of about 5%, compared to the numerical conditions obtained with the real geometry.

Focusing attention on the areas near the beginning of the holes it is clear how the numerical study produces an increase in effectiveness. This effect is clearly visible from the maps of effectiveness of Figure 4.28.

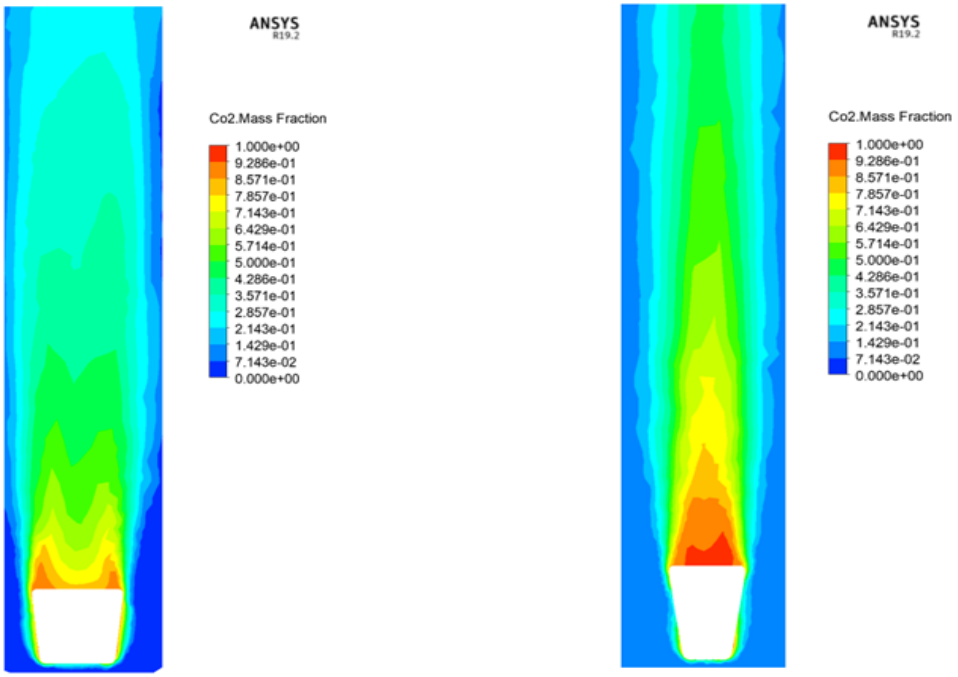

(a) First row (b) Third row

Figure 4.28 – Details of film cooling effectiveness maps

The behaviour highlighted could be due to the turbulence, which causes a return of flow upstream, but in this case, it is probably due to a diffusion of the numerical solution attributable to the sparse calculation grid and to the RANS approach adopted, which, however, showed a good approximation of the experimental data.

From Figure 4.28 it is evident the dual-horn conformation of the jet coming out of the first row of holes and how this phenomenon does not occur in the last row; this behaviour is verified by the maps obtained by Bacci experimentally. The comparison is reported in Figure 4.29. It should be noted that also for the experiments, in order to calculate the film cooling effectiveness, an average between 35% and 65% of the "span" of the blade is performed; for this reason, the boundary effects and the flow migration towards the midspan going to the trailing edge are not included in the one-dimensional profile of film cooling effectiveness. However, they are actually present and clearly visible in Figure 4.29 and they also can be found in the numerical analysis for the complete geometry. Comparing the results obtained it can be seen how a RANS approach can predict the real configuration of the film coming jet out of the holes, both for the first rows in which the dual-horn shape is confirmed and at the exit from the third hole in which this configuration does not occur.

For completeness, in Figure 4.30 the maps of the Mach number inside the film cooling holes are also shown. It can be seen that at the end of the cylindrical section area of the hole flow separation zones are formed, with greater intensity for the first two rows of holes. These zones, which are also supposed to be present in the experiments, however, are the results of the particular shape of the hole and of the inlet section and for this particular boundary conditions cannot be avoided.

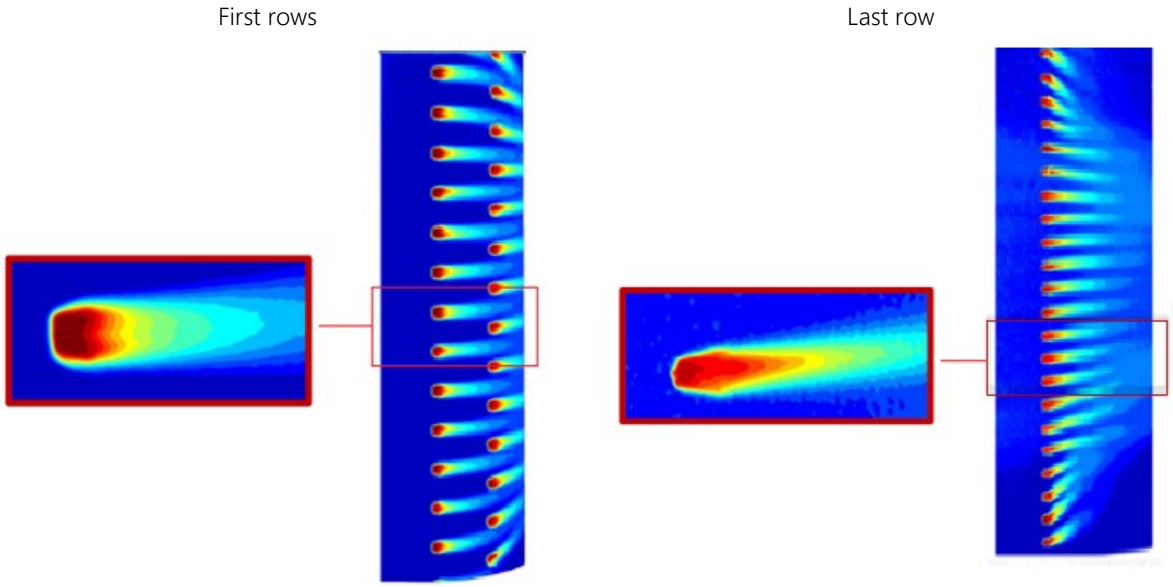

(a) Experimental results

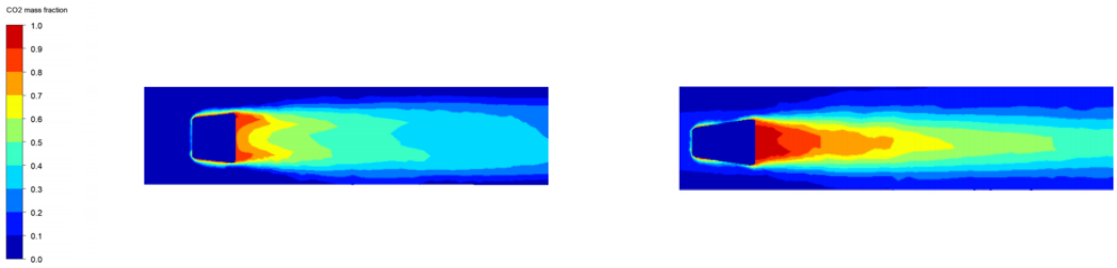

(b) Numerical results

Figure 4.29 – Comparison between experimental (a) and numerical results (b)

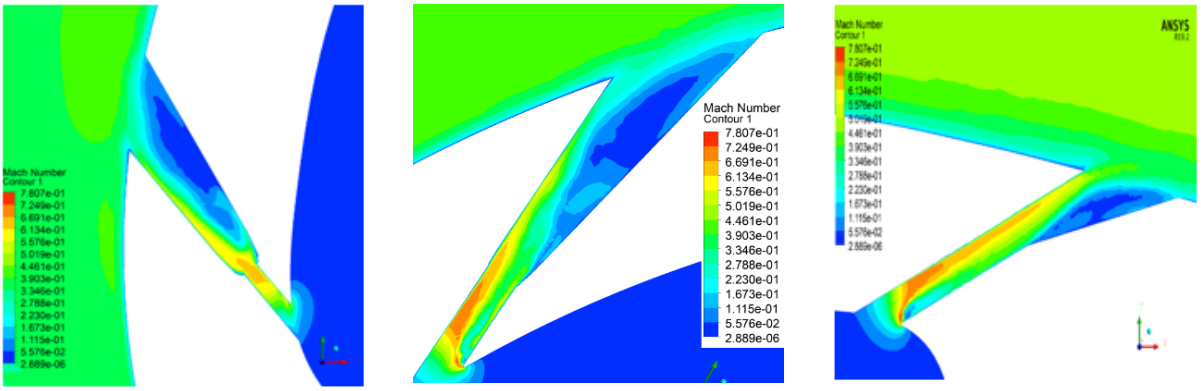

(a) First row (b) Second row (c) Third row

Figure 4.30 – Mach number inside the holes

4.3.3 - Unsteady approach

As far as the validation of the results is concerned, an unsteady approach is also adopted in order to show the capability of this approach for modelling the film cooling effect. It is beyond the scope of this activity to explain in detail all the governing equations relating to an unsteady CFD approach. Instead, an exploitation of this methodology with particular attention to the setup and the results will be provided in this chapter. It also stressed that this methodology could not be used for the uncertainty quantification analysis carried out later due to the high computational cost required (almost 10 times greater than a RANS approach).
In previous chapters, it is clear how a RANS approach could accurately approximate the experimental results. However, it is also clear that film cooling is a high unsteady phenomenon, especially near the exit of the hole. For this reason, an LES approach could probably be the best choice in order to obtain more reasonable results. Without entering too much into details, a few explanations of the unsteady procedure is given here. While RANS simulations solve the Navier-Stokes equations conveniently time-averaged and use turbulence models in order to "model" the turbulence, a LES approach is capable of simulating the larger-scale vortices (up to 80-90%, depending on the mesh sizing), modelling the turbulence only at the smaller scales. In order to capture the different scale sizes, a finer grid is usually required: this implies an increase in the computational cost required.
ANSYS Fluent v19.2 was used for the analysis. A particular simulation setup was imposed: the Stress-Blended Eddy Simulation (SBES) option. It should be highlighted that a wall-resolved LES approach would be unfeasible, due to the very large number of elements required to properly reproduce the boundary layer. Therefore, a hybrid RANS-LES approach has been employed. Such an approach has been proposed by Frank and Menter [119] as further development of the Detached Eddy Simulation (DES) model. As other hybrid models, it is based on a dynamic blend between RANS and LES closures for the eddy viscosity [120]:

$$v_t^{SBES} = f_s \cdot v_t^{RANS} + (1 - f_s) \cdot v_t^{LES} \qquad \text{Eq. 4-6}$$

The shielding function is adopted to prevent the use of LES subgrid model to unresolved boundary layers, where instead a RANS approach is imposed. Thus, a lower mesh resolution is demanded, allowing to consistently reduce the required computational effort. Regarding the RANS approach, a $k-\omega\ SST$ turbulence model was adopted, while for the unsteady approach a dynamic Smagorinsky subgrid-scale model was employed [121], [122], [123]. The advantage of this method is the amount of computational resources saved using a RANS approach in low-interest zone and a LES approach in high-interest zone. Therefore, the mesh was built appropriately using a high refinement in the vicinity of the hole and along the suction side, whereas far away from the blade profile a mesh similar to the one adopted for the previous simulation was used.
Regarding the specific test case, a new mesh sensitivity was required in order to properly adopt the new approach (including an unsteady test using the same grid used for the RANS simulation). The final selected grid features approximately 32 million elements. The general size remained the same as the one used for the RANS approach; however, 40 prismatic layers around the blade surface and inside the hole were adopted, instead of 10 used for the RANS simulation, in order to capture smaller scale turbulences. Moreover, a size of $1 \cdot 10^{-4} mm$ instead of $5 \cdot 10^{-4} mm$ was adopted for the refinement on the suction side of the blade.

Furthermore, a different layout and local bodies of influence were adopted in order to increase the mesh quality while keeping the computational cost acceptable. The medium grid selected for the RANS simulations has around 3 million whereas for the unsteady approach it ended up with 32 million elements (Figure 4.31). The unsteady simulation required approximately 13.000 CPU Hours in order to converge, in contrast with the 100 CPU Hours required by the RANS approach. It is clear also from this point of view that the uncertainty quantification could not be performed with this approach.

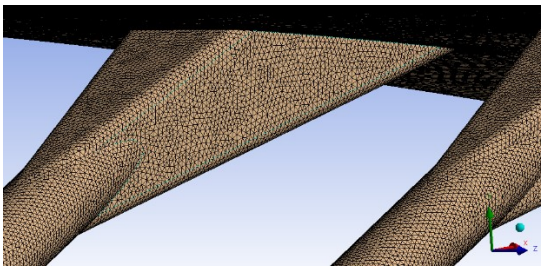

Figure 4.31 – 32 million elements mesh for unsteady calculation

An important thing to notice is the shielding function, defined by Fluent as the zone in which it solves for RANS equations (1) and where it solves for LES equations (0). Details of this could be found in Figure 4.32.

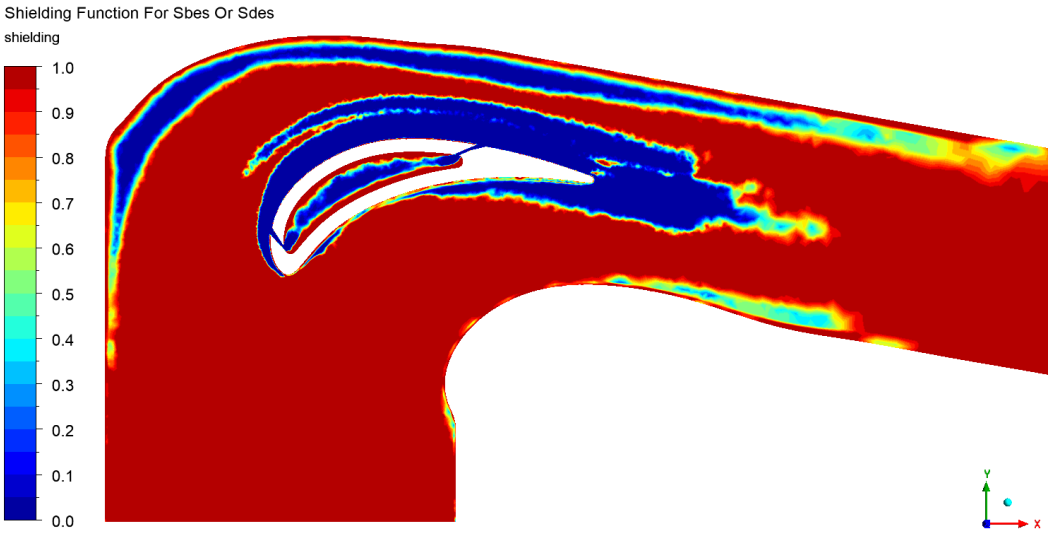

Figure 4.32 – Shielding function for SBES simulation

It is important to notice that, even if the majority of the zones are solved with RANS approach, especially the initial part, this does not affect the unsteady solutions obtained in the zone of interest, the suction side. In fact, a sensitivity analysis to the inlet turbulence intensity specified by the user was conducted and the results show, in accordance also to the previous RANS approach, how this parameter had a low effect on the film cooling effectiveness for this particular test case. This is a film cooling application and the first row of hole, indeed, is very close to the LE of the blade, causing a complete mixing of the flow immediately after the hole. Figure 4.33 provides the results for the instantaneous values of the CO_2 mass fraction for a plane that cut row 1 and 3 (a) and for the suction side (b). It is clearly visible the unsteady that occurs at the exit of the holes and which propagate through the surface moving towards the trailing edge of the blade.

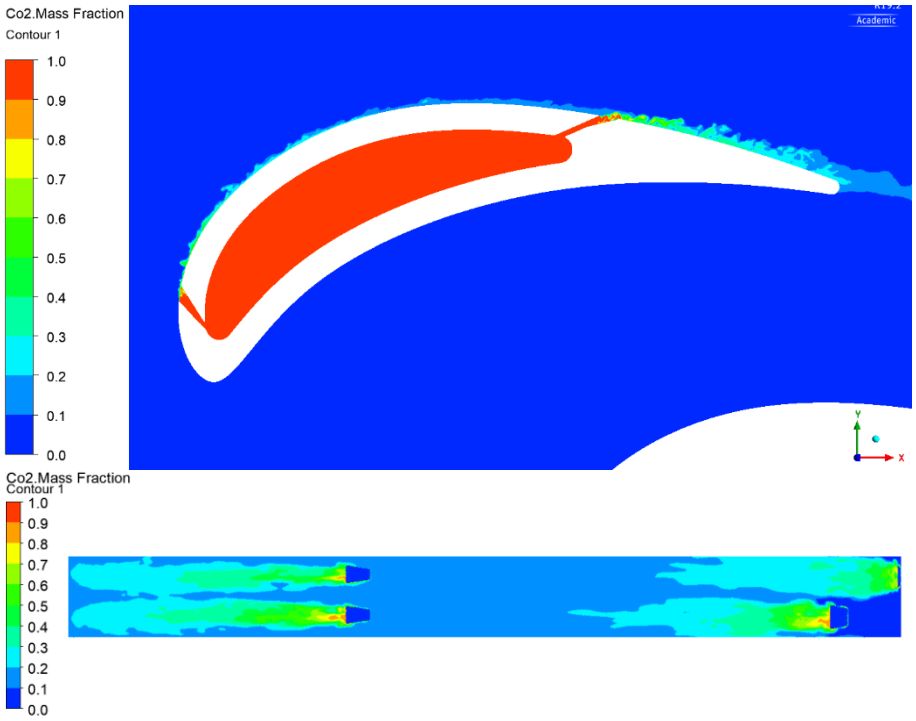

Figure 4.33 – Instantaneous CO_2 mass fraction a) cross-sectional view 1st and 3rd hole b) suction side

Figure 4.34 provides the same results but in average terms: here results are more similar to the one obtained with the full RANS approach. It is decided to show only the CO_2 mass fraction (equivalent to film cooling effectiveness) on the suction side for the sake of clarity.

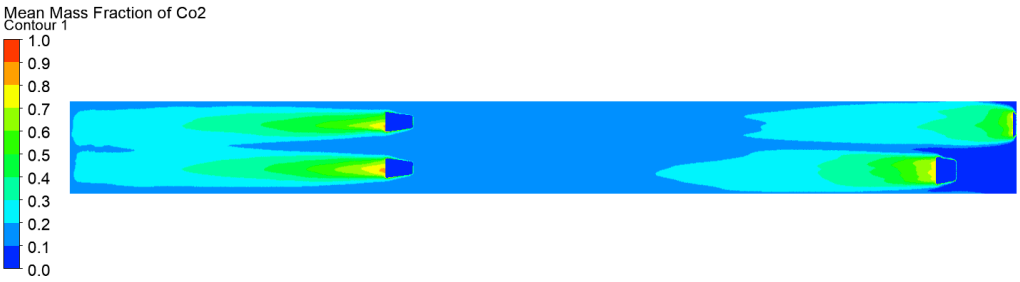

Figure 4.34 – Average CO_2 mass fraction for the suction side

As far as the result is concerned, Figure 4.35 shows the average film cooling effectiveness profile on the suction side for different approaches: the unsteady solution with the 32 million elements grid (SBES), the unsteady solution with the same mesh of the RANS approach (SBES_COARSE), the RANS approach and the experimental results. The first thing to notice is the fact the, obviously, unsteady approaches require finer meshes in order to better capture and solve turbulence with smaller scale. Here, results are not as good as expected: in fact, the SBES simulation, if compared to the RANS approach, has a closer agreement with the experiments in the last part of the blade, after the third row of holes, and for the peaks value, especially the ones for the 2nd and the 3rd row. However, the middle zone between the 2nd and the 3rd row has a slight overestimation with respect to both experiments and RANS. Moreover, the rate of decay immediately after

the hole does not follow precisely the experimental trend. This could be related to this particular test case and to the fact that only three rows of holes are widely distributed along the blade surface. In fact, with this configuration and with low blowing ratio, the medium-low turbulence mixing after the hole and the probably high isotropy of the turbulence could justify the worthy RANS results and the small differences between RANS and SBES approach.

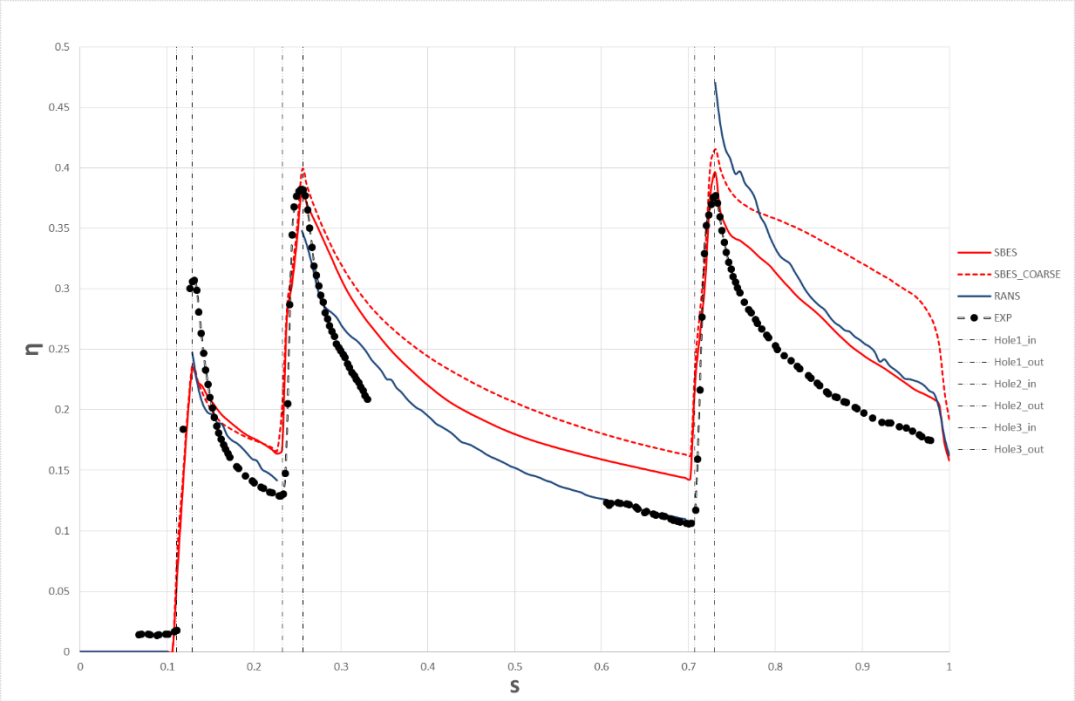

Figure 4.35 – Average film cooling effectiveness profiles on the suction side

It is reminded that this is a hybrid RANS-LES approach and not a full LES simulation, which would have required additional computational resources and, perhaps, would have had an even better agreement in average terms.

At the end of this chapter, it should be clear that, given the objectives of the thesis, the RANS approach is adopted for the uncertainty quantification analysis to be carried out. The huge additional amount of computational resources required by the SBES approach, looking at the results, on the one hand, does not justify this approach, and on the other hand would not have made it possible to implement the analysis itself.

4.4 - UQ analysis

The purpose of the study is to evaluate how the geometric uncertainties linked to the film cooling hole propagate on the results; in particular, the quantities used as a measure of reference were the film cooling effectiveness, the blowing ratio "BR", and the discharge coefficient "C_d".

Being aware of the works present in the literature regarding this field and of the computational expenditure inherent to the UQ analysis, it was decided to limit the dimension of the problem by considering only the effect of three uncertain variables on the output considered, as previously done in [26] and [73]. It should be noted that currently, in the literature, there are no uncertainty quantification studies applied to computational

fluid dynamics in which more than three random variables are evaluated. Additionally, regarding film cooling applications, there are no works based on real gas turbine blade geometry.
From the work done on the one-dimensional code described in chapter 3.3 -it was evident that a polynomial chaos expansion analysis based on the Gauss grid allows obtaining a good agreement with the Monte Carlo method even with a minimum polynomial order, minimizing the number of evaluations to be carried out. Therefore, it was decided to use this methodology which requires, with a unitary polynomial order and for three random variables considered, eight discrete simulations.
Since this type of study requires the modelling of uncertainties, in software terms this translates into the creation of a parametric CAD of the geometry analysed. It was decided to carry out all the work within the ANSYS Workbench suite. In particular, the eight required evaluations were carried out in series and automatically; this procedure was made possible with the parameterization of uncertainties divided into "design point" a priori defined: UQ activity was carried out a posteriori with respect to CFD simulations, in particular, after defining the uncertain variables, sampling was performed using DAKOTA, the points thus obtained were imposed in the respective "design points" of the ANSYS Workbench suite and only after completing all the simulations the UQ analysis was then carried out.

4.4.1 - Uncertain variables

As already mentioned, there were three uncertain variables considered; in particular, the quantities chosen were the angle of inclination of the film cooling hole, the fillet radius, and the dimension of the holes. For each one, considerations of a different nature have been made and described individually in the following chapters. As for the previous analysis, the selection of the collocation points was made according to what already described in Chapter 2.4.3 -and 2.4.4 -.

4.4.1.1 – Inclination angle of the hole

The angle of inclination of the holes is a variable that has not been considered in any of the works concerning uncertainty quantification literature. The choice of plausible values for this type of parameter was based on the manufacturing process considered and on the work done by Bunker [2], in which he indicates an average tolerance of $\pm 5°$ for all angles involving the film cooling hole: the inclination with respect to the internal flow, with respect to the external flow, and the angle with respect to the surface tangent to the hole. It should be noted that the inclination angle of the holes varies for the different rows of holes, as reported in Figure 4.36, for this reason, it has been chosen to set as uncertain variable a constant tilt angle with respect to the nominal axis of each hole.

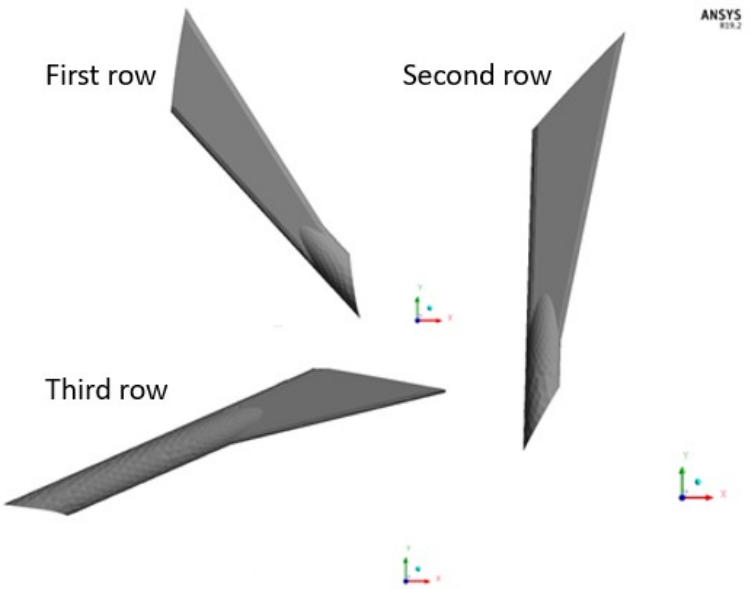

Figure 4.36 – Holes geometries

Since the holes are made by EDM, it was decided to rotate the hole with respect to the suction side surface of the aerodynamic profile. This type of approach was suggested by an industrial partner, who stressed that EDM drilling is a very accurate process and it is able to reproduce the nominal values imposed on the diameter of the hole, but at the same time suffers from the radial curvature of the profiles: this is due to the fact that for this type of process only the path of the machine tool and the point on the blade surface where the drilling begins are specified. For twisted blades, there may be a partial failure to drill or a complete failure to drill since the relative inclination between blade and tool may cause, for the same path specified for the machine tool, different drilling from the desired one. Moreover, from a CAD modelling point of view, a rotation with respect to any other point of the hole would have caused a considerable variation of the shaped area of the hole itself, resulting in a variation of the ratio between the areas defined in terms of area ratio (AR) and in total disagreement with the drilling manufacturing procedure used.
Initially, in order to evaluate the effects of the problem previously described, the idea was to set a greater uncertainty than the value suggested by Bunker [2]. However, the high vicinity of the first row of holes to the leading edge of the coolant supply plenum led to a critical condition for which the hole did not completely intersect the plenum. This condition is reported in Figure 4.37.

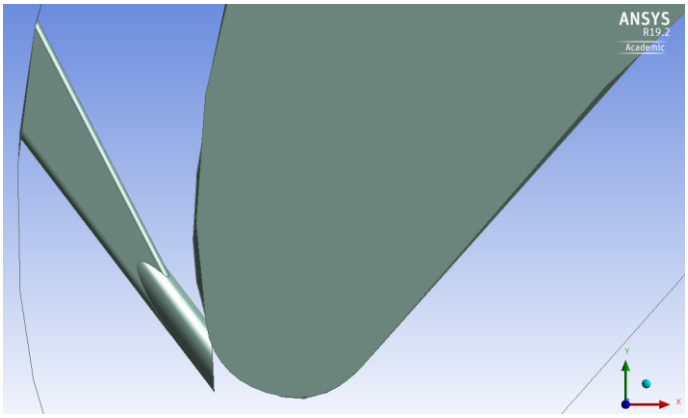

Figure 4.37 – First row of holes drilling problem

Assuming that such a configuration is discarded during the quality control phase after the profile has been drilled, it is considered that this type of conformation cannot actually be used in the real machine. Aiming to analyse the effect of this factor on the film cooling during real operating conditions, it was decided to reduce the amplitude of the uncertainty to the minimum value that would allow the complete drilling of the supply plenum to take place. For this reason, a Gaussian distribution with a mean null value was considered on the angle of inclination of the hole, coinciding, therefore, with the condition in which the angle of inclination is identical to the nominal one, and truncated to the extreme values of ±5°, in total agreement with what was reported by Bunker [2].

In conclusion, an uncertainty on the angle of inclination of the holes with a truncated normal distribution $\mathcal{N}(0°, 2.5°)$ has been considered. For the uncertainty quantification methodology chosen, this results in discrete simulations with two angles of inclination with respect to the nominal condition of ±2.2°.

The conditions analysed are reported in Figure 4.38.

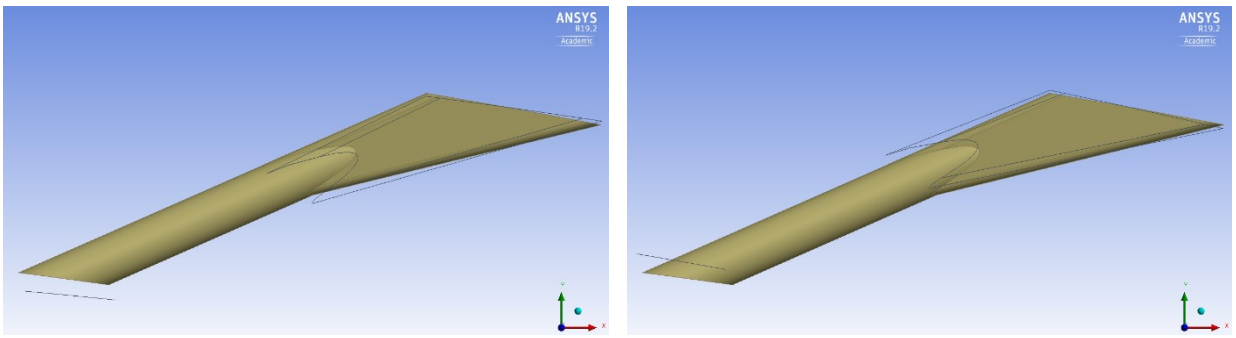

(a) Positive rotation (b) Negative rotation

Figure 4.38 – Inclination angle for the third row of holes

4.4.1.2 – Fillet radius

The second uncertainty considered in the study is the fillet radius of the film cooling holes. This type of geometrical dimension has already been the subject of a dedicated studies [72], [73] but, as already described, there were not exploited methods of stochastic expansion for this parameter.

The choice of this random variable precludes further comparisons with the baseline experimental work previously cited [114]: in this case, in fact, there was no fillet radius; however, it was decided to consider this parameter because, in real conditions, a connection for the cylindrical section of the hole is always present and, moreover, it is a factor that greatly influences the discharge coefficient of the hole. The random variable has been considered in dimensionless terms as r/D, in which r is the fillet radius and D is the diameter of the cylindrical section of the hole. For the definition of a plausible range of variability, reference has been made to [72], in which the variability reported is between $r/D = 0 \div 5\%$. In this activity it has been decided not to include the case with no fillet radius, but a variability of the connection radius has been imposed as a percentage of the nominal diameter. In particular, in analogy to what has been done in [72], a fillet radius included between $(1 \div 9\%)D$ has been considered. In terms of ratio r/D, this condition results in a variability between $r/D = (0.6 \div 5.4) \cdot 10^{-5}$; it is necessary to specify that a fillet radius equal to 1% of the diameter is extremely small and the result associated should be very close with the condition of no fillet radius. In order to be able to discretize the fillet radius in an appropriate way, these zones have been modelled with reduced size elements compared to the other parts of the fluid domain.

Also for this variable, it has been decided to impose a truncated normal distribution with extreme values placed at $\pm 2\sigma$; the distribution of the variable r/D in percentage is defined by $\mathcal{N}(5\%, 2\%)$. This variability, for the UQ method performed, requires the performance of simulations with discrete values of r/D equal to $1.94 \cdot 10^{-5}$ and $4.05 \cdot 10^{-5}$. The conditions analysed are shown in Figure 4.39.

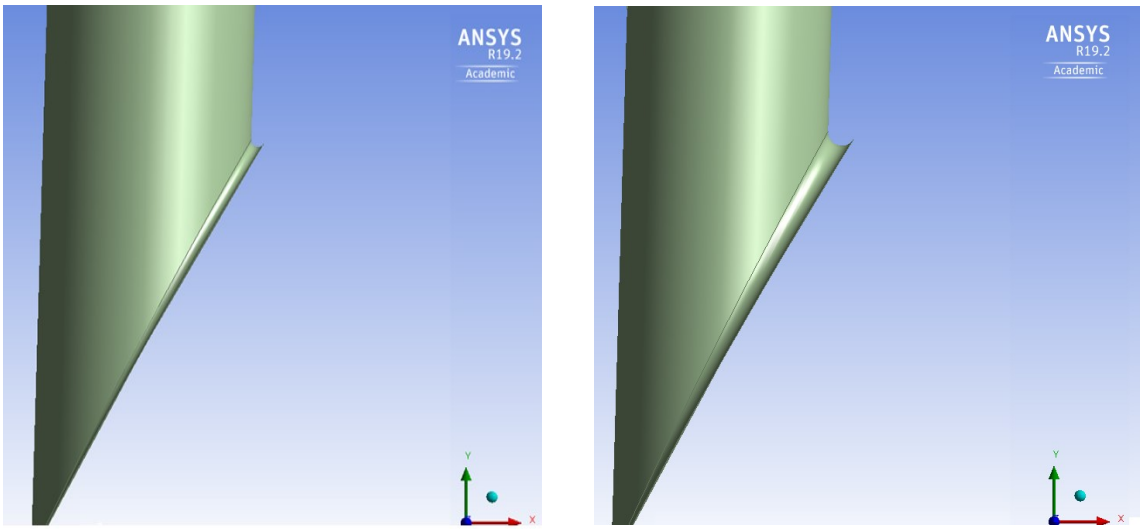

(a) $r/D = 1.94 \cdot 10^{-5}$ (b) $r/D = 4.05 \cdot 10^{-5}$

Figure 4.39 – Fillet radius evaluated points

4.4.1.3 – Scale factor

In order to evaluate the effects of drilling, it was decided to consider a scale factor compared to the nominal value: the overall size of the hole is going to increase or decrease while maintaining a constant area ratio.
By imposing a scale factor that is consistent with the manufacturing process used, given that EDM drilling has extremely small tolerances, this would have resulted in a range of uncertainty for the random variable considered exceptionally narrow with no difference in the output. In order to obtain a result that can be extended to different manufacturing processes, a hole size variability of 10% was therefore considered; this is a common tolerance value for the manufacturing processes carried out for additive manufacturing.
It should be noted that, regardless of the amplitude of the uncertain variable imposed, the sensitivity analysis will provide a general data which does not depend on the range previously imposed but on the solver used to perform the analysis and on the system considered.
As for the other two uncertain variables, also for scale factor a normal distribution centred in the unit value and truncated to the limit values $0.9 - 1.1$ was considered in order to associate the nominal size of the hole. In this way it is considered a dimension variation of the holes around 10% with respect to the nominal conditions; similarly to what has already been done, the standard deviation was set to be twice the distance between the mean value and an extreme value, or rather $\mathcal{N}(1, 0.05)$. This variability implies to perform two evaluations of the scale factors in the CFD analysis respectively of 0.956 and 1.04. In Figure 4.40 a comparison is proposed between the two factors used to carry out the analyses. For the sake of clarity, the last row of holes in which the two holes are respectively subject to the two different scale factors has been reported.

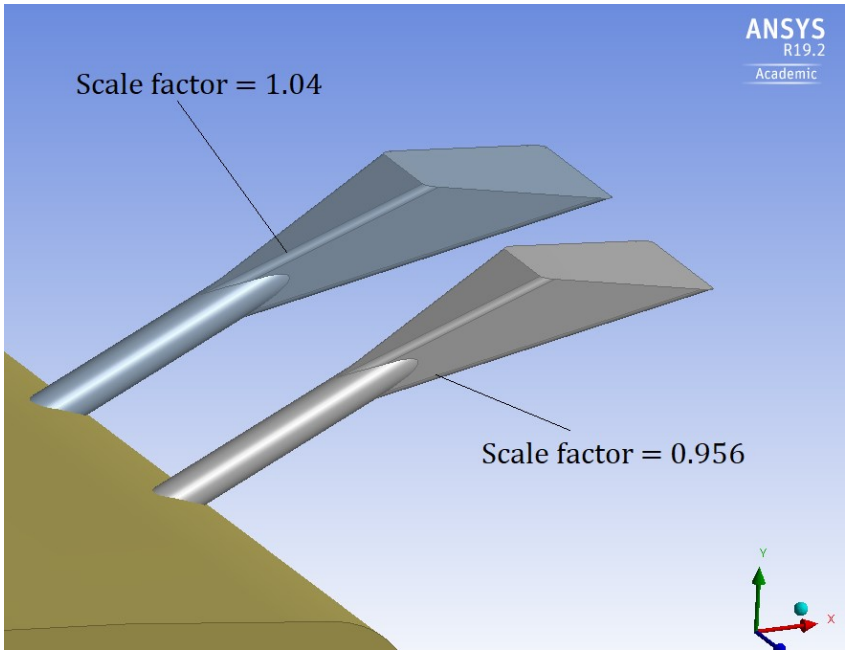

Figure 4.40 – Scale factors used for the evaluations

4.4.2 - Results

Regarding the development of the UQ study, the methodology of polynomial chaos expansion using a unitary order was considered, which requires eight discrete simulations for the three variables taken into account. In fact, as already seen in the previous chapter for the low order code, the 1st order approximation is able to reproduce with an optimum grade of accuracy the analysis. It is reminded that a unitary order with three input variables, for the tensor product method, means a 3rd order interpolating polynomial. In Table 4.3 the conditions imposed, for the three uncertain variables, in the eight simulations carried out through ANSYS Workbench are summarised.

Table 4.3 – Evaluations required

	$\boldsymbol{Angle}$	$\boldsymbol{Fillet\ radius}$	$\boldsymbol{Scale}$
$\boldsymbol{DP0}$	$-2.2°$	$1.94 \cdot 10^{-5}$	0.956
$\boldsymbol{DP1}$	$2.2°$	$1.94 \cdot 10^{-5}$	0.956
$\boldsymbol{DP2}$	$-2.2°$	$1.94 \cdot 10^{-5}$	1.04
$\boldsymbol{DP3}$	$2.2°$	$1.94 \cdot 10^{-5}$	1.04
$\boldsymbol{DP4}$	$-2.2°$	$4.05 \cdot 10^{-5}$	0.956
$\boldsymbol{DP5}$	$2.2°$	$4.05 \cdot 10^{-5}$	0.956
$\boldsymbol{DP6}$	$-2.2°$	$4.05 \cdot 10^{-5}$	1.04
$\boldsymbol{DP7}$	$2.2°$	$4.05 \cdot 10^{-5}$	1.04

Once the results of the eight simulations had been obtained, the UQ analysis was carried out through DAKOTA and the surrogate model is obtained. Subsequently, as in the previous chapter, the surrogate model was then called with a set of one thousand sample points.

This procedure was carried out for all three quantities: the film cooling effectiveness, the blowing ratio, and the discharge coefficient. In particular, for the effectiveness, the same types of graphs were obtained as those already proposed in the previous chapter for the study of the one-dimensional model, i.e. with development along the non-dimensional abscissa.

For the blowing ratio and the discharge coefficient it was necessary to have another kind of visualization of the results and to carry out an expensive data processing procedure, as it required the execution of further CFD analysis in the absence of film cooling in order to estimate the isentropic Mach number on the wall, necessary to calculate then BR and C_D.

The results obtained in terms of film cooling effectiveness are here reported and described. In chapter 4.3.2 -, the post-process of the data obtained from the CFD simulations has already been described.

In Figure 4.41 the estimated trends of the surrogate model in terms of mean, maximum and minimum value for the adiabatic effectiveness with respect to the non-dimensional of the "suction side" are reported.

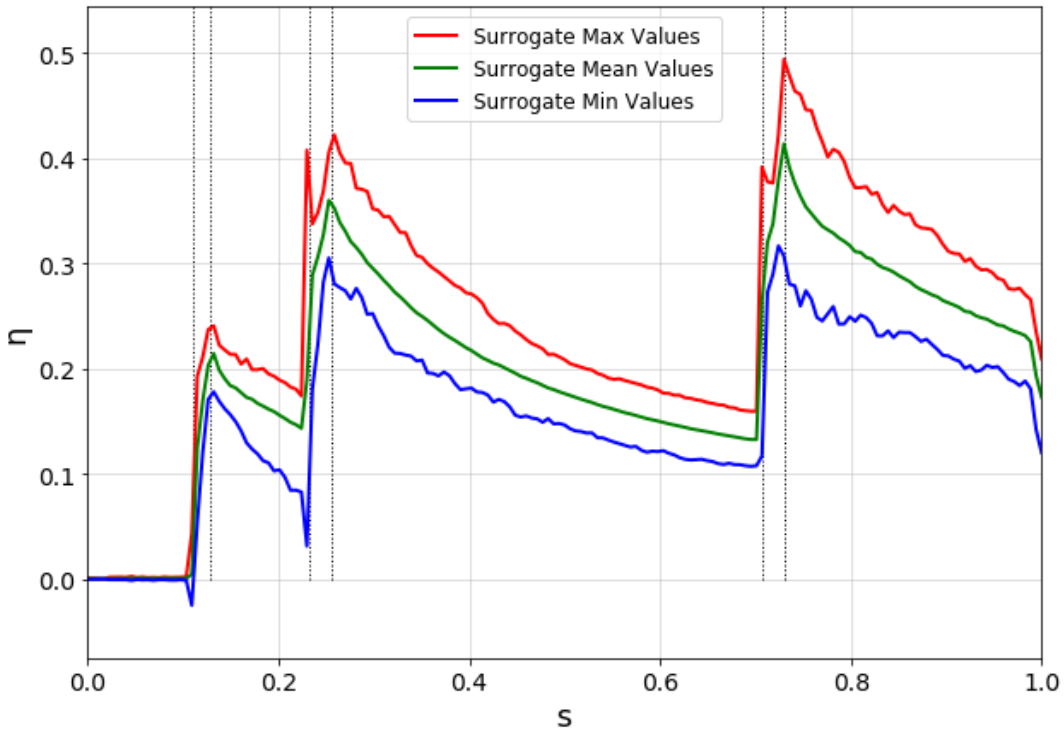

Figure 4.41 – Surrogate model results

Similar to the results obtained in the previous chapter, this graph should not focus the attention on the continuous development of the film effectiveness along the non-dimensional coordinate but only on the probabilities distributions read independently. In fact, considering, for example, the curve of the maximum values, the value generated at the non-dimensional abscissa 0.4 is completely independent of what was obtained for the abscissa 0.6. In other words, the points reported in the graph do not reflect a continuous evolution for the same evaluation, neither temporal nor even spatial; they are only the limit values of the probability distributions associated with a specific abscissa.

The graph shows peaks for the second and third rows of holes in terms of effectiveness immediately upstream of the holes for the line representing the maximum values, whereas for the minimum values a small valley can be noticed near the leading edge of the first and second rows of holes. This result is to be attributed to the post-process used: the interpolation necessary in order to create a vector of constant size for each profile, obtained from the intersection of a plane and the aerodynamic profile, and carrying out the average in the "spanwise" direction of the effectiveness of the film have generated null points. In fact, inside the holes there is no blade surface, so the values of effectiveness in the vicinity of these portions of the area have no physical significance, as already explained. From the graph, it is clear that the maximum variability between the potential results is downstream of the third row of holes, in which they reach a possible range of 20% immediately downstream of the hole and then settle at 15%. This can be attributed to the fact that in the blade radial portion considered, there are two holes and not a single hole as for the first two rows. Exploiting the procedure already used for the "low-order" analysis, it has been obtained the probability map for the film cooling effectiveness, shown in Figure 4.42.

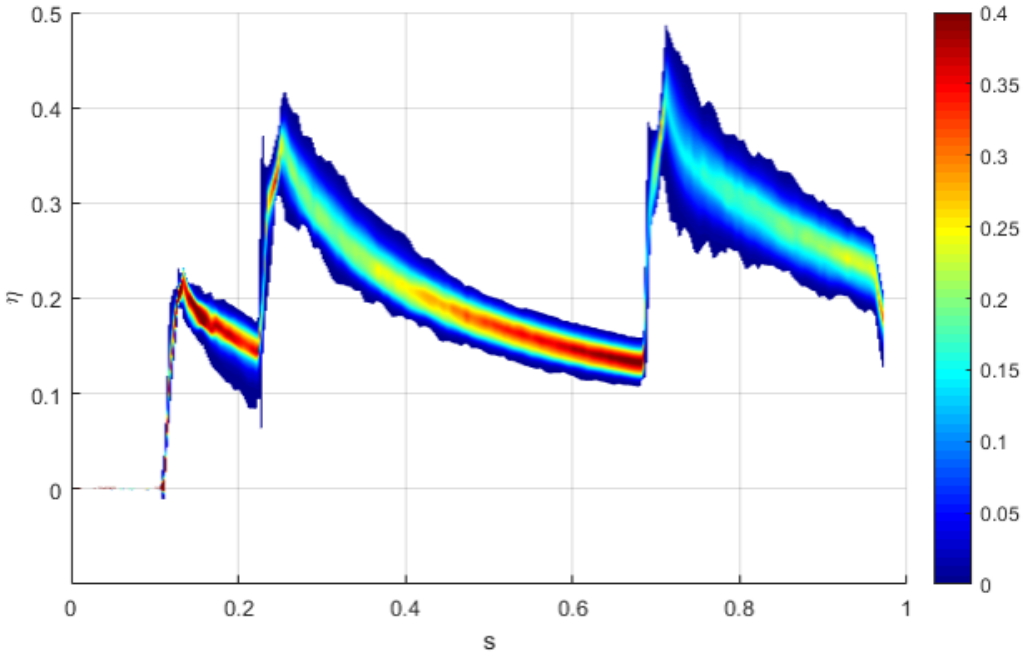

Figure 4.42 – Film cooling effectiveness probability map

From the graph, it is possible to evaluate in probabilistic terms what has already been described for Figure 4.41. The graph shows that downstream of the first hole there is an area defined by a high probability of occurrence, as well as in the wake of the second row of holes near the leading edge of the third row of holes. Even downstream of the third row of holes there is a zone with a higher probability of occurrence but with an intensity about halved to the maximum value found for the previous trails. On the contrary, immediately after the peak of the second and of the third row of hole there is the maximum uncertain zone: in fact, not only the range is the highest, especially for the third row, but also the colour map shows a widespread PDF. It is important to notice, in fact, that the uncertainty is not related to the range of possible value: the zone immediately before the second hole, in fact, features a high range of potential values for the film cooling effectiveness, but the PDF showed by the colour map indicates that this is a low uncertainty zone with a very low standard deviation. To obtain a complete picture, Figure 4.43 shows the sensitivity analysis of the three random variables using the Sobol's indices. For this case the first-degree indices which define how much the interaction between the variables affects the output considered are also reported.

It is underlined, once again, that the graph is a cumulative histogram, so the relative influence of a single parameter is to be read in terms related to its own coloured band and for each non-dimensional abscissa, each associated with the respective parameter in the study.

In the first part of the graph, all the parameters have a flat and comparable amplitude: in fact, in this area there is no film cooling protection as it is located upstream of the first row of holes. For this reason the sensitivity analysis is interesting only after the first row of holes, approximately at $s = 0.1$.

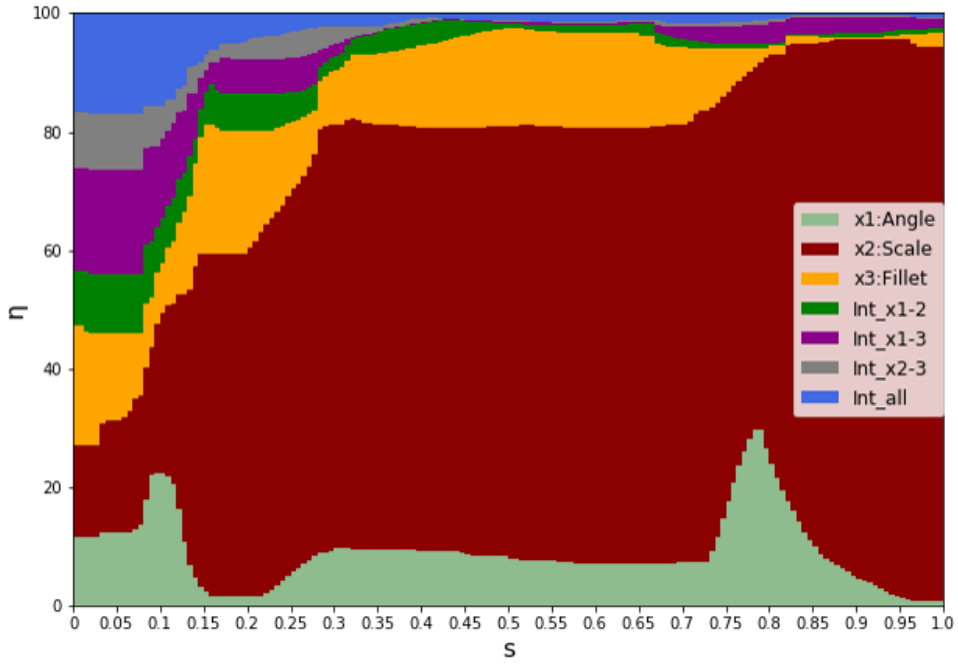

Figure 4.43 – Film cooling sensitivity analysis using Sobol's indices

Moving on to the analysis of the results, as one might expect, the maximum influence on η is given by the scale factor. Near the first and third rows of holes, there is a clearly visible increase in the Sobol's index connected to the inclination angle of the holes; the fact that this increase does not occur for the second row of holes can be attributed to the position and to the inclination angle of the hole itself. As it is clearly visible from Figure 4.44, the second hole is the one that, with the same variation in angle, sweeps over a surface that is more linear and less curved than the other holes, which means less deformation of the input area. By combining this aspect with the fact that the second row of holes does not determine either the start of the coverage, as in the case of the first row of holes, nor the point where it ends, as for the third row of holes, one can explain the lack of dependence of the effectiveness of the second row of holes with respect to the angle. Regarding the fillet radius, excluding the area upstream of the first row of holes, this has a reduced influence. It grows slightly between the first and second row of holes and downstream of this has a maximum and constant width up to the third row of holes, beyond which it has a collapse, assuming a minimal influence among all the parameters. The Sobol's indices linked to the interactions between the variables account for less than 10% in the area affected by film cooling effectiveness.

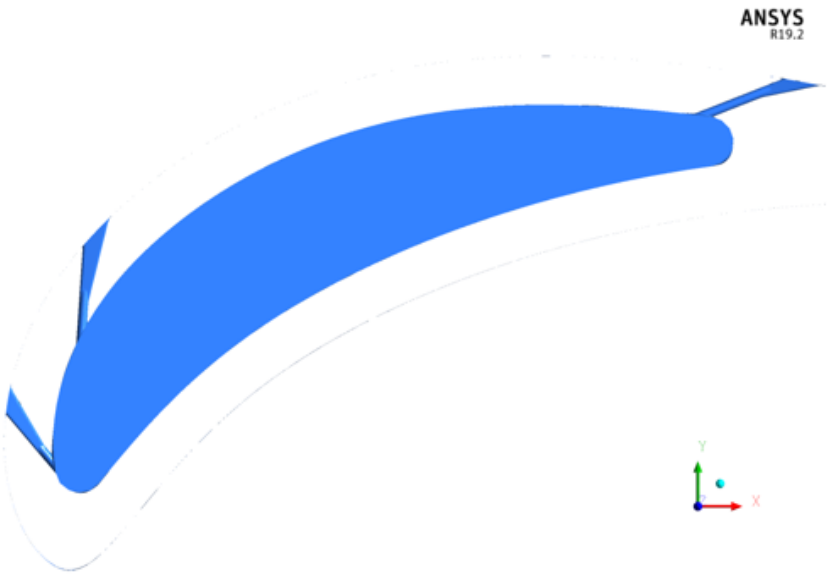

Figure 4.44 – Holes location

Moving on to the UQ analysis on the blowing ratio and on the discharge coefficient, for the post-processing it was necessary to carry out a CFD simulation in the absence of film cooling: in this way, it was possible to find the isentropic Mach number on the surface of the blade. This was necessary in order to calculate the blowing ratio; in fact, for a correct estimation and remembering Eq. 4-4, the velocity of the main flow around the holes of the film cooling is necessary.

Static pressure "P" was obtained on the exit areas of the holes and in order to obtain a single value, an average was carried out on the area; this information, combined with the total pressure "P_0" (imposed at the inlet of the duct) and the adiabatic constant γ of the air, from Eq. 4-7 it has been possible to obtain the Mach number in the vicinity of the film cooling hole.

$$\frac{P_0}{P} = \left(1 + \frac{\gamma - 1}{2} M^2\right)^{\frac{\gamma}{\gamma - 1}} \qquad \text{Eq. 4-7}$$

Having the Mach number and the total temperature "T_0" set as a boundary condition of the simulation, exploiting Eq. 4-8, it was possible to obtain the static temperature near the holes.

$$\frac{T_0}{T} = 1 + \frac{\gamma - 1}{2} M^2 \qquad \text{Eq. 4-8}$$

With the static temperature "T" and knowing the gas constant "R" of the air the speed of sound "a" was found, defined by Eq. 4-9.

$$a = \sqrt{\gamma R T} \qquad \text{Eq. 4-9}$$

Isolating the velocity from the definition of the Mach number from Eq. 4-10.

$$M = \frac{v}{a} \qquad \text{Eq. 4-10}$$

and the density by the perfect gas law, reported in Eq. 4-11, in which n is the molar mass of the air, it is possible to obtain the product $\rho_\infty v_\infty$, the denominator of Eq. 4-4.

$$P = \frac{\rho R T}{n} \qquad \text{Eq. 4-11}$$

For the calculation of the blowing ratio, the term at the numerator of Eq. 4-4 is given by the product between the density and the velocity of the coolant, which was obtained directly by dividing the flow rate of the hole by the passage area, using "ANSYS CFX post" for the post process of simulations. Obviously, this procedure was carried out for each hole of each condition of the eight simulated holes.

Regarding the discharge coefficient C_d, the work of Mazzei et al. [124] has been taken as a reference, in which the discharge coefficient for a generic film cooling hole is defined with the formulation shown in Eq. 4-12.

$$C_d = \frac{\dot{m}}{P_{0,c}\left(\frac{P_\infty}{P_{0,c}}\right)^{\frac{\gamma+1}{2\gamma}} \sqrt{\frac{2\gamma}{(\gamma-1)RT_{0,c}}\left(\left(\frac{P_{0,c}}{P_\infty}\right)^{\frac{\gamma-1}{\gamma}} - 1\right)\frac{\pi}{4}D^2}} \qquad \text{Eq. 4-12}$$

The capacity of the hole has been indicated to the numerator, the subscript "c" refers to the quantities of the coolant flow while the subscript "∞" indicates the quantities of the main flow and D the diameter of the cylindrical section of the hole.

Once all the quantities making up the blowing ratio BR and the discharge coefficient C_d have been defined, the results obtained from the UQ analysis are discussed. As for the film cooling effectiveness, the results generated by the surrogate model will be shown.

The probability distributions of the single blowing ratios for the three holes are reported in Figure 4.45.

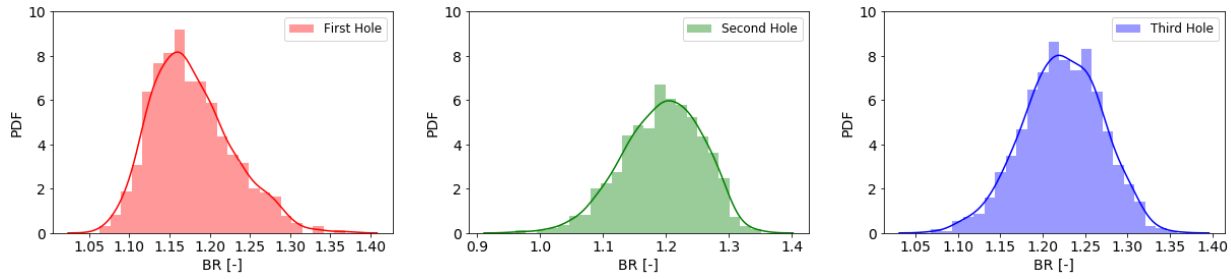

Figure 4.45 –BR probability distribution for the three rows of holes

It should be noted that for the third row of holes, only one hole was considered and not two. By doing this, it is possible to compare the blowing ratios of the single hole for the three rows on the blade. By reporting the three curves on a single graph, as shown in Figure 4.46, it is possible to do a more direct comparison.

It is possible to notice that the three holes have a more likely value different from each other. The first hole and the third have similar probability values but the two curves have a different modal value. In terms of BR the first row of holes is affected by a reduced value compared to the other two rows and the modal value of the third hole is the higher than that of the second line.

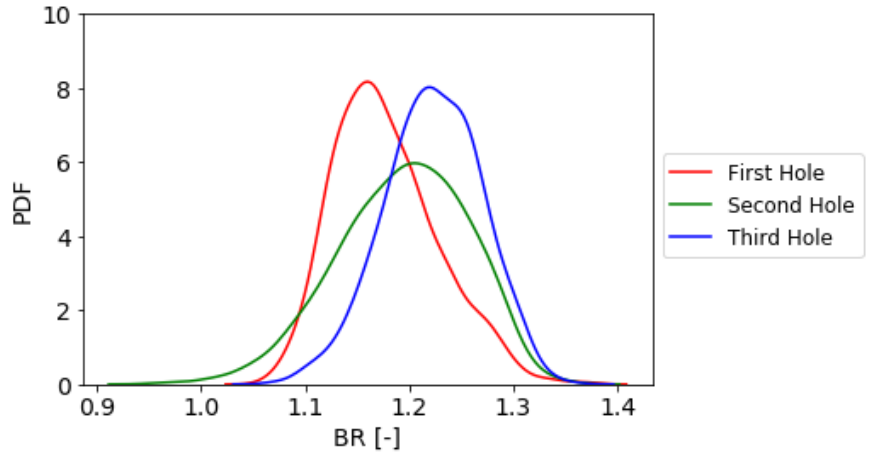

Figure 4.46 – BR probability distribution

The same types of graphs have been obtained also for the discharge coefficient, as shown in Figure 4.47

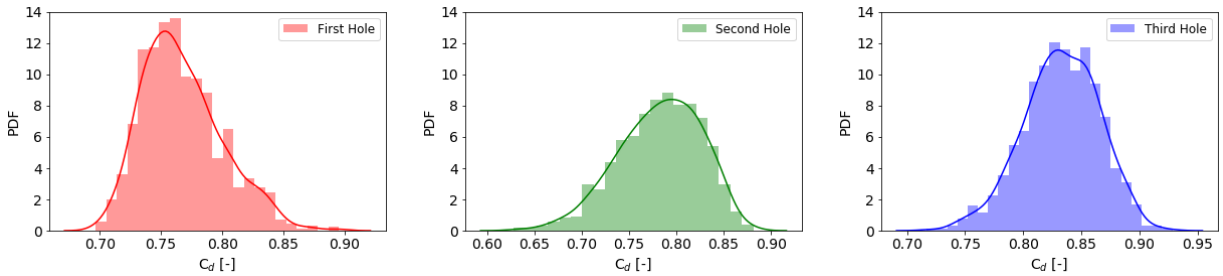

Figure 4.47 – C_d probability distribution for the three rows of holes

As for the blowing ratio, the comparison is also provided in a single graph (Figure 4.48). From the data obtained it is worth noting that the considerations already made for the trends of the blowing ratio are still valid: the graph is very similar, except for a greater probability of the modal values of the distributions for the first and third rows.

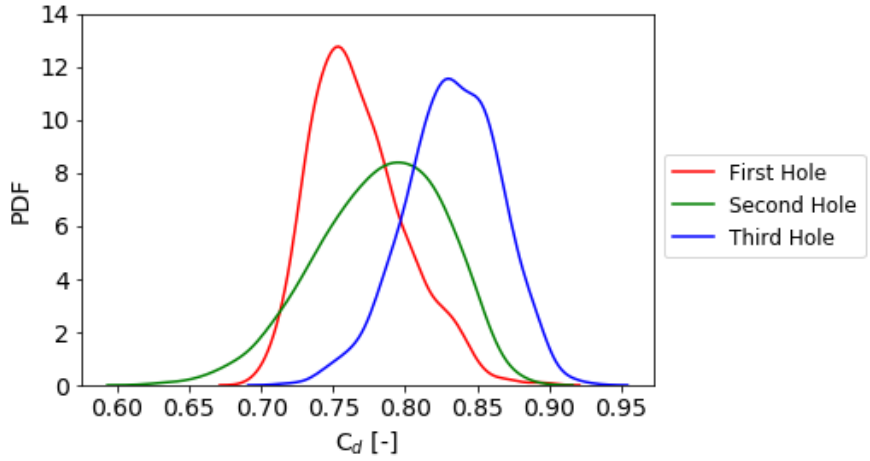

Figure 4.48 – C_d probability distribution

In conclusion, the sensitivity analysis to the three uncertain variables considered is also reported. The histograms containing the Sobol's indices are reported in Figure 4.49.

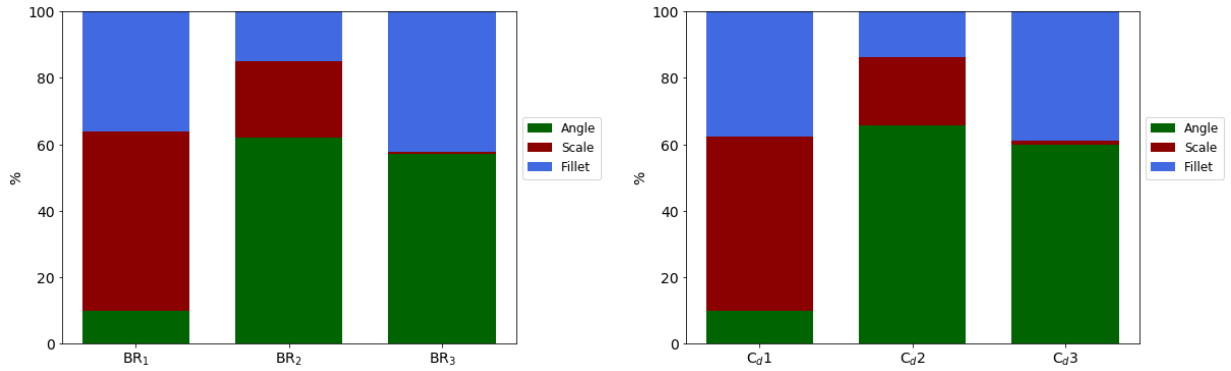

Figure 4.49 – Sensitivity analysis of BR and C_d to the three variables for the three holes

From the graph it is clear that the most influential parameters vary from hole to hole; this is not surprising because, both the conditions to which they are subjected and the size of the holes vary from row to row.
The high influence of the scale factor for the first row of holes may be due to the fact that in this area the pressure disposed of by the aerodynamic profile is fairly small, so, a variation in the size of the hole influences very much the coolant flow that passes through it. For the third row of holes, however, the opposite condition may apply: since this is the hole that has to work with the maximum pressure drop, being the closest to the trailing edge, the scale factor has a very limited influence on the two output quantities.
For the second row of holes, conversely to what emerged for the film cooling effectiveness, the parameter that most influences the BR and C_d in the hole inclination angle, followed by the scale factor, which in any case has a Sobol's index very similar to that of the fillet radius.
Given the high physical dependence between the two output quantities, it should not be surprising that the parameters that most influence the BR and C_d, for the same hole, are the same ones. For example, an increase in the fillet radius causes an increase in the discharge coefficient; but with the same diameter of the hole, for the continuity law, the velocity of the flow increases, which in turn causes an increase in the blowing ratio. Conversely, increasing the diameter of the hole does not cause a change in the discharge coefficient C_d, but it will produce an increase in flow rate without a change in the velocity, so the BR also remains unchanged.
As already mentioned, given the different geometries of the various rows of holes and the different fluid-dynamic conditions in which they are located, it is not possible to define a unique trend for the entire blade surface.

Conclusion

This thesis describes some of the main uncertainty quantification techniques used for turbomachinery applications. This methodology can evaluate the effect of uncertainties of one or more variables on selected output quantities; in particular, it allows to estimate the propagation of an error within a numerical code. These methodologies, if correctly used, can lead to a complete understanding of how the mathematical model approximates and solves the real physical problem; then, through the sensitivity analysis, it is possible to quantify, in mathematical terms, which quantities mostly affect the response functions considered.

The first activity was to validate the different methodologies of an uncertainty quantification analysis using the open-source code DAKOTA. For this reason, the study was performed on a one-dimensional code developed by DIEF of the University of Florence, which performs heat transfer analyses on combustors liner. A low-order approach has allowed to carry out a high number of evaluations with a relatively low computational cost. The fluid network under examination was provided by the industrial partner GE Avio Aero and simulates the behaviour of a combustor operating under lean flame conditions, developed and tested at CIAM during the European project LEMCOTEC.
The procedure established for this study has allowed comparing both the average trend and the maximum and minimum value for the different methods used. Furthermore, probability distribution maps were also obtained: in this case, a probability of occurrence was associated with each temperature of the liner and, spatially, for a specific non-dimensional abscissa.
Different types of analyses were carried out, specifically focusing on some key quantities of the one-dimensional code: geometrical, heat transfer tuning factors, thermal loads, and a final analysis including all the previous parameters. The conclusion was that the most influencing parameters on the selected output quantities are those related to temperature conditions and FAR in the combustion chamber, for which an uncertainty of 20% of these parameters causes a range of output variability of up to 54%. Also the factors related to the heat transfer are very influential on the liner wall temperature; the knowledge of how much these parameters influence the output is particularly interesting, especially for the preliminary design activities. For this type of analysis, it was recorded that an uncertainty of the heat transfer factors of 20% causes a variability of the wall temperature of up to 40%. Compared to the previous factors, the geometrical variables have a moderate influence on the output considered: less than 10%.
Regarding the UQ methodology, from this first application, it was evident how efficient the spectral expansion methods are. In fact, these methods can create a surrogate model with a reduced number of evaluations able to approximate the response function considered: for the model taken into consideration, for the geometrical analyses, only 4 discrete simulations required by the polynomial chaos method were sufficient to obtain the same range of variability obtained with 1000 simulations using the Monte Carlo method. For each analysis, the classical Monte Carlo analysis was compared with four stochastic expansion processes: Gauss quadrature, stochastic collocation, total order with LHS sampling, and Smolyak. It was demonstrated how the first two methods are the most effective when the number of variables considered is reduced (generally speaking, from 1 to 5). The polynomial chaos expansion technique with fixed total order

requires at least twice as many evaluations as the minimum required in order to obtain good results and the method could be effective when the number of variables moderate (from 3 to 7). During this first activity, the Smolyak grid was also validated, which is extremely effective when the number of random variables considered increases because other models (except for the Monte Carlo Simulation) suffer from the curse of dimensionality. For the complete analysis with 7 input variables, this calculation grid allowed to obtain, with 15 evaluations, the same output probability field obtained with 1000 evaluations carried out with the Monte Carlo method, against the 128 required for the Gauss grid (and, thus, for the stochastic collocation) and the 72 for the PCE of 2nd order.

The second part of the thesis was focused on carrying out an uncertainty quantification analysis on a high-fidelity computational fluid dynamics application. The case chosen was a real stator blade, made by additive manufacturing, of a second turbine stage. A previous experimental campaign was conducted on this vane profile in order to carry out the adiabatic effectiveness results: fluorescent paints sensitive to the partial pressure of oxygen (PSP) were used in order to assess the film cooling effectiveness.
The propagation of three geometric uncertainties acting on the film cooling holes was evaluated using the commercial CFD code ANSYS Fluent. The CFD analysis was also carried out using the analogy of heat and mass transfer through a two-fluid approach: air for the main flow and CO_2 for the coolant. The initial fluid domain was reduced in order to limit the calculation resources; after validating the procedure, the UQ analysis was carried out imposing three random variables: the streamwise angle of the holes, a scale factor, and the fillet radius. The effects of these uncertainties were evaluated on the film cooling effectiveness, on the blowing ratio and on the discharge coefficient of the holes.
Both steady (RANS) and unsteady (hybrid LES-RANS) simulations were carried out. For the UQ analysis, only the polynomial chaos approach with the Gauss grid method in conjunction with RANS simulations was used. The number of evaluations required was eight. The resources required were approximately 800 CPU Hours for the overall analysis.
The complicated physic of the problem, combined with the different geometry of the holes among the various rows, does not allow to obtain generalized results in absolute terms for all the output quantities. As far as the sensitivity analysis is concerned, it should be noted that the scale factor is the parameter that has the greatest impact on the film cooling effectiveness: it has an influence up to 60%. The angle of the holes near the first and third rows have an impact of 20% on the effectiveness. The greatest variability in film cooling effectiveness is achieved downstream of the third row of holes, where it can vary up to 20%. The behaviour of the discharge coefficient and the blowing ratio show the same trends, as one might expect due to the high physical dependencies between these parameters. As the non-dimensional abscissa increases, the most probable values of these two quantities tend to increase: the third hole is subject to a C_d and BR greater than the second row, which in turn feature values greater than the first row. The probability distributions of the two parameters for the first row of holes have the lowest standard deviation.
For the sensitivity analysis, there was no univocal trend of the results of the three rows of holes, but also in this case similar trends were obtained between the discharge coefficient and the blowing ratio.
The scale factor accounts for around 55% in the first row of holes, the fillet radius accounts for 35% and the inclination angle accounts only for 10%. For the second row, instead, the most influential parameter is the inclination angle, which affects the BR and C_d for 60% and the remaining two variables for 20% each. The

last row of holes is not dependent on the scale factor: the Sobol's index is lower than 1%. This changing behaviour is supposed to be attributed to the different pressure drop that the different rows of holes feature. For the second row the angle is the parameter that mostly affects the blowing ratio and the discharge coefficient, and also in this case it has an incidence of 60%; the remaining 40% depends on the fillet radius.

Bibliography

[1] D. Ballal e J. Zelina, «Progress in aeroengine technology (1993-2003),» *AIAA Journal of Aircraft,* pp. 43-50, 2004.

[2] R. Bunker, «The effects of manufacturing tolerances on gas turbine cooling,» in *ASME Turbo Expo 2008: Power for Land, Sea, and Air*, Berlin, Germany, 2008.

[3] D. Wilcox, Turbolence Modeling for CFD, California: DCW Industries, 1993.

[4] O. L. Maître e O. Knio, Spectral Methods for Uncertainty Quantification, Springer Science & Business Media, 2010.

[5] S. Kline e F. McClintock, «Describing Uncertainties in Single Sample Experiments,» *Mechanical Engineering, ,* 1953.

[6] R. Moffat, «Contributions to the Theory of Single-Sample Uncertainty Analysis,» *Journal of Fluids Engineering, ASME,* vol. 104, 1982.

[7] G. Iaccarino, «Quantification of Uncertainty in Flow Simulations Using Probabilistic Methods,» in *VKI Lecture Series*, Sint Genesius Rode, 2008.

[8] F. Hoffman e J. Hammonds, «Propagation of uncertainty in risk assessments: the need to distinguish between uncertainty due to lack of knowledge and uncertainty due to variability,» *Risk Analysis,* p. 707–12, 1994.

[9] AIAA, Guide for the Verification and Validation of Computational Fluid Dynamics Simulations, Reston, VA: AIAA-G-077-1998, 1998.

[10] J. Casti, Searching for certainty, New York: William Morrow, 1990.

[11] M. Emory, G. Iaccarino e G. M. Laskowski, «Uncertainty quantification in turbomachinery simulations,» in *ASME Turbo Expo: Turbomachinery Technical Conference and Exposition*, Seoul, 2016.

[12] S. Ferson e L. Ginzburg, «Different methods are needed to propagate ignorance and variability,» *Reliability Engineering & System Safety,* vol. 54, pp. 133-144, 1996.

[13] AGARD, A Selection of Experimental Test Cases for the Validation of CFD Codes, 1994.

[14] R. Flores, M. Miyasato, V. McDonell e G. Samuelsen, «Response of a model gas turbine combustor to variation in gaseous fuel composition,» *Journal of Engineering for Gas Turbines and Power,* vol. 123, pp. 824-831, 2001.

[15] G. McTaggart-Cowan, S. Rogak, S. Munshi, P. Hill e W. Bushe, «The influence of fuel composition on a heavy-duty, natural-gas direct-injection engine,» *Fuel,* vol. 3, n. 89, pp. 752-759, 2010.

[16] T. Lieuwen, V. McDonell, E. Petersen e D. Santavicca, «Fuel flexibility influences on premixed combustor blowout, flashback, autoignition, and stability,» *Journal of engineering for gas turbines and power,* vol. 1, n. 130, 2008.

[17] F. Montomoli, «Manufacturing/In-Service Uncertainty and Impact on Life and Performance of Gas Turbines/Aircraft Engines,» in *Uncertainty Quantification in Computational Fluid*, Springer International Publishing AG, 2019, pp. 1-31.

[18] R. Schnell, T. Lengyel-Kampmann e E. Nicke, «On the impact of geometric variability on fan aerodynamic performance, unsteady blade row interaction, and its mechanical characteristics,» *Journal of Turbomachinery,* vol. 136, 2014.

[19] A. Ghenaiet, S. Tan e R. Elder, «Prediction of an axial turbomachine performance degradation due to sand ingestion,» *Journal of Power and Energy,* p. 273–287, 2005.

[20] J. Klinner, A. Hergt e C. Willert, «Experimental investigation of the transonic flow around the leading edge of an eroded fan airfoil,» *Experiments in Fluids,* vol. 55, 2014.

[21] A. Wheeler, A. Sofia e R. Miller, «The effect of leading-edge geometry on wake interactions in compressors,» *Journal of Turbomachinery,* n. 131, pp. 1-8, 2009.

[22] M. Elmstrom, K. Millsaps e G. Hobson, «Impact of nonuniform leading edge coatings on the aerodynamic performance of compressor airfoils,» *Journal of Turbomachinery,* 2011.

[23] M. Goodhand, R. Miller e H. Lung, «The sensitivity of 2D compressor incidence range to in-service geometric variation,» *Proceedings of the ASME Turbo Expo,* p. 159–170, 2012.

[24] M. Massini, R. Miller e H. Hodson, «A new intermittent aspirated probe for the measurement of stagnation quantities in high temperature gases,» in *Proceedings of ASME Turbo Expo: Power for Land, Sea and Air* , Berlin, 2008.

[25] S. Salvadori, F. Montomoli e F. Martelli, «Aerothermal study of the unsteady flow field in a transonic gas turbine with inlet temperature distortions,» *Journal of Turbomachinery,* 2011.

[26] F. Montomoli e A.D'Ammaro, «Uncertainty Quantification and Conjugate Heat Transfer: A Stochastic Analysis,» *Journal of Turbomachinery,* p. Vol. 135, 2013.

[27] J. Kwak e J. Han, «Heat Transfer Coefficients and Film Cooling Effectiveness on the Squealer Tip of a Gas Turbine Blade,» *Journal of Turbomachinery,* vol. 125, n. 4, pp. 648-657, 2001.

[28] F. Larson e J. Miller, «A time temperature relationship for rupture and creep stresses,» *Transactions of ASME,* n. 74, p. 765 – 775, 1952.

[29] C. Stimpson, J. Snyder, K. Thole e D. Mongillo, «Effectiveness measurements of additively manufactured film cooling holes,» in *ASME Turbo Expo 2017*, Charlotte, North Carolina, 2017.

[30] C. Stimpson, J. Snyder, K. Thole e D. Mongillo, «Effects of Coolant Feed Direction on Additively Manufactured Film Cooling Holes,» *Journal of Turbomachinery,* vol. 140, 2018.

[31] M.Kapsis e L.He, «Analysis of aerothermal characteristics of surface microstructures,» *Journal of Fluids Engineering ASME,* vol. 140, 2018.

[32] R. Ghanem e A. Doostan, «On the construction and analysis of stochastic models:Characterization and propagation of the errors associated,» *Journal of Computational Physics,* n. 217, p. 63–81, 2006.

[33] W. Oberkampf e M. F. Barone, «Measures of agreement between computation and experiment: validation metrics,» *Journal of Computational Physics,* vol. 217, p. 5–36, 2006.

[34] F. Carazas e G. d. Souza, «Reliability Analysis of Gas Turbine,» in *Thermal Power Plant Performance Analysis*, London, Springer, 2012, pp. 189-220.

[35] J. Kappas, «Review of Risk and Reliability Methods for Aircraft Gas Turbine Engines,» DSTO Aeronautical and Maritime Research Laboratory , Fishermans Bend, Australia , 2002.

[36] B. Iooss, O. Lemaître, C. Meloni e G. Dellino, «A review on global sensitivity analysis methods,» in *Uncertainty management in Simulation Optimization of Complex Systems: Algorithms and Applications*, Springer, 2015, pp. 100-123.

[37] I. Sobol, «Sensitivity estimates for nonlinear mathematical models,» *Mathematical modelling and computational experiments,* vol. 1, n. 4, pp. 407 - 414, 1993.

[38] F. J. Cunha, The gas turbine handbook, NETL, 2006.

[39] J. Han e L. M. Wright, The gas turbine handbook, NETL, 2006.

[40] J. C. Han, «Turbine blade cooling studies at Texas A&M university: 1980-2004,» *Journal of thermophysics and heat transfer,* vol. 20, n. 2, pp. 161-187, 2006.

[41] I. Gibson, D. W. Rosen e B. Stucker, Additive manufacturing technologies, New York: Springer, 2010.

[42] M. Attran, «The rise of 3-D printing, the advantages of additive manufacturing over traditional manufacturing,» *Business Horizons,* vol. 60, pp. 677-688, 2017.

[43] C. Chu, G. Graf e D. W. Rosen, «Design for additive manufacturing of cellular structures,» *Computer-aided design and applications,* vol. 5, pp. 686-696, 2008.

[44] J. M. Wilson, C. Piya, Y. C. Shin, F. Zhao e K. Ramani, «Remanufacturing of tubine blades by laser direct deposition with its energy and environmental impact analysis,» *Journal of cleaner production,* vol. 80, pp. 170-178, 2014.

[45] O. Yilmaz, N. Gindy e J. Gao, «A repair and overhaul methodology for aeroengine components,» *Robotics and Computer-Integrated Manufacturing,* vol. 26, pp. 190-201, 2010.

[46] T. Petrat, B. Graf, A. Gumeniuk e M. Rethmeier, «Laser metal deposition as repair technology for a gas turbine burner made of inconel 718,» *Physics Procedia,* vol. 83, pp. 761-768, 2016.

[47] D. D. Gu, M. Meiners, K. Wissenbach e R. Poprawe, «Laser additive manufacturing of metallic components: materials, processes and mechanisms,» *International materials reviews,* vol. 57, n. 3, pp. 133-164, 2012.

[48] A. W. Gebisa e H. G. Lemu, «Additive manufacturing for the manufacture of gas turbine engine components: literature review and future perspectives,» in *ASME Turbo Expo: Turbomoachinery Technical Conference and Exposition*, Oslo, Norway, 2018.

[49] S. L. Sing, J. An, W. Y. Yeong e F. E. Wiria, «Laser and electron-beam powder-bed additive manufacturing of metallic implants: a review on processes, materials and designs,» *Journal of Orthopaedic Reserach,* vol. 34, n. 3, pp. 369-385, 2016.

[50] C. K. Chua e K. F. Leong, 3-D printing and additive manufacturing: principles and applciations, World Scientific Publishing Co. Inc., 2014.

[51] D. Xiu, Numerical Methods for Stochastic Computations: A Spectral Method Approach, Princeton, New Jersey: Princeton University Press, 2010.

[52] B. De Finetti, Teoria delle probabilità: sintesi introduttiva con appendice critica, Einaudi, 1970.

[53] G. Szego, Orthogonal Polynomials, Providence,Rhode Island: American Mathematical Society, 1939.

[54] T. Chihara, An Introduction to Orthogonal Polynomials, New York: Gordon and Breach, 1978.

[55] O. L. Maître e O. Knio, «Appendix B: Orthogonal Polynomials,» in *Spectral Methods for Uncertainty Quantification*, Springer Science & Business Media, 2010, pp. 499-513.

[56] J. W. R. Askey, «Some basic hypergeometric polynomials that generalized jacobi polynomials,» in *American Mathematical Society*, 1985.

[57] B. Adams, L. Bauman, W. Bohnhoff, K. Dalbey, M. Ebeida, J. Eddy, M. Eldred, P. Hough, K. Hu, J. Jakeman, J. Stephens, L. Swiler, D. Vigil e T. Wildey, «Dakota, A Multilevel Parallel Object-Oriented Framework for Design Optimization, Parameter Estimation, Uncertainty Quantification, and Sensitivity Analysis: Version 6.9 User's Manual,» Sandia Technical Report SAND2014-4253, November 2018.

[58] M. Rosenblatt, «Remarks on a multivariate transformation,» *The annals of mathematical statistics,* vol. 3, n. 23, pp. 470-472, 1952.

[59] J. Helton e J. Johnson, «Sampling-Based Methods for Uncertainty and Sensitivity Analysis,» *Reliability Engineering & System Safety,* vol. 10, n. 91, pp. 1175-1209, 2006.

[60] M. Eldred e J. Burkardt, «Comparison of Non-Intrusive Polynomial Chaos and Stochastic Collocation Methods for Uncertainty Quantification,» in *47th AIAA aerospace sciences meeting including the new horizons forum and aerospace exposition*, 2009.

[61] S.A.Smolyak, «Quadrature and interpolation formulas for tensor products of certain classes of functions,» *Soviet math.,* pp. 240-243, 1963.

[62] M. Baudin, A. Dutfoy, B. Iooss e A. Popelin, «OpenTURNS: An industrial software for uncertainty quantification in simulation,» 2015.

[63] J. Feinberg e H. P. Langtangen, «Chaospy: An open source tool for designing methods of uncertainty quantification,» *Journal of Computing Science,* vol. 11, pp. 46-57, 2015.

[64] S. Tennøe, G. Halnes e G. T. Einevoll, «Uncertainpy: A Python toolbox for uncertainty quantification and sensitivity analysis in computational neuroscience,» *Frontiers in neuroinformatics,* vol. 12, 2018.

[65] S. Marelli e B. Sudret, «UQLab: A Framework for Uncertainty Quantification in MATLAB,» *The 2nd International Conference on Vulnerability and Risk Analysis and Management ,* p. 2554–2563, 2014.

[66] G. Tang, G. Iaccarino e M. Eldred, «Global sensitivity analysis for stochastic collocation,» in *51st AIAA/ASME/ASCE/AHS/ASC Structures, Structural Dynamics, and Materials Conference*, Orlando, Florida, 2010.

[67] A. Durocher, P. Versailles, G. Bourque e J. M. Bergthorson, «Uncertainty Quantification of NOx Emissions Induced Through the Prompt Rout in Premixed Alkane Flames,» in *ASME Turbo Expo 2018: Turbomachinery Technical Conference and Exposition*, 2018.

[68] D. Goodwin, H. Moffat e R. Speth, «Cantera: An object-oriented software toolkit for chemical kinetics thermodynamics, and transport processes,» Caltech, Pasadena CA, 2009.

[69] M. Mueller, G. Iaccarino e H. Pitsch, «Chemical kinetic uncertainty quantification for large eddy simulation of turbulent nonpremixed combustion,» *Proceedings of the Combustion Institute,* vol. 34, pp. 1299-1306, 2013.

[70] F. M. A.D'Ammaro, «Uncertainty quantification and film cooling,» *Computers & Fluids,* p. 320–326, 2013.

[71] H. Babaee, X. Wan e S. Acharya, «Effect of uncertainty in blowing ratio on film cooling effectiveness,» *Journal of Heat Transfer,* vol. 136, n. 3, 2014.

[72] F. Montomoli, M. Massini, S. Salvadori e F.Martelli, «Geometrical Uncertainty and Film Cooling: Fillet Radii,» *Journal of Turbomachinery,* 2012.

[73] W.Shi, P. Chen, X. Li, J. Ren e H. Jiang, «Uncertainty Quantification of the Effects of Small Manufacturing Deviations on Film Cooling: A Fan-Shaped Hole,» *Aerospace,* vol. 46, 2019.

[74] A. Lefebvre, Gas Turbine Combustion, Taylor & Francis, 1998.

[75] ICAO, «Aviation benefits Report, International Civil Aviation,» 2017.

[76] M. Brunet, S. Aubry e R. Lafage, «The clean sky programme: environmental benefits at aircraft level,» in *15th AIAA Aviation Technology, Integration, and Operations Conference* , 2015.

[77] D. Bertini, L. Mazzei, A. Andreini e B. Facchini, «Multiphysics numerical investigation of an aeronautical lean burn combustor,» in *ASME TURBO EXPO 2019:Power for Land, Sea & Air*, Phoenix, Arizona, 2019.

[78] C. Ford e J. C. A. Walker, «The impact of compressor exit conditions on fuel injector,» in *ASME J Therm Eng Gas Turb Pwr*, 2012.

[79] G. Cerri, A. Giovannelli, L. Battisti e R. Fedrizzi, «Advances in effusive cooling techniques of gas turbines,» *Applied Thermal Engineering,* vol. 27, n. 4, pp. 692-698, 2007.

[80] G. Andrews, I. Khalifa, A. Asere e F. Bazdidi-Tehrani, «Full coverage effusion cooling with inclinated holes,» in *ASME Turbo Expo*, 1995.

[81] G. Andrews, A. Asere, M. Gupta e M. Mkpadi, «Full coverage discrete hole film cooling: the influence of hole size,» in *ASME 1985 International Gas Turbine Conference and Exhibit*, 1985.

[82] R.Krewinkel, «A review of gas turbine effusion cooling studies,» *International Journal of Heat and Mass Transfer,* pp. 706-722, 2013.

[83] P. Ligrani, M. Goodro, M. Fox e H. Moon, «Full-coverage film cooling: film effectiveness and heat transfer coefficients for dense and sparse hole arrays at different blowing ratios,» *Journal of Turbomachinery,* vol. 134, n. 6, 2012.

[84] Y. Hu e H. Ji, «Numerical study of the effect of blowing angle on cooling effectiveness of an effusion cooling,» in *ASME Turbo Expo 2004: Power for Land, Sea, and Air*, 2004.

[85] K. Gustafsson e T. Johansson, «An experimental study of surface temperature distribution on effusion-cooled plates,» *Transactions of the ASME:Journal of Engineering for Gas Turbines and Power,* vol. 123, n. 2, pp. 308-3016, 2001.

[86] A. Andreini, B.Facchini, A.Picchi, L.Tarchi e F.Turrini, «Experimental and Theoretical Investigation of Thermal Effectiveness in Multiperforated Plates for Combustor Liner Effusion Cooling,» *Journal of Turbomachinery,* p. Vol.136(9), 2014.

[87] A. Andreini, A. Bonini, G. Caciolli, B. Facchini e S. Taddei, «Numerical study of aerodynamic losses of effusion cooling holes in aero-engine combustor liners,» *Journal of Engineering for Gas Turbines and Power,* vol. 133, n. 2, 2011.

[88] J. Scrittore, K. Thole e S. Burd, «Experimental characterization of film-cooling effectiveness near combustor dilution holes,» *ASME Turbo Expo 2005: Power for Land, Sea, and Air,* pp. 1339-1347, 2005.

[89] L. Tarchi, B. Facchini, F. Maiuolo e D. Coutandin, «Experimental investigation on the effects of a large recirculating area on the performance of an effusion cooled combustor liner,» *Journal of Engineering for Gas Turbines and Power,* vol. 134, n. 4, 2012.

[90] D. Bertini, L. Mazzei, S. Puggelli, A. Andreini, B. Facchini, L. Bellocci e A. Santoriello, «Numerical and Experimental Investigation on an Effusion-Cooled Lean Burn Aeronautical Combustor: Aerothermal Field and Metal Temperature,» in *ASME Turbo Expo 2018: Turbomachinery Technical Conference and Exposition*, 2018.

[91] A. Andreini, C. Carcasci, A. Ceccherini, B. Facchini, M. Surace, D. Coutandin, S. Gori e A. Peschiulli, «Combustor Liner Temperature Prediction: A Preliminary Tool Development and Its Application on Effusion Cooling Systems,» *CEAS Aeronautical Journal.*

[92] A. Andreini, R. Becchi, B. Facchini, L. Mazzei, A. Picchi e A. Peschiulli, «Effusion Cooling System Optimization for Modern Lean Burn Combustor,» in *ASME Turbo Expo 2016: Turbomachinery Technical Conference and Exposition*, 2016.

[93] B. W. Silverman, Density estimation for statistics and data analysis, Routledge, 2018.

[94] J. Han e A. Rallabandi, «Turbine blade film cooling using PSP technique,» *Frontiers in Heat and Mass Transfer ,* vol. 1, n. 1, 2010.

[95] R. Goldestein, «Film Cooling,» *Advances in heat transfer,* vol. 7, pp. 321-379, 1971.

[96] S. Baldauf, M. Scheurlen, A. Schulz e S. Wittig, «Correlation of film-cooling effectiveness from thermographic measurements at enginelike conditions,» *Journal of Turbomachinery,* vol. 124, n. 4, pp. 686-698, 2002.

[97] R. J. Goldstein, E. Eckert, H. Chiang e E. Elovic, «Effect of surface roughness on film cooling performance,» *Journal of Engineering for Gas Turbines and Power,* vol. 107, n. 1, pp. 11-116, 1985.

[98] C. Saumweber, A. Schulz e S. Wittig, «Free-stream turbulence effects on film cooling with shaped holes,» *Journal of Turbomachinery,* vol. 125, n. 1, pp. 65-73, 2003.

[99] R. Bunker, «A review of shaped hole turbine film-cooling technology,» *Journal of heat transfer ,* vol. 127, n. 4, pp. 441-453, 2005.

[100] K. Takeishi e S. Aoki, «Contribution of Heat Transfer to Turbine Blades and Vanes for High Temperature Industrial Gas Turbines Part 1: Film Cooling.,» *Annals of the New York Academy of Sciences,* vol. 934, n. 1, pp. 305-312, 2001.

[101] S. Ekkad e J. Han, «A Review of Hole Geometry and Coolant Density Effect on Film Cooling,» in *ASME 2013 Heat Transfer Summer Conference collocated with the ASME 2013 7th International Conference on Energy Sustainability and the ASME 2013 11th International Conference on Fuel Cell Science, Engineering and Technology*, Minneapolis, Minnesota, 2013.

[102] D. Pedersen, E. Eckert e R. Goldstein, « Film cooling with large density differences between the mainstream and the secondary fluid measured by the heat-mass transfer analogy,» *Journal of Heat Transfer,* vol. 99, n. 4, pp. 620-627, 1977.

[103] Z. Gao, D. Narzary e J. Han, «Film-cooling on a gas turbine blade pressure side or suction side with compound angle shaped holes,» *Journal of Turbomachinery,* vol. 131, n. 1, 2009.

[104] M. Gritsch, W. Colban, H. Schär e K. Döbbeling, «Effect of hole geometry on the thermal performance of fan-shaped film cooling holes,» *Journal of Turbomachinery,* vol. 127, n. 4, pp. 718-725, 2005.

[105] R. Schroeder e K. Thole, « Adiabatic effectiveness measurements for a baseline shaped film cooling hole,» in *ASME Turbo Expo 2014: Turbine Technical Conference and Exposition*, Düsseldorf, Germany, 2014.

[106] R. Schroeder e K. Thole, «Effect of high freestream turbulence on flowfields of shaped film cooling holes,» *Journal of Turbomachinery,* vol. 138, n. 9, 2016.

[107] R. Schroeder e K. Thole, «Effect of In-Hole Roughness on Film Cooling From a Shaped Hole,» *Journal of Turbomachinery,* vol. 139, n. 3, 2017.

[108] C. Whitfield, R. Schroeder, K. Thole e S. Lewis, «Blockage effects from simulated thermal barrier coatings for cylindrical and shaped cooling holes,» *Journal of Turbomachinery,* vol. 137, n. 9, 2015.

[109] S. Haydt, S. Lynch e S. Lewis, «The effect of area ratio change via increased hole length for shaped film cooling holes with constant expansion angles,» *Journal of Turbomachinery,* vol. 140, n. 5, 2018.

[110] D. Bohn e R. Krewinkel, «Conjugate calculation of effusion cooling with realistic cooling hole geometries,» in *ASME Turbo Expo 2009: Power for Land, Sea and Air*, Orlando, Florida, 2009.

[111] M. Jovanovic, H. d. Lange e A. v. Steenhoven, «Influence of laser drilling imperfection on film cooling performances,» in *ASME Turbo Expo 2005: Power for Land, Sea, and Air*, Reno-Tahoe, Nevada, 2005.

[112] P. Aghasi, E. Gutmark e D. Munday, «Dependence of Film Cooling Effectiveness on 3D Printed Cooling Holes,» in *ASME Turbo Expo 2016: Turbomachinery Technical Conference and Exposition*, Seoul, South Korea, 2016.

[113] T. Bacci, A. Gamannossi, L. Mazzei, A. Picchi, L. Winchler, C. Carcasci, A. Andreini, L. Abba e S. Vagnoli, «Experimental and CFD analyses of a highly-loaded gas turbine blade,» *Energy Procedia,* vol. 126, pp. 770-777, 2017.

[114] T. Bacci, A. Picchi e B. Facchini, «Flat Plate and Turbine Vane Film-Cooling Performance with Laid-Back Fan-Shaped Holes,» *International Journal of Turbomachinery, Propulsion and Power,* vol. 4, n. 2, 2019.

[115] G. Boudier, L. Gicquel, T. Poinsot, D. Bissieres e C. Bérat, «Comparison of LES, RANS and experiments in an aeronautical gas turbine combustion chamber,» *Proceedings of the Combustion Institute,* vol. 31, n. 2, pp. 3075-3082, 2007.

[116] B. Facchini, A. Magi e A. S. D. Greco, «Conjugate heat transfer simulation of a radially cooled gas turbine vane,» in *ASME Turbo Expo 2004: Power for Land, Sea, and Air*, Vienna, Austria, 2004.

[117] G. Laskowski, A. Tolpadi e M. Ostrowski, «Heat transfer predictions of film cooled stationary turbine airfoils,» in *ASME Turbo Expo: Power for Land, Sea, and Air*, Montreal, Canada, 2007.

[118] M. Mansour, K. Hosseini, J. Liu e S. Goswami, «Assessment of the impact of laminar-turbulent transition on the accuracy of heat transfer coefficient prediction in high pressure turbines,» in *ASME Turbo Expo 2006: Power for Land, Sea, and Air*, Barcelona, Spain, 2006.

[119] T. Frank e F. Menter, «Validation of URANS SST and SBES in ANSYS CFD for the Turbulent Mixing of Two Parallel Planar Water Jets Impinging on a Stationary Pool,» *ASME 2017 Verification and Validation Symposium,* Vol. %1 di %2VVS2017-4047, May 2017.

[120] T. Lenzi, L. Palanti, A. Picchi, T. Bacci, L. Mazzei, A. Andreini, B. Facchini e I. Vitale, «Time-Resolved Flow Field Analysis of Effusion Cooling System with Representative Swirling Main Flow,» in *ASME TURBO EXPO 2019: Power for Land, Sea and Air*, Phoenix, AZ, USA, 2019.

[121] J. Smagorinsky, «General Circulation Experiments with the Primitive Equations,» *Monthly Weather Review,* vol. 91, n. 3, pp. 99-164, 1963.

[122] M. Germano, U. Piomelli, P. Moin e W. H. Cabot, «A Dynamic Subgrid-Scale Eddy Viscosity Model,» *Physics of Fluids,* vol. 3, n. 7, pp. 1760-1765, 1991.

[123] M. Germano, «Turbulence: The Filtering Approach,» *Journal of Fluid Mechanics,* vol. 238, pp. 325-336, 1992.

[124] L. Mazzei, L. Winchler e A. Andreini, «Development of a numerical correlation for the discharge coefficient of round inclined holes with low crossflow,» *Computers & Fluids,* vol. 152, pp. 182-192, 2017.